Detection of Polarization in the Cosmic Microwave Background using DASI

Thesis by

John M. Kovac

A Dissertation Submitted to
the Faculty of the Division of the Physical Sciences
in Candidacy for the Degree of
Doctor of Philosophy

The University of Chicago
Chicago, Illinois

2003
(Defended December 1, 2003)

Acknowledgements

It has been a rare experience to be a part of the DASI team, assembled and led by John Carlstrom here at the University of Chicago, and to witness the combination of talents which have brought this project along from its inception to final results. Many people deserve thanks for their help in making this progression possible, certainly more than I am able to acknowledge in the few paragraphs below. The DASI team itself, which has maintained a remarkable focus of effort for the past seven years, has remained relatively small. In the past two years, Erik Leitch, Clem Pryke, John Carlstrom, and I have worked closely to share the task of completing the DASI polarization results. The experience has left me with a lasting impression of awe and admiration for their talents. I am particularly grateful for the chance to have worked nearly full-time together with Erik for over a year on the observation, reduction, and calibration of the polarization data. I am also grateful to Nils Halverson for returning to Chicago to help during the final push, for his good company during years spent together working as co-graduate students on DASI, and for showing me how to do it right. I thank Bill Holzapfel and Mark Dragovan for helping to create DASI and get it to the South Pole, and for everything I have learned from them along the way.

Of the many people who have made the DASI polarization results possible, our winter-over operators Ben Reddall and Eric Sandberg must be mentioned first. I am grateful for valuable contributions from Kim Coble, Gene Davidson, Allan Day, Gene Drag, Jacob Kooi, Ellen LaRue, Mike Loh, Bob Lowenstein, Nancy Odalen, Bob, Dave and Ed Pernic, Ethan Schartman, Bob Spotz, Mike Whitehead, John Yamasaki, and our current winter-over Miles Smith. I thank the Center for Astrophysical Research in Antarctica, Raytheon Polar Services, and the U.S. Antarctic Program for their support of the DASI project. DASI has benefited tremendously from collaboration with our sister experiment, the Cosmic Background Imager (CBI), and I would like to thank John Cartwright, Steve Padin, Tony Readhead, Martin Shepherd and the entire CBI team at Caltech for their contributions.

My time as a graduate student at the University of Chicago has been extremely rewarding. I would like to thank many members of the Physics Department faculty for teaching me physics, and Nobuko McNeill in the department office for taking care of virtually everything else! I am grateful to the Grainger Foundation for their generous fellowship support while I finished this research. My experience here has been enriched by interactions with members and visitors of the new Center for Cosmological Physics. In particular, I acknowledge many illuminating conversations with Wayne Hu on the intricacies of CMB polarization and valuable suggestions from Steve Meyer, Lyman Page, Mike Turner, and Bruce Winstein on the presentation of our results. I thank Nils Halverson and Chris Greer for helpful comments on drafts of this thesis, and I thank the members of my committee, Profs. Sean Carroll, Steve Meyer, and Tom Rosenbaum, for their valuable feedback and help in bringing this thesis to completion.

To my advisor John Carlstrom, I will never be able to adequately express my thanks. In 1997 when John asked me to work on DASI, it was not an easy decision for me to remain here in Chicago for my graduate work. It is clear to me now that I have never made a better choice. I am profoundly grateful to John for his infinite support and confidence throughout these years and for all that I continue to learn from him, and to John, Mary, Will, Alice, and Sally for their warm hospitality to Saskia and me while this work was finished.

Had I not stayed in Chicago, I may never have met my beautiful wife Saskia, and for that event above all else I am grateful. I thank her and my parents for their unfailing love and support, without which I could never have reached this point, and to them I dedicate this thesis.

Abstract

The past several years have seen the emergence of a new standard cosmological model in which small temperature differences in the cosmic microwave background (CMB) on degree angular scales are understood to arise from acoustic oscillations in the hot plasma of the early universe sourced by primordial adiabatic density fluctuations. In the context of this model, recent measurements of the temperature fluctuations have led to profound conclusions about the origin, evolution and composition of the universe. Given knowledge of the temperature angular power spectrum, this theoretical framework yields a prediction for the level of the CMB polarization with essentially no free parameters. A determination of the CMB polarization would therefore provide a critical test of the underlying theoretical framework of this standard model.

In this thesis, we report the detection of polarized anisotropy in the Cosmic Microwave Background radiation with the Degree Angular Scale Interferometer (DASI), located at the Amundsen-Scott South Pole research station. Observations in all four Stokes parameters were obtained within two $3^{\circ}\!.4$ FWHM fields separated by one hour in Right Ascension. The fields were selected from the subset of fields observed with DASI in 2000 in which no point sources were detected and are located in regions of low Galactic synchrotron and dust emission. The temperature angular power spectrum is consistent with previous measurements and its measured frequency spectral index is -0.01 (-0.16 to 0.14 at 68% confidence), where zero corresponds to a 2.73 K Planck spectrum. The power spectrum of the detected polarization is consistent with theoretical predictions based on the interpretation of CMB anisotropy as arising from primordial scalar adiabatic fluctuations. Specifically, E-mode polarization is detected at high confidence (4.9σ). Assuming a shape for the power spectrum consistent with previous temperature measurements, the level found for the E-mode polarization is 0.80 (0.56 to 1.10), where the predicted level given previous temperature data is 0.9 to 1.1. At 95% confidence, an upper limit of 0.59 is set to the level of B-mode polarization with the same shape and normalization as the E-mode spectrum. The TE correlation of the temperature and E-mode polarization is detected at 95% confidence, and also found to be consistent with predictions. These results provide strong validation of the standard model framework for the origin of CMB anisotropy and lend confidence to the values of the cosmological parameters that have been derived from CMB measurements.

Contents

Acknowledgements iii

Abstract v

List Of Tables x

List Of Figures xi

1 Introduction **1**

1.1 The Cosmic Microwave Background 3

1.2 CMB Temperature Power Spectrum 5

1.2.1 Observations: a Concordance Universe? 9

1.3 CMB Polarization 15

1.3.1 Searching for Polarization 24

1.4 The Degree Angular Scale Interferometer 26

1.4.1 Plan of this Thesis 27

2 Interferometric CMB Measurement **29**

2.1 Polarized Visibility Response 30

2.1.1 CMB Response and the uv-Plane 37

2.1.2 CMB Sensitivity 41

2.2 Building the Theory Covariance Matrix 43

3 The DASI Instrument **50**

3.1 Physical Overview 51

3.1.1 South Pole site 51

3.1.2 DASI mount . . . 53
3.1.3 Shields . . . 54
3.2 The Signal Chain . . . 56
3.2.1 Receivers . . . 57
3.2.2 Downconversion and Correlation . . . 58
3.3 HEMT Amplifiers . . . 61
3.4 Broadband Polarizers . . . 65
3.4.1 Defining the Polarization State . . . 66
3.4.2 Action of a Waveguide Retarder Element . . . 69
3.4.3 Conventional Waveguide Polarizer Designs . . . 72
3.4.4 The Multiple Element Approach . . . 74
3.4.5 Design and Construction of the DASI Polarizers . . . 84
3.4.6 Tuning, Testing, and Installation . . . 86
3.4.7 Polarizer Switching . . . 89
3.4.8 New Design Directions . . . 90

4 Calibration **92**
4.1 Relative Gain and Phase Calibration . . . 93
4.2 Absolute Cross-polar Phase Calibration . . . 95
4.3 Absolute Gain Calibration . . . 99
4.4 Leakage Correction . . . 101
4.5 Beam Measurements and Off-Axis Leakage . . . 103

5 Observations and Data Reduction **108**
5.1 CMB Field Selection . . . 108
5.2 Observing Strategy . . . 110
5.3 Data Cuts . . . 113
5.4 Reduction . . . 116
5.5 Data Consistency Tests . . . 118

5.5.1 Noise Model . . . 118
5.5.2 χ^2 Consistency Tests . . . 121
5.6 Detection of Signal . . . 126
5.6.1 Temperature and Polarization Maps . . . 128
5.6.2 Significance . . . 132

6 Likelihood Analysis 134
6.1 Likelihood Analysis Formalism . . . 135
6.1.1 Likelihood Parameters . . . 138
6.1.2 Parameter window functions . . . 140
6.1.3 Point Source Constraints . . . 143
6.1.4 Off-axis Leakage Covariance . . . 143
6.1.5 Likelihood Evaluation . . . 144
6.1.6 Simulations and Parameter Recovery Tests . . . 145
6.1.7 Reporting of Likelihood Results . . . 146
6.1.8 Goodness-of-Fit Tests . . . 147
6.2 Likelihood Results . . . 149
6.2.1 Polarization Data Analyses and E and B Results . . . 149
6.2.2 Temperature Data Analyses and T Spectrum Results . . . 159
6.2.3 Joint Analyses and TE, TB, EB Cross Spectra Results . . . 163
6.3 Systematic Uncertainties . . . 166
6.3.1 Noise, Calibration, Offsets and Pointing . . . 166
6.3.2 Foregrounds . . . 170

7 Conclusions 176
7.1 Confidence of Detection . . . 177
7.2 New Data and Future Directions . . . 180

Bibliography 187

List of Tables

2.1 Theory covariance integral coefficients for the unpolarized case 45

2.2 Theory covariance integral coefficients for the full polarized case . . . 46

3.1 Achromatic circular polarizer solutions 82

3.2 Achromatic solutions for quarter- and half-wave retarders 83

4.1 Contributions to the absolute calibration uncertainty 100

5.1 Results of χ^2 consistency tests for temperature and polarization data. 125

6.1 Results of Likelihood Analyses from Polarization Data 160

6.2 Results of Likelihood Analyses from Temperature Data 162

6.3 Results of Likelihood Analyses from Joint Dataset 167

List of Figures

1.1 Degree-scale CMB temperature power spectrum measurements, 2001. 10

1.2 Cosmological parameters from DASI temperature measurements. . . . 12

1.3 E and B-mode polarization patterns. 16

1.4 CMB polarization generated by acoustic oscillations. 19

1.5 CMB polarization generated by gravity waves. 20

1.6 Standard model predictions for CMB power spectra. 22

1.7 Experimental limits to CMB polarization, 2002. 25

2.1 Interferometer response schematic. 31

2.2 Interferometry visibility response patterns. 35

2.3 Combinations of visibilities give nearly pure E and B-patterns. 36

2.4 Coverage of the uv-plane for the DASI array. 39

2.5 Response in the uv-plane of an $RL + LR$ combination baseline. . . . 40

3.1 The DASI telescope. 52

3.2 DASI mount and ground shield 53

3.3 The optics and cryogenic components of the DASI receivers. 57

3.4 The DASI downconverter and correlator mounted behind the faceplate. 59

3.5 The CBI/DASI analog complex correlator. 60

3.6 A DASI Ka-band HEMT amplifier. 61

3.7 The lab dewar and HEMT test setup. 62

3.8 Test results for HEMT serial number DASI-Ka36. 63

3.9 Receiver temperatures as installed on the DASI telescope. 64

3.10 Action of a conventional polarizer illustrated on Poincaré sphere. . . . 75

3.11 Action of two-element polarizer illustrated on Poincaré sphere. 75
3.12 Theoretical leakage for single vs. multi-element polarizers. 77
3.13 Drawing of the DASI broadband polarizers. 84
3.14 Phase retardation curves for the two DASI polarizer elements. 85
3.15 Installation of the DASI switchable achromatic polarizers. 86
3.16 Configuration for laboratory tests of circular polarizer performance. . 87
3.17 Measured leakage for the single-element and DASI polarizers. 88
3.18 Drawing of new W-band polarizer design. 90
3.19 Performance of new W-band polarizer design. 91
4.1 DASI absolute phase offsets. 96
4.2 DASI image of the Moon. 98
4.3 Comparison of leakage for single and multi-element polarizers. 101
4.4 DASI off-axis leakage measurements. 104
4.5 Observations of the molecular cloud complex NGC 6334. 106
5.1 CMB field locations compared to galactic foreground maps. 109
5.2 Polarization signal in the epoch split s/n > 1 modes. 127
5.3 Examples of two signal to noise eigenmodes. 129
5.4 Temperature maps of the CMB fields. 130
5.5 Polarization maps formed from high signal/noise eigenmodes. 131
6.1 Parameter window functions for shaped and flat band analyses. . . . 142
6.2 E/B flat bandpower results computed on restricted ranges of data. . 150
6.3 Comparison of spectrum shapes examined for E/B analysis. 151
6.4 Results from the shaped bandpower E/B polarization analysis. 153
6.5 Results from E/B Markov chain analysis. 154
6.6 Five-band likelihood results for the E, B, T, and TE spectra. 156
6.7 Results of $E/beta_E$ polarization amplitude/spectral-index analyses. . 157
6.8 Results of Scalar/Tensor polarization analysis. 158
6.9 Results of $T/beta_T$ temperature amplitude/spectral-index analyses. . 161

6.10 Results from the shaped bandpower $T/E/TE$ joint analysis. 163
6.11 Results from the 6 parameter $T/E/TE/TB/EB$ cross spectra analysis. 165
6.12 Simulations of off-axis leakage contribution to E/B results. 169
6.13 Simulations of point source contribution to E/B results. 173
7.1 New WMAP T and TE results with previous DASI results overplotted. 182
7.2 Preliminary E and B spectrum results including new DASI data. . . 184

Chapter 1

Introduction

Like the Universe itself, our understanding of the basic elements of cosmology has been expanding in recent years at an accelerating pace. Studies of the small temperature differences imprinted across the sky in the cosmic microwave background (CMB) have helped to establish a new standard model of cosmology (see, for example, Hu & Dodelson 2002), which supplements the highly successful hot big-bang paradigm (Kolb & Turner 1990) with a precise account of the early evolution of structure in the Universe. The matching of recently detected features in the angular power spectrum of the CMB with the detailed predictions of this model has been a dramatic success, which has not only boosted confidence in our understanding of the physical processes at work in the early Universe but also allowed free parameters of the model to be determined to a precision sufficient to answer some of the most profound questions of cosmology. If our model is correct, these measurements tell us we live in a universe that is 14 billion years old, spatially flat, composed mostly of dark matter and dark energy with only a small fraction of ordinary matter, and that all the diverse structure in it evolved from primordial density fluctuations which are consistent with a quantum mechanical origin in inflation. These remarkable conclusions are strengthened by their concordance with independent lines of evidence. The acceptance of this picture, and of the apparent success of the standard model in offering a complete description of CMB physics, has been heralded as the start of the era of "precision cosmology", in which ever more sensitive measurements of the CMB are expected to further refine our knowledge of the cosmological parameters and to allow us to probe beyond the standard model into the unknown physics of dark energy and inflation.

A critical test of this picture is offered by the polarization of the CMB. The standard model predicts that the same physical processes that create the observed features in the temperature power spectrum of the CMB must also cause this radiation to be faintly polarized. The statistical properties of this CMB polarization are characterized by angular power spectra which, like the temperature power spectrum, encode a wealth of information about the parameters which govern these processes and the primordial fluctuations which seed them. In fact, the greatest future promise of "precision cosmology" with the CMB may lie in the hope of characterizing these polarization spectra to high enough precision to break parameter degeneracies and to isolate new physics that is inaccessible in the temperature signal alone. However, the standard model predictions for the basic characteristics of the polarization signal—its amplitude, angular dependence, and geometric character—are already essentially fixed by our current knowledge of the temperature power spectrum. These predictions have therefore presented a compelling target to experimentalists: a sufficiently sensitive search for CMB polarization should either confirm a fundamental prediction of the standard model, or else cast into doubt much of what think we know about the early history of the Universe.

In this thesis, we report the detection of polarization of the cosmic microwave background radiation by the Degree Angular Scale Interferometer. DASI is a compact array of 13 radio telescopes, deployed to the Amundsen-Scott South Pole station in early 2000. It was specifically built to observe variations in CMB temperature and polarization on angular scales of $1.3 - 0.2°$ ($\ell \approx 140 - 900$). As an interferometer, it does this by directly measuring Fourier patterns in the CMB sky, which on these scales are ideally suited to characterizing the physics of the standard model and the resulting features of the temperature and polarization power spectra.

Before turning to the DASI polarization measurements, we begin in this chapter with a brief overview CMB physics and observations. We will focus on the standard model's explanation for the multiple peaks of the temperature power spectrum arising from acoustic oscillations of the primordial plasma, seeded by adiabatic density fluctuations. We describe how the observation of these temperature peaks, by DASI and by others, helped to fix both the parameters of the standard model and our expectations for the CMB polarization, the dominant component of which must also arise from these oscillations. We briefly recount the long history of increasingly sensitive observational limits on CMB polarization before giving an overview of the DASI experiment and an outline for the remainder of this thesis.

1.1 The Cosmic Microwave Background

The cosmic microwave background (CMB) radiation offers a snapshot of the infant Universe. As early as the late 1940's it was suggested by George Gamow and collaborators that extrapolation of the observed expansion of the Universe backwards in time implies a hot, dense beginning some 10-20 billion years ago which could explain the abundances of the light elements and which would leave the Universe with a calculable radiation temperature of ~ 5 K today (Alpher & Herman 1949; see also Partridge 1995 for a fascinating history of early CMB work). The discovery of the microwave background (Penzias & Wilson 1965) and the explanation of its origin (Dicke et al. 1965) helped to establish the credibility of not just the hot big bang model, but the entire enterprise of observational cosmology. It was explained that the radiation dates from the epoch of recombination, when the Universe was $\sim 400,000$ years old, and its expansion had cooled the primordial plasma to a temperature at which neutral hydrogen could form. This brought the rapid Thompson scattering of thermal photons and free electrons to an abrupt halt, ending the previous tight coupling between the radiation and baryonic matter in the Universe. The CMB photons which fill our sky come from the *surface of last scattering*, which is a spherical slice through the Universe at this epoch, centered on the Earth with a radius of ~ 14 billion light years.

The three fundamental observables of the CMB radiation—its frequency spectrum, its angular variation in intensity (or temperature), and its polarization—each carry a wealth of information about the Universe at at a redshift of ~ 1000, and each have been the target of intense theoretical and experimental investigation since Penzias and Wilson's initial detection. Measurements of the frequency spectrum culminating in the definitive results from the COBE FIRAS instrument (Mather et al. 1994; Fixsen et al. 1996) have found the isotropic component of the CMB to be extremely well characterized by a 2.728 ± 0.004 K blackbody, constraining the thermal history of the hot big bang and fixing what could be considered the first measured parameter of the precision cosmology era.

Aside from a dipole term with an amplitude of several milliKelvin, which arises from the Doppler shift of the radiation field due to proper motion of Earth with respect to the comoving cosmological rest frame, the intensity of the CMB is extremely isotropic, reflecting the homogeneity of the early Universe. Intrinsic CMB temperature anisotropies were first detected at a level of 10^{-5} by the COBE DMR instrument, observing on angular scales larger than 7° (Smoot et al. 1992). The last scattering surface at these scales probes regions of the Universe that were not yet in causal contact at the epoch of recombination, and thus reflect the primordial (acausal or super-horizon) inhomogeneities which set the initial conditions for structure formation. Observations since the DMR detection have focused on scales $\lesssim 1^\circ$, where gravitationally-driven evolution of the primordial inhomogeneities can enhance or suppress the temperature anisotropies generated at last scattering. The standard model gives a rich set of predictions for the resulting variation of anisotropy power with angular scale.

1.2 CMB Temperature Power Spectrum

In this section we briefly summarize the standard model physics of CMB temperature anisotropies. Many excellent reviews exist on this topic, and we recommend to the reader Hu (2003), Zaldarriaga (2003), or Hu & Dodelson (2002) (from which we will borrow) for complete, up-to-date treatments. Here we will simply attempt to introduce the essential elements of the statistics and acoustic phenomenology of the temperature anisotropies. We will see that the framework for describing and understanding CMB polarization is a natural extension of these elements.

The observable quantity for CMB temperature anisotropy is the distribution of variations in the blackbody temperature of the incident radiation field, measured by the scalar quantity $\Delta T\left(\hat{\mathbf{x}}\right)$ over the celestial sphere. It is natural to choose a spherical harmonic representation for this field

$$\Delta T\left(\hat{\mathbf{x}}\right) = \sum_{l,m} a_{lm} Y_{lm}\left(\hat{\mathbf{x}}\right) \tag{1.1}$$

The multipoles a_{lm} are a set of random variables whose distribution defines the temperature anisotropies. Statistical invariance under rotation implies that, except for the monopole, in the ensemble average $\langle a_{lm}\rangle_{\text{ens}} = 0$. The orthonormality properties of the Y_{lm} further give us

$$\langle a^*_{lm} a_{l'm'}\rangle = \delta_{ll'}\delta_{mm'}C_l \tag{1.2}$$

i.e., that the covariance in the a_{lm} basis is diagonal and independent of m. The C_l's define the temperature angular power spectrum of the CMB. We will see below that the linear perturbation theory describing the generation of CMB anisotropy leads to independent evolution of different Fourier modes. Thus, if the initial seed fluctuations are Gaussian, the a_{lm} are truly independent, and the power spectrum given by the C_l's completely specifies their distribution, expressing the total information content of the temperature anisotropies. For observations considering only small patches of sky, a two-dimensional Fourier basis with modes of angular wavenumber $u = l/2\pi$

(see Figure 1.3, left) may be substituted for the spherical harmonics. We will make use of this "flat sky approximation" extensively in future chapters.

There are three mechanisms which generate the primary temperature anisotropies we observe in the CMB. Fluctuations in the density of the photon-baryon fluid directly result in temperature variations of the local monopole radiation field Θ at the surface of last scattering (SLS). Fluctuations in the Newtonian potential Ψ also imprint temperature variations due to gravitational redshift of CMB photons as they climb out of local potential wells (the Sachs-Wolfe effect). The third contribution results from Doppler shifts due to perturbations of the photon-baryon velocity field $\mathbf{v}$ (the local dipole) at the SLS. We can write the observed CMB temperature variation as

$$\Delta T\left(\hat{\mathbf{x}}\right) = \left(\Theta + \Psi\right)|_{\mathrm{SLS}} + \left(\hat{\mathbf{x}} \cdot \mathbf{v}_{\gamma}\right)|_{\mathrm{SLS}} + \int_{\mathrm{SLS}}^{\mathrm{present}} d\eta \left(\dot{\Psi} - \dot{\Phi}\right), \tag{1.3}$$

where the first term combines the local monopole and Newtonian potential to express the *effective temperature* at the SLS, and the second term gives the local dipole contribution. The integral term reflects the fact that time evolution (indicated by overdots) of potential (Ψ) and curvature (Φ) fluctuations along the line of sight produce further net gravitational redshifts which can generate temperature anisotropies well after last scattering (the "integrated Sachs-Wolfe" (ISW) effect). Non-linear gravitational and scattering phenomena at late times also give rise to a variety of secondary temperature anisotropies (see Hu & Dodelson 2002 for an overview). However, degree-scale anisotropies are dominated by the first two terms of Eq. 1.3, and the shape of the power spectrum is essentially explained by the evolution of density and velocity fluctuations up to last scattering.

That evolution is governed by acoustic oscillations supported by the tightly-coupled photon-baryon plasma. While the mean free path $\dot{\tau}^{-1}$ is short, the plasma acts as a perfect fluid, with an effective inertial mass due to the combined photon and baryon momenta, and a pressure determined by the photon density. Writing the fluid equations (continuity and Euler) in Fourier space to leading order in $k/\dot{\tau}$ shows that each spatial Fourier mode evolves independently according to the acoustic oscillator equation (Hu & Sugiyama 1995),

$$\left(m_{\rm eff}\dot{\Theta}_k\right)^{\cdot} + \frac{k^2}{3}\Theta_k = -\frac{k^2}{3}m_{\rm eff}\Psi_k - \left(m_{\rm eff}\dot{\Phi}_k\right)^{\cdot} \quad . \tag{1.4}$$

The left side of this equation indicates oscillations in Θ_k of frequency $\omega^2 = k^2/3m_{\rm eff} = c_s^2k^2$, where the sound speed c_s approaches $1/\sqrt{3}$ the speed of light when the photons dominate $m_{\rm eff} \approx 1 + 3\rho_b/4\rho_\gamma$. The right side gives the gravitational forcing terms which displace the zero-point of the oscillation to $(\Theta + m_{\rm eff}\Psi) = 0$ and also can pump the amplitude as the evolution of the potentials is driven by the expansion rate of the Universe. With the composition and expansion of the Universe specified, all that is needed to solve Eq. 1.4 for amplitude of the fluctuations at last scattering is a specification of their initial state.

Inflation offers a simple quantum mechanism for generating nearly scale-invariant Gaussian curvature fluctuations on superhorizon scales in the first instants of time. Also known as adiabatic density (or scalar) fluctuations, in terms of our variables these initial conditions are $\Psi_k = -(3/2)\Theta_k \approx -\Phi_k$ for spatial modes k that enter the horizon during matter-domination. Any initial velocities $v_{\gamma,k} \propto \dot{\Theta}_k$ are generically suppressed on superhorizon scales by expansion, implying that all modes will start their oscillations with the same temporal phase. With these initial conditions, assuming matter-dominated expansion (constant Φ and Ψ) and neglecting baryons ($m_{\rm eff} \approx 1$) leads to simple solutions of Eq. 1.4 which are representative of the general acoustic evolution of the effective temperature and velocity for a spatial mode k:

$$(\Theta + \Psi)_k(\eta) = \frac{1}{3}\Psi_k(0)\cos(ks) \tag{1.5}$$

$$v_{\gamma,k}(\eta) = \frac{\sqrt{3}}{3}\Psi_k(0)\sin(ks)\,. \tag{1.6}$$

where the *sound horizon* $s = \int_0^\eta c_s d\eta'$ is the distance sound has traveled by time η.

At last scattering, the sound horizon sets the physical scale of the largest mode $k^{-1} = s/\pi$ which has reached maximum compression. Modes that at last scattering have completed a half-integral number of oscillations and are passing through extrema of rarefaction or compression form a harmonic series to smaller scales. The familiar acoustic peaks in the temperature angular power spectrum (see Fig. 1.1) correspond to the maximization of variation power in the effective temperature at these scales $\sim \cos^2(ks)$, projected onto the surface of last scattering.

The oscillator solutions show that the velocity (local dipole) of the photon-baryon fluid is out of phase with these peaks, being maximized for modes which are caught midway between compression and rarefaction. However, because these flows are parallel to the wavevector $\mathbf{v}_\gamma \parallel \mathbf{k}$, and the Doppler term in Eq. 1.3 comes from the line-of-sight velocity component, velocities can only contribute to the observed temperature anisotropies where $\mathbf{k}$ lies out of the plane of the surface of last scattering, which shifts the projected modulation for a given k to larger angular scales (looking ahead, see Fig. 1.4). The resulting contribution of the velocity fluctuations to the temperature power spectrum $\propto \sin^2(ks)$ is both reduced and smeared, only partly filling in the troughs between the acoustic peaks.

The CMB power spectra are calculated by modern codes such as CMBFAST (Seljak & Zaldarriaga 1996, which we use to generate all the theoretical spectra in this thesis) by numerically deriving solutions for the sources of anisotropy in Fourier space (analogous to our Eqs. 1.5, 1.6 for the SLS monopole and dipole) and, with appropriate (ultra)spherical Bessel functions, projecting these contributions onto the presently observable multipoles. This includes effects such as the evolution of potentials on the r.h.s. of Eq. 1.4 passing into the matter-dominated epoch, which pumps small-scale fluctuations, and the dynamical effect of baryons ($m_{\rm eff} > 1$) in displacing the oscillator zero-point, enhancing compressional (odd-numbered) acoustic peaks. The shape of the power spectrum is also affected by the duration of recombination, as the mean free path $\dot{\tau}^{-1}$ grows comparable to fluctuation wavelengths k^{-1}. The resulting photon diffusion damps oscillations to smaller scales (Silk damping), while the finite thickness of the last scattering "surface" also washes out smaller scale structure, causing a *damping tail* to dramatically taper the anisotropy power beyond $l \approx 1000$. Figure 1.1 illustrates the final shape given by the standard model for the degree-scale temperature power spectrum.

1.2.1 Observations: a Concordance Universe?

In the decade between the COBE-DMR detection of CMB anisotropy and the release of results from this work in the fall of 2002, a series of increasingly sensitive ground and balloon-based experiments filled in our picture of the CMB temperature power spectrum at degree and sub-degree scales.[1] The portrait revealed of the early Universe has proved remarkably consistent with predictions of the standard framework described above, with anticipated features of the power spectrum emerging one by one from the mosaic of measurements.

Soon after COBE, a number of experiments began detecting degree-scale anisotropy which confirmed a rise in the power spectrum out to $l \approx 200$, as expected from the pumping of potentials at the radiation-matter transition (most of these many experiments are referenced in Bond et al. 2000). The shape of the first acoustic peak was first clearly revealed by the TOCO, Boomerang, and MAXIMA experiments (Miller et al. 1999; Mauskopf et al. 2000; de Bernardis et al. 2000; Hanany et al. 2000). The sharpness of this feature strongly indicates a coherent evolution from initial conditions of adiabatic density fluctuations. The standard model gives the physical scale of the peak in terms of the sound horizon at last scattering; given this, the projection to our observed angular scale is highly sensitive to the spatial curvature of the Universe. Measuring this peak at $l \approx 220$ gives evidence that our Universe contains approximately the critical density $\Omega_{\rm tot} = \rho_{\rm tot}/\rho_{\rm critical} \approx 1$ required for spatial flatness.

[1] More recent measurements, including the beautiful WMAP satellite results, are discussed in Chapter 7.

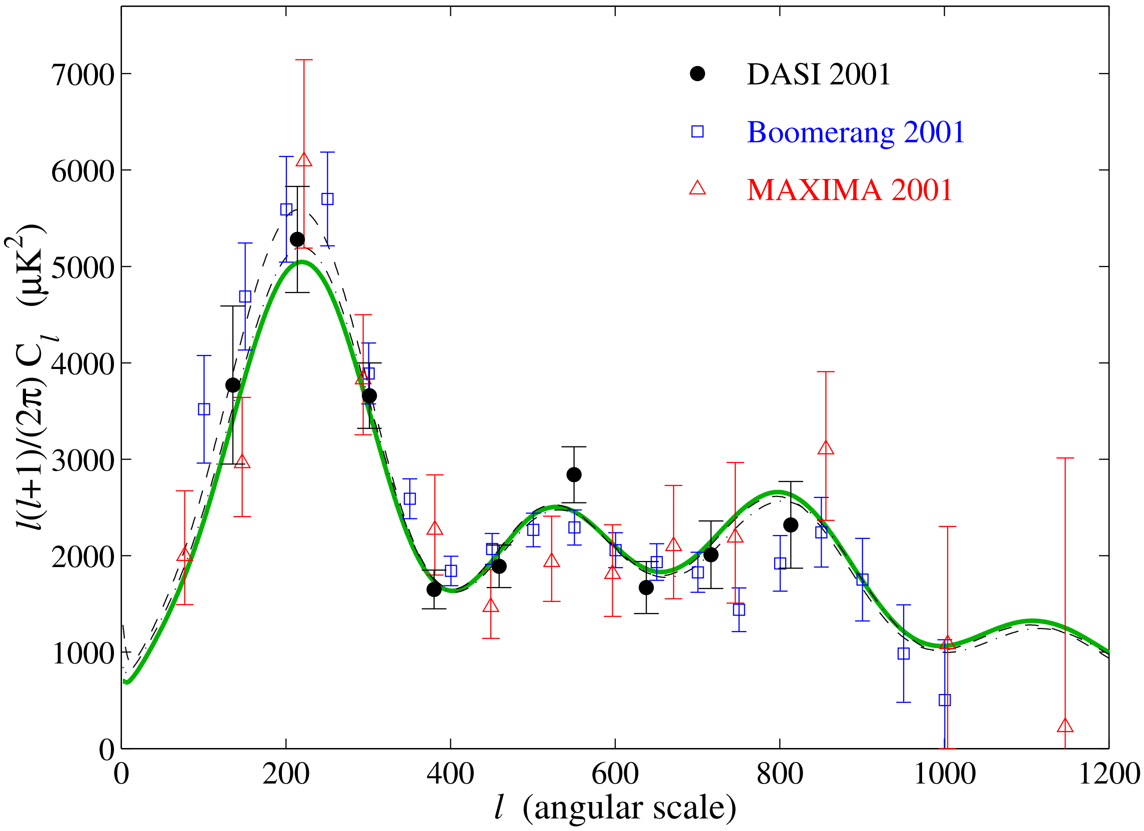

Figure 1.1 Measurements of the degree-scale CMB temperature power spectrum released at the April 2001 American Physical Society meeting in Washington, DC. Shown are the DASI results (Halverson et al. 2002) along with new analyses of the Boomerang (Netterfield et al. 2002) and MAXIMA-1 (Lee et al. 2001) data (excluding beam and calibration uncertainties). The measurements are in excellent agreement with each other and exhibit the acoustic peaks that are the expected signature of adiabatic density perturbations under the standard CMB model. Theoretical spectra calculated using this model with three different cosmological parameter combinations that fit this data well are shown: the *concordance model* (solid green), a similar model with higher τ (dashed), and a model with low h and high Ω_m (dot-dashed). See text for details. (Figure adapted from conclusion of Halverson (2002)).

In 2001, the acoustic interpretation of CMB physics received its strongest confirmation yet, with the detection of multiple acoustic peaks in the power spectrum out to $l \approx 1000$, revealed in measurements by the DASI telescope and new analyses by Boomerang and MAXIMA (Halverson et al. 2002; Netterfield et al. 2002; Lee et al. 2001). These measurements (illustrated in Fig. 1.1) fit perfectly within the predictions of the standard model, apparently tracking the evolution of the acoustic oscillations through initial compression, rarefaction, and second compression with enough precision to fix most of the parameters of the model quite well. At even finer angular scales, measurements by the CBI telescope traced the dissipation of power through the damping tail (Pearson et al. 2002; Scott & et al. 2002), lending confidence to the standard model account of recombination.

The power of these CMB temperature results to determine the cosmological parameters of the standard model is illustrated in Fig. 1.2, where we give parameter constraints derived from the DASI measurements (Pryke et al. 2002). These constraints are derived by comparing the power observed by DASI in the nine bands shown in Fig. 1.1 and at large scales by COBE against power spectra calculated for a seven parameter model grid. The first four parameters define the composition and expansion rate of the Universe, taken from combinations of the Hubble parameter h (units of 100 km s^{-1} Mpc^{-1}) and the present-day fraction of the critical density for baryons Ω_b, cold dark matter Ω_{cdm}, and dark energy Ω_Λ. Reionization, which can suppress small-scale power by rescattering CMB photons at late times, is parameterized by the optical depth τ to the SLS. Initial conditions are defined by the amplitude and power-law index of the primordial adiabatic density (scalar) fluctuations, parameterized by C_{10} and n_s.[2] Of the seven major parameters we consider, Figure 1.2 shows that the CMB temperature data alone (with a weak h prior) offer a very good

[2]Two similar parameters can be added to specify the primordial tensor fluctuations discussed in the next section. Inclusion of a running scalar index, a massive neutrino component, or a galaxy bias parameter for large-scale structure comparisons, can bring the number of parameters to twelve, though these additional parameters are not needed to explain the degree-scale temperature spectrum.

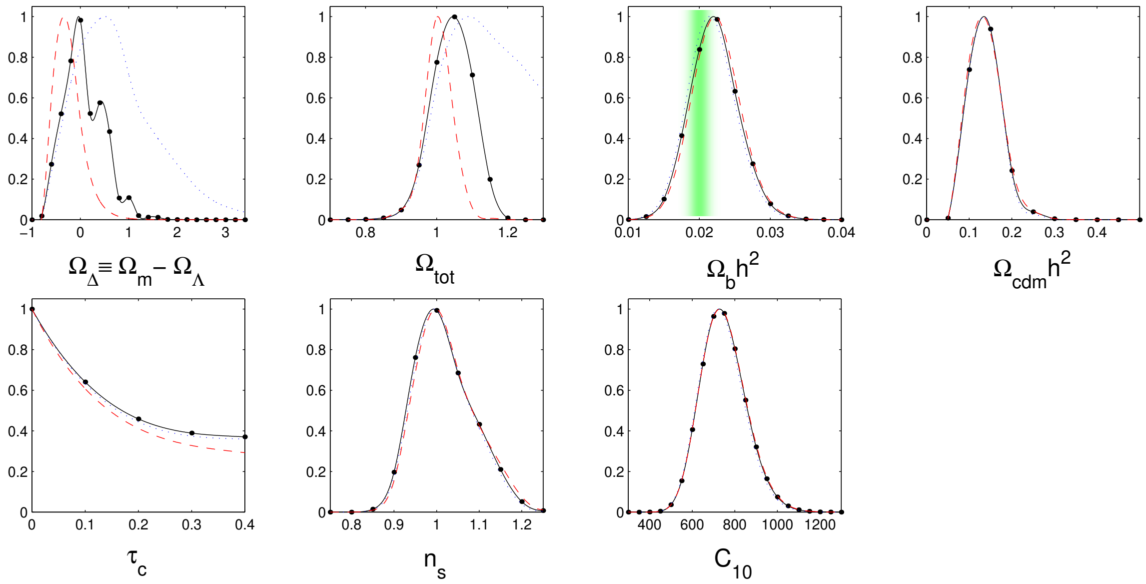

Figure 1.2 Cosmological parameter constraints from DASI temperature spectrum measurements. Shown are marginal likelihood distributions for parameters of the standard model, derived for three different priors on the Hubble parameter: no prior (dotted); a weak prior, $h > 0.45$ (solid); and a strong prior, $h = 0.72 \pm 0.08$ (dashed). Within the context of this model, degree scale CMB power spectrum measurements provide good constraints on each of these parameters except τ and Ω_Δ. The agreement of $\Omega_b h^2$ with the independent Big Bang Nucleosynthesis (BBN) constraint (green) is a crucial link between two pillars of observational cosmology (see text).

determination of five combinations.

The constraint on the physical baryon density $\Omega_b h^2 = 0.022^{+0.004}_{-0.003}$, as described above, comes from the influence of $m_{\rm eff}$ on the measured heights of the second acoustic peak compared to the first and third. This result is remarkably consistent with the Big Bang Nucleosynthesis (BBN) constraint $\Omega_b h^2 = 0.020 \pm 0.001$ derived from observations of primordial deuterium abundance (Burles et al. 2001). The concordance of these two independent determinations of the baryon content of the Universe, one involving nuclear physics in the first seconds of time, the other the acoustic dynamics of the CMB, is a major victory for the standard model.

The cold dark matter density $\Omega_{\rm cdm} h^2 = 0.14 \pm 0.04$ is also determined by the heights of the first three peaks as they trace the evolution of potential wells into the matter-domination epoch. The substantial height of the third peak is a direct signature of this non-baryonic dark matter, present in the early Universe in a $\sim$7:1 proportion to the baryons. This is consistent with the present-day dark matter content inferred from numerous observations, including cluster gas mass fractions (Grego et al. 2001; Mohr et al. 1999) and various dynamical cluster estimates (see Turner 2002 for a review).

Inflation makes three key predictions, two of which find support in this data. The constraint $\Omega_{\rm tot} = \Omega_m + \Omega_\Lambda = 1.04 \pm 0.06$, which improved from previous estimates by fixing the higher peaks, indicates the spatial curvature of the Universe is consistent with the precise flatness expected from an early inflationary burst of expansion. The spectral index $n_s = 1.01^{+0.08}_{-0.06}$, measured across the broad range of scales probed by COBE and DASI, confirms the approximate scale-invariance of the initial adiabatic density fluctuations. The amplitude of these fluctuations given by $C_{10} = 740 \pm 100$, while not predicted by inflation theory, is at the correct level to explain the power spectrum observed for present-day large scale structure (e.g. Wang et al. 2002).

The remaining parameters $\Omega_\Delta = \Omega_m - \Omega_\Lambda$ and τ are poorly constrained by the CMB temperature data alone. However, because $\Omega_{\rm tot}$ and $\Omega_m h^2$ are well-constrained, the introduction of external information about either the total matter density Ω_m or the Hubble parameter h dramatically tightens the limits on Ω_Δ. For example, including the HST Key project measurement $h = 0.72 \pm 0.08$ yields $\Omega_m = 0.40 \pm 0.15$ and $\Omega_\Lambda = 0.60 \pm 0.15$. This new measurement of the total matter density is consistent with long-converging estimates from galaxy surveys (which probe $\Omega_m h$). However, the implication that a dark energy component Ω_Λ dynamically akin to Einstein's cosmological constant dominates the present-day Universe would have shocked many (but not all, e.g. Krauss & Turner 1995), if not for recent results from high redshift supernovae. Two teams have searched for type Ia SN to serve as standardizable candles in tracking the recent expansion of the Universe, and have discovered an acceleration of the expansion rate that indicates a dark energy component dominates matter, $\Omega_\Lambda \sim \Omega_m + 0.3$ (Perlmutter et al. 1999; Riess et al. 1998).

The fact that the standard model offers an excellent fit to the observed temperature power spectrum (Fig. 1.1) is a strong argument for the validity of its assumptions. Each of the examples of concordance between cosmological parameters derived from this fit and independent lines of evidence further strengthens the case. The solid curve plotted in Fig. 1.1 is the CMBFAST-generated spectrum for what we will call the *concordance model*: $(\Omega_b, \Omega_{\rm cdm}, \Omega_\Lambda, \tau, n_s, h, C_{10}) = (0.05,0.35,0.60,0,1.00,0.65,700)$ (Ostriker & Steinhardt 1995; Krauss & Turner 1995). Two other theoretical spectra are shown to illustrate the two parameter combinations poorly-constrained by the CMB data. A model with $\tau = 0.17$ but otherwise similar parameters fits the data as well as the concordance model.[3] A model with $\Omega_\Delta = 0.4$ is marginally the best fit to the CMB data, but is less compatible with external measurements of h and Ω_m. The concordance model predicts the observed temperature spectrum very well, and we will use it as a point of reference throughout this thesis.

While the striking convergence of theory and observation in the new standard model of cosmology gives the impression of a solved problem, our concordance picture is actually a mosaic of unexplained, and in some cases unexpected mysteries. Although inflation offers a beautiful explanation for the observed spatial flatness and initial spectrum of adiabatic density fluctuations, this is only circumstantial evidence which by itself has limited power to illuminate the mechanism, energy scale, or even the certainty of the phenomenon. The apparent completeness of our account of the composition of the Universe masks a shocking ignorance of the nature of each component. Even the abundance of ordinary baryonic matter and its early origin in matter-antimatter asymmetry lacks a theoretical explanation. The dark matter particle, the dominant form of matter in the Universe, remains unknown, and though the CMB and local observations tell a consistent story of its abundance, questions

[3]This is the WMAPext preferred model discussed in Chapter 7

about its clustering dynamics persist. Most mysterious of all is the nature of the dark energy, the dominant component of the present-day Universe. Interpreted as the energy density of the vacuum state, field theory leads us to expect a value that is either exactly zero due to cancellations or else $\sim$120 orders of magnitude greater than observed (the "cosmological constant problem"). Moreover, the fact that Ω_b and $\Omega_{\rm cdm}$ are of the same order of magnitude is curious, but the fact that Ω_m and Ω_Λ are comparable today is downright disturbing (the "coincidence problem"), because this ratio evolves rapidly: $\Omega_\Lambda/\Omega_m \propto a^{-3w}$, where a is the expansion factor, and w describes the dark energy equation of state ($w = -1$ for a cosmological constant, $w < -0.5$ by current observations). Because of these two paradoxes, our current picture of the cosmological mix of matter and dark energy has been described as a "preposterous Universe" (Carroll 2001).

Much of our confidence in this current picture, and much of our hope for using precision cosmology to unravel its mysteries, depends on our understanding of the CMB. A direct test of the validity of standard model CMB physics would clearly be useful.

1.3 CMB Polarization

The same acoustic oscillations that are central to our understanding of the temperature power spectrum must also impart a polarization to the CMB (Kaiser 1983; Bond & Efstathiou 1984; Polnarev 1985). Polarization therefore provides a model-independent test of the acoustic paradigm on which our estimation of cosmological parameters from the CMB depends (Hu et al. 1997; Kinney 2001; Bucher et al. 2001). In addition, polarization measurements can in principle triple the number of observed CMB quantities, promising eventually to improve those parameter estimates dramatically (Zaldarriaga et al. 1997; Eisenstein et al. 1999).

For the two additional observables needed to describe CMB polarization, we can

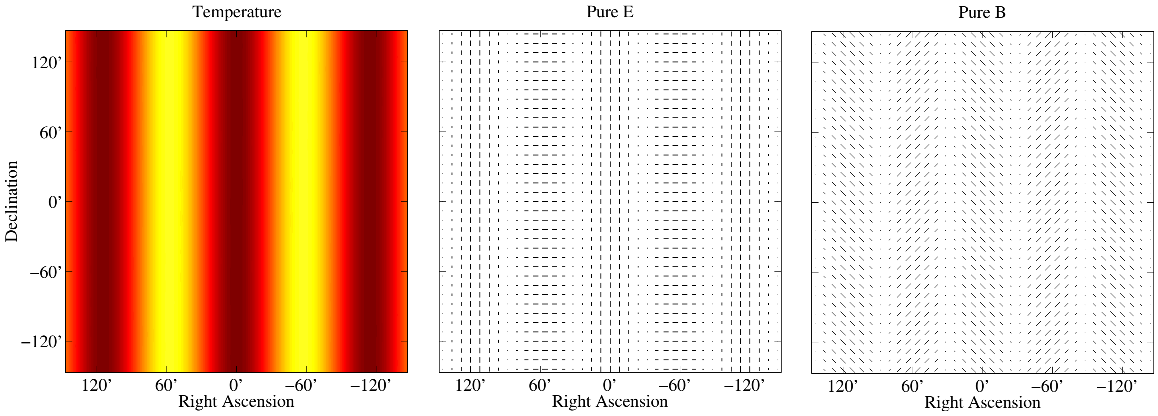

Figure 1.3 CMB temperature and polarization maps are best understood in terms of independent harmonic modes which reflect the underlying physics. Polarization maps can be decomposed into E and B-type patterns in much the same way a vector field can be decomposed into gradient and curl parts. A Fourier density mode (left) undergoing compression generates a pure E pattern (center), in which polarization is aligned parallel or perpendicular to the direction of modulation. For the B modes (right), polarization is $\pm 45°$ to this direction. Together, the E and B harmonic modes form a complete basis for polarization maps, just as conventional spherical harmonics (or on small patches of sky, Fourier modes) form a basis for temperature maps.

choose the linear Stokes parameters Q and U measured at each point on the sky. The same information is represented by the polarization amplitude $P = \sqrt{Q^2 + U^2}$ and linear orientation $\alpha = \frac{1}{2} \arctan U/Q$, typically depicted using headless polarization vectors. No circular polarization V is expected. Unlike T, the definition of Q and U depend on the orientation χ of coordinate axes, transforming as spin-2 variables: $Q + iU \rightarrow e^{-2i\chi} (Q + iU)$. For this reason, the expression analogous to Eq. 1.1 that gives the harmonic decomposition of polarization maps on the celestial sphere,

$$Q(\hat{\mathbf{x}}) \pm iU(\hat{\mathbf{x}}) = \sum_{l,m} - \left(a_{lm}^E \pm i a_{lm}^B\right) \ {}_{\pm 2}Y_{lm}(\hat{\mathbf{x}}) \tag{1.7}$$

is written in terms of combinations of spin-2 spherical harmonics ${}_{\pm 2}Y_{lm}$ (Newman & Penrose 1966; Kamionkowski et al. 1997b; Zaldarriaga & Seljak 1997). Two distinct sets of harmonic modes, called E and B-modes, correspond to the multipoles a_{lm}^E and a_{lm}^B and together form a complete basis for polarization maps. Their patterns are easily visualized in the flat sky approximation, where E and B-modes are simply Fourier modes of Q and U as defined in coordinates aligned with the 2-D wavevector $\mathbf{u}$ (Seljak 1997). Thus, for E-modes the polarization is aligned parallel or perpendicular to the direction of modulation, while for B-modes it is at $\pm 45°$ (Figure 1.3).

The polarization power spectra are defined

$$C_l^E = \left\langle a_{lm}^{E\,*} a_{lm}^E \right\rangle \qquad C_l^B = \left\langle a_{lm}^{B\,*} a_{lm}^B \right\rangle , \tag{1.8}$$

just as we defined the temperature spectrum (henceforth C_l^T) in Eq. 1.2. There are also three possible cross-spectra

$$C_l^{TE} = \left\langle a_{lm}^{T\,*} a_{lm}^E \right\rangle \qquad C_l^{TB} = \left\langle a_{lm}^{T\,*} a_{lm}^B \right\rangle \qquad C_l^{EB} = \left\langle a_{lm}^{E\,*} a_{lm}^B \right\rangle , \tag{1.9}$$

however, because the B-modes have opposite parity from E and T, parity conservation demands the last two of these to vanish. Assuming Gaussian fluctuations, the T, E, B, and TE spectra specify the complete statistics of the CMB temperature and polarization fields.

In contrast to the temperature anisotropies, CMB polarization arises from a single mechanism: the effect of a local quadrupole in the intensity of CMB photons at the point of their last scattering (Rees 1968). The Thompson scattering cross section σ_T has a directional dependence (e.g. Chandrasekhar 1960)

$$\frac{d\sigma}{d\Omega} = \frac{3}{8\pi} \left| \epsilon_{\text{in}} \cdot \epsilon_{\text{out}} \right| \sigma_T \tag{1.10}$$

on the incoming and outgoing polarization orientation. Because ϵ_{in} must be transverse, a free electron which "sees" a randomly polarized incident photon field with any $\pm \cos^2 \theta$ intensity variation will scatter those photons with an outgoing net linear polarization perpendicular (parallel) to this "hot" ("cold") quadrupole axis.

In the primordial plasma, rapid rescattering initially suppresses the local quadrupole, keeping the photon field randomly polarized and isotropic in the rest frame of the electrons. As recombination proceeds, the rapid growth of the mean free path $\dot{\tau}^{-1}$ allows the local photon field to probe spatial variations; the *second-to-last* scattering sets the conditions that generate the final polarization. Acoustic density oscillations create a local quadrupole from the spatial gradient of the local photon dipole v_γ, which is essentially the Doppler shift due to the photon-baryon velocity field (but also accounts for photon diffusion from hotter regions as tight coupling breaks down). For a spatial Fourier mode, the quadrupole amplitude is (Kaiser 1983)

$$q_{\gamma,k} = \frac{32}{15}\frac{k}{\dot{\tau}}v_{\gamma,k}. \tag{1.11}$$

This equation explains the shape and height of the polarization spectrum (Hu 2003). The factor of $k/\dot{\tau}$ reflects the fact that the local quadrupole probes the gradient in $v_{\gamma,k}$ on scales of the mean free path. Consequently, the polarization power ($\propto q^2$) rises at large scales as l^2 and peaks near the damping scale $l_d \approx 1000$ at a level roughly $(k_d/\dot{\tau})^2 \sim (1/10)^2$ the temperature power (Fig. 1.6). At smaller scales, the diffusion damping of the acoustic source $v_{\gamma,k}$ dominates, producing a damping tail similar to that of the temperature spectrum.

The pattern of CMB polarization generated by an acoustic oscillation is illustrated in Fig. 1.4. A spatial Fourier mode of wavevector $\mathbf{k}$ initially undergoes compression, the photon-baryon fluid flowing $\mathbf{v}_\gamma \parallel \mathbf{k}$ from effectively hot crests to cold troughs. The gradient in photon flow produces an $m = 0$ quadrupole in the local radiation field seen from troughs (or crests), with the hot (cold) axis parallel to the wavevector. The resulting polarization pattern in the surface of last scattering is like Fig. 1.3 (center), a pure E-mode. During the rarefaction phase the reversal of flows exchanges hot and cold, swapping the sign of the E-mode. Where the wavevector $\mathbf{k}$ is not perpendicular to our line of sight, the projected angular scale of the modulation is increased, and the amplitude of the polarization decreases as the square of the projected length of the hot (cold) quadrupole axis onto the SLS. The orientation is always parallel or perpendicular to $\mathbf{k}_{\text{proj}}$, the only direction defined by the system; density oscillations cannot generate B-mode polarization.

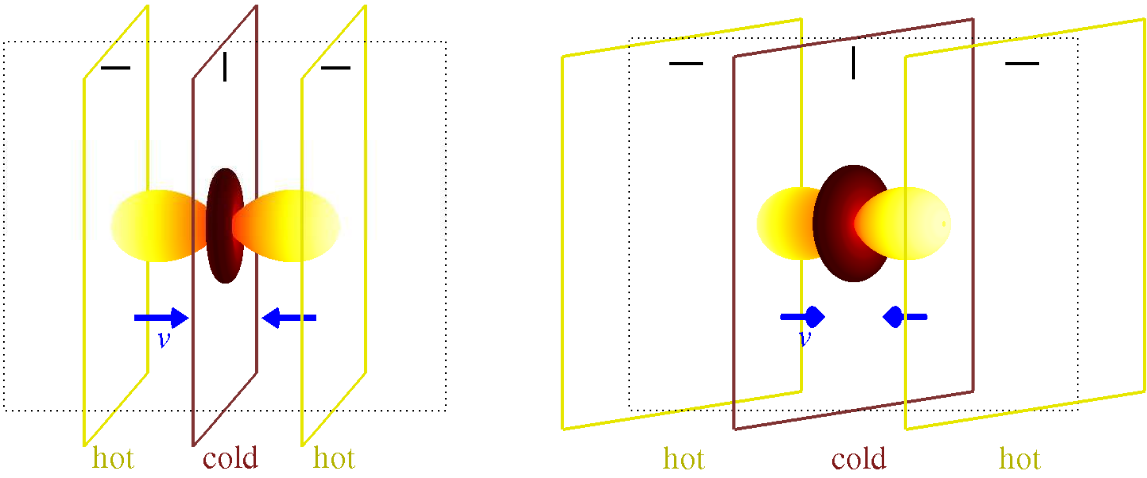

Figure 1.4 CMB polarization is directly generated by the acoustic oscillations during last scattering. As the spatial Fourier mode undergoes compression, the flow of photons $\mathbf{v}_\gamma$ from effectively hot crests toward effectively cold troughs produces an $m = 0$ quadrupole in the local radiation field seen from troughs (or crests), with the hot (cold) axis parallel to $\mathbf{k}$. This produces a pattern of linear polarization in the surface of last scattering (dotted frame) which alternates perpendicular and parallel to the projected wavevector. The angle with which $\mathbf{k}$ intersects the last scattering surface changes the projected scale of the modulation (left vs. right), but the pattern can only be E-mode (figure inspired by Hu & White 1997).

Since the velocities at last scattering are the source of this CMB polarization $q_{\gamma,k} \propto v_{\gamma,k}$, the acoustic peak structure of the E spectrum captures the evolution of these velocities on different scales. Our oscillator solutions Eqs. 1.5 and 1.6 showed that while the effective temperature traces a $\cos{(ks)}$ evolution, the velocities evolve as $\sin{(ks)}$, being maximized for modes which are caught midway between extreme compression and rarefaction. It is evident that the peaks in the E spectrum, with a $\sim \sin^2{(ks)}$ character, will be approximately 180 degrees out of phase from the temperature peaks ($\sim \cos^2{(ks)}$). The same is true of the Doppler contribution that partially fills the valleys of the temperature spectrum, but because the polarization is generated by *transverse* velocities $\mathbf{v}_\gamma \perp \hat{\mathbf{x}}$, its projection is a sharp function of angular scale. For this reason, the peaks in the E spectrum are more pronounced than those in the T spectrum (Fig. 1.6), and they offer a specific probe of the dynamics at the

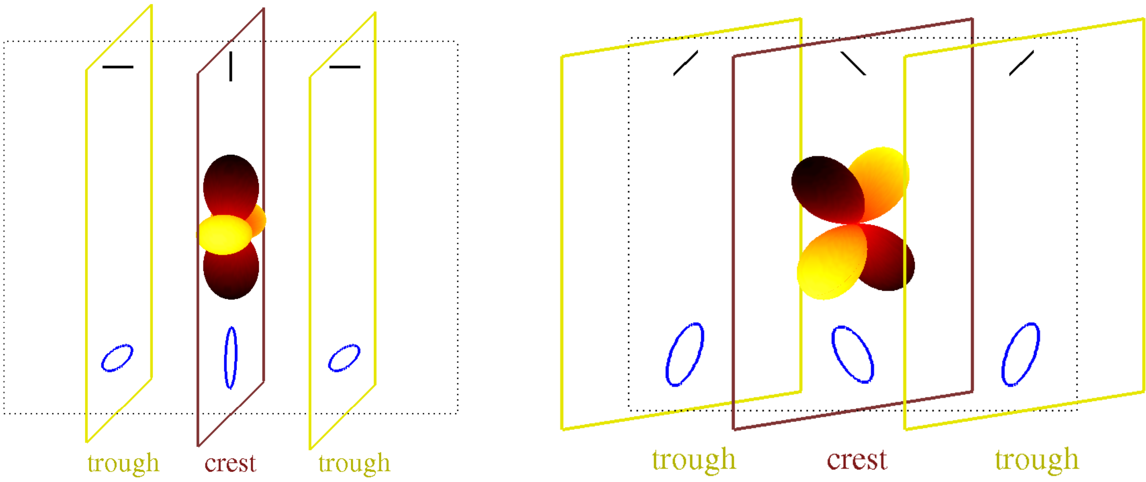

Figure 1.5 Tensor oscillations (gravity waves) present at last scattering could also contribute to CMB polarization. The transverse contraction/expansion of a standing gravity wave generates an $m = 2$ quadrupole in the local radiation field. Viewed edge-on ($\mathbf{k} \perp \hat{\mathbf{x}}$), a gravity wave with $+$ polarization projects one of its quadrupole axes onto the SLS (dotted frame), producing an E-mode pattern (left), while for a $\times$ wave the two axes cancel, giving no net polarization (not shown). However, when $\mathbf{k}$ intersects the SLS at an angle, both quadrupole axes of the $\times$ wave contribute to a net polarization on the SLS that is $\pm 45°$ to $\mathbf{k}_{\mathrm{proj}}$, producing a B-mode pattern (right).

epoch of decoupling (Zaldarriaga & Harari 1995).

It is clear that the CMB temperature and polarization anisotropy should be correlated at some level, because they are sourced by the same oscillations (Coulson et al. 1994). The spectrum of the TE correlation has roughly a $\sin(ks)\cos(ks)$ character, reflecting the fact that for a given mode, the sign of the generated E-mode reverses when the flow switches between compression and rarefaction, while the sign of the temperature signal reverses midway between these extrema. Zero crossings of the predicted TE spectrum, illustrated in Fig. 1.6, occur at the nulls of both the E and the T spectra. This unique signature in TE offers a powerful test of the underlying acoustic paradigm.

The acoustic oscillations come from primordial fluctuations in the curvature, or scalar component of the metric. Tensor metric perturbations, if present at last scattering, could also contribute to the CMB polarization (Polnarev 1985; Crittenden et al. 1993). Inflationary expansion generates a primordial spectrum of tensor perturbations which can be viewed as standing gravity waves. The time evolution of the gravity wave contraction/expansion transverse to $\mathbf{k}$ will redshift or blueshift photons in proportion to their mean free time-of-flight, producing an $m = 2$ local quadrupole. (Vector perturbations will produce an $m = 1$ quadrupole, but being suppressed by expansion these are not expected.) Figure 1.5 illustrates how the intrinsic polarization of the gravity waves with respect to the surface of last scattering leads to the generation of both E and B-mode CMB polarization (Seljak 1997; Kamionkowski et al. 1997a; Seljak & Zaldarriaga 1997). The tensor E spectrum will be unobservable, swamped by the much stronger scalar signal. The B modes are only generated by $\times$ gravity waves where $\mathbf{k}$ lies out of the plane of the SLS, so that similar to the Doppler T contribution, the tensor B spectrum is reduced compared to the tensor E spectrum,[4] with its features smeared and somewhat shifted to larger angular scales (see Fig. 1.6). The gravity waves oscillate coherently at a frequency $ck \approx \sqrt{3}c_s k$, so peaks in the tensor spectra occur with spacing that is $1/\sqrt{3}$ that of the acoustic peaks. Because the strength of the tensor quadrupole depends on the oscillation frequency and mean free path $q \propto k/\dot{\tau}$, the tensor polarization spectra rise like the scalar E spectrum, as $\sim l^2$ at large scales. However, like all radiation, gravity waves decay upon entering the horizon, so the tensor spectra peak at the horizon scale $l \sim 100$ and at smaller scales are rapidly damped.

The production of primordial gravity waves is the last and most distinctive of the three key predictions of inflation mentioned in the previous section. Detection of the B-spectrum of polarization arising from these inflationary gravity waves would be a monumental achievement for the CMB; not only would it be the "smoking gun" evidence that inflation occurred, but the energy scale and evolution of the process

[4] The actual ratio 8/13 is related to Clebsh-Gordan coefficients (Hu & White 1997).

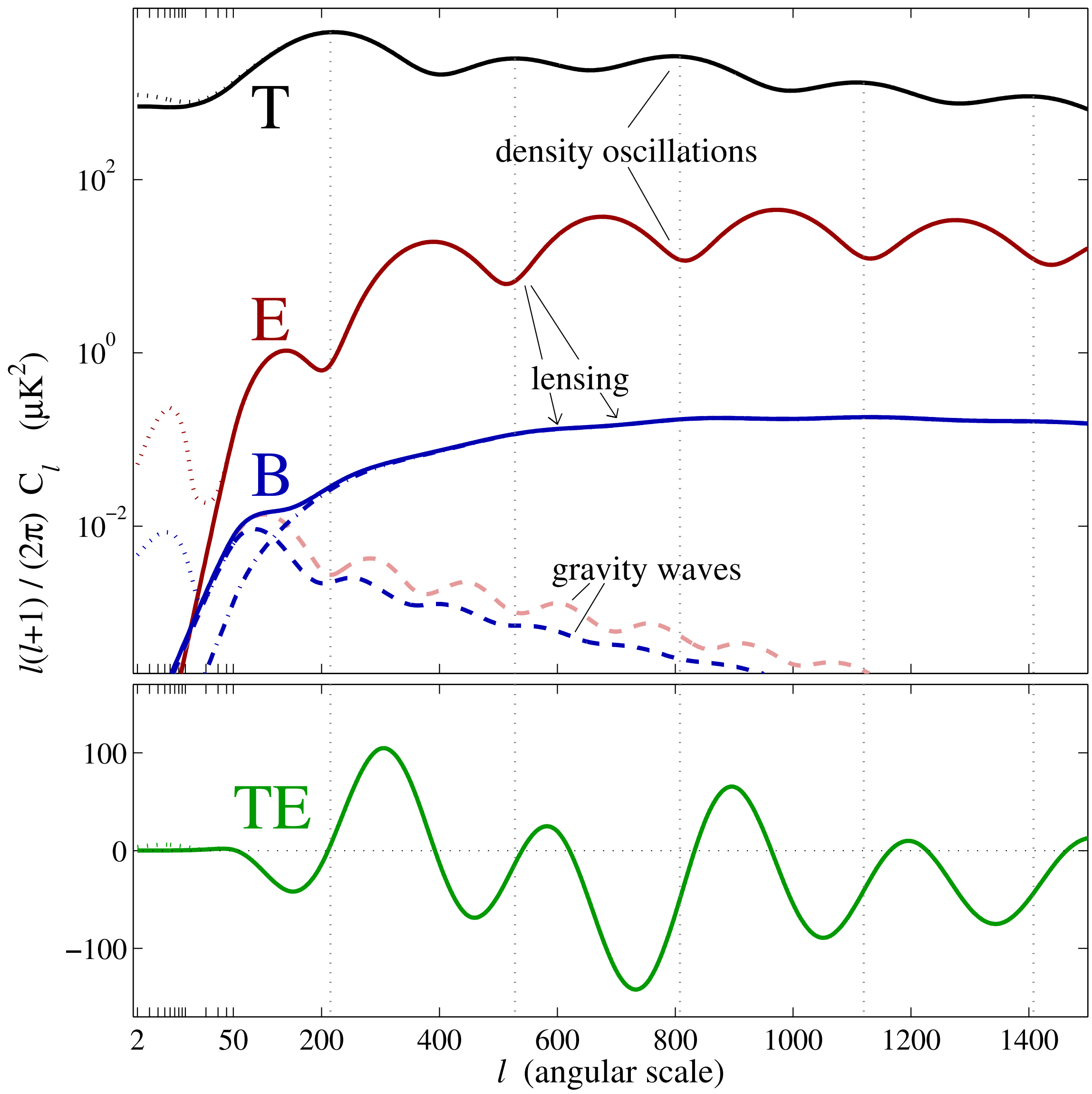

Figure 1.6 Standard model predictions for the CMB temperature and polarization power spectra. The temperature (T) and E-mode polarization (E) spectra are dominated by the dynamics of the acoustic oscillations, with a relationship encoded in their cross correlation spectrum (TE). Late-time distortion of E-modes by gravitational lensing produces a predictable level of B polarization (dot-dash), while the level of intrinsic E and B from primordial gravity waves (dashed lines) depends on the highly uncertain energy scale of inflation. The effect of early reionization (for $\tau = 0.17$) on each spectrum is shown by dotted lines at large scales. See text for details.

would be directly revealed in the level and slope of the tensor spectrum. Unfortunately, theory offers few lower limits on this level (e.g. Lyth 1997). Furthermore, the late-time distortion of E-modes by gravitational lensing from large scale structure also produces B polarization, with an envelope that roughly traces the shape of the E spectrum (Zaldarriaga & Seljak 1998). The detailed mapping of these lensing B modes could allow separation of a tensor B signal down to a minimum detectable inflationary energy scale of $\sim 10^{15}$ GeV (Hu & Okamoto 2002; Knox & Song 2002; Kesden et al. 2002). Mapping the lensing B signal will also allow accurate reconstruction of the lensing potential field, offering a powerful probe of the dark matter- and dark energy-dependent growth of structure. Possible applications include constraining the neutrino mass (Kaplinghat et al. 2003) or using cross-correlation with the ISW effect to test properties of the dark energy (Hu 2002).

These faint B-mode polarization signals, which could extend the reach of the standard model to physics at the earliest and latest times, are observational targets for the future. First, measurements of the predicted E and TE spectra will offer many opportunities to test and refine the core assumptions of the standard model. For example, observation of a peak in the E and TE spectra at large scales would be evidence of rescattering of CMB photons by early reionization (see Fig. 1.6, also Chapter 7). Comparison of the acoustic peaks of the E and T spectra allow precise constraints on isocurvature fluctuations or primordial spectrum features, the effects of which could be degenerate with cosmological parameters in the T spectrum alone. Detailed measurement of the shape of the E spectrum, which is sensitive to the way in which recombination occurred, will strictly limit the variation of fundamental constants (α, G), processes that would inject additional ionizing photons, or departures from the standard expansion history. For a review of these and other tests, see Zaldarriaga 2003.

Naturally, the first goal for experiments is the detection of CMB polarization, and the determination whether it has the level and E-mode character predicted by the standard model.

1.3.1 Searching for Polarization

The very low level of the expected CMB polarization signal, which peaks at $\lesssim 1\%$ of the power in the T spectrum, presents a great experimental challenge. As progress has been made in both sensitivity and control over systematic effects, from the earliest days of CMB measurements a series of careful experiments have achieved increasingly tight upper limits on the level of CMB polarization (see Staggs et al. 1999, for a review of CMB polarization measurements).

Penzias and Wilson set the first limit to the degree of polarization of the CMB in 1965, reporting that the new radiation they had discovered was isotropic and unpolarized within the limits of their observations (Penzias & Wilson 1965). Over the next 20 years, groups in Princeton, Italy, and Berkeley used dedicated polarimeters to set much more stringent upper limits at angular scales larger than several degrees (Caderni et al. 1978; Nanos 1979; Lubin & Smoot 1979, 1981; Lubin et al. 1983, see also Sironi et al. 1997). Although the focus of the COBE/DMR experiment was detecting the large scale temperature anisotropy, it also constrained the level of polarization at these scales (Smoot 1999). In 2001, the POLAR experiment set the best upper limits for E-mode and B-mode polarization at large angular scales, limiting these to 10 μK at 95% confidence for the multipole range $2 \leq l \leq 20$ (Keating et al. 2001).

At degree angular scales, the first limit to CMB polarization came from the Saskatoon experiment in 1993; during observations which detected temperature anisotropies at these scales, a constraint was placed on polarization (25 μK at 95% confidence for $l \sim 75$) which was the first reported limit lower than the level of the temperature signal. The best limit on similar angular scales was set by the PIQUE experiment (Hedman et al. 2002) — a 95% confidence upper limit of 8.4 μK to the E-mode signal, assuming no B-mode polarization. Analysis of polarization data from

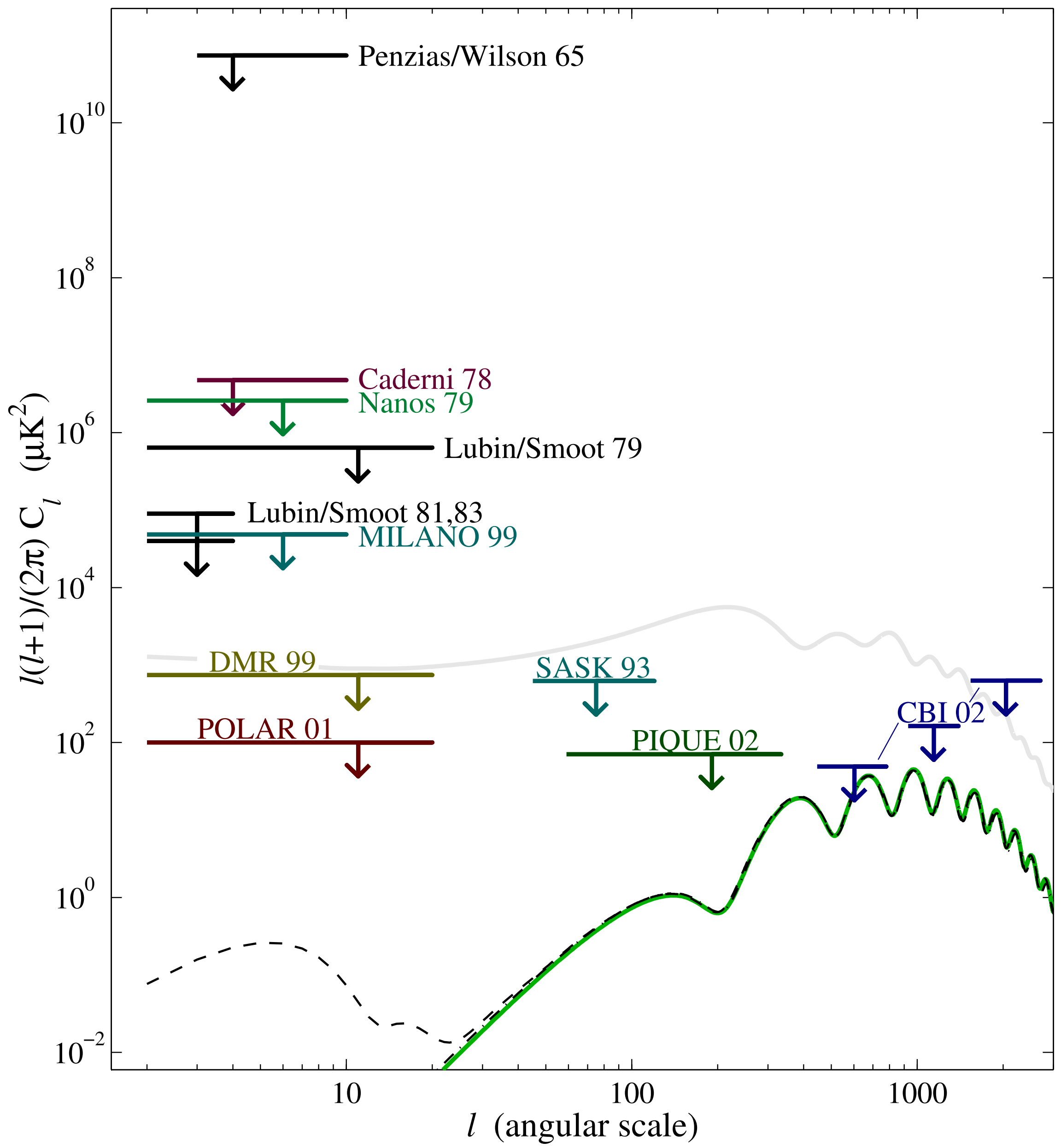

Figure 1.7 Increasingly tight experimental limits to the level of CMB polarization prior to the 2002 DASI detection. For reference, the expected level of E polarization is shown for the concordance model (solid green) and for $\tau = 0.17$ (dashed). The level of the temperature anisotropies is also shown (faint gray). See text for experimental references.

the Cosmic Background Interferometer (CBI) (Cartwright 2003) indicates upper limits similar to the PIQUE result, but on smaller scales. An attempt was also made to search for the TE correlation using the PIQUE polarization and Saskatoon temperature data (de Oliveira-Costa et al. 2003b).

Polarization measurements have also been pursued at much finer angular scales (of order an arcminute), resulting in several upper limits (e.g. Partridge et al. 1997; Subrahmanyan et al. 2000). These measurements, like those of the CBI, are notable for employing interferometry in the pursuit of CMB polarization. However, at these angular scales, corresponding to multipoles ~ 5000, the primary sources of CMB temperature and polarization anisotropy are strongly damped, and secondary anisotropies or foregrounds are expected to dominate (Hu & Dodelson 2002).

1.4 The Degree Angular Scale Interferometer

The Degree Angular Scale Interferometer (DASI) was conceived as an instrument that would take advantage of newly available low-noise HEMT amplifiers to combine interferometry with the appropriate sensitivity and angular resolution to explore the CMB power spectra in the region of the acoustic peaks. It would share many backend components with the CBI, a sister instrument to be developed at Caltech, which would pursue CMB measurements at smaller angular scales. Lead by John Carlstrom, work began on DASI at the University of Chicago in 1996. Early DASI publications chronicle the design of the instrument (e.g. Halverson et al. 1998) and theory of interferometric sensitivity to the CMB (White et al. 1999a,b).

DASI was shipped to the National Science Foundation Amundsen-Scott South Pole research station in November 1999, and in early 2000 began observations of CMB temperature anisotropy which continued throughout the following austral winter. The results of this first season, some of which have already been discussed, were released at the April 2001 APS meeting in Washington, DC, and presented in a series of three papers, published together (Leitch et al. 2002b; Halverson et al. 2002; Pryke et al. 2002, hereafter, Papers I, II and III, respectively). Paper I details the design of the instrument and observations, and includes maps of the 32 fields, each $3^\circ\!.4$ FWHM, in which temperature anisotropies were measured. Paper II presents the analysis and power spectrum results which revealed the presence of multiple acoustic peaks in the T spectrum (Fig. 1.1). Paper III gives the constraints obtained on cosmological parameters from these measurements (Fig. 1.2). The temperature observation results of Papers I-III are further detailed in the doctoral thesis of N. Halverson (2002).

1.4.1 Plan of this Thesis

Prior to the start of the 2001 season, DASI was modified to allow polarization measurements in all four Stokes parameters over the same l range as the previous measurements. Polarization data were obtained within two $3^\circ\!.4$ FWHM fields during the 2001 and 2002 austral winter seasons, and analysis of the data proceeded simultaneously with the observations. In September 2002, the results of this work were presented at the Cosmo-02 workshop in Chicago, IL. The E-mode polarization of the CMB was detected at high confidence ($\geq 4.9\sigma$). The level was found to be consistent with the E spectrum predicted to arise from acoustic oscillations due to primordial adiabatic scalar fluctuations under the standard model. No significant B-mode polarization was observed. The TE correlation of the temperature and E-mode polarization was detected at 95% confidence and also found to be consistent with predictions. This work was reported in two papers, published together. The modifications to the instrument, observational strategy, calibration and reduction of the polarization observations were presented in Paper IV (Leitch et al. 2002a). The data analysis and CMB polarization results were reported in Paper V (Kovac et al. 2002).

This thesis describes the DASI polarization measurements, from experimental design to final results. It incorporates all of the material that appeared in Paper V and much of that of Paper IV, especially within Chapters 4–6. The emphasis and organization of this thesis reflect the specific contributions of the author, which include the construction of the sensitivity-defining amplifiers and polarizers, the design of the polarization observing and calibration strategies, and the data analysis and likelihood results. Virtually every aspect of DASI, including these, has been the product of an extraordinary collaboration. The acknowledgments section and some notes in the text attempt to identify obvious contributions of other team members, but the production of Papers IV and V was essentially a team effort, and the use of the first person plural throughout this thesis is intended to acknowledge the DASI team—J. E. Carlstrom, M. Dragovan, N. W. Halverson, W. L. Holzapfel, J. M. Kovac, E. Leitch, C. Pryke, B. Reddall, and E. Sandberg—who are the co-authors of these results.

Beginning in Chapter 2, we discuss some advantages of interferometric observations of the CMB, emphasizing the match between the Fourier sky response pattern of a polarized interferometer and the E and B-mode patterns illustrated in Fig. 1.3. We also develop much of the formalism which we later apply in the analysis. Chapter 3 gives a brief overview of the DASI instrument and describes in some detail the HEMT amplifiers and the achromatic circular polarizers which were developed to give DASI precise polarization sensitivity. In Chapter 4, the actual polarization response of the instrument is verified, calibrated, and modeled using a number of dedicated observations. The CMB observations are discussed in Chapter 5, and the critical steps of data reduction, noise modeling, and consistency tests described. This chapter ends with the identification of a polarized signal in the CMB data, visibly apparent in a polarization map. Chapter 6 presents the method and results of the likelihood analyses which test the properties of the observed polarized signal, comparing it to various predictions of the standard model. Finally, in Chapter 7 we discuss these results, considering the statistical confidence of detection and the degree to which predictions of the standard model have been tested, and we conclude with a look ahead to new measurements and future directions for CMB polarization.

Chapter 2

Interferometric CMB Measurement

Most of the first attempts to use interferometry as a technique for measuring temperature and polarization variations of the CMB were made using existing large radio telescope arrays. While work by groups at the VLA (e.g. Fomalont et al. 1984; Partridge et al. 1988), ATCA (Subrahmanyan et al. 1993), and Ryle (Jones 1997) facilities produced upper limits at the very small angular scales accessible to these arrays, prototype compact instruments were developed to operate at angular scales more suited to the expected CMB signal (e.g. Timbie & Wilkinson 1984, see White et al. 1999a for other references). The advent of low-noise, broadband, millimeter-wave HEMT amplifiers (Pospieszalski et al. 1994) enabled the development of the modern generation of high-sensitivity CMB interferometer arrays, designed specifically to measure the CMB power spectra on angular scales of interest. In addition to DASI and its sister experiment the CBI, these purpose-built CMB interferometers include the VSA (Jones 1996) and the upcoming AMiBA experiment (Lo et al. 2001).

Interferometry has many attractive features for ground-based CMB measurements. Because they directly sample Fourier components of the sky, interferometers are well suited to measurements of the CMB angular power spectrum. Their angular sensitivity depends on array geometry rather than optical beam properties, offering an extremely stable and well-characterized sky response. This two dimensional response pattern is sampled instantaneously while inherently rejecting large-scale gradients in atmospheric emission. Multiple levels of fast phase switching, made possible by coherent amplification, downconversion and correlation, combine to offer superb rejection of instrumental offsets.

For observations of CMB polarization, interferometers offer several additional advantages. They can be constructed with compact, symmetrical optics that have small and stable instrumental polarization. Furthermore, linear combinations can be constructed from their direct output which are essentially pure E- and B-mode polarization response patterns on a variety of scales, closely matching the patterns illustrated in Fig. 1.3. This property of the data greatly facilitates the analysis and interpretation of the observed polarization in the context of the anticipated CMB polarization signals.

In the next chapter, we will discuss ways in which DASI's instrumental design attempts to take full advantage of these features offered by interferometry. Our focus in this chapter will be DASI's theoretical response to the CMB as a polarized interferometer. First we will derive the polarized sky response pattern for a single pair of receivers and examine the natural separation of E and B-mode polarization that it offers. Next we calculate the theory covariance matrix, which describes the statistical response of the complete dataset to the CMB power spectra. This matrix will become a basic tool of our analysis in Chapter 6. We conclude with a simple application of this matrix, as we discuss DASI's expected level of sensitivity to the polarization power spectra.

2.1 Polarized Visibility Response

The basic output of DASI's complex correlator is the *visibility*, a time-averaged cross-correlation of the electric fields measured by each pair of receivers in the array. To

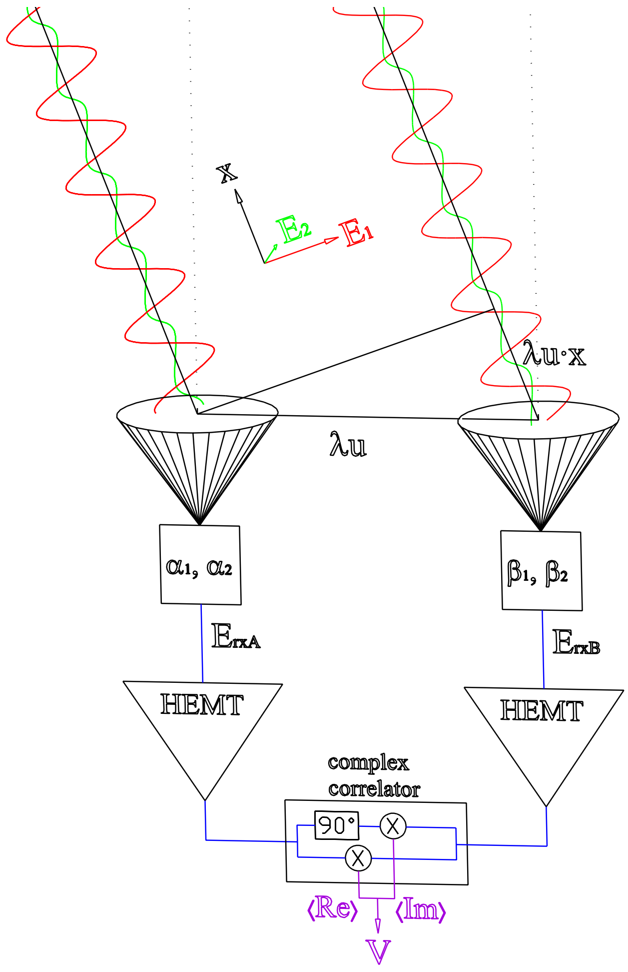

Figure 2.1 Schematic representation a single baseline $\mathbf{u}$ of an interferometer. An incident plane-wave signal has orthogonal electrical field components E_1 and E_2, which arrive at the receivers with relative path difference $\lambda\mathbf{u}\cdot\hat{\mathbf{x}}$. The focusing optics sample the electric field distribution across the aperture of each receiver, defining the directional sensitivity. The polarizing optics define the linear combination of field components ($E_{\mathrm{rxA}} \propto \alpha_1 E_1 + \alpha_2 E_2$) that is amplified and passed to the complex correlator.

derive the response of the visibility to polarized sky signals, we begin by considering the electric field as a superposition of incident plane waves. For an arbitrary quasi-monochromatic plane wave propagating in the $\mathbf{k} = -k\hat{\mathbf{x}}$ direction the electric field at location $\mathbf{x'}$ can be represented

$$\mathbf{E}\left(\mathbf{x}', t\right) = \left(\boldsymbol{\epsilon_1} E_1 + \boldsymbol{\epsilon_2} E_2\right) e^{i\mathbf{k}\cdot\mathbf{x}' - i\omega t} \ . \tag{2.1}$$

The Stokes parameters of the incident radiation field are defined

$$\begin{aligned}
I &\equiv \left\langle E_1^2 \right\rangle + \left\langle E_1^2 \right\rangle \qquad (= T) \\
Q &\equiv \left\langle E_1^2 \right\rangle - \left\langle E_1^2 \right\rangle \\
U &\equiv \left\langle 2\mathrm{Re}\left(E_1 E_2^*\right)\right\rangle \\
V &\equiv \left\langle 2\mathrm{Im}\left(E_1 E_2^*\right)\right\rangle \ .
\end{aligned} \tag{2.2}$$

It follows from these definitions that the Stokes parameters T and V are independent of the orientation of the polarization basis vectors $\boldsymbol{\epsilon_1}, \boldsymbol{\epsilon_2}$. A rotation χ of this basis about the line of sight results in the transformation of the linear polarization parameters

$$Q + iU \rightarrow e^{-2i\chi}\left(Q + iU\right) \tag{2.3}$$

quoted in Chapter 1. Choosing $\boldsymbol{\epsilon_1}$ and $\boldsymbol{\epsilon_2}$ to correspond to north and east on the sky, respectively, gives the standard astronomical definition of these parameters.

Figure 2.1 illustrates a plane wave incident on pair of receivers, A and B, which we identify with the *baseline* vector $\mathbf{u}$ that measures their separation in wavelengths. Receiver B measures the same incident field as receiver A, but with a relative phase delay $e^{2\pi i\mathbf{u}\cdot\hat{\mathbf{x}}}$ that is modulated as we vary the direction of incidence $\hat{\mathbf{x}}$ in the plane of the baseline. The focusing elements (§3.2.1) define the "primary beam" directional sensitivity by coupling the electric field incident across the aperture of each receiver to the dual-polarization signal admitted by its circular waveguide throat. Within each receiver's throat, polarizing optics (§3.4.5) further couple a particular linear combination of the complex fields E_1 and E_2 to the single-moded input of each HEMT amplifier. Neglecting the primary beam for now, the measured signals are

$$\begin{aligned} E_{\mathrm{rxA}}(t) &= (\alpha_1 E_1 + \alpha_2 E_2) && (2.4)\\ E_{\mathrm{rxB}}(t) &= (\beta_1 E_1 + \beta_2 E_2)\, e^{2\pi i \mathbf{u}\cdot\hat{\mathbf{x}}}\ . && (2.5) \end{aligned}$$

We will use the coefficients α_1, α_2 and β_1, β_2 to define the polarization states of receivers A and B, respectively.

For each baseline, the complex correlator measures the real and imaginary parts of the time-average

$$\begin{aligned} V^{AB}(\hat{\mathbf{x}}) &= \langle E_{\mathrm{rxA}} E^*_{\mathrm{rxB}} \rangle && (2.6)\\ &= \left\langle (\alpha_1 E_1 + \alpha_2 E_2)(\beta_1^* E_1^* + \beta_2^* E_2^*)\, e^{-2\pi i \mathbf{u}\cdot\hat{\mathbf{x}}} \right\rangle && (2.7)\\ &= e^{-2\pi i \mathbf{u}\cdot\hat{\mathbf{x}}} \left[\alpha_1\beta_1^* \left\langle E_1^2 \right\rangle + \alpha_2\beta_2^* \left\langle E_2^2 \right\rangle + \alpha_1\beta_2^* \langle E_1 E_2^* \rangle + \alpha_2\beta_1^* \langle E_1^* E_2 \rangle \right] && (2.8)\\ &= \frac{e^{-2\pi i \mathbf{u}\cdot\hat{\mathbf{x}}}}{2} [\alpha_1\beta_1^* (T+Q) + \alpha_2\beta_2^* (T-Q) \\ &\qquad + \alpha_1\beta_2^* (U+iV) + \alpha_2\beta_1^* (U-iV)] && (2.9)\\ &= \frac{e^{-2\pi i \mathbf{u}\cdot\hat{\mathbf{x}}}}{2} [(\alpha_1\beta_1^* + \alpha_2\beta_2^*)\, T + (\alpha_1\beta_1^* - \alpha_2\beta_2^*)\, Q \\ &\qquad + (\alpha_1\beta_2^* + \alpha_2\beta_1^*)\, U + i\,(\alpha_1\beta_2^* - \alpha_2\beta_1^*)\, V]\ . && (2.10) \end{aligned}$$

In the fourth line we have used our definitions Eq. 2.2 to rewrite the visibility response in terms of the Stokes parameters of the incident field. The general result, Eq. 2.10, is equivalent to (and simpler than) the expression given in (Thompson et al. 1991, Eq. 4.43), who credit its first derivation to Morris et al. (1964).

It is evident from Eq. 2.10 that the visibility response to an unpolarized signal T vanishes precisely when the polarization states of the two receivers are orthogonal, i.e. when $\alpha_1\beta_1^* + \alpha_2\beta_2^* = 0$. A receiver is set to a right circular (R) polarization state if it has equal response to E_1 and E_2 but with a $+90°$ phase shift, $\alpha_1/\alpha_2 = i$. The orthogonal state, left circular (L) polarization, is defined by $\beta_1/\beta_2 = -i$. If we design our polarizers so that all the receivers in the array are set to measure either pure left or pure right circular polarization, Eq. 2.10 gives the four possible combinations

$$\begin{aligned}
V^{RR}(\hat{\mathbf{x}}) &= [T+V]\, e^{-2\pi i \mathbf{u}\cdot\hat{\mathbf{x}}} \\
V^{LL}(\hat{\mathbf{x}}) &= [T-V]\, e^{-2\pi i \mathbf{u}\cdot\hat{\mathbf{x}}} \\
V^{RL}(\hat{\mathbf{x}}) &= [Q+iU]\, e^{-2\pi i \mathbf{u}\cdot\hat{\mathbf{x}}} \\
V^{LR}(\hat{\mathbf{x}}) &= [Q-iU]\, e^{-2\pi i \mathbf{u}\cdot\hat{\mathbf{x}}}\ .
\end{aligned} \tag{2.11}$$

Recovery of the full set of Stokes parameters for a given baseline requires the measurement of all four pairwise combinations of left and right circular polarization states (RR, LL, RL and LR), which we refer to as *Stokes states*. The co-polar states (RR, LL), are sensitive to the total intensity (and any incident net circular polarization), while the cross-polar states (RL, LR) measure linear polarization. The potential for residual total intensity response in the cross-polar visibilities due to *leakage* of the unwanted circular polarization state is discussed in §4.4; for the present, we assume ideal polarizers.

To obtain the full expression for the visibilities observed for a given baseline $\mathbf{u}_i$, we must integrate the plane-wave visibility response of Eqs. 2.11 over the field of view,

$$\begin{aligned}
V^{RR}(\mathbf{u}_i) &= \alpha_i \int d\hat{\mathbf{x}}\ A(\hat{\mathbf{x}},\nu_i)\,[T(\hat{\mathbf{x}})+V(\hat{\mathbf{x}})]\, e^{-2\pi i \mathbf{u}_i\cdot\hat{\mathbf{x}}} \\
V^{LL}(\mathbf{u}_i) &= \alpha_i \int d\hat{\mathbf{x}}\ A(\hat{\mathbf{x}},\nu_i)\,[T(\hat{\mathbf{x}})-V(\hat{\mathbf{x}})]\, e^{-2\pi i \mathbf{u}_i\cdot\hat{\mathbf{x}}} \\
V^{RL}(\mathbf{u}_i) &= \alpha_i \int d\hat{\mathbf{x}}\ A(\hat{\mathbf{x}},\nu_i)\,[Q(\hat{\mathbf{x}})+iU(\hat{\mathbf{x}})]\, e^{-2\pi i \mathbf{u}_i\cdot\mathbf{x}} \\
V^{LR}(\mathbf{u}_i) &= \alpha_i \int d\hat{\mathbf{x}}\ A(\hat{\mathbf{x}},\nu_i)\,[Q(\hat{\mathbf{x}})-iU(\hat{\mathbf{x}})]\, e^{-2\pi i \mathbf{u}_i\cdot\hat{\mathbf{x}}},
\end{aligned} \tag{2.12}$$

where $A(\hat{\mathbf{x}},\nu_i)$ specifies the primary beam power pattern at frequency ν_i, $T(\hat{\mathbf{x}})$, $Q(\hat{\mathbf{x}})$, $U(\hat{\mathbf{x}})$, and $V(\hat{\mathbf{x}})$ are specified in units of CMB temperature (μK), and $\alpha_i = \partial B_{\rm Planck}(\nu_i, T_{\rm CMB})/\partial T$ is the appropriate factor for converting from these units to flux density (Jy). Here we have assumed that the aperture field distributions of both receivers are identical and independent of polarization, so that the primary beam

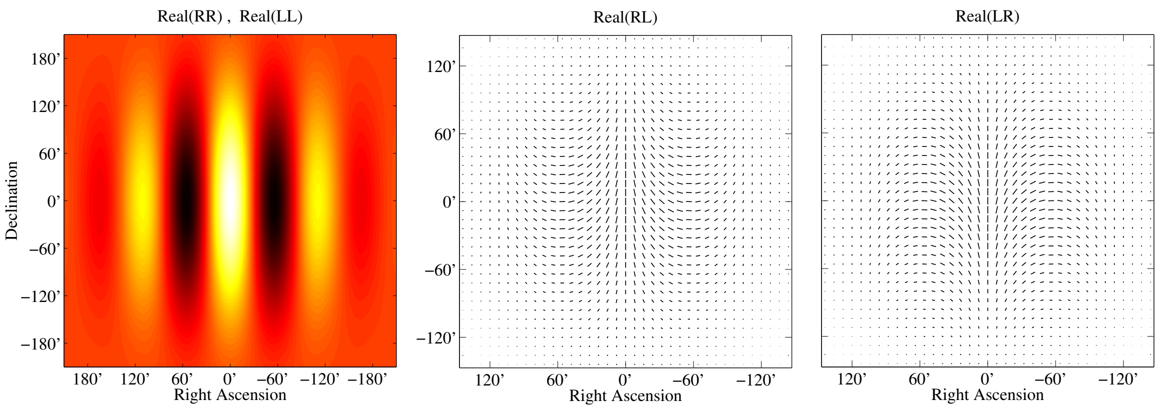

Figure 2.2 The fringe pattern of the co-polar visibility response (real part) to temperature is shown at left for one of DASI's shortest baselines ($u = 30$), oriented horizontally. RR and LL Stokes states have identical response to T. The analogous cross-polar response is to linear polarization is shown for RL and LR at right. Moving across the corrugation pattern, the change in relative phase delay combines with the $Q \pm iU$ response to cause a rotation of the plane of linear polarization response. The sense of the rotation is opposite for RL and LR.

$A(\hat{\mathbf{x}}, \nu)$ simply corresponds to the Fourier transform of the aperture field autocorrelation measured in wavelengths. Residual polarization dependence can produce off-axis leakage, considered in §4.5. In principle, the response should also be integrated over the finite correlated bandwidth $\Delta\nu$, to account for the *delay beam* destructive interference of the fringes $e^{-2\pi i \mathbf{u}_i \cdot \hat{\mathbf{x}}}$ many cycles from phase center that is caused by the scaling $|\mathbf{u}_i| \propto \nu$. However, for DASI the fractional correlated bandwidth (1 GHz / $\sim$ 30 GHz) is small enough compared to the ratio of the aperture diameter to the longest baseline (24 λ / 143 λ) that the primary beam dominates the delay beam, which can be neglected except for calculation of interfield correlations.

The sky response patterns that correspond to the integrands of Eq. 2.12 are illustrated in Fig. 2.2. The gradient in the phase term $e^{-2\pi i \mathbf{u}_i \cdot \hat{\mathbf{x}}}$ across the main beam in the direction parallel to the baseline results in a *corrugation* which, for the real part of the co-polar visibilities, gives a simple positive-negative fringe pattern. The same phase term modulating the $Q + iU$ response of the RL visibility rotates the plane

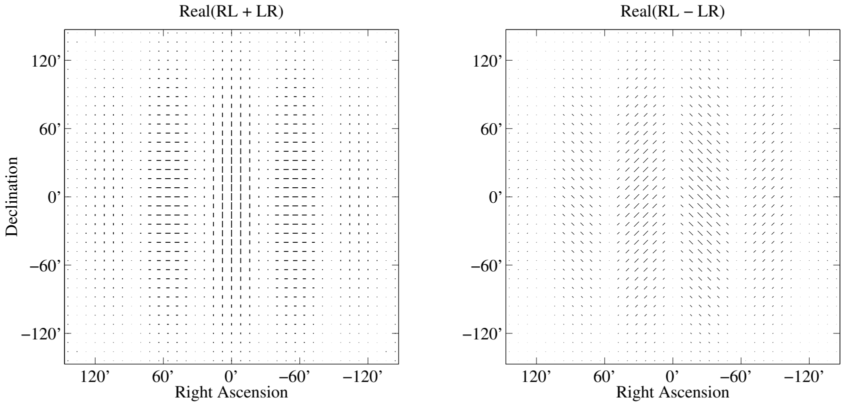

Figure 2.3 Linear combinations of the cross-polar visibilities RL and LR give nearly pure E and B-mode response patterns (compare Fig. 1.3). For a horizontal baseline, the E and B combinations result from simply adding and subtracting the patterns in Fig. 2.2. These patterns deviate from pure E or B only in the taper of the primary beam; for longer baselines the modulation scale is small compared to the primary beam, and the purity of the E/B separation becomes nearly perfect.

of linear polarization response, as in Eq. 2.3, at half the fringe rate. The $Q - iU$ response of the LR visibility is rotated by the phase gradient in the opposite sense.

It is apparent from Eq. 2.12 that the observed visibilities are closely related to the Fourier transform of the sky distribution of T, Q, and U—in fact, that if the primary beam $A(\hat{\mathbf{x}})$ were sufficiently broad, they would directly measure combinations of the Fourier mode $\mathbf{u}$ of these fields. In Chapter 1 we stated that in the flat-sky approximation, the E and B-modes are simply Fourier modes of Q and U as defined in coordinates rotated (using Eq. 2.3) to align with $\mathbf{u}$. Thus, as illustrated in Fig. 2.3, the separation of Q and U that comes from forming the combinations $RL + LR$ and $RL - LR$ offers, for a horizontal baseline, a nearly pure separation of the Fourier modes $\widetilde{E}(\mathbf{u})$ and $\widetilde{E}(\mathbf{u})$. For baselines of other orientations, a combination with an appropriate phase rotation accomplishes the same separation. Because interferometers directly measure nearly pure T, E and B Fourier modes on the sky, the data they produce easily lends itself to placing independent constraints on these power spectra.

2.1.1 CMB Response and the uv-Plane

So far, we have emphasized the interferometric response pattern in the sky plane. It is common practice in interferometry analysis to work mainly in the Fourier, or uv-plane. This approach is especially suited to analyzing response to the CMB, because in the flat sky approximation, the expected signal consists of uncorrelated Fourier modes.

The flat sky formalism offers an accurate description of CMB statistics within DASI's $3\overset{\circ}{.}4$ field of view (White et al. 1999a). In this approximation, the temperature power spectrum is defined

$$C_l^T \simeq C^T(u) \equiv \left\langle \widetilde{T}^*(\mathbf{u})\, \widetilde{T}(\mathbf{u}) \right\rangle , \tag{2.13}$$

where $\widetilde{T}(\mathbf{u})$ is the Fourier transform of $T(\mathbf{x})$ and $l/2\pi = |\mathbf{u}|$ gives the correspondence between multipole l and Fourier radius $u = |\mathbf{u}|$. The variance of the uncorrelated multipoles a_{lm} has been replaced by that of independent Fourier modes. The flat sky polarization spectra and cross spectra are similarly defined,

$$C^E(u) \equiv \left\langle \widetilde{E}^*(\mathbf{u})\, \widetilde{E}(\mathbf{u}) \right\rangle \qquad C^B(u) \equiv \left\langle \widetilde{B}^*(\mathbf{u})\, \widetilde{B}(\mathbf{u}) \right\rangle \tag{2.14}$$

$$C^{TE}(u) \equiv \left\langle \widetilde{T}^*(\mathbf{u})\, \widetilde{E}(\mathbf{u}) \right\rangle \quad C^{TB}(u) \equiv \left\langle \widetilde{T}^*(\mathbf{u})\, \widetilde{B}(\mathbf{u}) \right\rangle \quad C^{EB}(u) \equiv \left\langle \widetilde{E}^*(\mathbf{u})\, \widetilde{B}(\mathbf{u}) \right\rangle$$

The correspondence we have described between the Fourier modes of E, B and those of Q, U can be written

$$\begin{aligned} \widetilde{Q}(\mathbf{u}) &= \cos(2\chi)\, \widetilde{E}(\mathbf{u}) - \sin(2\chi)\, \widetilde{B}(\mathbf{u}) \\ \widetilde{U}(\mathbf{u}) &= \sin(2\chi)\, \widetilde{E}(\mathbf{u}) + \cos(2\chi)\, \widetilde{B}(\mathbf{u}) \ , \end{aligned} \tag{2.15}$$

where the uv-plane azimuthal angle $\chi = \arg(\mathbf{u})$ and the polarization orientation angle defining Q, U are both measured on the sky from north through east. Note that unlike in the sky plane, this transformation is strictly local in the uv-plane. Because $\widetilde{T}$, $\widetilde{Q}$, and $\widetilde{U}$ are Fourier transforms of real fields, conjugate points on the uv-plane are associated, e.g. $\widetilde{Q}(-\mathbf{u}) = \widetilde{Q}^*(\mathbf{u})$. (From the above, $\widetilde{E}(-\mathbf{u}) = \widetilde{E}^*(\mathbf{u})$ also, so we can define real fields on the sky $E(\hat{\mathbf{x}}), B(\hat{\mathbf{x}})$ through the inverse transform, although these fields—a scalar and pseudo-scalar, respectively—are non-local.) Translational invariance on the sky guarantees that in the uv-plane, except for conjugate points, there can be no non-local correlations in the CMB signals.

The visibility response in the uv-plane follows from Eqs. 2.12 and the convolution theorem, giving

$$\begin{aligned}
V^{RR}(\mathbf{u}_i) &= \alpha_i \int d\mathbf{u} \ \left[\widetilde{T}(\mathbf{u}) + \widetilde{V}(\mathbf{u})\right] \widetilde{A}(\mathbf{u}_i - \mathbf{u}, \nu_i) \\
V^{LL}(\mathbf{u}_i) &= \alpha_i \int d\mathbf{u} \ \left[\widetilde{T}(\mathbf{u}) - \widetilde{V}(\mathbf{u})\right] \widetilde{A}(\mathbf{u}_i - \mathbf{u}, \nu_i) \\
V^{RL}(\mathbf{u}_i) &= \alpha_i \int d\mathbf{u} \ \left[\widetilde{Q}(\mathbf{u}) + i\widetilde{U}(\mathbf{u})\right] \widetilde{A}(\mathbf{u}_i - \mathbf{u}, \nu_i) \\
V^{LR}(\mathbf{u}_i) &= \alpha_i \int d\mathbf{u} \ \left[\widetilde{Q}(\mathbf{u}) - i\widetilde{U}(\mathbf{u})\right] \widetilde{A}(\mathbf{u}_i - \mathbf{u}, \nu_i) \ ,
\end{aligned} \tag{2.16}$$

Using Eq. 2.15, the cross-polar visibilities can also written

$$\begin{aligned}
V^{RL}(\mathbf{u}_i) &= \alpha_i \int d\mathbf{u} \, e^{+2i\chi} \left[\widetilde{E}(\mathbf{u}) + i\widetilde{B}(\mathbf{u})\right] \widetilde{A}(\mathbf{u}_i - \mathbf{u}, \nu_i) \\
V^{LR}(\mathbf{u}_i) &= \alpha_i \int d\mathbf{u} \, e^{-2i\chi} \left[\widetilde{E}(\mathbf{u}) - i\widetilde{B}(\mathbf{u})\right] \widetilde{A}(\mathbf{u}_i - \mathbf{u}, \nu_i) \ .
\end{aligned} \tag{2.17}$$

In these equations, the Fourier transform of the primary beam power pattern $\widetilde{A}$ is equal to the autocorrelation of the aperture field distribution. This is an azimuthally symmetric function that peaks at $\widetilde{A}(0)$; its radial profile is given exactly in Halverson (2002). The finite extent of the aperture clearly implies $\widetilde{A}(\mathbf{u}) \neq 0$ only for $|\mathbf{u}| < D_\lambda$, the aperture diameter in wavelengths. Eq. 2.16 tells us that the visibilities measured for each baseline are samples at $\mathbf{u}_i$ in the uv-plane of combinations of $\widetilde{T}$, $\widetilde{Q}$, and $\widetilde{U}$ convolved with this relatively compact function. The uv-plane sampling for the $\mathbf{u}_i$ (i = 1...78) baselines of the DASI array is illustrated in Fig. 2.4. The 6-fold rotational symmetry apparent in the figure results from a 3-fold symmetry of the array configuration, together with the association of conjugate uv points. DASI's shortest and longest baselines at 35-36 GHz are $u = 30$ and $u = 143$, corresponding

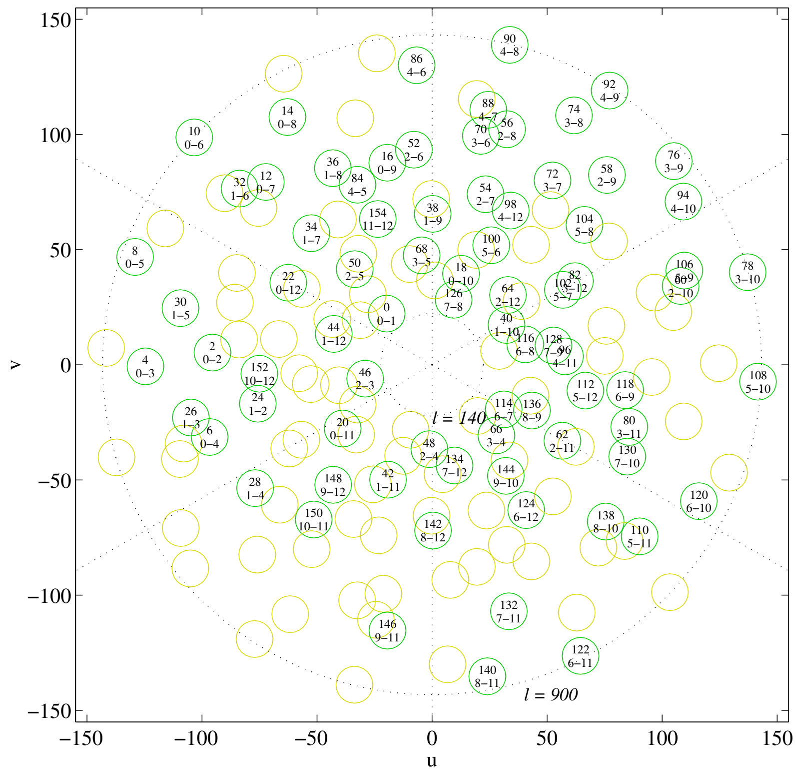

Figure 2.4 Coverage of the uv-plane for visibilities measured by the DASI array. Pairs of the 13 receivers (0..12) in the array give 78 baselines (0..154, odd numbers index the imaginary parts). The baseline vectors $\mathbf{u}_i = (\mathbf{x}_B - \mathbf{x}_A)/\lambda$ connecting the two receivers are circled in green and labeled, while conjugate points $-\mathbf{u}_i$ are circled in yellow. To improve clarity, the circles are drawn at 1/3 the actual limiting radius of $\widetilde{A}$, and baselines are drawn only for one frequency band (35-36 GHz); the pattern scales in proportion to frequency for each of the nine other bands (26-35 GHz). The resulting 780 effective baselines have a high degree of overlap in their uv-coverage.

to $l = 187$ and $l = 900$ respectively. For each of the nine lower frequency bands (26-35 GHz) the baseline lengths and radius of $\widetilde{A}$ decrease in proportion to frequency, making the shortest baseline $u = 22$ ($l = 140$) measured at 26-27 GHz.

The CMB power spectra and Eqs. 2.13–2.15) determine the variance and covariance of $\widetilde{T}, \widetilde{Q}, \widetilde{U}$ at independent points in the uv-plane, while Eqs. 2.16 tell how the observed visibilities sample these modes. This completely specifies the CMB response

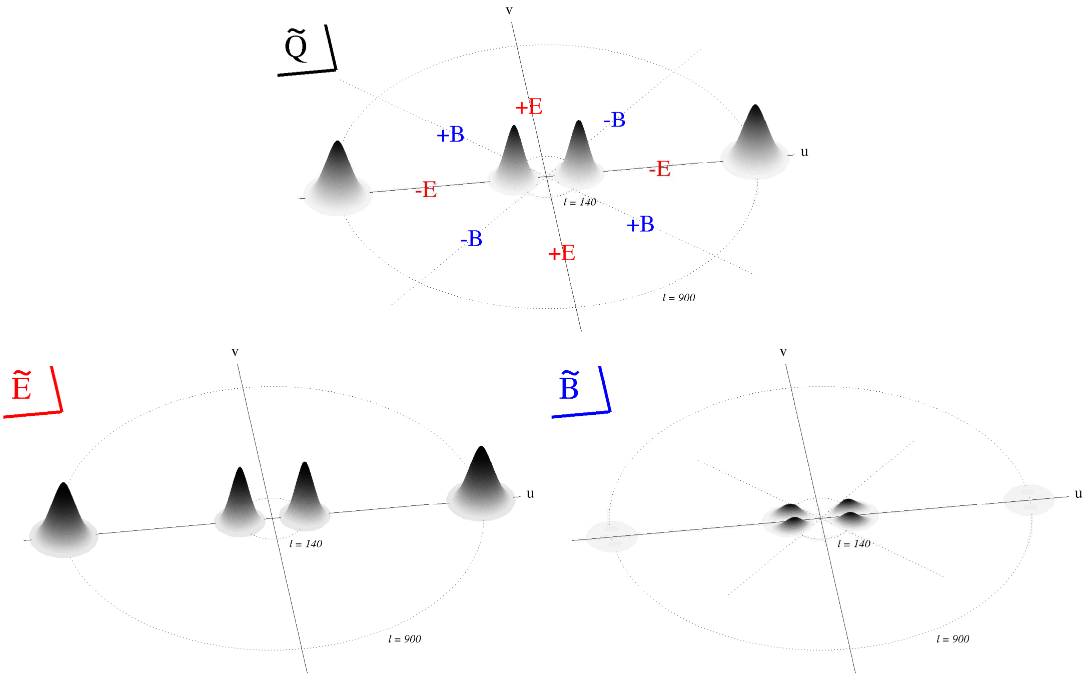

Figure 2.5 Response in the uv-plane of the $RL+LR$ combination shown in the left panel of Fig. 2.3. The two baselines illustrated are DASI's shortest and longest ($u = 22$ and $u = 143$, corresponding to $l = 140$ and $l = 900$)), oriented horizontally. Response is shown at both $\mathbf{u}_i$ and $-\mathbf{u}_i$ to emphasize the association of these points. The upper panel shows the uv-plane window function in the Q plane, the lower panels show the same response after using Eqs. 2.15 to transform points in this plane to $\widetilde{E}$ and $\widetilde{B}$. The E and B spectrum window functions are azimuthal integrals of these plots. This data combination samples mainly $\widetilde{E}$, and for long baselines the B response nearly vanishes.

of the experiment; we can use these equations to calculate and to understand the expected variance and covariance of the CMB signal in our dataset.

For example, in the previous section we considered the data combination $RL+LR$ for a single horizontal baseline. By Eq. 2.16 this combination measures $\widetilde{Q}$ convolved with $\widetilde{A}$, sampling modes in the uv-plane near $\mathbf{u_i}$. This is illustrated in the top panel of Fig. 2.5 for DASI's shortest and longest baselines ($u = 22$ and $u = 143$). Each baseline's response is shown at both $\mathbf{u}_i$ and the conjugate point $-\mathbf{u}_i$. The uv-plane window function is proportional to $|\widetilde{A}\,(\mathbf{u}_i - \mathbf{u}, \nu_i)\,|^2$, reflecting the contribution of

$\left\langle |\widetilde{Q}(\mathbf{u})|^2 \right\rangle$ at each independent uv point to the variance of the observed signal.

The lower two panels of Fig. 2.5 illustrate the result of using Eqs. 2.15 to transform $\widetilde{Q}$ to $\widetilde{E}$ and $\widetilde{B}$, deriving uv-plane window functions for the E and B contributions to the $RL + LR$ signal. The same result follows directly from Eq. 2.17; an unavoidable contribution of B to this mostly-E data combination arises from the variation of the azimuthal angle χ across the sampled region $\widetilde{A}\left(\mathbf{u}_i - \mathbf{u}, \nu_i\right)$. For long baselines $u_i \gg D_\lambda$ this variation becomes insignificant. E and B-spectrum window functions can be obtained as azimuthal integral of these uv-plane plots.

2.1.2 CMB Sensitivity

As illustrated in Fig. 2.5, the total area under the visibility window functions depends only on $|\widetilde{A}\left(\mathbf{u}, \nu_i\right)|^2$ and does not change with baseline length. For discussions of CMB sensitivity, it is helpful to temporarily change the units of Eq. 2.16, dispensing with the factor α_i which converts from units of CMB temperature to the more traditional units of Jy at beam center. In temperature units, it is appropriate to normalize the integral of the beam power pattern $\int d\hat{\mathbf{x}}\ A(\hat{\mathbf{x}}) = 1$ rather than its peak. Consequently, $\widetilde{A}(0) = 1$, i.e. the window function peak is normalized, and the area under the window function $\int d\mathbf{u}|\widetilde{A}(\mathbf{u})|^2$ is a dimensionless factor which scales as D_λ^2. For DASI at 31 GHz, this factor is 146.

For the concordance model, the second peak of the CMB E-spectrum rises at $l = 350$ to $l(l+1)C_l^E/(2\pi) \approx 15\mu K^2$ (using the conventionally plotted units), which gives $C^E(u) \simeq C_l^E = 0.00077\mu K^2$. Consider a baseline length $u \approx 55$ that is matched to this peak. If we approximate $C^E(u)$ as constant over the window function, and consider our $(RL + LR)/2$ combination with nearly pure E sensitivity, the expected variance of the polarization signal measured for this baseline is $\sim 0.00077 \times 146 = 0.11\mu K^2$.

The noise equivalent temperature of either the real or imaginary output of a complex correlator is (Thompson et al. 1991)

$$C_{\rm noise} = \frac{T_{\rm sys}}{\eta_Q\sqrt{2\Delta\nu\Delta t}} \ . \qquad (2.18)$$

For a typical DASI system temperature $T_{\rm sys} = 30K$ (see §3.3), correlator efficiency ≈ 1, and correlated bandwidth 1 GHz, this noise is $670\mu K/Hz^{1/2}$. To reach a signal-to-noise of one on either the real or imaginary part of the $(RL+LR)/2$ combination can be expected to take $\approx 10,300$ hours of continuous integration. This is far more than is practical even from the South Pole—as discussed in Chapter 5, our final dataset includes $\sim 1/10$ this integration time in each Stokes state. However, DASI's 780 baselines exhibit a high degree of overlap in their sampling of the uv-plane (see Fig. 2.4). It is clear that to search for a CMB polarization signal in the DASI dataset, it will be necessary to model and make use of the significant correlations between the response of different visibilities. Calculation of the complete visibility covariance matrix (of which the window functions we have discussed contribute only the diagonal part) is the subject of the next section.

Before turning to that task, we offer a few general remarks on CMB sensitivity and the uv-plane. The first is that a *scale invariant* power spectrum, one for which $l(l+1)C_l =$ constant, has power in the uv-plane that scales as $C(u) \propto u^{-2}$. We noted above that (in units of temperature) the area under a visibility window function scales as D_λ^2. Consequently, when observing a scale-invariant signal, increasing a baseline length with fixed D_λ reduces the rms signal-to-noise proportionally. However, scaling an entire array by some factor—both the aperture diameters and baseline lengths—broadens the window functions but leaves the sensitivity level to a scale-invariant spectrum unchanged. For a rising power spectrum like the E, an array scaled to target the signal maximum $l \sim 1000$ (e.g. CBI vs. DASI) should reach a detection in the minimum integration time.

For a fixed baseline length (or angular scale), increasing the aperture diameter increases the rms signal-to-noise in proportion to D_λ, although broader uv window functions offer less spectral resolution (Δl) and, as we have seen, worse E/B separation. The limiting case is a close-packed array, which in the limit of large N can easily be seen to offer raw sensitivity on the angular scales spanned by its baselines equivalent to that of a single-dish telescope of the same total aperture with N focal-plane receivers (e.g. Crane & Napier 1989). The DASI array has only a few "close-packed" baselines—its design reflects the goal of exploiting the advantages of interferometric measurement while providing useful sensitivity over the maximum practical range of angular scales for a single aperture size.

2.2 Building the Theory Covariance Matrix

In our analysis of data from DASI, we will consider the real and imaginary parts of each observed visibility as separate data elements. We arrange these 2 parts $\times$ 78 baselines $\times$ 10 frequency bands $\times$ 4 Stokes states into a 6240 element datavector for each separate array pointing. In this section, we calculate the full 6240 $\times$ 6240 matrix that gives the covariance of the signal in this datavector as a function of each of the CMB power spectra.

This theory covariance matrix will play a central role in the likelihood analysis of Chapter 6. It will be unnecessary to explicitly form data combinations like the $RL + LR$ example of the previous section to isolate E or B signals; the covariance between the Stokes states for a single baseline reflects their intrinsically separate response to the E and B spectra, while the covariance between baselines adjacent in the uv-plane contributes additional statistical power to separate these signals. The response of the dataset to the cross-spectra is also naturally expressed in the covariance matrix.

The general expression for an element of the theory covariance matrix, the covariance due to the CMB signal between two visibilities labeled i and j, is given

$$
\begin{aligned}
C_{Tij} &\equiv \left\langle V^{PS_i}(\mathbf{u}_i) V^{PS_j}(\mathbf{u}_j) \right\rangle \\
&= \alpha_i \alpha_j \frac{1}{2} \int d\mathbf{u}\, C^T(u)\, \widetilde{A}(\mathbf{u}_i - \mathbf{u}, \nu_i) \left[\tau_1 \widetilde{A}(\mathbf{u}_j - \mathbf{u}, \nu_j) + \tau_2 \widetilde{A}(\mathbf{u}_j + \mathbf{u}, \nu_j) \right] \\
&\quad + \frac{1}{2} \int d\mathbf{u}\, C^E(u)\, \widetilde{A}(\mathbf{u}_i - \mathbf{u}, \nu_i) \left[\varepsilon_1 \widetilde{A}(\mathbf{u}_j - \mathbf{u}, \nu_j) + \varepsilon_2 \widetilde{A}(\mathbf{u}_j + \mathbf{u}, \nu_j) \right] \\
&\quad + \frac{1}{2} \int d\mathbf{u}\, C^B(u)\, \widetilde{A}(\mathbf{u}_i - \mathbf{u}, \nu_i) \left[\beta_1 \widetilde{A}(\mathbf{u}_j - \mathbf{u}, \nu_j) + \beta_2 \widetilde{A}(\mathbf{u}_j + \mathbf{u}, \nu_j) \right] \\
&\quad + \frac{1}{2} \int d\mathbf{u}\, C^{TE}(u)\, \widetilde{A}(\mathbf{u}_i - \mathbf{u}, \nu_i) \left[\vartheta_1 \widetilde{A}(\mathbf{u}_j - \mathbf{u}, \nu_j) + \vartheta_2 \widetilde{A}(\mathbf{u}_j + \mathbf{u}, \nu_j) \right] \\
&\quad + \frac{1}{2} \int d\mathbf{u}\, C^{TB}(u)\, \widetilde{A}(\mathbf{u}_i - \mathbf{u}, \nu_i) \left[\zeta_1 \widetilde{A}(\mathbf{u}_j - \mathbf{u}, \nu_j) + \zeta_2 \widetilde{A}(\mathbf{u}_j + \mathbf{u}, \nu_j) \right] \\
&\quad + \frac{1}{2} \int d\mathbf{u}\, C^{EB}(u)\, \widetilde{A}(\mathbf{u}_i - \mathbf{u}, \nu_i) \left[\kappa_1 \widetilde{A}(\mathbf{u}_j - \mathbf{u}, \nu_j) + \kappa_2 \widetilde{A}(\mathbf{u}_j + \mathbf{u}, \nu_j) \right] .
\end{aligned}
\tag{2.19}
$$

The form of this expression follows directly from Eqs. 2.16 and 2.17. Here, PS_i and PS_j indicate the real/imaginary part and Stokes state for visibilities i and j (e.g. $\mathrm{Re}\,(RL)_i$). The factors α_i, α_j convert, as before, to flux density, while the factor of $1/2$ arises because we have separated the real and imaginary parts of the visibility.

The uv-plane window functions that appear in the integrands of Eq. 2.19 multiplying each of the power spectra have the form of the product of the aperture autocorrelation $\widetilde{A}(\nu_i)$ centered at $\mathbf{u}_i$ with the same function centered at $\mathbf{u}_j$, multiplied by coefficients $(\tau_1, ...)$ that we derive below. This overlap integral is only nonzero for baselines close in the uv-plane: $|\mathbf{u}_i - \mathbf{u}_j| < D_{\lambda i} + D_{\lambda j}$. Association of conjugate points is accounted for by also including $\widetilde{A}(\nu_j)$ centered at $-\mathbf{u}_j$. For the diagonal elements $i = j$, these overlap integrals are equivalent to the variance window functions considered in the previous section (see Fig. 2.5).

For the unpolarized case, we need consider only the first line of Eq. 2.19, and the real and imaginary parts of Stokes state RR. The coefficients τ_1, τ_2 in this case are given simply, according to Table 2.1. This case is discussed extensively in Halverson

$\tau_1 \quad \tau_2 \quad =$	$\mathrm{Re}\,(RR)_j$		$\mathrm{Im}\,(RR)_j$	
$\mathrm{Re}\,(RR)_i$	1	1	0	0
$\mathrm{Im}\,(RR)_i$	0	0	1	−1

Table 2.1 Theory covariance calculation coefficients for the unpolarized case. The coefficients τ_1, τ_2 are zero for Stokes state combinations not included in the table.

(2002), and we have built on this formalism to include polarized response to the other five CMB spectra. A program `covtheory.c` was originally authored by N. Halverson to calculate the temperature covariance matrix overlap integrals to arbitrary numerical precision. This code has been extended to treat the covariances of all Stokes states and power spectrum combinations represented in Eq.2.19, and is used for numerical calculation of all theory covariance matrices in our analyses.

The coefficients for the full polarized case, which also indicate how covariances involving at least one cross-polar visibility respond to each of the two CMB polarization spectra and three cross spectra, are given in Table 2.2. It can be seen that, like the $\widetilde{E}$ and $\widetilde{B}$ visibility response, these coefficients generally depend on the uv-plane azimuthal angle χ.

The coefficients can be directly derived from Eqs. 2.16 and 2.17 for each cell of Table 2.2. For example, if both i and j measure $\mathrm{Re}\,(RL)$ for their respective baselines,

$$
\begin{aligned}
C_{Tij} &= \left\langle V^{\mathrm{Re}(RL)}\left(\mathbf{u}_i\right) V^{\mathrm{Re}(RL)}\left(\mathbf{u}_j\right)\right\rangle \\
&= \int d\mathbf{u} \int d\mathbf{u}' \left\langle \mathrm{Re}\left(e^{i2\chi}\left(\widetilde{E}\left(\mathbf{u}\right)+i\widetilde{B}\left(\mathbf{u}\right)\right)\right) \mathrm{Re}\left(e^{i2\chi'}\left(\widetilde{E}\left(\mathbf{u}'\right)+i\widetilde{B}\left(\mathbf{u}'\right)\right)\right)\right\rangle \\
&\qquad \times \widetilde{A}\left(\mathbf{u}_i-\mathbf{u},\nu_i\right)\widetilde{A}\left(\mathbf{u}_j-\mathbf{u}',\nu_j\right) \ . \qquad (2.20)
\end{aligned}
$$

$\begin{matrix}\varepsilon_1 & \varepsilon_2\\ \beta_1 & \beta_2\\ \kappa_1 & \kappa_2\\ \hline \vartheta_1 & \vartheta_2\\ \zeta_1 & \zeta_2\end{matrix}$	=	$\mathrm{Re}\,(RL)_j$	$\mathrm{Im}\,(RL)_j$	$\mathrm{Re}\,(LR)_j$	$\mathrm{Im}\,(LR)_j$
$\mathrm{Re}\,(RL)_i$		$\begin{matrix}1 & \cos 4\chi\\ 1 & -\cos 4\chi\\ 0 & -2\sin 4\chi\end{matrix}$	$\begin{matrix}0 & \sin 4\chi\\ 0 & -\sin 4\chi\\ 0 & 2\cos 4\chi\end{matrix}$	$\begin{matrix}\cos 4\chi & 1\\ -\cos 4\chi & 1\\ -2\sin 4\chi & 0\end{matrix}$	$\begin{matrix}-\sin 4\chi & 0\\ \sin 4\chi & 0\\ -2\cos 4\chi & 0\end{matrix}$
$\mathrm{Im}\,(RL)_i$		$\begin{matrix}0 & \sin 4\chi\\ 0 & -\sin 4\chi\\ 0 & 2\cos 4\chi\end{matrix}$	$\begin{matrix}1 & -\cos 4\chi\\ 1 & \cos 4\chi\\ 0 & 2\sin 4\chi\end{matrix}$	$\begin{matrix}\sin 4\chi & 0\\ -\sin 4\chi & 0\\ 2\cos 4\chi & 0\end{matrix}$	$\begin{matrix}\cos 4\chi & -1\\ -\cos 4\chi & -1\\ -2\sin 4\chi & 0\end{matrix}$
$\mathrm{Re}\,(LR)_i$		$\begin{matrix}\cos 4\chi & 1\\ -\cos 4\chi & 1\\ -2\sin 4\chi & 0\end{matrix}$	$\begin{matrix}\sin 4\chi & 0\\ -\sin 4\chi & 0\\ 2\cos 4\chi & 0\end{matrix}$	$\begin{matrix}1 & \cos 4\chi\\ 1 & -\cos 4\chi\\ 0 & -2\sin 4\chi\end{matrix}$	$\begin{matrix}0 & -\sin 4\chi\\ 0 & \sin 4\chi\\ 0 & -2\cos 4\chi\end{matrix}$
$\mathrm{Im}\,(LR)_i$		$\begin{matrix}-\sin 4\chi & 0\\ \sin 4\chi & 0\\ -2\cos 4\chi & 0\end{matrix}$	$\begin{matrix}\cos 4\chi & -1\\ -\cos 4\chi & -1\\ -2\sin 4\chi & 0\end{matrix}$	$\begin{matrix}0 & -\sin 4\chi\\ 0 & \sin 4\chi\\ 0 & -2\cos 4\chi\end{matrix}$	$\begin{matrix}1 & -\cos 4\chi\\ 1 & \cos 4\chi\\ 0 & 2\sin 4\chi\end{matrix}$
$\mathrm{Re}\,(RR)_i$		$\begin{matrix}\cos 2\chi & \cos 2\chi\\ -\sin 2\chi & -\sin 2\chi\end{matrix}$	$\begin{matrix}\sin 2\chi & \sin 2\chi\\ \cos 2\chi & \cos 2\chi\end{matrix}$	$\begin{matrix}\cos 2\chi & \cos 2\chi\\ -\sin 2\chi & -\sin 2\chi\end{matrix}$	$\begin{matrix}-\sin 2\chi & -\sin 2\chi\\ -\cos 2\chi & -\cos 2\chi\end{matrix}$
$\mathrm{Im}\,(RR)_i$		$\begin{matrix}-\sin 2\chi & \sin 2\chi\\ -\cos 2\chi & \cos 2\chi\end{matrix}$	$\begin{matrix}\cos 2\chi & -\cos 2\chi\\ -\sin 2\chi & \sin 2\chi\end{matrix}$	$\begin{matrix}\sin 2\chi & -\sin 2\chi\\ \cos 2\chi & -\cos 2\chi\end{matrix}$	$\begin{matrix}\cos 2\chi & -\cos 2\chi\\ -\sin 2\chi & \sin 2\chi\end{matrix}$

Table 2.2 Theory covariance calculation coefficients for the full polarized case. The pattern of coefficients given in each cell of the table is specified at upper left. The table is symmetrical, so that the entries of the two right-most columns ($\mathrm{Re}\,(RR)_j$ and $\mathrm{Im}\,(RR)_j$, omitted to save space) can be read in the bottom rows, except for the $RR_i \times RR_j$ portion which is identical to Table 2.1.

We can evaluate the expectation value in the integrand

$$\begin{aligned}
&\left\langle \mathrm{Re}\left(e^{i2\chi}\left(\widetilde{E}\left(\mathbf{u}\right)+i\widetilde{B}\left(\mathbf{u}\right)\right)\right)\mathrm{Re}\left(e^{i2\chi'}\left(\widetilde{E}\left(\mathbf{u}'\right)+i\widetilde{B}\left(\mathbf{u}'\right)\right)\right)\right\rangle \\
&\quad= \left\langle \mathrm{Re}\left(e^{i2\chi}\widetilde{E}\left(\mathbf{u}\right)\right)\mathrm{Re}\left(e^{i2\chi'}\widetilde{E}\left(\mathbf{u}'\right)\right)\right\rangle + \left\langle \mathrm{Re}\left(e^{i2\chi}i\widetilde{B}\left(\mathbf{u}\right)\right)\mathrm{Re}\left(e^{i2\chi'}i\widetilde{B}\left(\mathbf{u}'\right)\right)\right\rangle \\
&\qquad+ \left\langle \mathrm{Re}\left(e^{i2\chi}\widetilde{E}\left(\mathbf{u}\right)\right)\mathrm{Re}\left(e^{i2\chi'}i\widetilde{B}\left(\mathbf{u}'\right)\right)\right\rangle + \left\langle \mathrm{Re}\left(e^{i2\chi}i\widetilde{B}\left(\mathbf{u}\right)\right)\mathrm{Re}\left(e^{i2\chi'}\widetilde{E}\left(\mathbf{u}'\right)\right)\right\rangle \\
&\quad= \left\langle \frac{1}{2}\left(e^{i2\chi}\widetilde{E}\left(\mathbf{u}\right)+e^{-i2\chi}\widetilde{E}\left(-\mathbf{u}\right)\right)\frac{1}{2}\left(e^{i2\chi'}\widetilde{E}\left(\mathbf{u}'\right)+e^{-i2\chi'}\widetilde{E}\left(-\mathbf{u}'\right)\right)\right\rangle \\
&\qquad+ \left\langle \frac{1}{2}\left(e^{i2\chi}i\widetilde{B}\left(\mathbf{u}\right)-e^{-i2\chi}i\widetilde{B}\left(-\mathbf{u}\right)\right)\frac{1}{2}\left(e^{i2\chi'}i\widetilde{B}\left(\mathbf{u}'\right)-e^{-i2\chi'}i\widetilde{B}\left(-\mathbf{u}'\right)\right)\right\rangle \\
&\qquad+ \left\langle \frac{1}{2}\left(e^{i2\chi}\widetilde{E}\left(\mathbf{u}\right)+e^{-i2\chi}\widetilde{E}\left(-\mathbf{u}\right)\right)\frac{1}{2}\left(e^{i2\chi'}i\widetilde{B}\left(\mathbf{u}'\right)-e^{-i2\chi'}i\widetilde{B}\left(-\mathbf{u}'\right)\right)\right\rangle \\
&\qquad+ \left\langle \frac{1}{2}\left(e^{i2\chi}i\widetilde{B}\left(\mathbf{u}\right)-e^{-i2\chi}i\widetilde{B}\left(-\mathbf{u}\right)\right)\frac{1}{2}\left(e^{i2\chi'}\widetilde{E}\left(\mathbf{u}'\right)+e^{-i2\chi'}\widetilde{E}\left(-\mathbf{u}'\right)\right)\right\rangle \ . \qquad (2.21)
\end{aligned}$$

Multiplying out these terms and substituting our power spectrum definitions Eqs. 2.13-2.14 gives

$$
\begin{aligned}
= \; & \frac{1}{4}C^{E}(u)\left[\left(e^{i2(\chi+\chi')}+e^{i2(-\chi-\chi')}\right)\delta(-\mathbf{u},\mathbf{u}')+\left(e^{i2(\chi-\chi')}+e^{i2(-\chi+\chi')}\right)\delta(\mathbf{u},\mathbf{u}')\right] \\
& +\frac{1}{4}C^{B}(u)\left[\left(-e^{i2(\chi+\chi')}-e^{i2(-\chi-\chi')}\right)\delta(-\mathbf{u},\mathbf{u}')+\left(e^{i2(\chi-\chi')}+e^{i2(-\chi+\chi')}\right)\delta(\mathbf{u},\mathbf{u}')\right] \\
& +\frac{i}{4}C^{EB}(u)\left[\left(e^{i2(\chi+\chi')}-e^{i2(-\chi-\chi')}\right)\delta(-\mathbf{u},\mathbf{u}')+\left(-e^{i2(\chi-\chi')}+e^{i2(-\chi+\chi')}\right)\delta(\mathbf{u},\mathbf{u}')\right] \\
& +\frac{i}{4}C^{EB}(u)\left[\left(e^{i2(\chi+\chi')}-e^{i2(-\chi-\chi')}\right)\delta(-\mathbf{u},\mathbf{u}')+\left(e^{i2(\chi-\chi')}-e^{i2(-\chi+\chi')}\right)\delta(\mathbf{u},\mathbf{u}')\right] \\
= \; & \frac{1}{2}C^{E}(u)\left[\delta(\mathbf{u},\mathbf{u}')+\cos(4\chi)\,\delta(-\mathbf{u},\mathbf{u}')\right] \\
& +\frac{1}{2}C^{B}(u)\left[\delta(\mathbf{u},\mathbf{u}')-\cos(4\chi)\,\delta(-\mathbf{u},\mathbf{u}')\right] \\
& +\frac{1}{2}C^{EB}(u)\left[-2\sin(4\chi)\,\delta(-\mathbf{u},\mathbf{u}')\right] \; .
\end{aligned}
\tag{2.22}
$$

Substituting this back into Eq. 2.20, we have

$$
\begin{aligned}
C_{Tij}= \; & \int d\mathbf{u}\int d\mathbf{u}'\frac{1}{2}C^{E}(u)\left[\delta(\mathbf{u},\mathbf{u}')+\cos(4\chi)\,\delta(-\mathbf{u},\mathbf{u}')\right]\widetilde{A}(\mathbf{u}_i-\mathbf{u},\nu_i)\,\widetilde{A}(\mathbf{u}_j-\mathbf{u}',\nu_j) \\
& +\int d\mathbf{u}\int d\mathbf{u}'\frac{1}{2}C^{B}(u)\left[\delta(\mathbf{u},\mathbf{u}')-\cos(4\chi)\,\delta(-\mathbf{u},\mathbf{u}')\right]\widetilde{A}(\mathbf{u}_i-\mathbf{u},\nu_i)\,\widetilde{A}(\mathbf{u}_j-\mathbf{u}',\nu_j) \\
& +\int d\mathbf{u}\int d\mathbf{u}'\frac{1}{2}C^{EB}(u)\left[0-2\sin(4\chi)\,\delta(-\mathbf{u},\mathbf{u}')\right]\widetilde{A}(\mathbf{u}_i-\mathbf{u},\nu_i)\,\widetilde{A}(\mathbf{u}_j-\mathbf{u}',\nu_j) \\
= \; & \frac{1}{2}\int d\mathbf{u}\,C^{E}(u)\,\widetilde{A}(\mathbf{u}_i-\mathbf{u},\nu_i)\left[\widetilde{A}(\mathbf{u}_j-\mathbf{u},\nu_j)+\cos(4\chi)\,\widetilde{A}(\mathbf{u}_j+\mathbf{u},\nu_j)\right] \\
& +\frac{1}{2}\int d\mathbf{u}\,C^{B}(u)\,\widetilde{A}(\mathbf{u}_i-\mathbf{u},\nu_i)\left[\widetilde{A}(\mathbf{u}_j-\mathbf{u},\nu_j)-\cos(4\chi)\,\widetilde{A}(\mathbf{u}_j+\mathbf{u},\nu_j)\right] \\
& +\frac{1}{2}\int d\mathbf{u}\,C^{EB}(u)\,\widetilde{A}(\mathbf{u}_i-\mathbf{u},\nu_i)\left[0-2\sin(4\chi)\,\widetilde{A}(\mathbf{u}_j+\mathbf{u},\nu_j)\right] \; ,
\end{aligned}
\tag{2.23}
$$

which is our final result.

The coefficients for the other visibility combinations can be derived in a similarly direct manner, but a less tedious approach is to use Eqs.2.16 and 2.17 to write the visibility uv-plane point response in matrix form

$$\begin{bmatrix} \mathrm{Re}\left(RL\left(\mathbf{u}\right)\right) \\ \mathrm{Im}\left(RL\left(\mathbf{u}\right)\right) \\ \mathrm{Re}\left(LR\left(\mathbf{u}\right)\right) \\ \mathrm{Im}\left(LR\left(\mathbf{u}\right)\right) \\ \mathrm{Re}\left(RR\left(\mathbf{u}\right)\right) \\ \mathrm{Im}\left(RR\left(\mathbf{u}\right)\right) \end{bmatrix} = \begin{bmatrix} \cos(2\chi) & -\sin(2\chi) & -\sin(2\chi) & -\cos(2\chi) & 0 & 0 \\ \sin(2\chi) & \cos(2\chi) & \cos(2\chi) & -\sin(2\chi) & 0 & 0 \\ \cos(2\chi) & \sin(2\chi) & -\sin(2\chi) & \cos(2\chi) & 0 & 0 \\ -\sin(2\chi) & \cos(2\chi) & -\cos(2\chi) & -\sin(2\chi) & 0 & 0 \\ 0 & 0 & 0 & 0 & 1 & 0 \\ 0 & 0 & 0 & 0 & 0 & 1 \end{bmatrix} \begin{bmatrix} \mathrm{Re}\left(\widetilde{E}\left(\mathbf{u}\right)\right) \\ \mathrm{Im}\left(\widetilde{E}\left(\mathbf{u}\right)\right) \\ \mathrm{Re}\left(\widetilde{B}\left(\mathbf{u}\right)\right) \\ \mathrm{Im}\left(\widetilde{B}\left(\mathbf{u}\right)\right) \\ \mathrm{Re}\left(\widetilde{T}\left(\mathbf{u}\right)\right) \\ \mathrm{Im}\left(\widetilde{T}\left(\mathbf{u}\right)\right) \end{bmatrix} \tag{2.24}$$

Call this matrix $\mathbf{T}$, and let us generically label the coefficients for each of the six power spectra in Eq. 2.19 as ξ_1, ξ_2. It is trivial to write the 6×6 matrices $\mathbf{C}_{\xi 1,2}$ that give the covariance of the vector on the right due to each of the power spectra and for each of the cases (1) $\mathbf{u}_i = \mathbf{u}_j$ and (2) $\mathbf{u}_i = -\mathbf{u}_j$. Acting with $\mathbf{T}$ on each these matrices, $\mathbf{T}\mathbf{C}_{\xi 1,2}\mathbf{T}^t = \mathbf{\Xi_{1,2}}$, gives the covariance in the basis of the vector at left, that of the visibility uv-plane point response. Each of the resulting matrices $\Xi_{1,2}$ gives the values of a particular coefficient ξ_1 or ξ_2 within all the cells of Table 2.2.

A similar approach simplifies the derivation of the *interfield* covariance, where visibilities i and j are measured on different fields which are near enough for the CMB signals in each to be sustantially correlated. The translation to a different pointing center for the visibility j results in a relative phase gradient

$$\gamma(\mathbf{u}) = 2\pi\mathbf{u} \cdot (\hat{\mathbf{x}}_i - \hat{\mathbf{x}}_j) \tag{2.25}$$

which applies to the visibility uv-plane point response, and must be included inside the integrals of Eqs.2.16 and 2.17. The rotation by angle γ between the real and imaginary parts of the point response of j across the uv-plane can be accounted for by applying a matrix $\mathbf{R}$ to the previous 6×6 coefficient matrices $\Xi \rightarrow \mathbf{R}\Xi$, where $\mathbf{R}$ is a block-diagonal matrix of 2×2 real rotation matrices. The resulting coefficients for Eq. 2.19 are trigonometric functions of both γ and χ. Although the interfield covariance is straightforward to calculate, we have found it to be negligible for the DASI fields at the separation distance ($8.6°$) used for the two difference fields of the polarization observations, so this effect is not included in the covariance matrices we use to analyze the polarization data in Chapters 5 and 6.

Chapter 3

The DASI Instrument

DASI is a compact interferometric array, specifically designed to measure anisotropies in the temperature and polarization of the Cosmic Microwave Background (CMB) at degree and sub-degree angular scales from the South Pole.

The array consists of 13 horn antennas mounted on a rigid faceplate in a three-fold symmetric pattern. Following each antenna is a cooled, low-noise HEMT amplifier optimized for the 26 – 36 GHz DASI band. The signals from the receivers are combined in a broadband analog correlator that computes the complex visibilities, between pairs of receivers in ten 1-GHz bands. All components of the signal chain including the correlator are rigidly mounted directly behind the faceplate, providing exceptional gain and phase stability. The locations of the horns in the faceplate are optimized to provide uniform uv-plane sampling over the multipole range $l \sim 140 - 900$ (§2.1.1). The thirteen horn/lens antennas that comprise the DASI array are compact, axially symmetric, and sealed from the environment, yielding small and extremely stable instrumental polarization. Additional systematic control comes from multiple levels of phase switching and field differencing constructed to remove instrumental offsets. The DASI mount is fully steerable in elevation and azimuth with the additional ability to rotate the entire horn array about the faceplate axis. The flexibility of this mount allows us to track any field visible to us from the South Pole continuously at constant elevation angle, and to observe it in redundant faceplate orientations which allow sensitive tests for residual systematic effects.

As described in §1.4, DASI was shipped from the University of Chicago to its observing site at the South Pole in November 1999, and results of the subsequent observations of temperature anisotropies in the CMB made during the 2000 austral winter were reported in Papers I, II, and III. The DASI telescope in this configuration has been extensively described in Paper I and in Halverson (2002). In this chapter we give only a brief overview of most aspects of the DASI instrument, referring to these references for a more complete discussion. We describe in more detail the hardware that has been modified or added for the 2000–2001 polarization observations, for example the ground and sunshields. These modifications were originally reported in Paper IV. We also give some details regarding the microassembly and testing of the HEMT amplifiers and other RF components of the signal chain. Finally, we dedicate a substantial portion of this chapter to the switchable achromatic circular polarizers which were developed in 2000 and installed in early 2001 to enable DASI to observe with polarization sensitivity to all four Stokes parameters, as described in the previous chapter, with minimal contamination of the polarized signal from instrumental polarization effects.

3.1 Physical Overview

3.1.1 South Pole site

The National Science Foundation Amundsen-Scott Station is located at the geographic South Pole, on the interior ice plateau of Antarctica at an altitude of 2800m. As was detailed in Paper I and Lay & Halverson (2000), the sky above the South Pole is extremely dry and stable, resulting in 30 GHz opacity $0.01 < \tau < 0.02$ and atmospheric noise contamination far below DASI's instrumental noise at least 95% of the time. In addition to the excellent atmospheric conditions, from the South Pole

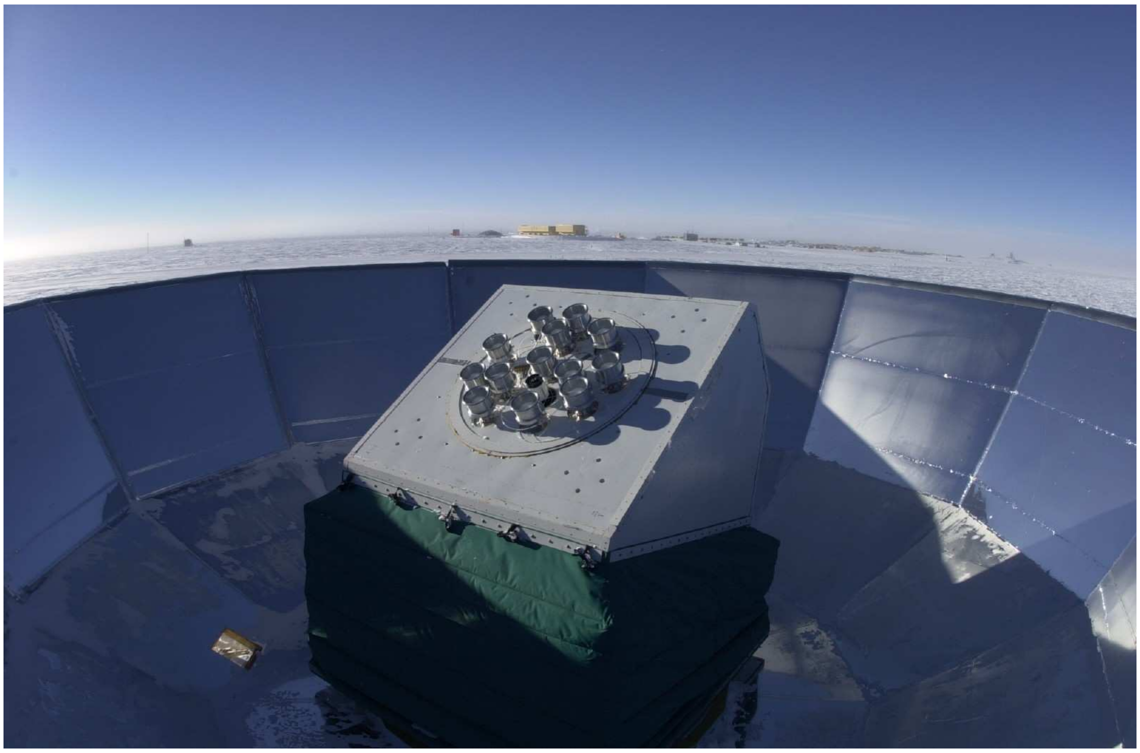

Figure 3.1 A photograph of the DASI telescope installed within its ground shield at the South Pole site. The National Science Foundation Amundsen-Scott South Pole Station is visible on the horizon.

it is possible to track a given field continuously at constant elevation angle. The sky that is accessible for observation from the Pole includes some of the largest regions of minimal galactic foreground emission on the celestial sphere (see §5.1). These characteristics of the Pole make it the ideal location for the long, deep integrations needed to detect the CMB polarization signal.

DASI is designed to exploit these advantages in the course of extremely long integrations on selected fields. The design of the telescope also reflects the particular environmental challenges of South Pole observations. During the six months of the year for which the Sun (the strongest source of contamination) is below the horizon, presenting optimal observing conditions, the average ambient temperature is -60C. Very long integration times demand a design that can ensure reliable telescope performance during this period.

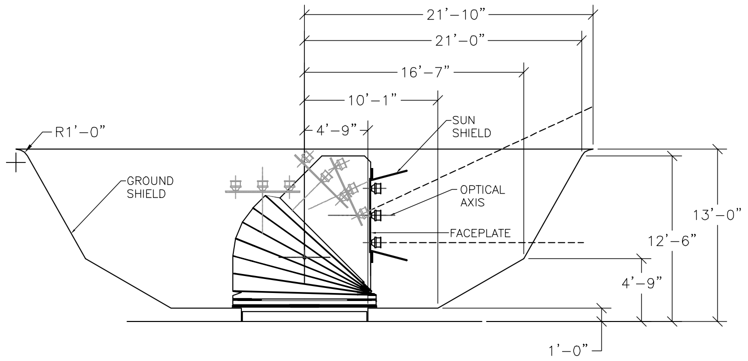

Figure 3.2 Mount and ground shield geometry. The DASI mount is shown at 0° elevation, with faceplate positions also shown at the minimum unobstructed observing elevation 25° as well as $45°, 90°$. For this range of elevations, the ground shields are designed to reflect sidelobes of the horns to the cold sky, and to prevent sidelobes from seeing other horns in reflection, in order to minimize crosstalk.

Access to the site is limited to the short summer season, from November to early February, and all components of the telescope must be designed to disassemble to fit within an LC-130 cargo plane ($\sim 9' \times 8' \times 8'$ maximum pallet size) and to be reassembled efficiently on-site.

3.1.2 DASI mount

The DASI telescope mount addresses the requirements of reliable winter-over operation at the South Pole by enclosing all serviceable components of the system except for the antennas themselves within an easily accessible shirtsleeve environment. Its unique design accomplishes this while allowing steering and tracking of the faceplate array through a full range of motion in azimuth, elevation, and $> 360°$ rotation about the boresite axis.

The DASI mount, which was engineered and fabricated in conjunction with TIW/Vertex,[1] is illustrated in Figs. 3.1 and 3.2. Heavy box steel construction lends the mount extreme rigidity and immunity to flexure; the combined weight of the

[1]now TripointGlobal/Vertex/RSI, 2211 Lawson Lane Santa Clara, Calif. 95054

telescope, when fully equipped and operational, is approximately 35,000 lbs. It is supported by the inner of two concentric towers attached to the Martin A. Pomerantz Observatory (MAPO), 0.7 km from the geographic South Pole. The inner tower is mechanically isolated from the outer tower, which supports the ground shield and the room beneath the telescope. This room houses helium compressors, drive amplifiers, and an air handling unit for managing waste heat from the telescope and compressors.

A ladder passes from this compressor room to the interior space of the telescope through a 32" opening within the azimuth bearing and cable wraps. In addition to power and data cables, the azimuth, elevation, and theta axis cable wraps accommodate 14 1.2" diameter corrugated stainless steel helium lines to supply the closed-cycle refrigerators of each receiver, so that these wraps occupy a substantial portion of the volume of the mount. An insulated fabric bellows permits motion in the elevation axis while maintaining the interior of the telescope and drive assemblies at room temperature using only waste heat from the telescope control and correlator electronics. The compressor room and mount are kept at slight positive pressure, so that a constant outward airflow through the azimuth and faceplate brush seals eliminates ice buildup there. The space inside the mount is sufficient to comfortably inspect and service all the components of the signal chain (see Fig. 3.4).

3.1.3 Shields

The groundshield illustrated in Figs. 3.1 and 3.2 was intended to be erected at the time of DASI's commissioning during the 1999 – 2000 austral summer, but due to construction scheduling conflicts at the South Pole, its construction was delayed until November 2000. As a result, the temperature observations of 2000 were conducted without the benefit of the groundshield, and analysis strategies to remove effects of the (highly stable) ground contamination signal were employed, with the sacrifice of degrees of freedom in the dataset which was especially acute at the shortest baselines (see §5.2).

The groundshield was in place for the entirety of the polarization observations presented here. It is designed to reflect the antenna sidelobes onto the cold sky, and consists of three concentric rings of twelve panels, the innermost horizontal, the outer two rising at a pitch which increases from $\sim 36°$ for the inner ring to $\sim 60°$ for the outer (see Fig. 3.2). The panels were designed to minimize crosstalk between array elements; panels are configured to prevent sidelobes up to 90° off-axis from seeing any other horns in reflection. The top of the outermost ring extends to a height of 13 feet above the roofline. The uppermost border of the shield is rolled with a 1 foot radius to reduce diffraction around the edge, and all gaps between panels are covered with aluminum adhesive tape. Four of the upper panels are hinged and may be lowered to allow observations of planets or a test transmitter mounted at a distance of 800m on the roof of one of the station buildings. Without lowering the shields, the minimum observing elevation is $\sim 25°$.

During polarization observations, two fields were alternately observed in consecutive 1-hour blocks over the same azimuth range (see §5.2), and we can probe for residual contamination from the ground by forming the difference between successive 1-hour means. In the 2000 data, taken without the groundshield, comparison of the variance in these 2-hour differences to the variance in data differenced at the 8-second integration rate indicates a significant (5%) noise excess, dominated by the data on the shortest baselines. In the 2001 co-polar data, taken with the groundshield in place, the noise excess has dropped by nearly an order of magnitude. The upper limit to noise excess in the cross-polar data is a factor of $3-4$ lower still, indicating that any residual signal from the ground is largely unpolarized.

During the austral summer of $2001-2002$, a separate sunshield was also constructed, which was in place throughout the 2002 observations. It consists of a lightweight conical shield, made from the top ~ 3 feet of a spare shield from the

TopHat experiment,[2] which attaches rigidly to the front face of the telescope, completely enclosing, but not rotating with, the faceplate. With a diameter at the attachment point of 62.93″, and an opening angle of 15°, the shield is designed to prevent any sidelobe of an antenna from seeing the Sun or Moon when the telescope is pointed $> 65°$ away from either of these sources. It was hoped that this shield would extend the effective observing season into the months of March and October, during which the Sun is well above the horizon. In the 2001 season, even with the ground shields in place, when observing $< 90°$ from the Sun during these months, its contamination was evident as long-period fringing in visibility data which caused us to exclude that data.

The sunshield was left in place throughout the 2002 winter season, and it is found that during periods when the Moon is above the horizon but below 10° elevation, the data from 2002 show evidence of excess noise, while the 2001 data do not. Evidently, during periods when the Moon is within the opening angle of the sunshield, secondary reflection off the top portion of the sunshield can actually contaminate the short-baseline data when the Moon would otherwise be screened by the ground shield. Accordingly, a stricter cut on the Moon elevation is applied to the 2002 data than to the 2001 data (see §5.3).

3.2 The Signal Chain

The schematic signal chain depicted in Fig. 2.1 is suitable for illustrating the interferometer response, but it neglects a number of components, including the stages of downconversion of the RF signal that are critical to the heterodyne phase switching that gives DASI its immunity to instrumental offsets. Below, we briefly discuss the entire signal chain, including the receivers, downconverter, and correlator. In subsequent sections we will particularly address the achromatic polarizers and the HEMT

[2] Courtesy of the TopHat collaboration.

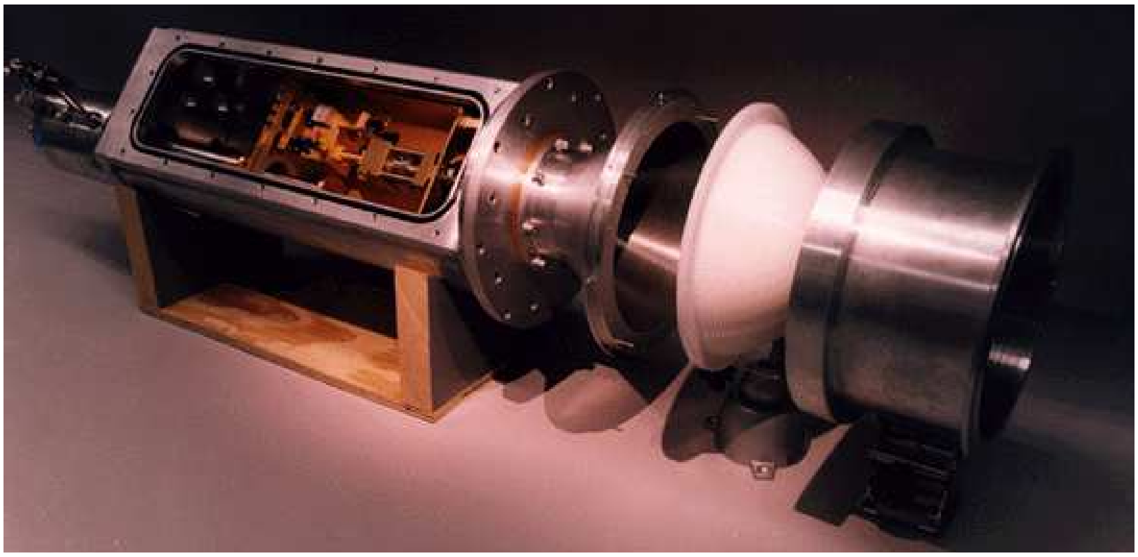

Figure 3.3 The optics and cryogenic components of the DASI receivers. From right to left, the corrugated shroud, HDPE lens, and horn that comprise the antenna. Within the cryostat are the mechanically switchable polarizers, HEMT amplifiers, and other 26-36 GHz waveguide components leading to the mixer, which outputs the 2-12 GHz IF on coax.

amplifiers, both of which are located at the input of the receivers and define the sensitivity of the experiment.

3.2.1 Receivers

The antenna of each of the 13 receivers in the DASI array consists of a lensed, corrugated feed horn, 20 cm in diameter, surrounded by a corrugated shroud to suppress cross-talk between the horns. To make the array maximally compact, the receiver dewars were designed to fit entirely within the footprint of the horns; the shortest baseline is 25.1 cm.

The design of the horn/lens optics and the cryogenic design of the receivers are described extensively in Halverson (2002). The meniscus lens, constructed of high density polyethylene (HDPE), enables high aperture efficiency (0.84) to be achieved with a compact, 30° semi-flare angle corrugated horn. The lenses have circular anti-reflection grooves and a high-angle refracting hyperbolic front surface which were not designed to minimize off-axis instrumental polarization (§4.5); however, the axial symmetry of the optical system ensures minimal on-axis effects. The shroud is sealed with 0.002" mylar, which is kept under positive pressure with dry nitrogen gas to eliminate frosting.

At the throat of the horn, a circular waveguide vacuum break leads directly to the achromatic polarizers described in §3.4. After the transition to WR-28 rectangular waveguide, a front-end isolator further eliminates cross-talk, and a -30 dB directional coupler allows injection of a common noise source for calibration, before the 26-36 GHz signal enters the 4-stage InP Ka-band HEMT amplifier (§3.3). Here, gain of $\sim$ 30 dB ensures that subsequent components of the signal chain make negligible contributions to the system temperature, T_{sys}. All of the RF components inside the vacuum break are cooled by a closed cycle helium refrigerator to 10 K. Cryogenic mixers downconvert the RF signals of each of the 13 receivers to a 2-12 GHz IF, using 38 GHz Gunn diode local oscillators. These are phase modulated 0/180° relative to each other in a 25.6 μs interval Walsh switching sequence.

3.2.2 Downconversion and Correlation

The 2-12 GHz IF signal passes out of each receiver on coax and into the downconverter, a custom 9U VME-sized crate which (like the internal noise source) was based on a shared CBI-DASI design by J. Cartwright (2003). In the downconverter, the IF is amplified and channelized by a filter bank into 10 consecutive 1 GHz bands. The resulting 13 $\times$ 10 signals are each mixed down to 1–2 GHz, further amplified, and level-set attenuated to the +16 dB input level required by the correlator. Contract microassembly of 160 downconverter modules (130 + spares) for DASI was done by Micro-Precision Technologies.[3] Unfortunately, testing of these modules (conducted by E. Schartman) revealed a large fraction in need of wirebonding and component rework, and considerable effort was spent in Chicago and, in some cases, with a

[3]Micro-Precision Technologies, Inc., 12B Manor Parkway, Salem NH 03079.

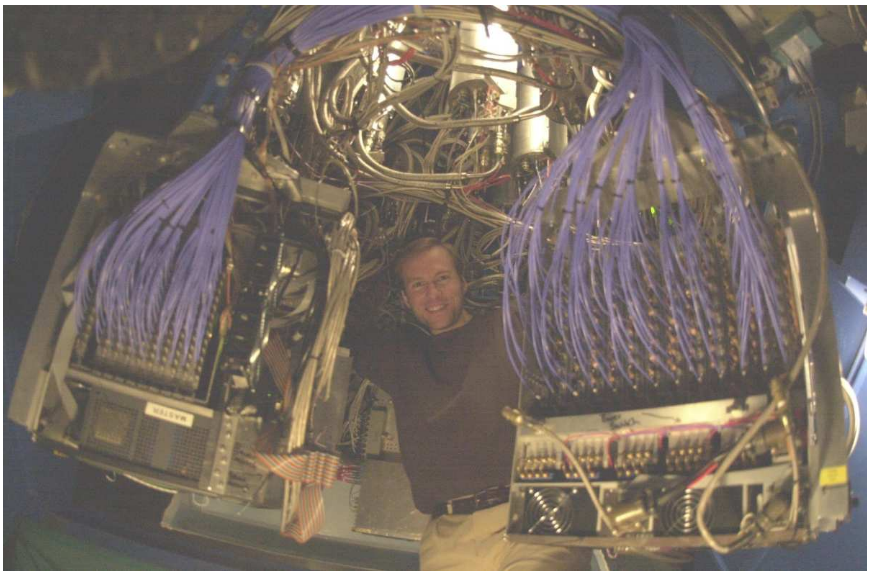

Figure 3.4 The backend of the DASI signal chain, consisting of the downconverter (right) and correlator (left), are mounted in the shirtsleeve service space directly behind the receivers and faceplate. Both of these components are common to DASI and CBI.

wirebonder brought to the South Pole to produce 130 working channels at the time of telescope commissioning, all of which have remained functional.

From the downconverter, the signals pass to the complex correlator (see Fig. 3.4). This compact analog correlator, which offers 1.56 THz of total correlation bandwidth within a single 9U VME chassis, was designed by S. Padin for the CBI and DASI (Padin et al. 2001), and represents a major technological achievement. On each of 10 correlator boards (see Fig. 3.5), 1–2 GHz signals from the 13 receivers are input along the diagonal of a multiplier module matrix and are split to travel along horizontal and vertical microstrips, with and without a 90° phase delay. At each of the 156 intersections, Gilbert cell multipliers form the real and imaginary parts of each of the visibilities, which are digitized, accumulated, and read out by the control computer at 0.84s intervals. Correlator offsets are eliminated by accumulation with a sign that changes to demodulate the 0/180° LO Walsh switching.

Although the microassembly of the correlator modules (unlike that of the HEMT

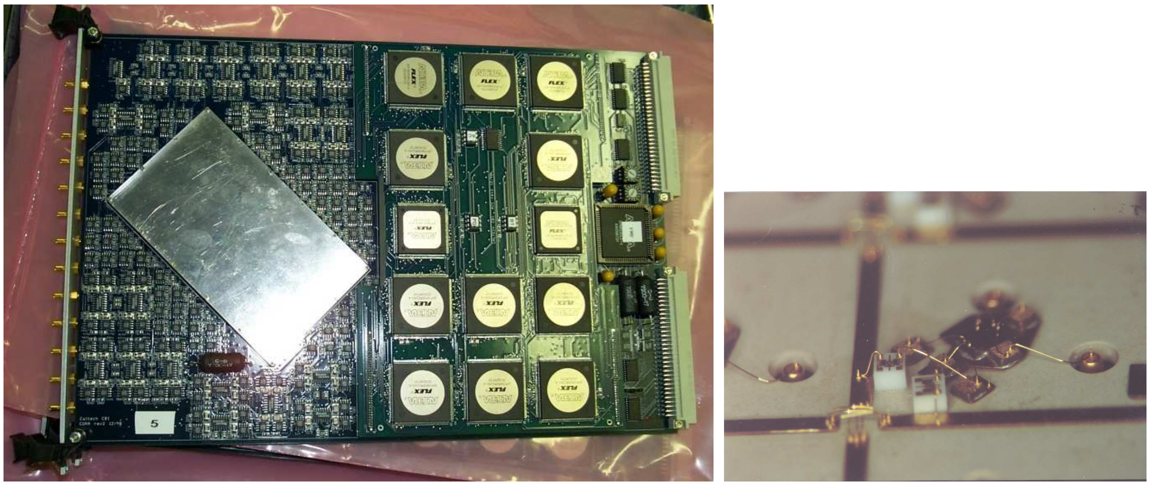

Figure 3.5 The CBI/DASI analog complex correlator, designed by S. Padin. At left, one of the 10 correlator boards that are visible in the correlator crate in Fig. 3.4. The rectangular multiplier module accepts 1 GHz bandwidth inputs from 13 receivers along the diagonal of its matrix. At right, one of its 156 Gilbert multiplier cells is shown. (The input wirebonds of this cell are actually in contact with each other, an assembly error.)

amplifiers) does not require tuning steps or a demanding level of precision, it does constitute a project of considerable scale, and would be the most severe challenge for future expansion of DASI-like arrays. Each multiplier module includes 156 Gilbert cell circuits and similar number of matrix cross-over junctions, 13 90° phase transformers, and 13 total power detectors, requiring a total of 3627 wirebonds. Contract microassembly of 12 multiplier modules (10+2 spares) was also done by Micro-Precision Technologies, and unfortunately, each module was found to have several dozen assembly errors which eventually had to be corrected with wirebonding and component rework at Chicago or with the wirebonder brought to the South Pole. By the time of commissioning, all but 3 of the 1560 multiplier channels worked properly and have remained functional. During the course of this testing, it was discovered that phase and amplitude offsets between the real and imaginary channels occasionally exhibited patterns consistent with substantial standing waves on the multiplier matrix, indicating poor termination of these microstrips. These offsets are removed in the real/imaginary correlator calibration described in §4.1, and as expected are extremely

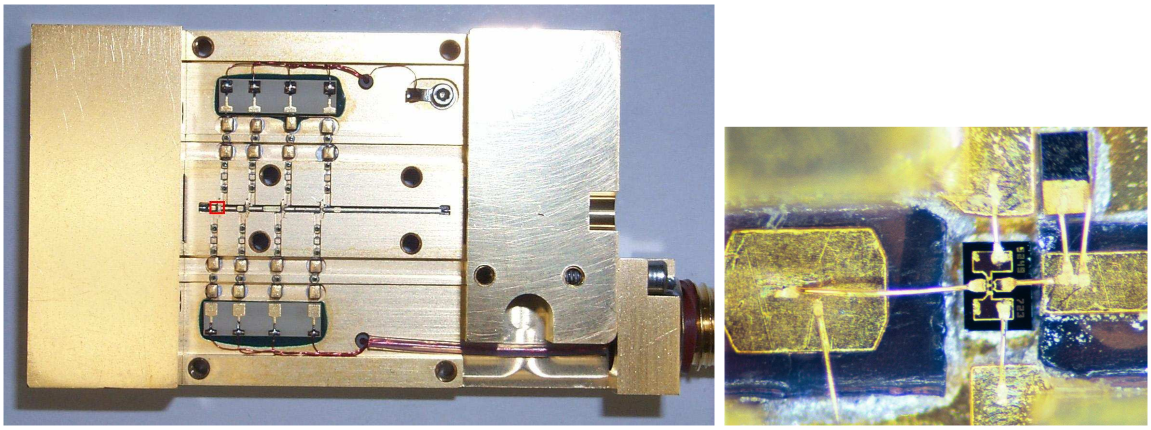

Figure 3.6 A DASI Ka-band HEMT amplifier, constructed at the University of Chicago to an NRAO design (Pospieszalski et al. 1995). At left, the four InP stages of amplification are visible along the microstrip channel between the probes that couple to the input (left) and output waveguide ports on the reverse side. The first HEMT stage (red box) is magnified at right. The input (gate, left) bond shown is 21 mils long; its geometry strongly impacts the amplifier tuning.

stable, so further effort was not expended to correct them.

3.3 HEMT Amplifiers

The sensitivity of the DASI array is made possible by the development of broadband, low-noise cryogenic millimeter-wave HEMT amplifiers (Pospieszalski et al. 1994, 1995). The Ka-band 4 stage indium phosphide HEMT amplifiers used by DASI were built according to a design by M. Pospieszalski, developed at the NRAO Central Development Laboratory in Charlottesville, VA. In the summer of 1997, the author spent six weeks at the NRAO Central Development Laboratory (with J. Cartwright of the CBI and E. Blackhurst of the VSA), learning the assembly, testing, and tuning techniques necessary to implement this chip-and-wire amplifier design.

A total of 17 Ka-band HEMT amplifiers were built at the University of Chicago for DASI. One of these amplifiers is illustrated in Fig. 3.6, with the 4 InP stages of amplification visible along the central RF channel. The FET sources are grounded,

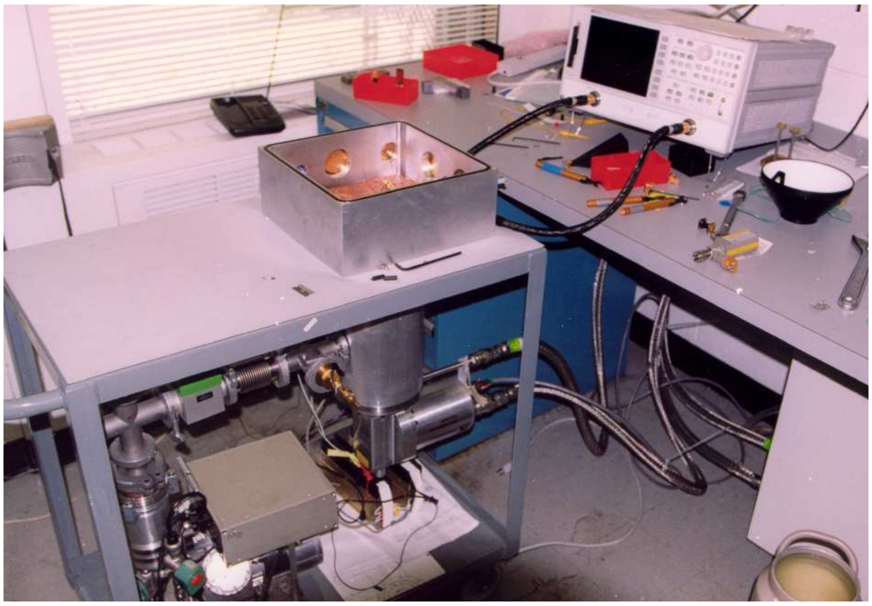

Figure 3.7 The lab dewar and HEMT test setup, including the HP8722D vector network analyzer used to measure the S-parameters. (The warm rectangular horn used for noise measurements is visible on the benchtop.)

while individual gate and drain DC biases for each stage are brought in on the channels visible below and above (respectively) the RF channel. The bias channels contain π-type RF filters tuned to restrict the RF power to the central channel; the outer components of these bias channels (chip resistors and capacitors, with wire bonds acting as inductors) are not dimensionally critical, and contract microassembly[4] produced satisfactory results for the bias circuity for a portion of the DASI amplifiers. However, repeatable electrical performance depends critically on the placement of the small components of the RF channel (microstrip substrates, capacitors, tuning stubs, HEMTs, and wirebonds) to < 1 mil (18 μm) tolerances. A laboratory was assembled at the University of Chicago with the necessary tools (microscopes, wirebonder, microdispenser, massive work surface, etc.) to perform this precision assembly for the 17 amplifiers.

A test cryostat was constructed (Fig. 3.7) with ports configurable to offer WR-28

[4]Orbital Sciences Corporation, 21839 Atlantic Blvd Dulles, VA 20166.

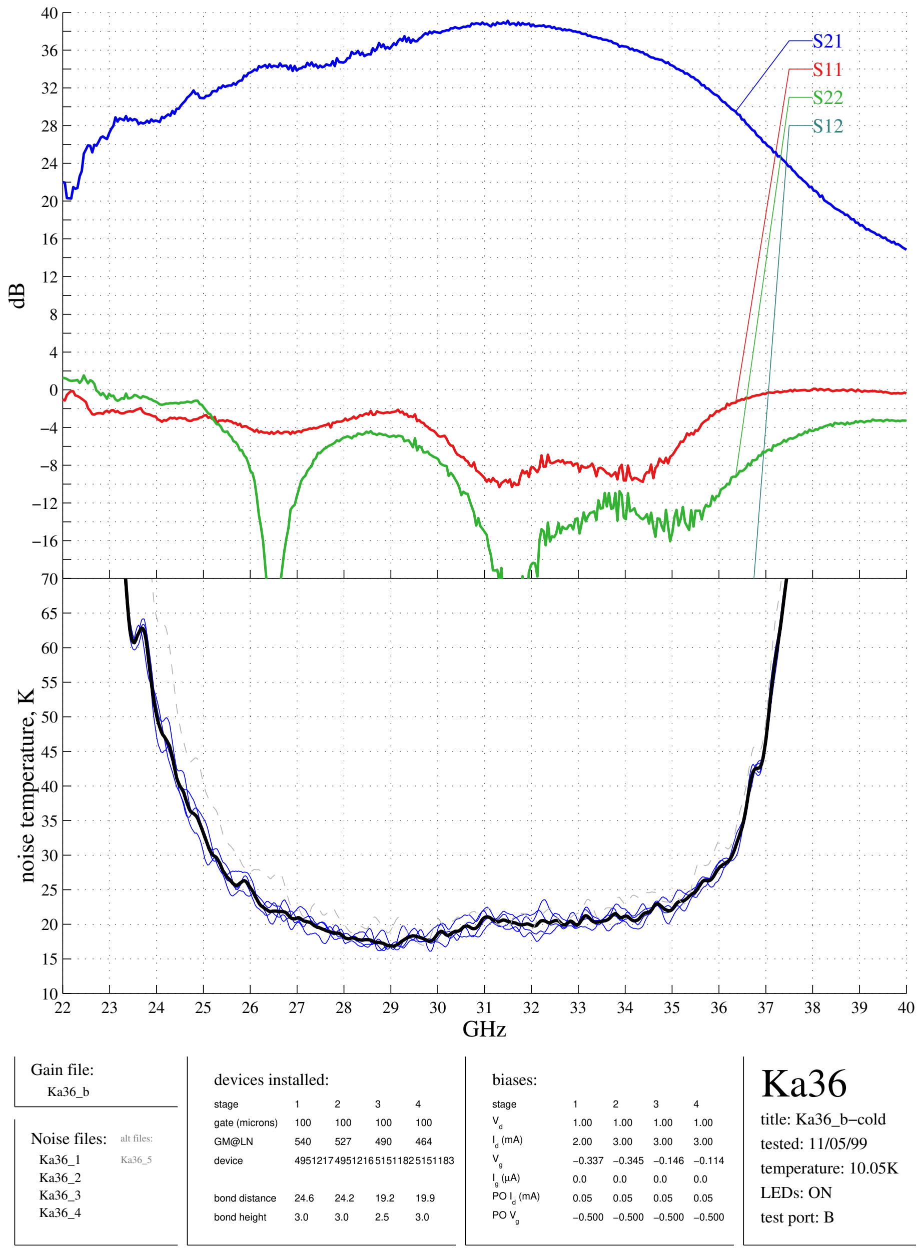

Figure 3.8 Test results for HEMT serial number DASI-Ka36, showing typical amplifier gain (S_{21} is forward gain) and noise curves for the optimized bias settings. The noise has a ~ 10 K systematic offset due to the warm waveguide and horn.

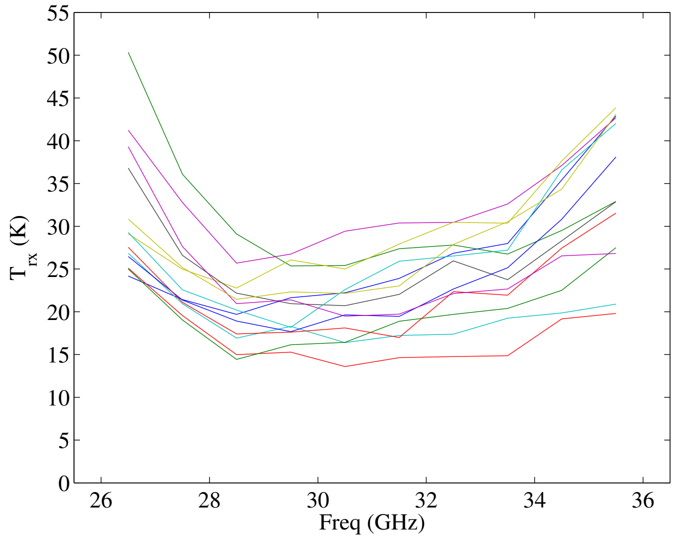

Figure 3.9 Receiver temperatures for the 13 receivers installed on DASI for the absolute calibration of February 2001. The warm lens, horn and throat and the front end isolator together contribute an average of 8–12 K; most of the variability with frequency and between receivers is due to the HEMT amplifiers. (Identical to Fig. 4.8 of Halverson 2002.)

waveguide input and output feedthroughs for two amplifiers, which could be cooled to their operating temperature 10K in 90 minutes. This greatly facilitated the testing and subsequent tuning necessary in this amplifier design. Most tuning was accomplished by adjustment of the gate bond geometry, which determines the inductance and parasitic capacitance at the input of each HEMT. Because of the fragility of the gate bonding pads (which are 1 mil across, approximately the size of the wirebond itself), it was imperative to adjust the gate bond geometry at the substrate end, either by stamping down the bond to shorten it or cutting it free with a scalpel to readjust the loop height. With these tuning adjustments, the noise curves of each amplifier could be shifted to match the 26-36 GHz RF band used by DASI. The automation of the test procedure allowed further optimization of the noise and gain curves by adjustment of the bias parameters (drain voltage and current) for each amplifier stage. Occasionally these adjustments were also used to supress oscillations between amplifier stages. Final gain (S-parameters) and noise curves measured for one amplifier in the standard test setup are shown in Fig. 3.8.

Installed on the telescope, the DASI HEMT amplifiers have performed reliably and have achieved minimum amplifier noise temperatures that in the best cases are inferred to be $\sim$ 10 K across 28-34 GHz, although there is significant variability in performance between amplifiers, with certain examples rising to $\sim$ 30 K at the band edges. The warm lens, horn, and throat together contribute 7-8 K to $T_{\rm sys}$, and the front end isolator adds another 2 K, resulting in receiver temperatures for DASI that generally vary between 20–40 K for all receivers across the full 26-36 GHz band (Fig. 3.9).

3.4 Broadband Polarizers

The DASI lens, horn, and throat are by their symmetry dual moded, admitting both linear polarizations of the electric field with exactly the same (on axis) coupling. However, each of DASI's receivers has a single HEMT amplifier, and each correlator board is designed to accommodate only 13 inputs, so DASI cannot use orthomode transformers to measure two orthogonal polarization states simultaneously. Instead, one linear combination of the incoming fields must be selected. We use a mechanically switchable waveguide polarizer, inserted between the amplifier and the feedhorn, to select between right circular and left circular polarization states, R and L. The polarizers for each receiver are switched on a 1-hour Walsh cycle, with the result that over the full period of the cycle, every pair of receivers spends an equal amount of time in all four Stokes states.

The standard approach for producing a switchable waveguide circular polarizer uses a $\lambda/4$ retarder oriented 45° to the E-field of the linear polarization accepted by the transition to rectangular waveguide. This retarder is often a simple dielectric vane inserted in the circular waveguide; at 30 GHz, the loss in the dielectric and corresponding contribution to the system temperature are negligible if the vane is cooled. The circular waveguide which holds the vane can be mechanically rotated along the waveguide axis by $\pm 45°$ to select R or L.

Unfortunately, a conventional $\lambda/4$ retarder typically admits a contribution from the unwanted circular polarization state, referred to as *leakage*, which grows quickly as a function of the offset from the design frequency. As discussed in §4.4, this leakage results in instrumental polarization for the cross-polar visibilities. Due to DASI's large fractional bandwidth, the leakage for a simple quarter-wave retarder polarizer would cause the contamination from the CMB temperature signal to exceed the level of the expected CMB polarization signal at the band edges.

With the goal of reducing the DASI's broadband instrumental polarization to insignificant levels, we investigated polarizer designs using multiple retarder elements and found that there are solutions to meet any specified polarization purity and bandwidth. In this section, we describe the theory and design of the DASI two-element circular polarizers, which we describe as *achromatic* because they cancel offset-frequency errors to first order. We will begin by defining variables to describe the polarization state and leakage, and then discuss the limitations of conventional waveguide retarder designs. A formalism for deriving achromatic multiple-element designs is presented, along with the simplest solutions. We next discuss the actual DASI polarizers, describing their construction, tuning, and installation as well as their mechanical switching. The University of Chicago has applied for a United States patent related to this polarizer design, and much of the material in this section is drawn from that application (Kovac & Carlstrom 2002). We conclude the section with a mention of current efforts to further optimize polarizer design.

3.4.1 Defining the Polarization State

In Chapter 2 we described a quasimonochromatic plane wave incident on a DASI receiver by the complex amplitudes E_1, E_2 of the electric field measured in a linear basis $\boldsymbol{\epsilon_1}, \boldsymbol{\epsilon_2}$ (Eq. 2.1). For an on-axis plane wave, we can imagine these fields defined in the far field of the optics, or (properly accounting for antenna gain) equivalently in the throat of the axially symmetric horn. We stated that the polarizing optics couple a particular linear combination of these fields to the amplifier input (Eq. 2.4),

$$E_{\mathrm{rxA}}\left(t\right) = \left(\alpha_1 E_1 + \alpha_2 E_2\right), \tag{3.1}$$

where the coefficients α_1, α_2 define the polarization state of the receiver. There are four degrees of freedom in these two complex coefficients, but typically we treat the overall amplitude and phase of the signal as a component of the complex gain of the receiver, so that we can normalize these coefficients, e.g. $\alpha_1^2 + \alpha_2^2 = 1$, and define the polarization state in terms of the two degrees of freedom in the complex ratio that specifies their relative amplitude and phase. A right circular (R) polarization state is defined by equal response to E_1 and E_2 with a $+90°$ phase shift, $\alpha_1/\alpha_2 = i$, or with our specific normalization, $[\alpha_1, \alpha_2] = [e^{+i\pi/4}, e^{-i\pi/4}]/\sqrt{2}$. The orthogonal L receiver state is defined similarly, $\alpha_1/\alpha_2 = -i$ (or $[\alpha_1, \alpha_2] = [e^{-i\pi/4}, e^{+i\pi/4}]/\sqrt{2}$). We can likewise talk about the polarization state of the incident radiation itself in the same terms by considering the relative amplitude and phase $(E_1/E_2)^*$. However, we will generally visualize the device in transmission, so that the polarization states are defined for E_1/E_2 just as for α_1/α_2.

Our notation associates polarization states with points on the complex plane, or with normalized complex 2-vectors. It is common in the literature to see these two degrees of freedom represented as pairs of angles which associate polarization states with points on the *Poincaré sphere* (e.g. Kraus 1986). Orthogonal states are at opposite points of this sphere; in Fig. 3.10 we show L at top and R at bottom, while linear polarization states are located around the equator, rotating through 90° at opposite points. The pair of angles γ and δ that are defined as the arctangent of the amplitude ratio $|E_2| \,/\, |E_1|$ and the phase difference, respectively,

$$\gamma\left(E_1, E_2\right) = \tan^{-1}\frac{|E_2|}{|E_1|} \qquad 0 \leq \gamma \leq \frac{\pi}{2} \tag{3.2}$$

$$\delta\left(E_1, E_2\right) = \arg(E_2) - \arg\left(E_1\right) \qquad -\pi < \delta \leq \pi\ , \tag{3.3}$$

specify a mapping onto the Poincaré sphere, where 2γ is the polar angle from the equatorial point that marks the vertical linear state (aligned N-S on the sky), and δ is the azimuthal angle measured about this point CCW from the equator towards the L pole. Equivalently, the pair of angles ϵ and τ

$$\epsilon(\gamma,\delta) = \frac{1}{2}\sin^{-1}(\sin 2\gamma \sin\delta) \qquad -\frac{\pi}{4} \leq \epsilon \leq \frac{\pi}{4} \tag{3.4}$$

$$\tau(\gamma,\delta) = \frac{1}{2}\tan^{-1}(\tan 2\gamma \cos\delta) \qquad 0 \leq \tau < \pi \tag{3.5}$$

are respectively the arctangent of the inverse axial ratio and the tilt angle of the *polarization ellipse* which is traced by the real electric field vector in time. The angles 2ϵ and 2τ specify the latitude and longitude of the polarization state on the Poincaré sphere as we have oriented it. However, the singularity of these coordinates at the circular polarization poles makes them less suitable for measuring small deviations from those points. The Poincaré sphere will be useful to us as a tool for visualizing the action of multi-element polarizers. We will see below that each element acts on the polarization state complex 2-vectors as elements of $SU(2)$. The equivalent action on the Poincaré sphere representation is as an element of $SO(3)$, a solid rotation of the sphere, as we will describe.

If a polarization state of a receiver is given as a complex 2-vector $[\alpha_1, \alpha_2]$, its voltage response to R or L is the complex vector product with those polarization states,

$$V^R = \frac{e^{-i\pi/4}}{\sqrt{2}}(\alpha_1 + i\alpha_2) \tag{3.6}$$

$$V^L = \frac{e^{+i\pi/4}}{\sqrt{2}}(\alpha_1 - i\alpha_2)\ . \tag{3.7}$$

If a polarization state is nominally R, we define its *leakage* D^R as the complex ratio of the unwanted state (L) response to the nominal state response:

$$\begin{aligned} D^R &= \frac{V^L}{V^R} \approx V^L && (3.8)\\ &= \frac{e^{+i\pi/4}}{\sqrt{2}}\left(\alpha_1 - i\alpha_2\right) && (3.9)\\ &\approx \frac{1}{2}\left(\frac{\alpha_1}{\alpha_2} - i\right) , && (3.10)\end{aligned}$$

where we have twice made use of the approximation $[\alpha_1, \alpha_2] \approx [e^{+i\pi/4}, e^{-i\pi/4}]/\sqrt{2}$. The leakage of a nominally L state is defined similarly, giving $D^L = (\alpha_1/\alpha_2 + i)/2$.

The complex leakage defines a map from the region around the R or L poles of the Poincaré sphere to the complex plane. Other terminology used to describe deviations from pure circular polarization states includes the *cross-polarization*, which is the leakage power $|D_R|^2$ in dB, and equals the negative *isolation* in dB.[5] The axial ratio of the polarization ellipse associated with this leakage is clearly

$$AR = \frac{1 + |D_R|}{1 - |D_R|}. \qquad (3.11)$$

Finally, from Eq. 3.10 it is evident that a polarizer which produces equal amplitudes for E_1 and E_2 but a phase delay $\Delta\phi$ that is not a perfect $\lambda/4$ results in a leakage $|D_R| \approx (\Delta\phi - \pi/2)/2$.

3.4.2 Action of a Waveguide Retarder Element

Waveguide circular polarizers are one example of a class of devices sometimes known as "phase shifters," "phase retarders," or simply "retarders" in dual-polarization waveguide. These devices are common components in microwave and millimeter-wave antenna feed systems for communications, radar, and astronomical applications. Quarter-wave retarders can be used as circular polarizers to couple linearly polarized components to either or both circular polarization states. Half-wave retarders can

[5]Like leakage, these terms can alternatively be defined in reference to linear polarization states.

be used to alter the overall phase or angle of linear polarization of a signal. In applications where the orientation or the retardation of these devices may be varied, these components are commonly used to switch between linear, left-circular, and right-circular polarizations or to continuously vary the phase or polarization state of a signal.

We will first describe a generic ideal retarder. The input and output ports of a generic retarder are dual polarization waveguides which are usually of circular or square cross section, although they may also be rectangular or elliptical, ridged or corrugated, or generally of any other type which admits propagation of two orthogonal electric field signal components. These two signal components can be labeled at the input of the device as $V_{x,\mathrm{in}}$ and $V_{y,\mathrm{in}}$ and similarly at the output as $V_{x,\mathrm{out}}$ and $V_{y,\mathrm{out}}$. The action of a generic retarder is to delay the propagation of the signal component with a specific linear electric field orientation compared to the propagation of the orthogonal signal component. The orientation of the electric fields of these two signal components, which are orthogonal linear eigenmodes of the device, define the *principal axes* of the retarder. If the $x-$ and $y-$axes are chosen to align with these principle axes of the retarder, and if the insertion loss of the retarder is negligible, then the action of this ideal retarder can be described very simply,

$$V_{x,\mathrm{out}} = e^{-i\phi_a} V_{x,\mathrm{in}} \tag{3.12}$$

$$V_{y,\mathrm{out}} = e^{-i(\phi_a+\Delta\phi)} V_{y,\mathrm{in}}. \tag{3.13}$$

The common phase shift ϕ_a is unimportant to the action of the retarder; usually it is only the relative retardation $\Delta\phi$ that is relevant in applications.

If the retarder is rotated such that its principle axes are not aligned with the $x-$ and $y-$axes, but are offset at an angle θ, then the action of the ideal retarder can be described

$$\begin{bmatrix} V_{x,\mathrm{out}} \\ V_{y,\mathrm{out}} \end{bmatrix} = \begin{bmatrix} \cos\theta & \sin\theta \\ -\sin\theta & \cos\theta \end{bmatrix} \begin{bmatrix} e^{-i\phi_a} & 0 \\ 0 & e^{-i(\phi_a+\Delta\phi)} \end{bmatrix} \begin{bmatrix} \cos\theta & -\sin\theta \\ \sin\theta & \cos\theta \end{bmatrix} \begin{bmatrix} V_{x,\mathrm{in}} \\ V_{y,\mathrm{in}} \end{bmatrix} \tag{3.14}$$

If we neglect the overall phase ϕ_a, then the r.h.s. gives a matrix $S(\Delta\phi, \theta)$ that represents the action of the retarder, and depends only on the retardation $\Delta\phi$ and the orientation θ.

An ideal circular polarizer is realized by a quarter-wave retarder $\Delta\phi = 90°$ set at orientation $\theta = 45°$, so that

$$\begin{bmatrix} V_{x,\text{out}} \\ V_{y,\text{out}} \end{bmatrix} = \frac{1}{\sqrt{2}} \begin{bmatrix} e^{+i\pi/4} & -e^{+i\pi/4} \\ e^{-i\pi/4} & e^{-i\pi/4} \end{bmatrix} \begin{bmatrix} V_{x,\text{in}} \\ V_{y,\text{in}} \end{bmatrix}. \tag{3.15}$$

If at the input we excite only $V_{x,\text{in}}$ (with $V_{y,\text{in}} = 0$), corresponding to a pure linearly polarized input signal, then at the output $V_{x,\text{out}}$ and $V_{y,\text{out}}$ will have equal amplitude but with a $-90°$ relative phase shift, corresponding to pure right-handed circular polarization. If the orientation of the retarder is changed to $-45°$, then the opposite (left-handed) circular polarization is produced, and if the orientation is $0°$ then linear polarization is transmitted. In reception (as the DASI polarizers are used), if the receiver couples only to $V_{x,\text{in}}$ the resulting polarization states are similarly defined.

Another common application is a linear polarization rotator, which can be realized as a half-wave retarder $\Delta\phi = 180°$ with a variable orientation θ. For this device,

$$\begin{bmatrix} V_{x,\text{out}} \\ V_{y,\text{out}} \end{bmatrix} = \begin{bmatrix} \cos 2\theta & -\sin 2\theta \\ -\sin 2\theta & -\cos 2\theta \end{bmatrix} \begin{bmatrix} V_{x,\text{in}} \\ V_{y,\text{in}} \end{bmatrix}. \tag{3.16}$$

If again at the input we excite only $V_{x,\text{in}}$ (with $V_{y,\text{in}} = 0$), corresponding to a pure linearly polarized signal, then at the output we will still have a linearly polarized signal, but with its $E-$field orientation rotated by an angle -2θ. A combination of a quarter-wave retarder with a variable orientation θ_1 followed by a half-wave retarder with a variable orientation θ_2 may be used to couple an input signal of a given polarization state (e.g. pure linear V_x) to any desired output polarization state, with arbitrary ellipticity and polarization orientation.

The action of any single retarder element in transforming input to output polarization states can easily be visualized as a rotation of the Poincaré sphere. The axis of rotation is fixed by the linear eigenmodes of the retarder (i.e. the linear states which are aligned with the principal axes) found at 2θ around the equator of the sphere, and the rotation angle is equal to $\Delta\phi$. For example, the action of a single-element circular polarizer is illustrated in Fig. 3.10. Linear states at $\pm 45°$ are preserved with only a relative phase shift, but the horizontal input state is rotated by $\propto \Delta\phi \approx 90°$ up to the L pole.

3.4.3 Conventional Waveguide Polarizer Designs

Conventional waveguide retarder designs work by introducing structures or changes in cross-section that are aligned with the principle axes of the retarder, so as to cause the electrical properties of the waveguide about these axes to differ. As a result, signals with electrical fields oriented along either of these axes will differ in their propagation constant $\beta \equiv d\phi/dL$ producing a total relative phase shift $\Delta\phi = L(\beta_x - \beta_y)$ which may be tuned by controlling the overall physical length L of the retarder or the propagation constant asymmetry $\beta_x - \beta_y$. It is thus relatively easy to arrange a retarder to have a desired retardation $\Delta\phi_0$ at some particular frequency ν_0. If the two propagation constants were strictly proportional to the frequency of the signals, as in free space, then for a fixed overall length the retardation would be proportional to frequency

$$\Delta\phi\,(\nu) \propto \nu \tag{3.17}$$

resulting in relative retardation greater than $\Delta\phi_0$ at frequencies higher than ν_0, and a retardation less than $\Delta\phi_0$ at frequencies lower than ν_0. In waveguide, however, the propagation constant for each mode typically depends not only on frequency but also on the cross-sectional geometry and on any other structures whose electrical properties affect the propagation of that particular mode. The designer's degree of control over the functional dependence $\beta_x\,(\nu)$ generally increases with increasing complexity of the cross-sectional geometry and/or the structures that affect the propagation of that mode. This control may be exploited to arrange for $\Delta\phi\,(\nu)$ to be flatter than the linear dependence implied by Eq. 3.17. To achieve high-bandwidth, is desirable to choose a cross-sectional geometry and/or structures within the waveguide which not only introduce the desired relative phase shift, but which also flatten $\Delta\phi(\nu)$ as much as possible over the desired band of operation.

Examples of conventional retarder design strategies are illustrated in Uher et al. (1993) for the case of quarter-wave retarders intended for use as circular polarizers. Designs which only introduce a bilateral asymmetry in empty waveguide of uniform cross section (e.g. rectangular or elliptical wall heights, longitudinal ridges, etc.) ultimately change only the relative cutoff frequencies $\nu_{c,x}$ and $\nu_{c,y}$ of the two eigenmodes; because the propagation constants in this case are given by $\beta_x = \sqrt{k^2 - k_{c,x}^2}$, $\beta_y = \sqrt{k^2 - k_{c,y}^2}$ the resulting curves $\Delta\phi(\nu)$ will increase monotonically across the band. More sophisticated designs load the walls or volume of the waveguide using corrugations or dielectric slabs to effectively alter the relative asymptotic behavior of the propagation constants, so that within the operating band a minimum may be achieved in $\Delta\phi(\nu)$ at which it is first-order invariant in frequency. For examples see (Uher et al. 1993, fig.3.8.40a) and (Lier & Schaug-Pettersen 1988, fig 1b). This minimum may be located exactly at a frequency ν_0 for which $\Delta\phi(\nu_0) = \Delta\phi_0$, maximizing flatness at that frequency, or at a nearby frequency so that $\Delta\phi(\nu) = \Delta\phi_0$ has solutions at two different frequencies, which is usually preferable for maximum usable bandwidth. Still more sophisticated designs tailor the different loading of opposite pairs of walls to cause the asymptotic behavior of each mode to be approached at different rates, lending another degree of control which can be used to achieve a second-order invariance in $\Delta\phi(\nu)$, or alternately permit a form of $\Delta\phi(\nu)$ for which $\Delta\phi(\nu) = \Delta\phi_0$ has solutions at three frequencies (Lier & Schaug-Pettersen 1988; Srikanth 1997).

Practical retarder designs must not only control the value of $\Delta\phi_0$ and the flatness of the curve $\Delta\phi(\nu)$, but must also have transition sections that are matched to produce suitably low return loss. They must have suitably low ohmic and dielectric losses in the waveguide walls and control structures. They must avoid excitation of unwanted higher-order modes. They must meet additional constraints of manufacturability and repeatability. All of these tend to limit the complexity of structures in practical conventional retarder designs.

The performance achieved by Lier & Schaug-Pettersen (1988) appears to be near the practical and theoretical limits of this approach. They effectively achieve a second-order invariance in $\Delta\phi\,(\nu)$ for a quarter-wave retarder with $\Delta\phi = 90° \pm 0.7°$ over a 28% bandwidth. Used as a circular polarizer, this corresponds to a very low leakage of $|D_R| \leq 0.0062$ across this band, although the leakage grows rapidly outside these band edges.

A common feature of all of these conventional retarder (and polarizer) designs is that their cross sections are symmetrical about the principle axes, which do not change throughout their length.

3.4.4 The Multiple Element Approach

A number of approaches were investigated to attempt to overcome the theoretical limitations of conventional retarders in designing a broadband circular polarizer for DASI. These included waveguide designs for reflective or inductive networks or cascaded parallel phase shifter segments, each of which were rejected as likely to be too lossy, bulky, or complex. The approach we chose is to combine two or more individual retarders at different angles in specific combinations, discussed below, to cancel the frequency variation of the performance of the compound device to any desired order of accuracy. Each element of the compound polarizer or retarder is itself a conventional retarder, and may be constructed according to any of the conventional retarder designs discussed above. Generally, the more elements in the compound design, the higher the order at which the frequency variation of the performance can be canceled, or alternatively the greater the bandwidth over which a given precision specification can be met.

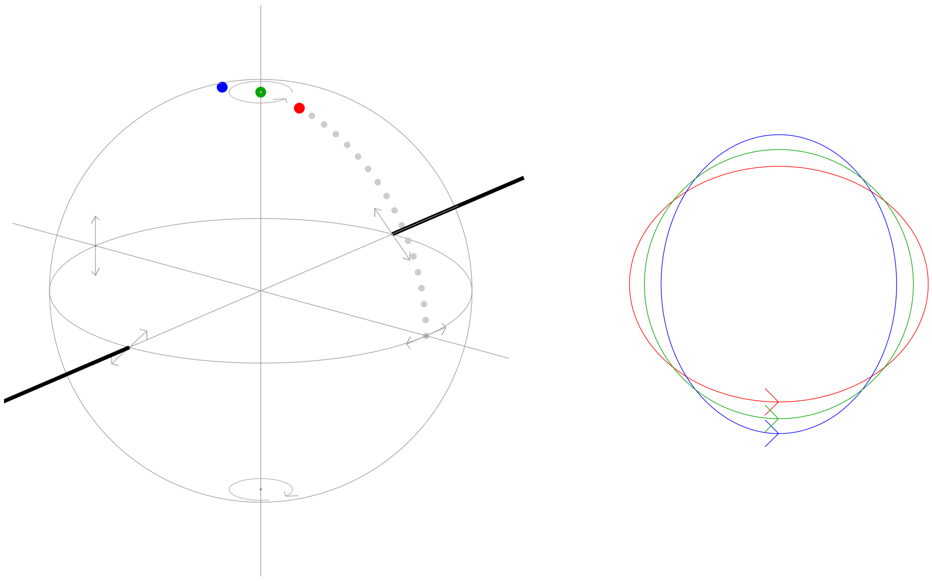

Figure 3.10 The action of a conventional polarizer is illustrated on the Poincaré sphere. Polarization ellipses to the right.

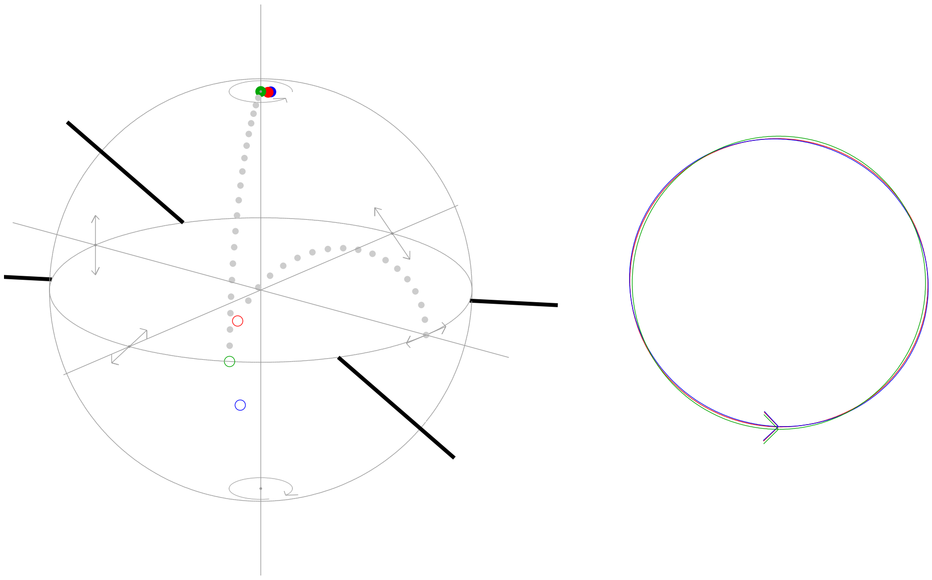

Figure 3.11 The action of the two-element polarizer is illustrated on the Poincaré sphere. The chromatic dispersion on the Poincaré sphere is proportional to the path length of the action of each element. In this design, these two lengths are equal, canceling first order chromatic variation.

The combination of multiple birefringent plates to produce achromatic performance in free-space quarter- and half-wave plates has long been understood (Pancharatnam 1955). The analogous combination of individual waveguide retarder elements, which can be designed so that the frequency variation of $\Delta\phi\,(\nu)$ for each is also suppressed, will cause the cancellation of the frequency variation in the performance of the compound device to be further enhanced. For example, Fig. 3.12 illustrates the performance of a typical conventional quarter-wave retarder used as a circular polarizer. This typical retarder already has a single minimum in $\Delta\phi\,(\nu)$ (at which $\Delta\phi$ is first-order invariant in frequency), allowing it to achieve a precision of $|D_R| \leq 0.02$ over 35% bandwidth. Using this type of retarder in a compound two-element circular polarizer design, it is possible to achieve performance that is frequency invariant up to third-order, or alternatively to have high precision over a much broader bandwidth, as is illustrated. Increasing the number of elements to more than two improves the flatness further, and with a small number of elements it is possible to achieve extremely high precision over the entire usable bandwidth of the waveguide.

The situation for compound quarter-wave, half-wave, and other retarders is similar. A general procedure for deriving the specific combinations of retarder elements and orientations that yield the highest order of frequency invariance for a given kind of compound device (e.g. a three-element half-wave retarder) is described below. The most useful solutions for compound circular polarizers, quarter-wave, and half-wave retarders using up to four elements are reported.

Before tuning to the mathematical formalism, let us consider the simplest two-element circular polarizer, the design used by DASI, to illustrate the approach. As described above, Fig. 3.10 depicts the action of a single-element quarter-wave retarder, oriented at 45°, as a rotation of the Poincaré sphere. The angle of rotation for each frequency is given by $\Delta\phi$, causing the horizontal input state to be rotated to output states dispersed around the L pole. The two-element design (Fig. 3.10) corrects this dispersion using a combination of nominal quarter-wave and half-wave retarders

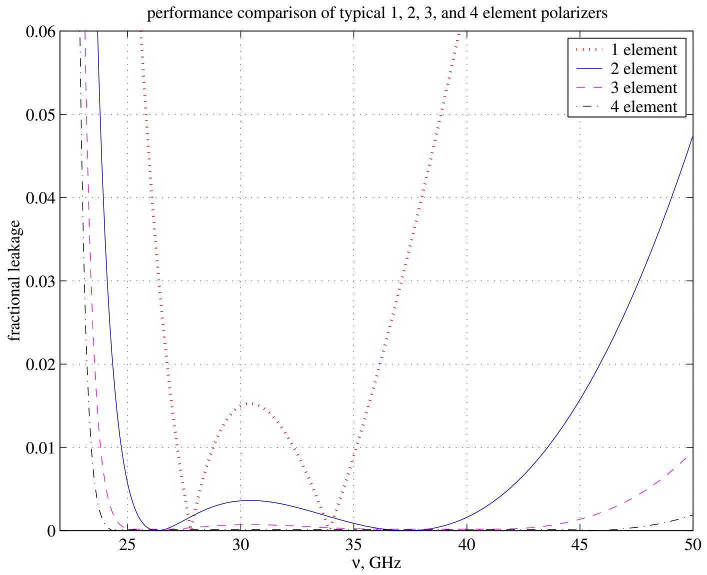

Figure 3.12 Comparison of the theoretical leakage achievable with single and multi-element circular polarizers. Shown are the theoretical minimum leakage for a single-element polarizer (dashed line) and for multi-element polarizers of 2-elements (solid line), 3 elements (dot-dash line), and 4 elements (dot-dot-dash line) according to the designs of Table 3.1.

whose $\Delta\phi$ curves are strictly proportional. The half-wave retarder, oriented at 15°, introduces a rotation of the plane of the linear polarization at the design frequency (to 30°), also introducing a frequency dispersion error. The quarter-wave retarder is oriented at $75° = 45° + 30°$ to produce the desired circular polarization. The orientation of the half-wave retarder to the incident polarization is chosen so that the path lengths traveled on the Poincaré sphere for the two retarders are equal; because these paths intersect tangentially this results in their dispersion effects canceling to first order. The entire assembly can be mechanically rotated by 90° to select L or R polarization. The offset angle between the two retarder elements is held fixed at 60°. We will describe the DASI polarizers in more detail in §3.4.5.

Formalism

Recall that the action of a single retarder element on complex 2-vector polarization states can be represented by the matrix $S(\Delta\phi, \theta)$ defined by Eq. 3.14. The action of a compound retarder composed of n retarder elements can be written

$$\begin{bmatrix} V_{x,\mathrm{out}} \\ V_{y,\mathrm{out}} \end{bmatrix} = S(\Delta\phi_n, \theta_n) \cdots S(\Delta\phi_2, \theta_2)\, S(\Delta\phi_1, \theta_1) \begin{bmatrix} V_{x,\mathrm{in}} \\ V_{y,\mathrm{in}} \end{bmatrix}. \tag{3.18}$$

We will express the action of the compound retarder as a (generally frequency-dependent) 2×2 complex matrix,

$$S_{\mathrm{compound}} = S(\Delta\phi_n, \theta_n) \cdots S(\Delta\phi_2, \theta_2)\, S(\Delta\phi_1, \theta_1) \tag{3.19}$$

$$= \begin{bmatrix} S_{31} & S_{32} \\ S_{41} & S_{42} \end{bmatrix}. \tag{3.20}$$

Such matrices used in this context are sometimes referred to as Jones matrices. The labeling that we choose for the complex elements S_{31}, etc., of this matrix reflects that they are also actually elements of the 4×4 scattering matrix, as it is conventionally defined in microwave engineering literature, for the compound retarder considered as a 4-port device with ports $[V_{x,\mathrm{in}}, V_{y,\mathrm{in}}, V_{x,\mathrm{out}}, V_{y,\mathrm{out}}]$. It is also possible to derive the values of these elements by combining the full 4×4 scattering matrices of each of the individual retarder elements, and in this way reflections and internal losses can be accounted for exactly. If these are small, so that as above the retarders can be regarded as ideal, then the matrix S_{compound} will be unitary. Because we have allowed an overall phase to be removed, the determinant of this matrix $\det(S_{\mathrm{compound}}) = 1$. It follows that $S_{\mathrm{compound}} \in SU(2)$ and can be written

$$S_{\mathrm{compound}} = \begin{bmatrix} S_{31} & S_{32} \\ -(S_{32})^* & (S_{31})^* \end{bmatrix} \quad \text{with } |S_{31}|^2 + |S_{32}|^2 = 1. \tag{3.21}$$

Three degrees of freedom determine the matrix S_{compound}, and thus define the action of the device at a given frequency. For example, we can choose these parameters to be the phase of S_{31}, $a \equiv \arg(S_{31})$, the phase of S_{32}, $b \equiv \arg(S_{32})$, and the ratio of their amplitudes, $r \equiv |S_{31}| / |S_{32}|$. Equivalently, three parameters specify the action as a general rotation of the Poincaré sphere, with two angles specifying the location of one of the two opposite polarization eigenstates of the device, and the third giving the rotation angle, which is their relative phase shift.

Any frequency variation of these parameters will be due to the frequency variation of the retardations $\Delta\phi_i(\nu)$ of each of the individual elements, $i = 1...n$, which comprise the compound device. Using a as an example,

$$a = a\left(\Delta\phi_1(\nu), \Delta\phi_2(\nu), .., \Delta\phi_n(\nu), \theta_1, \theta_2, ..., \theta_n\right) \tag{3.22}$$

If each retarder element is chosen to be of a similar construction, although scaled in length to produce the specified retardation at a central frequency $\Delta\phi_{0i} \equiv \Delta\phi_i(\nu_0)$, we expect the fractional variation with frequency $\delta(\nu)$ to be the same for all retarders,

$$\Delta\phi_i(\nu) = [1 + \delta(\nu)]\,\Delta\phi_{0i}. \tag{3.23}$$

See Fig. 3.14 for an illustration of this for the DASI polarizer retarders. This greatly simplifies our expression for the frequency dependence of a,

$$a = a\left(\delta(\nu), \Delta\phi_{01}, \Delta\phi_{02}, .., \Delta\phi_{0n}, \theta_1, \theta_2, ..., \theta_n\right). \tag{3.24}$$

For a given retarder application, our task is to find a set of values for the $2n$ parameters $(\Delta\phi_{01}, \Delta\phi_{02}, .., \Delta\phi_{0n}, \theta_1, \theta_2, ..., \theta_n)$ such that at the center frequency, a achieves its design value $a = a_0$ and also one or more of the higher derivatives $\delta a/\partial\delta$, $\partial^2 a/\partial\delta^2$... vanish. If the application requires other parameters (e.g., b and r) to take specific values, we can write a set of $2n$ equations

$$
2n \text{ equations} \left\{ \begin{array}{rl}
a_0 = & a(\delta\left(\nu_0\right), \overbrace{\Delta\phi_{01}, \Delta\phi_{02}, .., \Delta\phi_{0n}, \theta_1, \theta_2, ..., \theta_n}^{2n \text{ variables}}) \\
0 = & a'\left(\delta\left(\nu_0\right), \Delta\phi_{01}, \Delta\phi_{02}, .., \Delta\phi_{0n}, \theta_1, \theta_2, ..., \theta_n\right) \\
0 = & a''\left(\delta\left(\nu_0\right), \Delta\phi_{01}, \Delta\phi_{02}, .., \Delta\phi_{0n}, \theta_1, \theta_2, ..., \theta_n\right) \\
.. & \quad ... \\
b_0 = & b\left(\delta\left(\nu_0\right), \Delta\phi_{01}, \Delta\phi_{02}, .., \Delta\phi_{0n}, \theta_1, \theta_2, ..., \theta_n\right) \\
0 = & b'\left(\delta\left(\nu_0\right), \Delta\phi_{01}, \Delta\phi_{02}, .., \Delta\phi_{0n}, \theta_1, \theta_2, ..., \theta_n\right) \\
.. & \quad ... \\
r_0 = & r\left(\delta\left(\nu_0\right), \Delta\phi_{01}, \Delta\phi_{02}, .., \Delta\phi_{0n}, \theta_1, \theta_2, ..., \theta_n\right) \\
0 = & r'\left(\delta\left(\nu_0\right), \Delta\phi_{01}, \Delta\phi_{02}, .., \Delta\phi_{0n}, \theta_1, \theta_2, ..., \theta_n\right) \\
.. & \quad ...
\end{array} \right. \tag{3.25}
$$

where a prime denotes a partial derivative with respect to δ. These can be solved for the $2n$ parameters $(\Delta\phi_{01}, \Delta\phi_{02}, .., \Delta\phi_{0n}, \theta_1, \theta_2, ..., \theta_n)$ which cause a, b, r to take their required values, and also to be invariant to variations in δ each to some specified order. The equations above tend to be too cumbersome to manipulate analytically, but may be easily evaluated numerically by calculating

$$
S_{\text{compound}}\left(\delta, \Delta\phi_{01}, \Delta\phi_{02}, .., \Delta\phi_{0n}, \theta_1, \theta_2, ..., \theta_n\right) \tag{3.26}
$$

using the matrix equations given above. Solutions for $(\Delta\phi_{01}, \Delta\phi_{02}, .., \Delta\phi_{0n}, \theta_1, \theta_2, ..., \theta_n)$ can readily be found using numerical grid search algorithms.

Note that in finding these solutions, no reference is made to the form of $\delta\left(\nu\right)$. If the retarder elements are designed so that at the central frequency v_0 their retardations are first-order frequency invariant, then if we expand $\delta\left(\nu\right)$ about ν_0, the leading order variation will be quadratic, $\delta \propto \left(\nu - \nu_0\right)^2$. Similarly, if a solution for parameters of a compound device is found that satisfies the equation $a' = 0$, but the second derivative of a is unconstrained, then the leading order variation of a will be quadratic in δ, or quartic in frequency. Thus, by combining first-order frequency-invariant retarders in a compound design which cancels $a' = 0$ to first order, the performance parameter a is frequency-invariant to third order. If the compound design cancels $a'' = 0$ to second order, the result is that a is frequency-invariant to fifth order. We call such solutions *maximally flat*, because they achieve the highest possible precision near a central frequency. Alternatively, several different frequencies can be substituted for the central frequency ν_0 in Eq. 3.25, resulting in $a(\nu) = a_0$ at up to four different frequencies for the $a' = 0$ case, and up to six frequencies for the $a'' = 0$ case. This latter approach we call *bandwidth optimized*, because it generally allows one to achieve a given performance specification for $|a - a_0|$ over the widest possible bandwidth. Typically it leads to a solution for parameters $(\Delta\phi_{01}, \Delta\phi_{02}, .., \Delta\phi_{0n}, \theta_1, \theta_2, ..., \theta_n)$ which differs very slightly from the maximally flat solution.

The numerical approach allows the equations to account for realistic small differences in the fractional variation δ of each element, which often arise from the non-uniformity of cross-section necessary for adequate matching sections. In this case, the equations are solved directly with respect to ν rather than δ. Likewise, it is possible to account for impact on the parameters of the effects of absorption and return loss. If these are small, the solutions will again differ only slightly from the maximally flat solutions, and optimization algorithms can take these as a starting point.

Solutions

The action of a right-handed circular polarizer is to couple a linearly polarized signal incident at $V_{x,\text{in}}$ to $V_{x,\text{out}}$ and $V_{y,\text{out}}$ with equal amplitudes but with a $-90°$ relative phase shift. In terms of the parameters defined above, this implies $r = 1$ and $(a - b) = \pi/2$. By the unitarity of the matrix S_{compound}, $V_{y,\text{in}}$ will be coupled to left-handed circular polarization. As we have seen before, only two parameters need to be constrained, and equivalently to constraining r and $(a - b)$, we can choose to set

circular polarizer designs:

n	constrained:	$\Delta\phi_{01}$	θ_1	$\Delta\phi_{02}$	θ_2	$\Delta\phi_{03}$	θ_3	$\Delta\phi_{04}$	θ_4
1	x, y	90°	45°						
2	x, y, x', y'	180°	15°	90°	75°				
3	x, y, x', y', x'', y''	180°	6.05°	180°	34.68°	90°	102.27°		
4	$x, y, x', y', x'', y'', x''', y'''$	180°	23.13°	180°	151.80°	180°	53.53°	90°	74.71°

Table 3.1 Theory covariance calculation coefficients for the full polarized case. The pattern of coefficients given in each cell of the table is specified at upper left. The table is symmetrical, so that the entries of the two right-most columns ($\mathrm{Re}\,(RR)_j$ and $\mathrm{Im}\,(RR)_j$, omitted to save space) can be read in the bottom rows, except for the $RR_i \times RR_j$ portion which is identical to Table 2.1.

the real and imaginary parts of the leakage to zero

$$x = \mathrm{Re}\,(D_R)\,, \qquad x_0 = 0 \tag{3.27}$$

$$y = \mathrm{Im}\,(D_R)\,, \qquad y_0 = 0 \tag{3.28}$$

when solving the system Eq. 3.25. Because we have two parameters, for an n-element compound circular polarizer, we use the $2n$ equations to constrain the parameter values and their first $n-1$ derivatives. For $n = 1...4$, our numerical search easily identifies the simplest maximally-flat designs, given in Table 3.1.

The performance of these designs (with some bandwidth optimization), using typical dielectric-loaded retarder elements, is illustrated in Fig. 3.12. It can be seen that even the two-element design offers a large advantage in bandwidth and precision over the conventional single-element polarizer.

The unconstrained degree of freedom in these designs represents the relative phase shift between the R and L circular states. Frequency variation of this parameter, which is directly evident in the cross-polar phase calibration (Fig. 4.1), presents no problems for DASI given its narrow (1 GHz) correlated bandwidth.

For applications which make broadband use of arbitrary linear combinations of the signals due to $V_{x,\mathrm{in}}$ and $V_{y,\mathrm{in}}$, generally all three parameters of the action must be constrained. For example, half-wave retarders are often used as linear polarization

quarter-wave designs:

n	constrained:	$\Delta\phi_{01}$	θ_1	$\Delta\phi_{02}$	θ_2	$\Delta\phi_{03}$	θ_3	$\Delta\phi_{04}$	θ_4
1	$x, z, (y = 0 \text{ also})$	90°	0°						
2	x, y, z, z'	90°	0°	360°	52.24°				
3	x, y, z, x', y', z'	115.18°	30.98°	180°	140.28°	115.18°	30.98°		
4	$x, y, z, x', y', z', x'', z''$	250.48°	17.36°	180°	115.84°	180°	166.57°	140.77°	60.95°

half-wave designs:

n	constrained:	$\Delta\phi_{01}$	θ_1	$\Delta\phi_{02}$	θ_2	$\Delta\phi_{03}$	θ_3	$\Delta\phi_{04}$	θ_4
1	$x, z, (y = 0 \text{ also})$	180°	0°						
2	x, y, z, z'	180°	90°	360°	30°				
3	x, y, z, x', y', z'	180°	60°	180°	120°	180°	60°		
4	$x, y, z, x', y', z', x'', y''$	180°	90°	180°	37.78°	360°	23.28°	180°	127.78°

Table 3.2 Theory covariance calculation coefficients for the full polarized case. The pattern of coefficients given in each cell of the table is specified at upper left. The table is symmetrical, so that the entries of the two right-most columns ($\mathrm{Re}\,(RR)_j$ and $\mathrm{Im}\,(RR)_j$, omitted to save space) can be read in the bottom rows, except for the $RR_i \times RR_j$ portion which is identical to Table 2.1.

rotators, with the overall orientation angle of the device continuously variable, so that the input signal may be any combination of $V_{x,\mathrm{in}}$ and $V_{y,\mathrm{in}}$. Similarly, quarter-wave retarders can be used to switch between circular and linear response; for either of these devices, if the third parameter is left unconstrained (as for the circular polarizers above), the orientation angle of the linear output will be unconstrained, and will generally vary with frequency.

For these designs, three parameters we choose to constrain are

$$x = \mathrm{Re}\,(S_{41})\,, \qquad x_0 = 0 \tag{3.29}$$

$$y = \mathrm{Im}\,(S_{41})\,, \qquad y_0 = 0 \tag{3.30}$$

$$z = \arg\,(S_{31}) - \arg\,(S_{42}) = \Delta\phi_{\mathrm{effective}}. \tag{3.31}$$

For quarter-wave retarders, we constrain $z_0 = \pi/2$. For half-wave retarders, we constrain $z_0 = \pi$. Because we have 3 parameters, for an n-element compound retarder, we must choose which of higher derivatives of these parameters to constrain with our

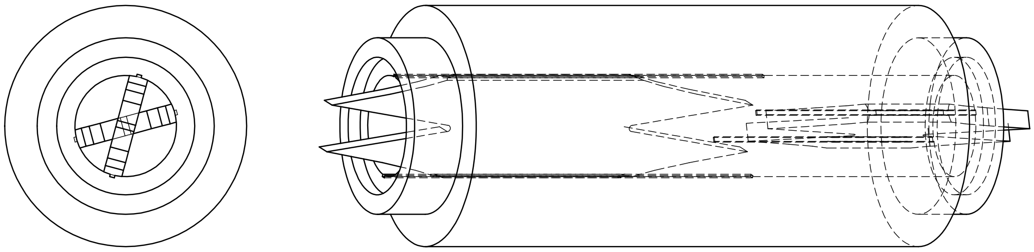

Figure 3.13 Drawing of the DASI broadband polarizers. Shown is the rotating barrel piece and the two dielectric retarder elements which it houses. The brass barrel is driven by a gear (not shown) mounted around its midline, and rotates on dry ball bearings which run in the square races at either end, just outside of the step which forms a choke groove. The dual-pointed profile of the polystyrene dielectric pieces minimized coupling to the unwanted TM_{11} mode. Waveguide diameter is 0.315", total length of the barrel is 2.016".

$2n$ equations. For various choices and for $n = 1...4$, our numerical search identifies the simplest maximally-flat quarter-wave and half-wave solutions given in Table 3.2. Several of these designs have previously been reported in the literature in the context of achromatic birefringent wave-plates (e.g. Pancharatnam 1955).

3.4.5 Design and Construction of the DASI Polarizers

A two-element circular polarizer design based on dielectric slab retarders was selected for the DASI polarizers. The construction of this device is illustrated in Fig. 3.13. The rotating circular waveguide section is based on a prior design for CBI/DASI rotating phase shifters. It is machined from brass, and is gold-plated. Each end of the waveguide section incorporates an outer step (OD 0.5490 in.) that forms a race for a ball-bearing, allowing the section to rotate freely. A gear is fixed to the outer diameter of the waveguide section to allow it to be driven to any desired orientation. Each end of the waveguide section also incorporates an inner step (diameter 0.4280 in.) which forms a choke groove at the bearing gap, preventing leakage of microwave

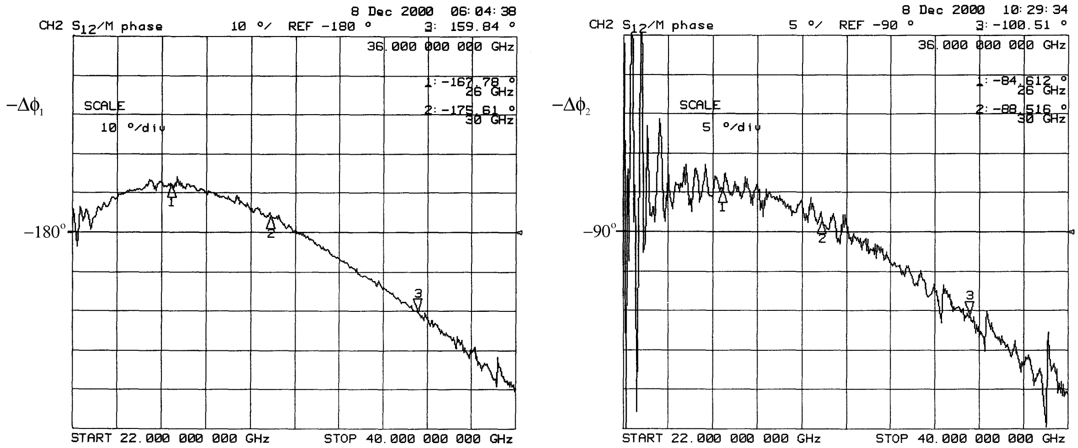

Figure 3.14 Phase retardation curves $\Delta\phi_1$ and $\Delta\phi_2$ measured individually for the two DASI polarizer elements of Fig. 3.13.

power through the gap. The inner walls of the waveguide section are broached with two pairs of precise grooves, a long pair and a short pair, set at 60° from each other. These hold and define the angular orientation of the dielectric slab retarder elements. The first retarder element, $\Delta\phi_{01} = 180°$, slides into the long grooves, and the second retarder element, $\Delta\phi_{02} = 90°$, slides into the short grooves from the opposite end.

The two retarder elements are dielectric slabs made from 60 mil thick stock polystyrene, which was chosen for its low dielectric loss, dimensional stability, and ease of machinability. In order to improve match, minimizing reflections at the ends of the slabs, the profiles of those ends taper to points, as illustrated in Fig. 3b and 3c. The particular choice of the dual-pointed profile was optimized to eliminate excitation of the unwanted TM_{11} mode. The edges of the slabs are keyed with ridges, which fit into the grooves of the waveguide section. The slabs are press-fit, and are secured in place with one small dot of epoxy.

The design also incorporates an absorbing vane at the circular to rectangular transition to suppress the reflected linear polarized mode, eliminating standing waves.

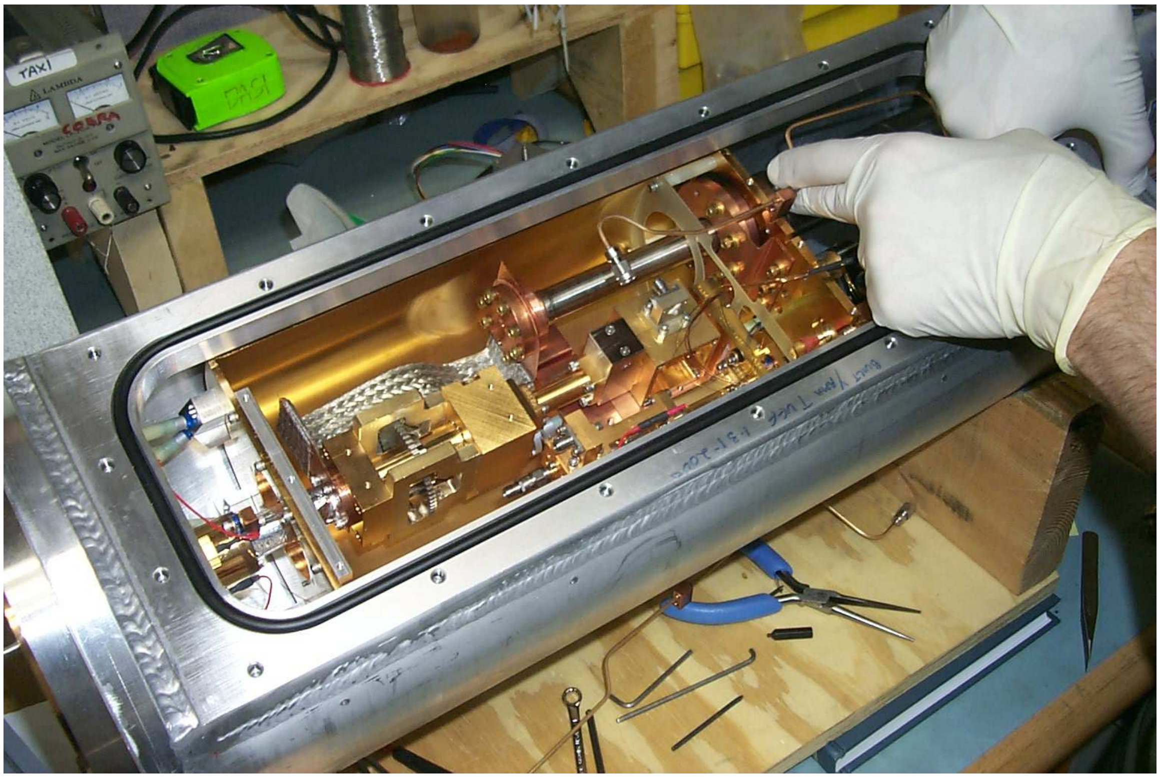

Figure 3.15 Installation of the DASI switchable achromatic polarizers. The gear which drives the rotating polarizer barrel 90° between the determined optimal R and L settings is visible.

3.4.6 Tuning, Testing, and Installation

The retardation curves $\Delta\phi_1(\nu)$ and $\Delta\phi_2(\nu)$, measured separately for the two DASI retarder elements using a vector network analyzer, are shown in Fig. 3.14. Together with return loss measurements, these were critical in optimizing the lengths and profiles of the retarder elements to obtain minimal reflections (< -20 dB) and a good match between the fractional variation with frequency $\delta(\nu)$ for these two retarders. The variation $\delta(\nu)$ vanishes to first-order at $\nu_0 \approx 26$ GHz. Unfortunately, this is at the edge, not the center, of the desired operating band 26-36GHz. A choice of waveguide diameter smaller than 0.315 in. of the existing rotating section design would have shifted this ν_0 up toward our band center, but time constraints prevented that optimization. Nonetheless, even though the variation $\delta(\nu)$ is not optimally

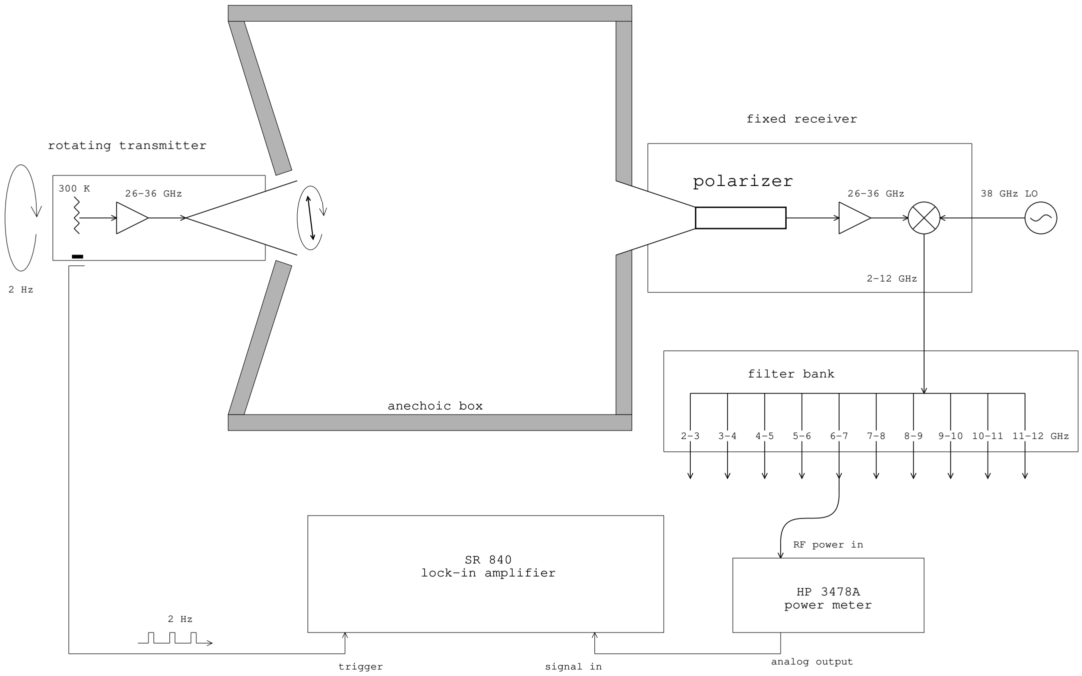

Figure 3.16 Configuration for laboratory tests of circular polarizer performance. A transmitter which produces a broadband linearly polarized signal is rotated continuously at 2 Hz (120 RPM). If the fixed receiver is fitted with a perfect circular polarizer, the power output will be steady. Any ellipticity of the polarizer will cause a modulation of the power output as the orientation of the linear signal changes. The SR840 lock-in amplifier measures this synchronous modulation, allowing the axial ratio and orientation of the ellipse to be determined. The LO, mixer, and filter bank allow the power meter to select each of ten sub-bands within 26-36 GHz, to measure performance across that frequency range.

flattened for these retarder elements, the cancellation of this variation due to the compound design leads to excellent broadband precision for this polarizer.

The performance of the complete assembled compound polarizer was measured with the polarizer installed in a DASI receiver, using a benchtop setup illustrated in Fig. 3.16. A transmitter which produces a strong, broadband, linearly polarized signal is rotated continuously about the axis of its horn at 2 Hz. The horn of the fixed receiver couples directly to this rotating linear signal in an anechoic box made of Eccosorb[6] to eliminate multiple reflections. Total power received in each of DASI's

[6]Emerson & Cuming Microwave Products, 28 York Ave. Randolph, MA 02368 USA.

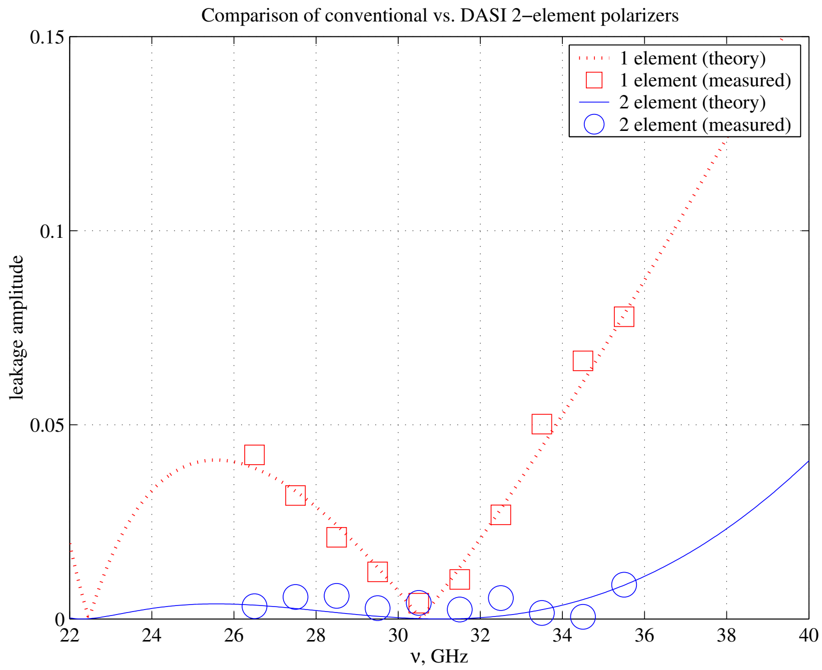

Figure 3.17 Benchtop measurements of the leakage for a single-element circular polarizer and the DASI two-element polarizers. The theoretical minimum leakage is shown for this single-element design (dashed line) and for the DASI design (solid line). The amplitudes of the complex leakages measured with the setup illustrated in Fig. 3.16 are shown at each of the 10 DASI frequency bands for the single-element polarizer (squares) and the DASI polarizer (circles).

ten sub-bands within 26-36 GHz is measured through a filter band by a power meter and lockin amplifier triggered at twice the horn rotation frequency. In this way, the phase and amplitude of the signal modulation directly measure the orientation and axial ratio of the receiver's polarization ellipse, determining the complex leakage at each frequency.

These benchtop measurements were used in tuning the DASI polarizers to minimize the leakage across the band. Three degrees of freedom were available in the tuning process. The orientation setting of the polarizer (see below) is set to effectively zero the imaginary part of the complex leakage in the coordinates used for these measurements. The real part of the leakage is zeroed by controlling the difference in thickness of the dielectric slabs, which after an initial test were precisely lapped to produce a final tuning. The common thickness of the slabs, which after tuning averaged 52.5 mils, was adjusted to effectively scale the design point of the curves of Fig. 3.14, adjusting these to minimize the frequency variation from 26-36 GHz.

Fig. 3.17 illustrates the results of final benchtop measurements for one DASI compound polarizer. For comparison, a conventional single-element polarizer built using the same type of retarder is shown. In both cases, the measured leakage amplitudes closely match the theoretical predictions. The interferometric leakage performance of the polarizers as installed on the DASI telescope is consistent with these benchtop measurements (§4.4).

3.4.7 Polarizer Switching

The repeatability of the polarization leakages is even more critical than their magnitude, since the leakages, if stable, can be corrected for in the data analysis. For DASI the stability of the polarizers is set by the repeatability and accuracy which with the angle is set. The polarizers are driven by a stepper motor with a $0\overset{\circ}{.}9$ half-step, geared down by a factor of three using anti-backlash gears, to provide $0\overset{\circ}{.}30$ steps of the polarizer assembly. The position of the polarizer is read by an encoder with $0\overset{\circ}{.}12$ steps. All of the hardware is contained under vacuum within the receiver cryostats. The motor and encoder are warm, but the polarizer assembly is cooled to ~ 10 K. With 2.5 counts of the encoder for each half step of the motor, we can ensure a repeatable return to the same position. We have verified that the stepper motor holds the polarizer position to better than half of an encoder count ($< 0\overset{\circ}{.}06$) for the entire season. This accuracy translates to a variation in the leakage of less than 0.1%. Astronomical tests of the stability of the leakages on long time scales are given in §4.4.

During polarization observations, the polarizer for each receiver is switched between L and R on a Walsh sequence which spends an equal amount of time in each state, i.e., $\sum_i f_i = 0$ if we represent the two states as $f \in \pm 1$. The product of two Walsh functions is another Walsh function, so that $\sum_{i,n\neq m} f_i^n f_i^m = 0$, from which it

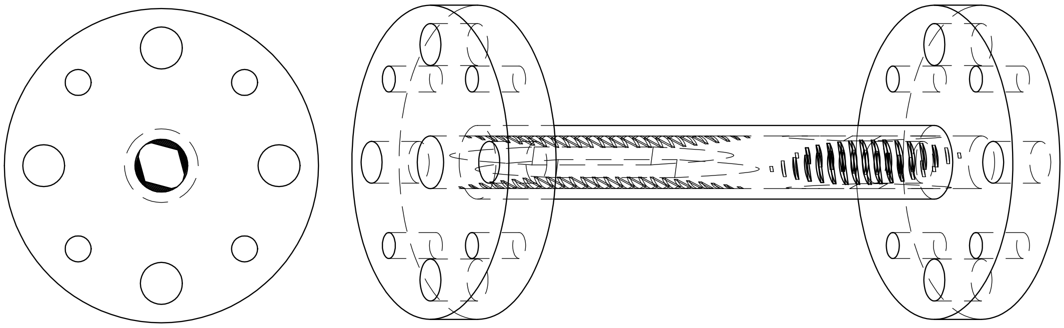

Figure 3.18 Drawing of a new all-metal W-band polarizer design. This design replaces the dielectric elements of the DASI broadband polarizers with a combination of corrugations and indented waveguide walls, but uses the same two-element circular polarizer combination of retarder lengths and angles. Waveguide diameter is 0.122", total length is 1.5".

follows that over the course of a full Walsh cycle each baseline of the interferometer spends an equal amount of time in each of the four Stokes states, although different baselines sample different Stokes states at any given time. For the CMB polarization observations, a Walsh function of period 16 with a time step of 200 seconds was used, so that over the course of an hour, every Stokes state is sampled by every baseline for approximately 13 minutes.

3.4.8 New Design Directions

Since the construction of the DASI polarizers, further efforts have been made to optimize the performance attainable with multiple-element polarizer designs. Because simultaneous dual-polarization receivers are desirable for future applications, we have not concentrated on the switching mechanism, but for fixed designs have attempted to optimize all dimensions, including waveguide diameter through the polarizer, to maximize bandwidth and minimize leakage. We have explored designs which replace the differential loading of the dielectric slab with that of metal corrugations on the

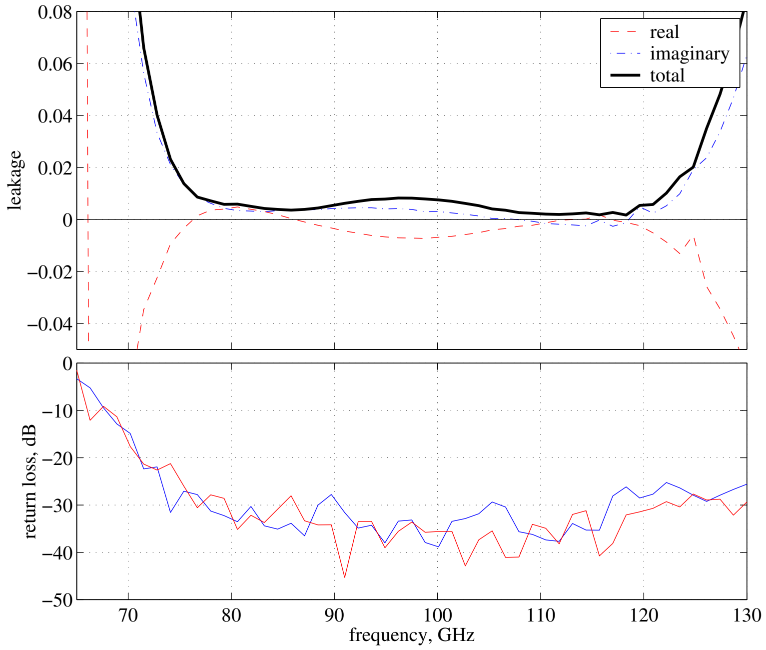

Figure 3.19 Modeled performance of the new W-band polarizer design. Ansoft HFSS software was used to simulate operation over the indicated range of frequencies.

circular waveguide walls. All metal designs in principle offer more repeatable manufacturability, less performance variation from room to cryogenic temperature, and lower ultimate loss, and moreover are easily scalable to a wide range of frequencies limited only by the electroforming manufacture process.

Fig. 3.18 illustrates a two-element all metal design scaled to W-band (75-125 GHz) dimensions. Fig. 3.19 reports the expected performance of this design, modeled with Ansoft HFSS software 3-D electromagnetic simulation software. The ultimate polarization precision achievable using this design over a 50% waveguide bandwidth is likely to be limited not by the polarizer, but by limitations on existing broadband orthomode transformers.

Chapter 4

Calibration

In Chapter 2 we derived the equations that describe DASI's idealized instrumental response. For each visibility that is output by the correlator, we found the response pattern to the Stokes parameters of signals on the sky (Eq. 2.12) and in the Fourier plane (Eq. 2.16), and we calculated the resulting covariance of the data due to each of the CMB power spectra (Eq. 2.19). In practice, each "raw" visibility has a complex gain factor which must be properly characterized in order to calibrate the phase of the corrugation and determine the amplitude in units of flux. Also, although the DASI polarizers are designed to minimize deviations from pure R or L circular response, residual leakages will cause the cross-polar visibilities to have sensitivity to the temperature signal which must be characterized and corrected in order to recover the ideal response expressed in those equations. Finally, variations across the primary beam in the effective polarization state received by each antenna lead to off-axis leakage of the temperature signal which must be modeled with extensions to the formalism presented in Chapter 2.

During the course of the 2001 – 2002 polarization observations, considerable effort was expended to characterize DASI's polarization response using observations of astronomical sources and of aperture-filling temperature and polarization references. These calibration observations, which were reported in Paper IV, are described in this chapter in some detail. Astronomical observations which provide independent checks of these calibrations lend confidence that we understand the various aspects of DASI's instrumental response to a level (precision better than 1%) that is more than adequate to accurately measure the expected E-mode polarization of the CMB.

4.1 Relative Gain and Phase Calibration

The complex gain factors for DASI's co-polar visibilities are easily determined, baseline by baseline, by observing a bright unpolarized point source. We base this calibration on daily observations of the bright HII region RCW38, which is described at length in Paper I. Observations of this compact source serve to define zero-phase for each of the complex co-polar visibilities, and comparison of the measured "raw" amplitude to the absolute flux scale that we have derived for this source (see §4.3) define the amplitude of the baseline's complex gain factor. The relative gain of the real and imaginary channels of the correlator itself, as well as corrections to ensure their orthogonality, are also determined daily on a baseline-by-baseline basis, using observations of the internal noise source made while inserting an additional $\pm 90°$ phase switch on each receiver.

The cross-polar complex gain factors could also easily be directly determined, baseline by baseline, with observations of a bright polarized source. However, bright polarized sources are scarce at high frequencies, and few are well studied in the southern hemisphere. The low gain of DASI's 20-cm feed horns, moreover, makes it impracticable to observe all but the brightest sources, in total intensity or otherwise, and the brightest sources at 30 GHz are typically compact HII regions, whose polarization fraction is expected to be negligible. We therefore derive the full calibration through observations of an unpolarized source. The gains for the pairs of receivers $m - n$ that comprise each baseline can be decomposed into antenna-based factors, which will allow us to construct the cross-polar gains from the antenna-based gain factors derived from the co-polar visibilities.

The signal chain of each receiver introduces a unique phase offset and gain variation to the electric field measured at the correlator, so that the expression for this field must be modified by a receiver-dependent complex gain, $\tilde{E}_m = g_m E_m$, where g_m depends on the polarization state of the receiver. Furthermore, the DASI analog correlator will introduce baseline-dependent complex gains g_{mn}, independent of polarization state, so that the measured visibilities are given by:

$$\begin{aligned}
\tilde{V}^{RR}_{mn} &= g^R_m g^{R^*}_n g_{mn} V^{RR}_{mn} \equiv G^{RR}_{mn} V^{RR}_{mn} \\
\tilde{V}^{LL}_{mn} &= g^L_m g^{L^*}_n g_{mn} V^{LL}_{mn} \equiv G^{LL}_{mn} V^{LL}_{mn} \\
\tilde{V}^{RL}_{mn} &= g^R_m g^{L^*}_n g_{mn} V^{RL}_{mn} \equiv G^{RL}_{mn} V^{RL}_{mn} \\
\tilde{V}^{LR}_{mn} &= g^L_m g^{R^*}_n g_{mn} V^{LR}_{mn} \equiv G^{LR}_{mn} V^{LR}_{mn}.
\end{aligned} \tag{4.1}$$

As described above, the co-polar gain factors G^{RR}_{mn} and G^{LL}_{mn} are easily derived for each baseline (mn) from observations of a bright unpolarized point source or extended source whose intrinsic visibility structure is known (if we take the circular polarization S_V to be zero). Our goal is to determine the G^{RL}_{mn} and G^{LR}_{mn} (at least to a single overall phase $\Delta\phi$) without requiring cross-polarized observations of a bright polarized source.

It can be seen from Equation 4.1 that this may be accomplished by working in terms of the ratios of complex gains, dividing our baseline-based co-polar gain factors

$$\frac{G^{LL}_{mn}}{G^{RR}_{mn}} = \frac{g^L_m g^{L*}_n g_{mn}}{g^R_m g^{R*}_n g_{mn}} = \left(\frac{g^L}{g^R}\right)_m \left(\frac{g^L}{g^R}\right)^*_n \tag{4.2}$$

to exactly cancel the analog correlator gains g_{mn}. For DASI, in each of the ten frequency bands this yields an overconstrained set of 78 complex equations which can be solved for the 13 antenna-based ratios $(g^L/g^R)_k$.

It is easy to see that the solution is only unique up to an overall common phase of the ratios, an ambiguity we resolve by setting the phase the ratios for a particular receiver to zero, keeping its true absolute cross-polar phase offset $\Delta\phi \equiv \phi_R - \phi_L$ as a single parameter to be determined later. With the ratios $(g^L/g^R)_k$ in hand, the baseline complex gains for the cross-polarized channels can be recovered from the co-polar solutions,

$$\begin{aligned}\left(\frac{g^L}{g^R}\right)^*_n G^{RR}_{mn} &= \left(\frac{g^L}{g^R}\right)^*_n g^R_m g^{R*}_n g_{mn} = e^{-i\Delta\phi} G^{RL}_{mn} \\ \left(\frac{g^L}{g^R}\right)_m G^{RR}_{mn} &= \left(\frac{g^L}{g^R}\right)_m g^R_m g^{R*}_n g_{mn} = e^{i\Delta\phi} G^{LR}_{mn} \ .\end{aligned} \tag{4.3}$$

We have constructed the cross-polar calibration factors from the antenna-based solutions, but only up to the unknown phase difference between R and L for our reference antenna. This overall phase offset, while leaving the amplitude of the cross-polar visibilities unaffected, will apparently rotate the plane of the observed polarization at each point on the sky, mixing power between S_Q and S_U, or between E and B. Determination of the offset, which is critical to obtaining a clean separation of CMB power into the E and B-modes, can only be accomplished by observing a source whose plane of polarization is known, as described in the next section.

As described in §5.2, twice a day we observe RCW38 with all receivers in R and all in L states for 35 minutes each, determining the individual complex gains for both the co-polar and cross-polar visibilities with statistical uncertainties $< 2\%$. Over many days of observation, these daily statistical uncertainties make a negligible contribution to our systematic error budget. Several of data consistency tests described in §5.5.2 are highly sensitive to possible systematic inconsistencies in the relative determination of the baseline complex gains, and find none.

4.2 Absolute Cross-polar Phase Calibration

In order to determine the phase offset left unspecified by the complex gain calibration described above, we require a source whose polarization angle (though not amplitude) is known. As we have noted, however, no suitably strong polarized astronomical sources are available. We create a source of known polarization angle by observing an unpolarized source through polarizing wire grids. At centimeter wavelengths, grids with wire spacing $\lesssim \lambda/3$ are easy to construct; using 34-gauge copper wire, thirteen

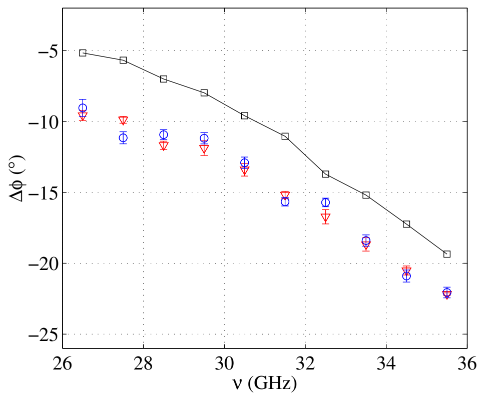

Figure 4.1 DASI absolute phase offsets. Shown are phase offsets determined from wire grid observations (triangles) and from the Moon (circles). Also shown are benchtop measurements of the same polarizer (solid line, squares), with an arbitrary offset subtracted.

wire grids were wound with a spacing of 0.05″ and epoxied between steel rims. These rims attach directly to the exterior of the corrugated shrouds and completely cover the aperture of the DASI horns.

The same source used for gain calibration of the visibilities, RCW38, was observed with the wire grids attached in two orientations, one with wires parallel to the ground, and the other with grids (but not receivers) rotated by 45 degrees with respect to the first. It was confirmed that in the second orientation the apparent phase of the cross-polar visibilities shifted by $\pm 90^\circ$ relative to the first, as indicated by Equation 2.12.

Additional observations in which the faceplate, receivers, and grids were rotated as a unit confirmed to high precision that the phase of the "raw" visibility output depends, as it should, only on the grid angle measured with respect to the receivers. With a proper determination of the absolute cross-polar phase offset $\Delta\phi$, the cross-polar calibration factors of Eq. 4.3 will give zero-phase for both V^{RL} and V^{LR} when observing a N-S oriented polarized source ($+Q$) located at phase center, for a *specific* faceplate position defined to be $\psi = 0$. Rotation of the faceplate modulates the apparent orientation of a polarized source on the sky according to Eq. 2.3, which must be corrected. The overall absolute phase offset calibration factor is then $e^{\mp i(\Delta\phi - 2\psi)}$.

The measured absolute phase offsets $\Delta\phi(\nu)$ are shown in Fig. 4.1. These offsets show a trend in frequency which is a direct consequence of the achromatic polarizer design discussed in §3.4. As the figure shows, this trend is in excellent agreement with expectations from benchtop measurements of the polarizers, where the expected trend is shown with an arbitrary offset subtracted. These phase offsets were measured in 2001 August and again in 2002 February and were found to agree within measurement errors. As discussed below, we can restrict the intrinsic polarization fraction of RCW38 to $< 0.09\%$ at our observing frequency; since the grids create a polarized source with an effective polarization fraction of 100%, any intrinsic polarized flux at this level will have a negligible effect on the measurements of the absolute phase offsets. From the wire-grid observations, we derive the phase offset in each frequency band with an uncertainty of $\lesssim 0.^\circ4$.

As an independent check of this phase offset calibration, the Moon was observed at three different epochs during 2001–2002. At centimeter wavelengths, radiation from the Moon is dominated by thermal emission from the regolith, typically from the first $\sim 10 - 20$ cm of the Moon's surface. This radiation is intrinsically unpolarized, but scattering off the dielectric discontinuity at the surface will induce polarization; the tangentially polarized component is preferentially reflected, leading to a net radial polarization pattern across the disk of the Moon. This polarization amplitude decreases to zero at the center and increases to a maximum at the limb (see Moffat 1972 for a comparable result at 21 cm, and Mitchell & De Pater 1994 for a similar discussion and map of the microwave polarization of Mercury).

Observations of the Moon were made with DASI during 2001 – 2002 at several epochs, and at various phases of the Moon. All show excellent agreement with the expected radial polarization pattern, and the consistency between epochs attests to the stability of the absolute phase offset. In Fig. 4.2 we present a polarized map of the Moon made during 21 – 22 August 2001, when the Moon was nearly full. These data

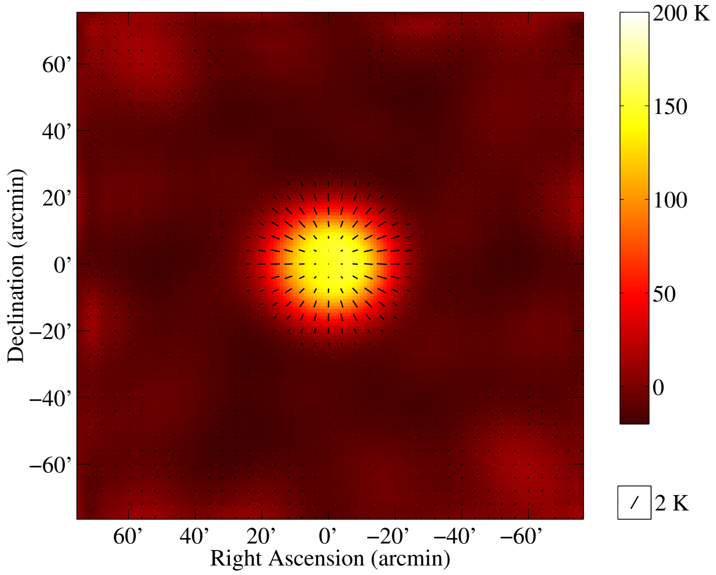

Figure 4.2 DASI image of the Moon. Shown is the total intensity map (colorscale), with measured polarization vectors overplotted, demonstrating the expected radial polarization pattern. In these maps the synthesized beam has $\sim 22'$ FWHM, which is used to give and approximate pixel-based conversion to temperature units.

have been corrected for instrumental leakages (§4.4) and the absolute phase offset determined from wire grid observations has been applied.

Any residual phase offset in the cross-polar visibilities will introduce a vorticity to the polarization vectors (technically, it introduces a non-zero B-mode component to the pattern), from which we can derive an independent measure of the cross-polar phase offsets. These results, also shown in Fig. 4.1, are consistent with the offsets measured with the wire grid polarizers, to within the $\sim 0\overset{\circ}{.}4$ measurement errors. As discussed in §6.3, errors in the absolute phase offset of this magnitude have a negligible effect on the power spectral analysis.

4.3 Absolute Gain Calibration

Absolute calibration of the telescope was achieved through measurements of external thermal loads. These loads consisted of beam-filling samples of corrugated Eccosorb,[1] thermally insulated and held at either LN_2 or ambient air temperature. The total power response of each of the 13 receivers $\times$ 10 bands was measured at the input of the correlator with a calibrated power meter, and the response to the internal noise source (the stability of which is continuously monitored with a separate meter) was calibrated with reference to these loads. This calibration was immediately transferred to the astronomical reference RCW38, which was observed at six redundant faceplate positions to derive a flux model for all baselines and frequencies.

This procedure, which takes a total of ~ 48 hours, was repeated at the beginning and end of both the 2001 and 2002 seasons. Because daily calibrations are referenced to RCW38, an extended HII emission region with no significant time variability, the principal purpose of repeating this calibration transfer is to test the repeatability of the procedure. Table 4.1 gives each of the contributions to the final uncertainty on the absolute overall flux scale calibration $\sigma\left(S_{\rm point}\right)$. The flux scales resulting from each of the calibrations done at different epochs are found to agree within 0.3%, consistent with our estimate of $\sim 1\%$ uncertainty due to statistical variability in the load measurement and transfer procedure. Using the data consistency tests described in §5.5.2, we can place upper limits on the final uncertainty resulting from the daily RCW38 complex gain calibrations, finding that the combined effects of daily statistical uncertainties (2% per baseline, see §4.1 above) and possible systematic discrepencies between baselines are negligible ($< 0.1\%$). Uncertainties on atmospheric opacity τ and the relative correlation efficiency for the internal noise source and an astronomical source at phase center $\eta_{\rm ns}/\eta_{\rm ps}$ contribute $< 1\%$. These uncertainties are dominated by those of the optical coupling and effective temperatures of the

[1] Emerson & Cuming Microwave Products, 28 York Ave. Randolph, MA 02368 USA.

uncertainty	level	cause of uncertainty	$\sigma\,(S_{\rm point})$	$\sigma\,(C_l)$
$\sigma\,(\text{mean}\,(S_{\rm epoch2}/S_{\rm epoch1}))$	1%	statistical error in load cal and transfer	1%	2%
$\sigma\,(\text{mean}\,(\text{daily}\ G_{mn}))$	$< 0.1\%$	error from daily gain calibrations	$< 0.1\%$	$< 0.2\%$
τ, $\eta_{\rm ns}/\eta_{\rm ps}$,	$< 1\%$	systematic error on various efficiencies	$< 1\%$	$< 2\%$
$T_{\rm amb} - T_{\rm ln2}$	5K	systematic Δ load temperature error	3%	6%
A_e	4%	effective aperture (beam error)	4%	4%
		totals:	5.2%	8%

Table 4.1 Each of the various contributions to the overall absolute calibration uncertainty on the flux scale $\sigma\,(S_{\rm point})$ and the CMB power spectra $\sigma\,(C_l)$. See text for details.

thermal loads (which are monitored with calibrated DT-470 diodes), which together contribute 3% to the overall flux scale uncertainty.

Each of the flux scale uncertainties given so far contributes to a fractional uncertainty on the CMB power spectra, derived from the covariance of the visibilities, as $\sigma\,(C_l) \sim 2\sigma\,(S_{\rm point})$. The 4% uncertainty in aperture efficiency A_e, determined from comparisons of measured and theoretical primary beam widths (Halverson 2002), directly translates to an uncertainty on the point-source gain for the definition of the absolute flux scale. However, for CMB measurements this uncertainty effectively scales the area of the window function $\widetilde{A}\,(\mathbf{u}, \nu_i)$ defined in Chapter 2. The effect on the expected variance of the visibility CMB signal is proportional to A_e, leading to a 4% uncertainty. The covariance of highly correlated visibilities is also effected, and in simulations we have found that this actually leads to a cancellation of errors for power spectrum estimates from the highly-correlated visibilities at lower l, decreasing from 4% at $l = 900$ to 1% at $l = 140$. However, because the other uncertainties contributing to $\sigma\,(C_l)$ dominate this effect, it is found that it is an excellent approximation to adopt an overall calibration uncertainty of 8% ($1\,\sigma$), expressed as a fractional uncertainty on the C_l bandpowers (4% in $\Delta T/T$). This common calibration uncertainty applies equally to all parameters which estimate amplitudes of temperature and polarization

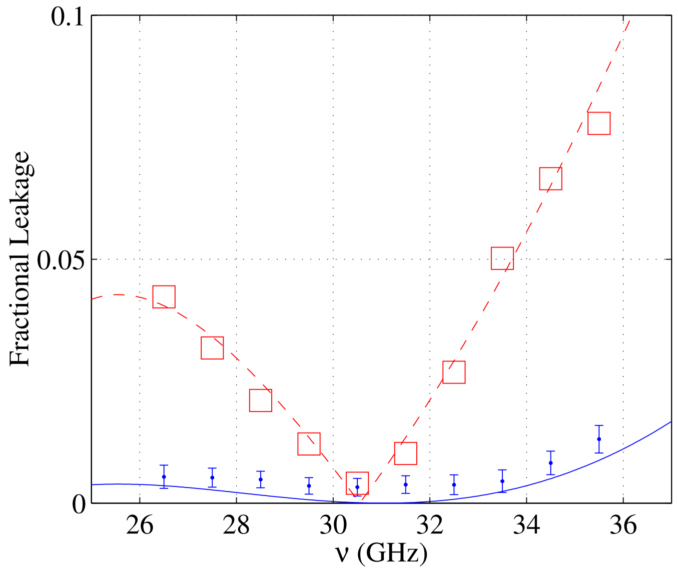

Figure 4.3 The average on-axis instrumental polarization for the 13 DASI receivers, determined by interferometric observations of RCW38, is plotted (points and errorbars) in comparison to the theoretical minimum (solid line) for the DASI 2-element polarizer design. The average DASI polarizer performance as installed on the telescope is comparable to the results obtained from benchtop measurements (see Fig. 3.17). It compares favorably to the leakage obtainable with a conventional single-element design (dashed line is theoretical minimum; squares are benchtop results).

power spectra in the analyses presented here.

4.4 Leakage Correction

For ideal circular polarizers, the cross-polar visibilities are strictly proportional to linear combinations of the Stokes parameters Q and U. However, the imperfect rejection of the unwanted polarization state, as described in Chapter 3 by a complex leakage D_m for each receiver m which depends on frequency, leads to additional terms in the cross-polar visibilities proportional to the total intensity T. From our general expression Eq. 2.10, using the circular leakage definitions $D_m^R = (\alpha_1/\alpha_2 - i)/2$ and $D_n^L = (\beta_1/\beta_2 + i)/2$, we can see that the leakages modify the cross-polar visibility response in Eq. 2.11 to

$$\begin{aligned} V_{mn}^{RL} &= [Q + iU]\, e^{-2i\psi} + [D_m^R + D_n^{L*}]T \\ V_{mn}^{LR} &= [Q - iU]\, e^{+2i\psi} + [D_m^L + D_n^{R*}]T \ . \end{aligned} \qquad (4.4)$$

Here for clarity we have suppressed the $\hat{x}$-dependent phase term of the corrugation pattern, but have included the phase dependence of the polarization signal on the faceplate-rotation ψ prior to applying the correction for this effect.

From Equation 4.4, it can be seen that the leakages are irrotational in the reference frame of the instrument, while any contribution to the visibilities from intrinsic source polarization will have a phase modulated by the faceplate rotation. The data can therefore be fit for an offset plus a sinusoidal modulation to isolate the leakages. Equivalently, when observations are made at three or six-fold symmetric faceplate rotations, the cross-polar visibilities for a radially symmetric source can simply be averaged over faceplate rotations to cancel the intrinsic term.

To determine the magnitude of the leakages, RCW38 was observed at six faceplate rotations separated by 60°, for approximately 3 hours at each faceplate position, resulting in an rms noise on the baseline leakages of 0.8% (of T). As can be seen from Equation 4.4, however, the baseline leakages are simply linear combinations of antenna-based terms, and can therefore be solved for the antenna-based leakages D_m, yielding a typical error of 0.3% on the antenna-based leakages. Typical antenna-based leakage amplitudes range from $\lesssim 1\%$ over much of the frequency band, to $\sim 2\%$ at the highest frequency. (As for the relative gain calibration, this procedure leaves a single unconstrained degree of freedom—the average of $D^R - D^{L*}$—which is irrelevant for the visibilities and can be set to zero). The averages of the antenna-based leakages $D^{R,L}$ are shown in Fig. 4.3. As described in §3.4.6, prior to installation on the telescope, the polarizers were optimized in a benchtop test setup to minimize the leakage response; as can be seen in Fig. 4.3, these astronomical observations indicate that we have achieved close to the theoretical minimum.

The leakages were measured once in August 2001, and again in April 2002 and July 2002, and the baseline leakages show excellent agreement between all three epochs. The higher s/n antenna-based leakages show similarly good agreement between August 2001 and April 2002, with residuals at all frequencies $\lesssim 1\%$, with the exception of three receivers. The polarizers for these receivers were retuned during the 2001 – 2002 austral summer, and systematic offsets can clearly be seen in the antenna-based residuals between these two epochs, the largest being approximately 2.5% in amplitude. Residuals between the April 2002 and July 2002 leakages are $\lesssim 1\%$ at all frequencies. Variations in the leakages of this magnitude are expected to have a negligible impact on the analysis presented in Chapter 6.

As discussed above, the parallactic angle modulation can be used to eliminate the leakage and place a limit on the intrinsic source polarization. Averaging over the three epochs at which the leakages were measured, it is found that the polarization amplitude of RCW38, $P = (Q^2 + U^2)^{1/2}$, is less than 0.09% of T at all frequencies.

Given the low level of DASI's leakages, the mixing of power from temperature into polarization in the uncorrected visibilities is expected to be a minor effect at most (see §6.3). Nonetheless, in the analysis presented in this thesis, the cross-polar data have in all cases been corrected to remove this effect using the co-polar data and the leakages determined from RCW38.

4.5 Beam Measurements and Off-Axis Leakage

Although the polarizers were optimized for low on-axis leakage response, the lensed feed horns themselves will induce an instrumental polarization which varies across the primary beam. In particular, the lenses have a significant radius of curvature and are cut with circular anti-reflection grooves (§3.2.1), both of which can be expected to produce a radial/tangential asymmetry in linear polarization transmission. Because there are no elements in the optical system that break the rotational symmetry, the

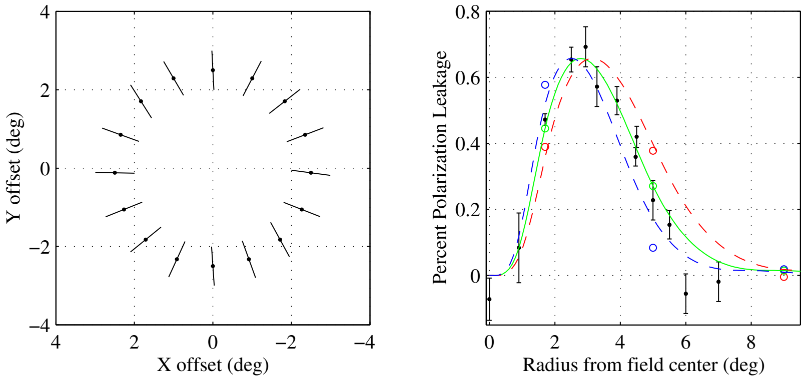

Figure 4.4 DASI off-axis leakage measurements. At left are shown the measured direction and relative magnitude of the instrumental leakage for a ring of 2.5° offset pointings on RCW38. At right, the amplitude of the instrumental polarization is shown versus radius from field center. Moon data are shown as red, green and blue circles corresponding to the frequency bands 26 – 29, 29 – 33, and 33 – 36 GHz respectively. RCW38 data for the full 26 – 36 GHz band are shown as black points. The green line is a spline interpolation of the 29 – 33 GHz Moon data, and the red and blue dashed lines are the interpolation scaled to 27.5 and 34.5 GHz respectively. See text for further discussion.

off-axis leakage is expected to be azimuthally symmetric, depending only on the angle from the phase center.

To measure the off-axis response of the feeds, observations of RCW38 were made with the source at 16 offset positions in a 2.5° radius ring. The direction of the instrumental leakage is shown in the left panel of Fig. 4.4. Within the measurement uncertainty this data is consistent with a simple radial pattern. The radial amplitude profile of this off-axis leakage was characterized by observations of RCW38 and the Moon at various offsets (see Fig. 4.4). The Moon data have extremely high signal-to-noise, permitting a separation of the data into several frequency bands.

In Chapter 2 we derived the sky response pattern of the visibilities (Eq. 2.12) under the assumption that the aperture field distributions our receivers are independent of polarization state, so that the primary beam $A(\hat{\mathbf{x}}, \nu)$ simply corresponds to the Fourier transform of the autocorrelation $\widetilde{A}\,(\mathbf{u}, \nu_i)$ of this aperture field. Consider a receiver with a pure R polarization state defined at the throat of the horn. The circular symmetry of our optics indicates that any ellipticity of the polarization state of the electric field across the aperture must be either radial or tangential. This defines the phase of the L polarized *leakage field* $E_D((x))$ to be $2i\chi$ relative to the usual (R polarized) aperture field $E((x))$; only the amplitude is unconstrained. Given a radial amplitude profile for the aperture leakage field (which must go to zero at both the aperture center and at the edge), we can derive its T window function in the uv plane as its convolution with the usual aperture field $E_D * E((u))$ measured in wavelengths, or the corresponding (complex) off-axis leakage beam as the Fourier transform of this. If the physical aperture field distributions are assumed to be frequency-independent, such that it scales with frequency when measured in wavelengths, the width of the leakage beam is expected to scale inversely with frequency.

Modeling the off-axis leakage in this way, trying simple polynomial radial profiles for the aperture leakage field, we are able to reproduce the general shape and frequency dependence of the off-axis leakage beam measurements shown in Fig. 4.4, but fail to replicate the sharp rise in amplitude seen between 1° and 2°. We therefore fit an empirical model by spline interpolation of the Moon data for the 29 – 33 GHz band (together with a point from RCW38 at 0.9° offset). The effect is assumed to scale with frequency in the same manner as the aperture field, and indeed this is supported by the Moon data at other frequencies. Additionally, the beam-offset RCW38 data confirms the validity of the model, agreeing within the measurement uncertainty.

The off-axis leakage rises to a maximum of $\sim 0.7\%$ near 3° from beam center. With the on-axis polarizer leakage subtracted to $\lesssim 0.3\%$ (see above), the off-axis leakage that remains, while still quite small compared to the expected level of polarized CMB signal (see §6.3), is the dominant instrumental polarization contribution. Although the visibilities cannot be individually corrected to remove this effect (as they can for the on-axis leakage), it may be incorporated in the analysis of the CMB data. Using our spline fit to the offset data, we account for this effect by modeling the

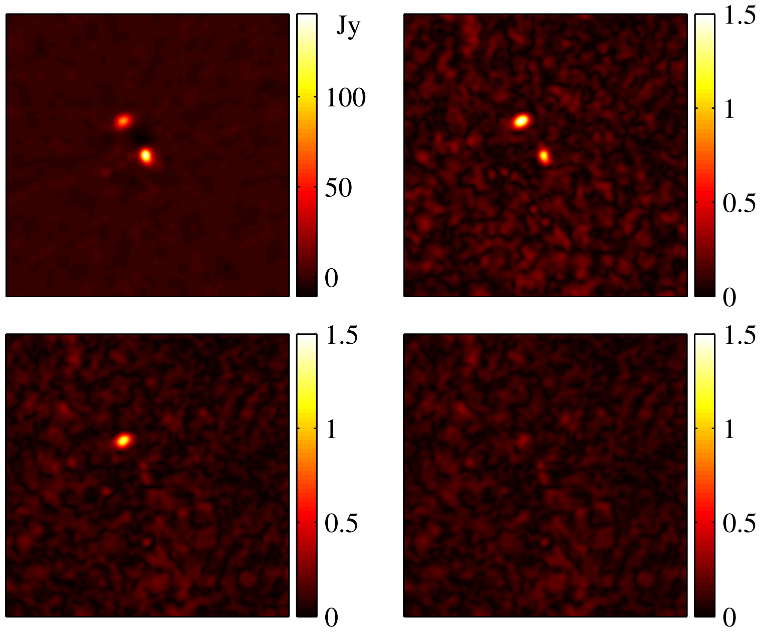

Figure 4.5 Observations of the molecular cloud complex NGC 6334. At top left, a total intensity map. Top right, a map of $P = (S_Q^2 + S_U^2)^{1/2}$, uncorrected for leakage, showing structure correlated with the total intensity map, and at a level consistent with instrumental polarization. Bottom left, a map of P corrected for on-axis leakage. The central source has disappeared, and the on-axis residuals are consistent with intrinsic source polarization $< 0.14\%$. Bottom right, a map of P corrected for off-axis leakage, using the profiles shown in Fig. 4.4. Fields are 12.8° across, with R.A. increasing to the left. All intensity scales are in Jy (figure courtesy of E. Leitch).

contribution of the off-axis leakage to the signal covariance matrix as described in §6.1.4. The inclusion of off-axis leakage covariance effectively corrects the small effect ($\lesssim 4\%$) of this leakage on the likelihood results, as discussed in §6.3.

As an illustration of the effects of the on-axis and off-axis leakages and our ability to accurately correct them, polarization observations of the Galactic source NGC 6334 are shown in Fig.4.5.[2] These observations were made in August 2001, centered on R.A. $= 17^{\rm h}20^{\rm m}$, Dec. $= -35°50'$ (J2000). NGC 6334 is a massive and complex star-forming region with multiple radio-bright lobes. The figure shows maps

[2]These observations were analyzed by E. Leitch, who played a key role in implementing the calibration procedures described in this chapter.

of total intensity T and total polarized flux P. Unlike the other maps presented in this thesis, here the artifacts of the uv sampling of the array have been reduced by an application of the CLEAN algorithm (Högbom 1974). At DASI's $\sim 22'$ resolution, the microwave emission from the ridge is concentrated in two regions of comparable flux, one on-center, the second near the half-power point of the primary beam, offering an excellent illustration of the on-axis and off-axis leakages. As can be seen in the second panel, the uncorrected P map shows emission coincident with these regions, at a level consistent with the instrumental leakages. Application of the on-axis leakage correction to the visibilities completely removes the central source in the polarization map, demonstrating that we can correct for instrumental leakage to better than 0.2%. Applying the off-axis leakage profile in the image plane similarly accounts for the second source.

Chapter 5

Observations and Data Reduction

5.1 CMB Field Selection

In its first season of operation, DASI measured CMB temperature anisotropies in 32 widely spaced fields, each with the $3\overset{\circ}{.}4$ FWHM size of the primary beam. The goal of those observations was a precise measurement of the temperature power spectrum. With high signal-to-noise on each field, observation of this large number of fields minimized sample variance for the power spectral estimates, while the wide separation facilitated design of the observing strategy and analysis. For the polarization observations, two fields were selected from the original 32 for extremely deep integration. Separated by one hour of Right Ascension, at R.A. $= 23^h30^m$ and R.A. $= 00^h30^m$, Dec. $= -55°$, these were the C2 and C3 fields of the original eight-field "C" row.

The locations of the original 32 fields were selected to lie both at high elevation angle to minimize ground pickup and at high galactic latitude to minimize foreground contamination. The IRAS 100 μm maps of Finkbeiner et al. (1999) and the 408 MHz maps of Haslam et al. (1981) were used to avoid regions of significant emission from galactic dust and synchrotron, respectively (see Figure 5.1).

As described in Paper I and Halverson (2002), our previous temperature observations produced clear detections of 28 point sources in the 32 fields with 31 GHz fluxes in the range 80 mJy to 2.8 Jy. All of these sources had identifiable counterparts in the

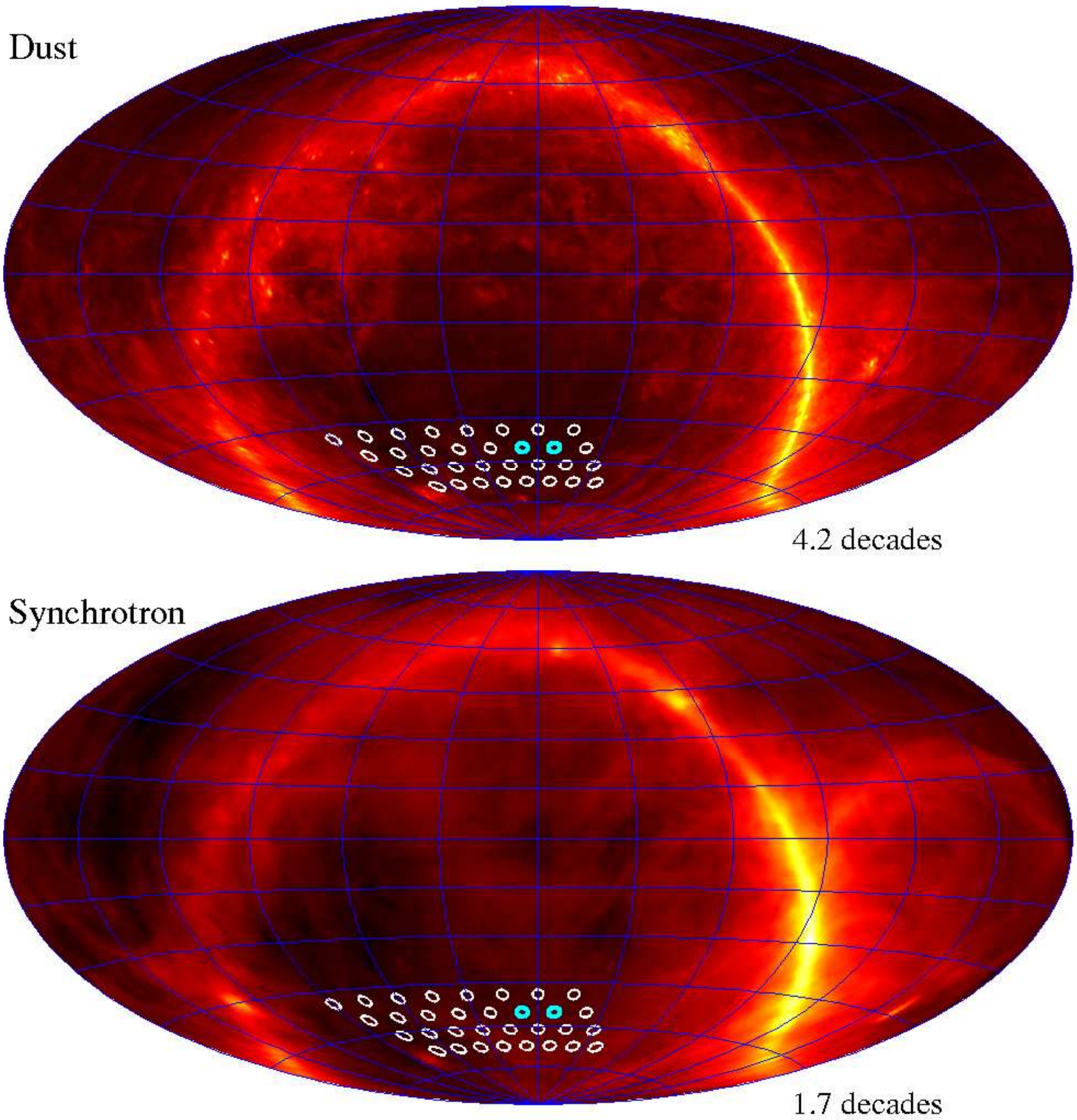

Figure 5.1 Locations of the original 32 DASI fields with the two polarization fields highlighted, shown in equatorial coordinates with R.A. = 0 h at center. The polarization fields, at R.A. = 23^h30^m and R.A. = 00^h30^m, Dec. = $-55°$, lie in the cleanest 6% and 25% of the sky with respect to the IRAS 100 μm galactic dust map of (Finkbeiner et al. 1999) and the 408 MHz synchrotron map of Haslam et al. (1981), reproduced here with log colorscales covering 4.2 and 1.7 decades of intensity, respectively.

5 GHz Parkes-MIT-NRAO (PMN) catalog (Wright et al. 1994), and are effectively masked out in analysis of our temperature data.

We chose our polarization fields, C2 and C3, from among the 13 of the original 32 fields which had no detectable point sources in our 2000 data. This pair, which lie at Galactic latitudes $-58\overset{\circ}{.}4$ and $-61\overset{\circ}{.}9$, were selected upon further consideration of our dust and synchrotron templates. The respective brightnesses of the IRAS and Haslam maps within this pair of fields lie at the 6% and 25% points of their integral distributions taken over the whole sky.

5.2 Observing Strategy

The data presented in this thesis were acquired from 10 April to 27 October 2001, and again from 14 February to 11 July 2002. Our CMB polarization observations were scheduled as self-contained 24 h (sidereal) blocks, beginning each day at 2:00 LST. In all, we obtained 162 such days of data in 2001, and 109 in 2002, for a total of 271 days before the cuts described in the next section. The remaining 52 days were spent mainly on observations to calibrate on- and off-axis leakages and absolute gain and cross-polar phase offsets as described in Chapter 4, as well as periodically scheduled observations to determine the pointing model of the telescope. Each day of CMB observations was composed of 20 hours of integration on our polarization fields, bracketed by various daily calibration observations.

The presence of near-field ground contamination at a level above the CMB signal was the guiding concern in designing our observing strategy. During the temperature observations of DASI's first season (2000), made before the installation of the groundshield, eight fields in a given row were successively tracked for one hour each over the same range in azimuth. Within an observing day this was repeated twice (over two 15° azimuth sectors which had been verified to have relatively low ground signal), for 16 hours of CMB integration. The common ground signal was effectively removed in the analysis using a constraint matrix formalism that removed two degrees of freedom (a constant and a linear drift) from the eight independent observations for most visibilities, and three for the shortest baselines which showed the greatest ground pickup. The ground signal was found to be quite stable on time scales longer than eight hours, so that analyzing this first-season data while removing only a constant mode gave very similar power spectrum results, with inconsistencies appearing only at a low level in the χ^2 tests.

The installation of the groundshield before the start of the polarization observations in 2001 reduced unpolarized ground contamination by an order of magnitude, with polarized contamination at least a factor of three lower still (see §3.1.3). Nonetheless, for reliable isolation of the sky signal from residual ground contamination, a subtraction scheme is unavoidable. For the polarization observations, the strategy of simply differencing two adjacent fields was selected as offering the deepest possible integration in a given total observing time. With this simple differencing strategy the observing efficiency is only 50% (one out of two observed modes is discarded). Observing more adjacent fields before ground subtraction would offer a higher efficiency (as in our first season), but in the noise-dominated initial detection phase this is more than offset by the spreading out of signal-to-noise. Simulations indicated that only after two complete seasons would a three-field strategy (with one subtracted ground mode) begin to yield smaller uncertainties on some l-ranges of the predicted CMB E-spectrum, with the deeper two-field approach still offering higher confidence of detection.

During the 20 hours of daily CMB integration, the telescope alternated between the fields every hour, tracking them over the same ten 15° azimuth sectors. Within each hour, the polarizers of the 13 receivers are stepped through one full period-16 Walsh sequence with a step time of 200 s, producing a complete observation in ~ 3200 seconds which equally visits all four Stokes states on all baselines, with a timing that is precisely reproduced over each azimuth sector. Temperature (co-polar) data are visibility data in which the polarizers from both receivers are in the left (LL Stokes state) or right (RR Stokes state) circularly polarized state; polarization (cross-polar) data are those in which the polarizers are in opposite states (LR or RL Stokes state).

Observations were performed at two distinct rotations of the array faceplate, separated by 60°. Given the three-fold symmetry of the array configuration, this rotation causes each of the original visibilities to be observed with a different pair of receivers, from a different position on the telescope mount (i.e. rotated by 180°). In changing both instrument and ground, this provides a powerful level of consistency checks on the sky signal as described in §5.5.2 below. Within each 24 h day observations were made at a fixed faceplate rotation, but the faceplate position was alternated roughly every day, so that approximately half the polarization data were acquired in each orientation.

Within each day, the 20 hours of CMB observations were bracketed by observations of the bright HII region RCW38 which serves as our primary calibrator. This source is described in some detail in Paper I. During the temperature observations of 2000 (in which calibrators were reobserved between each 8-hour CMB block, limiting CMB integration to 16 hours each day) instrumental gains were found to be stable at the $\sim 1\%$ level over many days, indicating that observing the source at the beginning and end of each day is sufficient. Each calibration observation includes 35 minutes of integration on RCW38 in each of the RR and LL configurations, from which the instrumental gains were determined for both the co-polar and cross-polar visibilities, as discussed in §4.1. In 35 minutes, we achieve uncertainties of $\lesssim 2\%$ on each of the co-polar and cross-polar visibility gains. The RCW38 gain calibrations were in turn bracketed by skydips from which atmospheric opacity was determined, and by injections of the noise source used to calibrate the complex correlator, also discussed in §4.1.

5.3 Data Cuts

Observations are excluded from the analysis, or *cut*, if they are considered suspect due to hardware problems, inadequate calibration, contamination from Moon or Sun signal, poor weather, or similar effects. In §5.5, we describe noise model and consistency statistics that are much more sensitive to these effects than are the actual results of our likelihood analysis, allowing us to be certain that the final results are unaffected by contamination.

In practice, our different data cuts are implemented at various stages of the data reduction process that is outlined in the next section. Many of the basic cuts are applied directly to the raw visibility data as it is initially averaged and calibrated into one-hour observations by the `dasi` software. Higher-level cuts are applied within the `matlab`-based reduction code during the formation of the data vector. A few cuts described below, like those based on calibrator stability, are actually applied at both stages, the higher-level cut being at a more restrictive level, to facilitate examining the dependence of the consistency statistics on these cut levels. For the sake of clarity our discussion of each of the data cuts below only loosely follows the order in which they are implemented, but rather organizes the cuts according to functional categories.

In the first category of cuts, we reject visibilities for which monitoring data from the telescope indicate obvious hardware malfunction, or simply non-ideal conditions. For each receiver, these conditions include cryogenics failure, loss of local oscillator phase lock, total powers outside the normal range, and (very rare) mechanical glitches in the polarizer stepper motors, any of which cause all visibilities associated with the affected receiver to be cut. Individual visibilities are also cut when complex correlator calibration (see §4.1) indicates large offsets between the real and imaginary channel multipliers. An additional cut, and the only one based on the individual data values, is a $> 30\sigma$ outlier cut to reject rare ($\ll 0.1\%$ of the data) hardware glitches. These basic cuts, all implemented on the raw visibility data, collectively reject $\sim 26\%$ of the data.

The second category of cuts is based on the phase and amplitude stability of the calibrator observations. Co-polar data are cut for which the calibrator amplitude varies by $> 10\%$ over 24 hours, or for which the calibrator phase varies by $> 15^\circ$. For the cross-polar data, these limits are relaxed to 15% and 20°, as the lower signal cross-polar data are dominated by thermal noise, and are therefore relatively insensitive to random errors in the daily calibration. We also reject data for which bracketing calibrator observations have been lost due to other cuts. The calibrator cuts reject $\sim 5\%$ of the data.

A third category of cuts are based on the elevation and position of the Sun and Moon. Co-polar visibilities are cut whenever the Sun was above the horizon. The cross-polar visibilities show little evidence for contamination from the Sun at low elevations, and are rejected only when the Sun elevation exceeds $> 5^\circ$, or when the Sun is above the horizon and closer than 90° to the either the CMB or calibrator fields. Of the total 271 days considered in our analysis, 18% were close enough to the polar sunset or sunrise to be excluded by these criteria. On the excluded days when the sun is quite high above the horizon, its effects become considerable in several of the other cut criteria, for example in the calibrator stability cuts. For this reason, the sun cut is applied to the dataset before calculating the other cut fractions quoted here. The Moon rises and sets once a month at the Pole, and passes within 45° of the CMB fields. For the 2001 data, co-polar data were rejected when the Moon was $> 10^\circ$ above the horizon and closer than 80° and 60° to the CMB and calibrator fields, respectively. Again, a less stringent cut is imposed on the cross-polar data: they are rejected when the Moon is within 50° of the fields and $> 17^\circ$ above the horizon (at which elevation it is still blocked by the groundshield). For the 2002 data, there is evidence that the sunshield may actually increase susceptibility to Moon pickup through secondary reflections when the Moon would otherwise be blocked by the ground shield. This evidence appeared in the co-polar data χ^2 tests described in

§5.5.2, which indicated slight but significant inconsistencies in a few subsets for just the 2002 data until a stricter co-polar moon cut was adopted. We conservatively chose to cut the 2002 co-polar data whenever the Moon is above the horizon. Although no similar evidence was found in the cross-polar data for Moon contamination at any cut levels, stricter 2002 cuts were adopted for these also, using threshold of 60° from the fields and elevation exceeding 14°. The final Moon cuts reject 29% of the co-polar data and 8% of the cross-polar data.

Our weather cut is based on the maximum significance of the correlations we calculate between channels in the 8.4-s data (§5.5.1). We find that this statistic (which is dominated by the shortest co-polar baselines) reliably identifies the rare periods of storm or unusual humidity at the Pole. An entire day is cut if the maximum off-diagonal correlation coefficient in the data correlation matrix exceeds 8σ significance, referred to Gaussian uncorrelated noise. We find that none of the consistency or noise model tests of §5.5 depend strongly on the level of this cut. A total of 22 days are cut by this test in addition to those rejected by the solar and lunar cuts.

A final category of cuts is based on derived noise statistics which identify unusual performance of the correlator hardware. We construct a correlator offset cut by calculating the sum of visibilities over consecutive pairs of 1-h observations, averaged over 24 hours, and over all baselines for each of DASI's 10 correlator boards. This quantity is sensitive to output of the correlator that remains constant between observations of the two CMB fields. All data are rejected for an entire correlator on days when there is evidence for offsets large compared to the thermal noise. Not surprisingly, this statistic rejects data for all correlator boards taken during sunset 2002, but also rejects data from a single board which showed unusually large offsets throughout much of 2002. This effect had been causing slight ($\sim 0.6\%$) excesses in the long-to-short timescale noise statistics of §5.5.1 which disappeared after implementation of the cut. Of data not previously rejected, this cut removes an additional 1.9%. Another cut rejects data from an entire correlator on days when the 1-hour variance, averaged over all baselines of that correlator, is grossly discrepant with the mean variance over 2001 – 2002. Data are rejected on a per-baseline basis if the variance within any 1-hour period falls on the extreme tails of the expected reduced χ^2 distribution. Together, these variance cuts reject a negligible fraction of the data.

In summary, over the 271 days of CMB observation 49% of the co-polar and 24% of the cross-polar data were excluded due to the location of either the sun or moon. Of the remaining "dark time" data, all other cuts described above together excluded 39% of the co-polar visibilities and 36% of the cross-polar visibilities from further consideration in the analysis. For each of the cuts, the results are insensitive to small variations in the chosen cut levels. As these cut levels are varied, in cases where evidence for residual contamination eventually appears, it appears first in either the χ^2 consistency tests on differenced data sets of §5.5.2 (as in the example of the co-polar data Moon cut) or in the noise model test statistics of §5.5.1 (as for the correlator offset cut). All of the likelihood results are found to be insensitive even to quite large variations in the precise cut thresholds, and we are confident that the thresholds settings introduce no significant bias in the CMB analysis.

5.4 Reduction

Data reduction consists of a series of steps to calibrate and reduce the dataset to a manageable size for our subsequent analysis.

The output of the DASI correlator, comprising real and imaginary visibilities for 78 baselines in 10 frequency bands, for a total of 1560 channels, is integrated and archived to disk during CMB observations at 8.4-s intervals. The data reduction begins using a powerful and flexible software package called `dasi` (authored by E. Leitch) to read each day of data from this archive. Using the daily bracketing observations of RCW38, this software applies relative gain and phase calibrations to the raw visibilities, forming antenna-based co-polar solutions to calibrate the cross-polar

Stokes states, as described in §4.1. After applying basic cuts, the calibrated 8.4-s integrations are combined over each 1 hour observation for each of the four Stokes states. The resulting dataset, 6240 visibilities $\times$ 20 hours $\times$ 271 days of observation, is then output to a second software package for higher level manipulation.

This higher-level reduction software is implemented as a library of `matlab` scripts and functions, which was authored for the polarization analysis using code described in (Halverson 2002) as a starting point. After applying the cuts described in the previous section, data from remaining identical 1 hour observations are combined and arranged into a vector. The corresponding noise covariance matrix is also constructed at this point according to the model discussed in the next section. Subsequent calibration, subtraction, combination, and compression procedures are implemented as matrix operations on this datavector and accompanying noise matrix. First, on-axis leakage corrections and absolute cross-polar phase calibration, both based on observations described in Chapter 4, are applied to the data in this manner. Likewise, sequential one-hour observations of the two fields in the same 15° azimuth range are differenced to remove any common ground signal, using a normalization $(\text{field1} - \text{field2})/\sqrt{2}$ which preserves the variance of the sky signal.

Except in the case where the dataset is split for use in the χ^2 consistency tests in §5.5.2, observations from different faceplate rotation angles, epochs, and azimuth ranges are all combined, as well as the two co-polar Stokes states, LL and RR. The resulting datavector, after cuts, has $N = 4344$ out of a possible 4680 elements ($6240 \times 3/4 = 4680$, where the 3/4 results from the combination of LL and RR). We call this the uncompressed dataset, and it contains all of the information in our observations of the differenced fields for Stokes parameters I, Q, and U.

5.5 Data Consistency Tests

In our analysis, we consider the datavector to be the sum of the actual sky signal and instrumental noise: $\mathbf{\Delta} = \mathbf{s} + \mathbf{n}$. The noise vector $\mathbf{n}$ is hypothesized to be Gaussian and random, with zero mean, so that the noise model is completely specified by a known covariance matrix $\mathbf{C}_N \equiv \langle \mathbf{n}\mathbf{n}^t \rangle$. Any significant excess variance observed in the data vector $\mathbf{\Delta}$ will be interpreted as signal. In the likelihood analysis of the next chapter, we characterize the total covariance of the dataset $\mathbf{C} = \mathbf{C}_T(\kappa) + \mathbf{C}_N$ in terms of parameters κ that specify the covariance $\mathbf{C}_T$ of this sky signal. This is the conventional approach to CMB data analysis, and it is clear that for it to succeed, the assumptions about the noise model and the accuracy of the noise covariance matrix must be thoroughly tested. This is especially true for our dataset, for which long integrations have been used to reach unprecedented levels of sensitivity in an attempt to measure the very small signal covariances expected from the polarization of the CMB.

5.5.1 Noise Model

Our noise model is based on the hypothesis that after the cuts described in the previous section, noise in the remaining differenced visibility data is Gaussian and white, with no significant noise correlations between different baselines, frequency bands, real/imaginary pairs, or Stokes states. According to this model, the noise covariance matrix as first constructed for the visibility datavector contains only diagonal elements, calculated from short timescale estimates of thermal noise as described below. The noise matrix remains highly sparse after calibration and compression transformations. This is a remarkably simple noise model; it is not unusual for single-dish CMB experiments to require considerable modeling effort to describe temporal and interchannel noise correlations introduced by 1/f detector noise, atmosphere, ground pickup and other effects. DASI benefits from its interferometric technique and observing strategy in the removal of correlated noise effects through multiple levels of differencing. Slow and fast phase switching as well as field differencing are used to minimize potentially variable systematic offsets that could otherwise contribute a non-thermal component to the noise. The observing strategy also includes Walsh sequencing of the Stokes states, observations over multiple azimuth ranges and faceplate rotation angles, and repeated observations of the same visibilities on the sky throughout the observing run to allow checks for systematic offsets and verification that the sky signal is repeatable. We have carefully tested the noise properties of the data to validate the use of our model.

Noise for each visibility is estimated by calculating the variance in the 8.4-s integrations over the period of 1 hr, before field differencing. To test that this noise estimate is accurate, we compare it with two other short timescale noise estimates, calculated from the variance in 8.4-s integrations over the 1-hr observations after field differencing and from the variance in sequential pairs of 8.4-s integrations. Any contributions from non-thermal sources of noise, such as offsets from ground pickup, would appear differently in each of these estimates. We find that all three agree within 0.06% for co-polar data and 0.03% for cross-polar data, averaged over all visibilities after data cuts.

Noise in the combined datavector is calculated directly from these short timescale estimates. After cuts, noise levels for each visibility are extremely consistent over time; the observed variation between 1-hr observations is dominated by the sample variance on these 1-hr noise estimates (each formed from $\sim$ 100 8.4-s samples). For this reason, uniform weights are used in combining 1-hr observations. This also avoids issues of bias in the combined noise estimates which would arise if weights were based on the 1-hr noise estimates.

We compare the final noise estimates (based on short timescale noise) to the variance of the 1-hr binned visibilities over the entire dataset (up to 2700 1-hr observations, over a period spanning 457 days). The ratio of long timescale to short timescale noise variance, averaged over all combined visibilities after data cuts, is 1.003 for the co-polar data and 1.005 for the cross-polar data, remarkably close to unity. Together with the results of the χ^2 consistency tests below (§5.5.2), these results demonstrate that the noise is white and integrates down from timescales of a few seconds to thousands of hours. We find that scaling the diagonal noise by 1% makes a negligible difference in the reported likelihood results (see §6.3).

To test for potential off-diagonal correlations in the noise, we calculate a 6240×6240 correlation coefficient matrix from the 8.4-s integrations for each day of observations.[1] To increase our sensitivity to correlated noise, we use only data obtained simultaneously for a given pair of data vector elements. Due to the Walsh sequencing of the Stokes states, a variable number of 8.4-s integrations M are used to calculate each off-diagonal element, so we assess the significance of the correlation coefficient in units of $\sigma = 1/\sqrt{M-1}$. Our weather cut statistic is the daily maximum off-diagonal correlation coefficient significance (see §5.3).

We use the mean data correlation coefficient matrix over all days, after weather cuts, to test for residual correlations over the entire dataset. We find that 1864 (0.016%) of the off-diagonal elements exceed a significance of 5.5σ, when about one such event is expected for uncorrelated Gaussian noise. The outliers are dominated by correlations between real/imaginary pairs of the same baseline, frequency band, and Stokes state, and between different frequency bands of the same baseline and Stokes state. For the real/imaginary pairs, the maximum correlation coefficient amplitude is 0.14, with an estimated mean amplitude of 0.02; for interband correlations the maximum amplitude and estimated mean are 0.04 and 0.003, respectively. We have tested alternative noise models which include these residual correlations in the likelihood analysis and find that they have a negligible impact on the results (see

[1]Examination of this matrix and alternative noise statistics was led by N. Halverson.

§6.3).

5.5.2 χ^2 Consistency Tests

As a simple and sensitive test of data consistency, we construct a χ^2 statistic from various splits and subsets of the visibility data. Splitting the data into two sets of observations that should measure the same sky signal, we form the statistic for both the sum and difference data vectors,

$$\chi^2 = \mathbf{\Delta}^t \mathbf{C}_N^{-1} \mathbf{\Delta}, \tag{5.1}$$

where $\mathbf{\Delta} = (\mathbf{\Delta_1} \pm \mathbf{\Delta_2})/2$ is the sum or difference data vector, and $\mathbf{C}_N = (\mathbf{C}_{N1} + \mathbf{C}_{N2})/4$ is the corresponding noise covariance matrix. The χ^2 statistics for the difference data vector, with the common sky signal component subtracted, test for systematic contamination of the data and mis-estimates of the noise model. The χ^2's for the sum data vector test for the presence of a sky signal in a straightforward way that is independent of the likelihood analyses that will be used to parameterize and constrain that signal.

We split the data for the difference and sum data vectors in five different ways:

1. Year – 2001 data vs. 2002 data,

2. Epoch – the first half of observations of a given visibility vs. the second half,

3. Azimuth range – east five vs. west five observation azimuth ranges,

4. Faceplate position – observations at a faceplate rotation angle of 0° vs. a rotation angle of 60°, and

5. Stokes state – co-polar observations in which both polarizers are observing left circularly polarized light (LL Stokes state) vs. those in which both are observing right circularly polarized light (RR Stokes state).

These splits were done on the combined 2001/2002 dataset and (except for the first split type) on 2001 and 2002 datasets separately, to test for persistent trends or obvious differences between the years. The faceplate position split is particularly powerful, since the six-fold symmetry of the (u, v) plane coverage allows us to measure the same sky signal for a given baseline with a different pair of receivers, different backend hardware, and at a different position on the faceplate with respect to the ground shields. This split is therefore sensitive not only to any offsets that may depend on these factors, but also to any discrepancies in calibration or sky response. The co-polar split tests the amplitude and phase calibration between polarizer states, and tests for the presence of circularly polarized signal.

For each of these splits, different subsets can be examined: co-polar data only, cross-polar data only (for all except the Stokes state split), various l-ranges (as determined by baseline length in units of wavelength), and subsets formed from any of these which isolate modes with the highest expected signal to noise (s/n). The construction of the high s/n subsets assumes a particular theoretical signal template in order to define the s/n eigenmode basis for that subset, as discussed in the next section. For this we use the concordance model defined in §6.1.1, although we find the results are not strongly dependent on choice of model. Note that the definitions of which modes are included in the high s/n subsets are made in terms of average theoretical signal, without any reference to the actual data. These subsets are more sensitive to certain classes of systematic effects in the difference data vector and more sensitive to the expected sky signal in the sum data vector, that otherwise may be masked by noise.

In Table 5.1, we present the difference and sum χ^2 values for each of splits and subsets examined for the combined 2001/2002 dataset (similar tests were also performed on each of the seasons separately). In each case we give the degrees of freedom, χ^2 value, and probability to exceed (PTE) this value in the χ^2 cumulative distribution function. For all of the 296 different split/subset combinations that were examined,

Temperature Data			Difference		Sum	
Split Type	Subset	# DOF	χ^2	PTE	χ^2	PTE
Year	full	1448	1474.2	0.31	23188.7	$< 1 \times 10^{-16}$
	high s/n	144	149.6	0.36	20675.8	$< 1 \times 10^{-16}$
	s/n > 1	320	337.1	0.24	21932.2	$< 1 \times 10^{-16}$
	l range 0–245	184	202.6	0.17	10566.3	$< 1 \times 10^{-16}$
	l range 0–245 high s/n	36	38.2	0.37	10355.1	$< 1 \times 10^{-16}$
	l range 245–420	398	389.7	0.61	7676.0	$< 1 \times 10^{-16}$
	l range 245–420 high s/n	79	88.9	0.21	7294.3	$< 1 \times 10^{-16}$
	l range 420–596	422	410.5	0.65	3122.5	$< 1 \times 10^{-16}$
	l range 420–596 high s/n	84	73.5	0.79	2727.8	$< 1 \times 10^{-16}$
	l range 596–772	336	367.8	0.11	1379.5	$< 1 \times 10^{-16}$
	l range 596–772 high s/n	67	82.3	0.10	991.8	$< 1 \times 10^{-16}$
	l range 772–1100	108	103.7	0.60	444.4	$< 1 \times 10^{-16}$
	l range 772–1100 high s/n	21	22.2	0.39	307.7	$< 1 \times 10^{-16}$
Epoch	full	1520	1546.3	0.31	32767.2	$< 1 \times 10^{-16}$
	high s/n	152	139.1	0.76	29702.0	$< 1 \times 10^{-16}$
	s/n > 1	348	366.5	0.24	31430.0	$< 1 \times 10^{-16}$
	l range 0–245	200	231.5	0.06	15373.5	$< 1 \times 10^{-16}$
	l range 0–245 high s/n	40	39.1	0.51	15112.0	$< 1 \times 10^{-16}$
	l range 245–420	424	453.9	0.15	10780.9	$< 1 \times 10^{-16}$
	l range 245–420 high s/n	84	104.1	0.07	10302.6	$< 1 \times 10^{-16}$
	l range 420–596	440	444.4	0.43	4156.0	$< 1 \times 10^{-16}$
	l range 420–596 high s/n	88	86.1	0.54	3723.4	$< 1 \times 10^{-16}$
	l range 596–772	348	305.2	0.95	1902.1	$< 1 \times 10^{-16}$
	l range 596–772 high s/n	69	63.8	0.65	1437.5	$< 1 \times 10^{-16}$
	l range 772–1100	108	111.3	0.39	554.8	$< 1 \times 10^{-16}$
	l range 772–1100 high s/n	21	29.2	0.11	398.7	$< 1 \times 10^{-16}$
Azimuth range	full	1520	1542.6	0.34	32763.8	$< 1 \times 10^{-16}$
	high s/n	152	163.0	0.26	29698.6	$< 1 \times 10^{-16}$
	s/n > 1	348	355.2	0.38	31426.9	$< 1 \times 10^{-16}$
	l range 0–245	200	203.7	0.41	15369.4	$< 1 \times 10^{-16}$
	l range 0–245 high s/n	40	39.1	0.51	15108.6	$< 1 \times 10^{-16}$
	l range 245–420	424	436.5	0.33	10780.7	$< 1 \times 10^{-16}$
	l range 245–420 high s/n	84	110.4	0.03	10302.6	$< 1 \times 10^{-16}$
	l range 420–596	440	442.1	0.46	4156.8	$< 1 \times 10^{-16}$
	l range 420–596 high s/n	88	89.9	0.43	3724.7	$< 1 \times 10^{-16}$
	l range 596–772	348	351.6	0.44	1902.0	$< 1 \times 10^{-16}$
	l range 596–772 high s/n	69	87.7	0.06	1437.2	$< 1 \times 10^{-16}$
	l range 772–1100	108	108.8	0.46	554.8	$< 1 \times 10^{-16}$
	l range 772–1100 high s/n	21	17.1	0.71	398.5	$< 1 \times 10^{-16}$
Faceplate position	full	1318	1415.2	0.03	27446.6	$< 1 \times 10^{-16}$
	high s/n	131	158.5	0.05	24537.4	$< 1 \times 10^{-16}$
	s/n > 1	331	365.3	0.09	26270.1	$< 1 \times 10^{-16}$
	l range 0–245	178	214.6	0.03	12883.6	$< 1 \times 10^{-16}$
	l range 0–245 high s/n	35	35.5	0.44	12628.7	$< 1 \times 10^{-16}$
	l range 245–420	362	407.5	0.05	9150.2	$< 1 \times 10^{-16}$
	l range 245–420 high s/n	72	75.0	0.38	8700.4	$< 1 \times 10^{-16}$
	l range 420–596	378	408.2	0.14	3301.1	$< 1 \times 10^{-16}$

Table 5.1 Results of χ^2 consistency tests (continued)

Temperature Data (continued)			Difference		Sum	
Split Type	Subset	# DOF	χ^2	PTE	χ^2	PTE
Faceplate	l range 420–596 high s/n	75	93.7	0.07	2889.2	$< 1 \times 10^{-16}$
position	l range 596–772	308	281.9	0.85	1633.2	$< 1 \times 10^{-16}$
	l range 596–772 high s/n	61	60.4	0.50	1197.4	$< 1 \times 10^{-16}$
	l range 772–1100	92	103.1	0.20	478.4	$< 1 \times 10^{-16}$
	l range 772–1100 high s/n	18	18.5	0.42	306.8	$< 1 \times 10^{-16}$
Stokes	full	1524	1556.6	0.27	33050.6	$< 1 \times 10^{-16}$
state	high s/n	152	122.1	0.96	29970.3	$< 1 \times 10^{-16}$
	s/n > 1	350	358.2	0.37	31722.5	$< 1 \times 10^{-16}$
	l range 0–245	202	199.8	0.53	15512.6	$< 1 \times 10^{-16}$
	l range 0–245 high s/n	40	32.4	0.80	15251.8	$< 1 \times 10^{-16}$
	l range 245–420	424	425.8	0.47	10876.1	$< 1 \times 10^{-16}$
	l range 245–420 high s/n	84	104.2	0.07	10401.0	$< 1 \times 10^{-16}$
	l range 420–596	442	475.7	0.13	4184.7	$< 1 \times 10^{-16}$
	l range 420–596 high s/n	88	98.1	0.22	3746.2	$< 1 \times 10^{-16}$
	l range 596–772	348	349.6	0.47	1922.5	$< 1 \times 10^{-16}$
	l range 596–772 high s/n	69	64.3	0.64	1449.1	$< 1 \times 10^{-16}$
	l range 772–1100	108	105.7	0.55	554.7	$< 1 \times 10^{-16}$
	l range 772–1100 high s/n	21	15.8	0.78	398.9	$< 1 \times 10^{-16}$

Polarization Data			Difference		Sum	
Split Type	Subset	# DOF	χ^2	PTE	χ^2	PTE
Year	full	2896	2949.4	0.24	2925.2	0.35
	high s/n	289	299.5	0.32	396.7	2.6×10^{-5}
	s/n > 1	30	34.4	0.27	82.4	8.7×10^{-7}
	l range 0–245	368	385.9	0.25	315.0	0.98
	l range 0–245 high s/n	73	61.0	0.84	64.5	0.75
	l range 245–420	796	862.2	0.05	829.4	0.20
	l range 245–420 high s/n	159	176.0	0.17	223.8	5.4×10^{-4}
	l range 420–596	844	861.0	0.33	837.3	0.56
	l range 420–596 high s/n	168	181.3	0.23	189.7	0.12
	l range 596–772	672	648.1	0.74	704.4	0.19
	l range 596–772 high s/n	134	139.5	0.35	160.0	0.06
	l range 772–1100	216	192.3	0.88	239.1	0.13
	l range 772–1100 high s/n	43	32.3	0.88	47.6	0.29
Epoch	full	3040	2907.0	0.96	3112.2	0.18
	high s/n	304	292.4	0.67	421.3	9.3×10^{-6}
	s/n > 1	34	29.2	0.70	98.6	3.3×10^{-8}
	l range 0–245	400	389.2	0.64	373.7	0.82
	l range 0–245 high s/n	80	101.0	0.06	98.9	0.08
	l range 245–420	848	836.5	0.60	823.8	0.72
	l range 245–420 high s/n	169	182.4	0.23	246.3	9.6×10^{-5}
	l range 420–596	880	799.1	0.98	929.4	0.12
	l range 420–596 high s/n	176	133.4	0.99	211.8	0.03
	l range 596–772	696	686.4	0.60	751.1	0.07
	l range 596–772 high s/n	139	142.7	0.40	153.4	0.19
	l range 772–1100	216	195.9	0.83	234.2	0.19
	l range 772–1100 high s/n	43	36.8	0.74	48.1	0.27

Table 5.1 Results of χ^2 consistency tests (continued)

Polarization Data (continued)			Difference		Sum	
Split Type	Subset	# DOF	χ^2	PTE	χ^2	PTE
Azimuth range	full	3040	3071.1	0.34	3113.0	0.17
	high s/n	304	316.8	0.29	421.0	9.8×10^{-6}
	s/n > 1	34	38.7	0.27	98.6	3.3×10^{-8}
	l range 0–245	400	398.4	0.51	374.1	0.82
	l range 0–245 high s/n	80	78.4	0.53	98.8	0.08
	l range 245–420	848	847.1	0.50	824.6	0.71
	l range 245–420 high s/n	169	156.9	0.74	246.2	9.8×10^{-5}
	l range 420–596	880	887.2	0.43	929.1	0.12
	l range 420–596 high s/n	176	170.7	0.60	211.8	0.03
	l range 596–772	696	708.9	0.36	750.5	0.07
	l range 596–772 high s/n	139	142.0	0.41	153.2	0.19
	l range 772–1100	216	229.5	0.25	234.6	0.18
	l range 772–1100 high s/n	43	32.4	0.88	47.9	0.28
Faceplate position	full	2636	2710.4	0.15	2722.2	0.12
	high s/n	263	257.2	0.59	374.0	7.8×10^{-6}
	s/n > 1	32	43.6	0.08	97.5	1.6×10^{-8}
	l range 0–245	356	364.9	0.36	337.4	0.75
	l range 0–245 high s/n	71	58.7	0.85	81.5	0.18
	l range 245–420	724	771.3	0.11	744.2	0.29
	l range 245–420 high s/n	144	143.1	0.51	225.4	1.7×10^{-5}
	l range 420–596	756	757.7	0.48	794.1	0.16
	l range 420–596 high s/n	151	161.7	0.26	175.3	0.09
	l range 596–772	616	610.7	0.55	633.4	0.30
	l range 596–772 high s/n	123	110.0	0.79	138.0	0.17
	l range 772–1100	184	205.8	0.13	213.2	0.07
	l range 772–1100 high s/n	36	23.8	0.94	37.8	0.39

Table 5.1 Results of χ^2 consistency tests for each of the splits and subsets examined for the combined 2001/2002 dataset. Visibility data containing the same sky signal is split to form two data vectors; using the instrument noise model, the χ^2 statistic is then calculated on both the difference and sum data vectors. Also tabulated are the number of degrees of freedom (# DOF), and probability to exceed (PTE) the value in the χ^2 cumulative distribution function, to show the significance of the result (PTE values indicated as $< 1 \times 10^{-16}$ are zero to the precision with which we calculate the χ^2 cumulative distribution function). Difference data χ^2 values test for systematic effects in the data, while comparisons with sum data values test for the presence of a repeatable sky signal. Temperature (co-polar) data are visibility data in which the polarizers from both receivers are in the left (LL Stokes state) or right (RR Stokes state) circularly polarized state; polarization (cross-polar) data are those in which the polarizers are in opposite states (LR or RL Stokes state). The s/n > 1 subset is the subset of eigenmodes of the data with expected s/n > 1, while the high s/n subsets include the 10% highest s/n modes for the full l range and the 20% highest for the restricted l range subsets. See §5.5.2 for further description of the data split types and subsets. In addition, we calculate similar statistics for the 2001 and 2002 datasets separately, for a total of 296 χ^2 tests for various split types and subsets, and find no obvious trends that would indicate systematic contamination of the data.

the χ^2 values for the difference data appear consistent with noise; among these 296 difference data χ^2's, there are two with a PTE < 0.01 (the lowest is 0.003), one with a PTE > 0.99, and the rest appear uniformly distributed between this range. There are no apparent trends or outliers among the various subsets or splits.

5.6 Detection of Signal

Given that the data show remarkable consistency in χ^2 tests of the difference data vectors, the χ^2 values of the sum data vectors can be used to test for the presence of sky signal, independently of the likelihood analysis methods described below in §6.1. In the co-polar data, which we expect to contain a strong CMB temperature signal, all splits and subsets show highly significant χ^2 values (PTE $< 1 \times 10^{-16}$, the precision to which we calculate the cumulative distribution function).

The high s/n eigenmode subsets isolate the modes in the data expected to have greatest sensitivity to the expected sky signal. These subsets are constructed by transforming the data vector to a basis in which both the noise matrix and an assumed theory matrix are diagonal (Bond et al. 1998). The transformation we use is

$$\Delta \rightarrow [\mathbf{KR}]^t \, \Delta \tag{5.2}$$

$$\mathbf{C}_N \rightarrow [\mathbf{KR}]^t \, \mathbf{C}_N \, [\mathbf{KR}] = \mathbf{R}^t \mathbf{I} \mathbf{R} = \mathbf{I} \tag{5.3}$$

$$\mathbf{C}_N \rightarrow [\mathbf{KR}]^t \, \mathbf{C}_T \, [\mathbf{KR}] = \mathbf{R}^t \left[\mathbf{K}^t \mathbf{C}_T \mathbf{K}\right] \mathbf{R} = \mathbf{D} \tag{5.4}$$

where $\mathbf{K}$ is the inverse of the Cholesky factorization of $\mathbf{C}_N$ and $\mathbf{R}$ and $\mathbf{D}$ are respectively the matrix of eigenmodes and the (diagonal) matrix of eigenvalues of $\mathbf{K}^t\mathbf{C}_T\mathbf{K}$. These eigenvalues give the expected s/n ratio of the independent modes now measured by elements of the transformed data vector. We do not make use of this transformation for our likelihood analysis, but for calculation of the χ^2 statistics, which give equal weight to all considered modes, the isolation of high s/n subsets is a powerful tool.

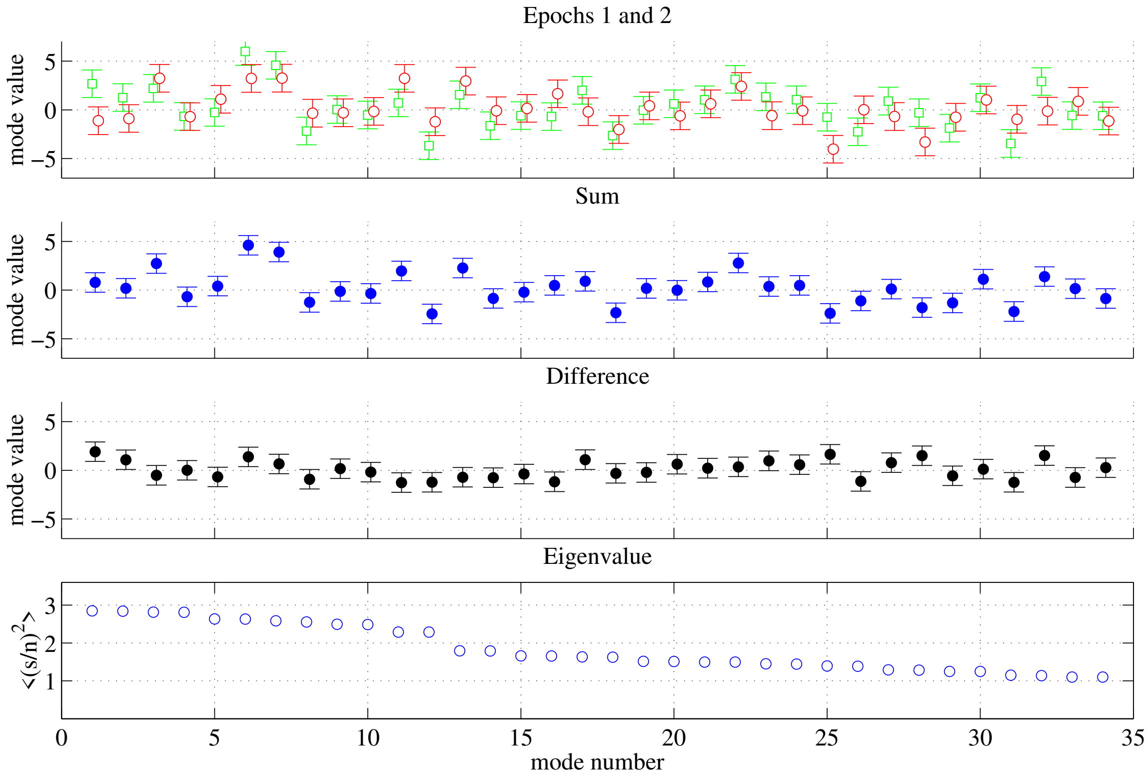

Figure 5.2 Polarization signal seen in signal to noise eigenmodes of the cross-polar data split by epoch. The upper panel shows the values of the 34 modes with s/n > 1 for the two separate epochs. The second panel shows the result of combining the two epochs, and the third panel shows the result of differencing them to remove any sky signal. The χ^2 values (Table 5.1) indicate that the scatter in the difference is consistent with noise, while the sum reveals a signal with probability 3.3×10^{-8}. Units in this s/n basis are chosen such that each mode has noise variance $= 1$. The expected signal variance for each mode is given by the eigenvalues in the fourth panel.

The number of modes with expected s/n > 1 gives an indication of the power of the experiment to constrain the sky signal expected under the concordance model. As can be seen in the various splits in Table 5.1, we have sensitivity with an expected s/n > 1 to ~ 340 temperature (co-polar) modes, and ~ 34 polarization (cross-polar) modes (see Table 5.1). With such a large number of high s/n CMB temperature modes expected, it is not surprising that the χ^2 statistics reveal a strong signal in all splits and subsets of the co-polar data.

For the cross-polar data, the χ^2 values calculated for the ~ 34 s/n > 1 modes in the sum data vectors also reveal a highly significant signal. Under each of the data splits examined in Table 5.1, the sum χ^2 value calculated for this subset of modes is inconsistent with instrumental noise, at levels in the range PTE $= 1.6 \times 10^{-8}$ to 8.7×10^{-7}. This is illustrated for the epoch-split s/n > 1 subset in Figure 5.2. The scatter in the values of the 34 summed modes (second panel) greatly exceeds that expected from noise (reflected by the errorbars), while the scatter in the differenced modes (third panel) gives a chi^2 consistent with the noise model. This simple and powerful test indicates that we have detected, with high significance, the presence of a polarized signal in the data, and that this signal is repeatable in all of the data splits.

In general, the formation of the high s/n eigenmodes does not depend strongly on the assumed model (Bond et al. 1998). We have verified that a wide range of CMBFAST-generated models for the E-mode polarization signal identify subsets of the data which show a polarized signal at similar significance to those from the concordance model. The modes that make up these subsets have sky response patterns that are mainly "E" in character, matching the expected signal (see Figure 5.3). DASI has equal sensitivity to B-mode polarization, and by switching the polarization in the assumed theory model from E to B we can isolate similar subsets of the ~ 34 modes in our data which maximize sensitivity to B-polarization. For these modes, the χ^2 values do not show a significant signal in excess of the noise. This test offers evidence that the signal we have detected in our polarized data is predominantly E-mode. We will further investigate the E vs. B nature of our polarized signal in the likelihood analysis.

5.6.1 Temperature and Polarization Maps

We can offer a visual representation of the signals revealed in our χ^2 analyses by constructing maps from the sum and difference data vectors, and comparing the level

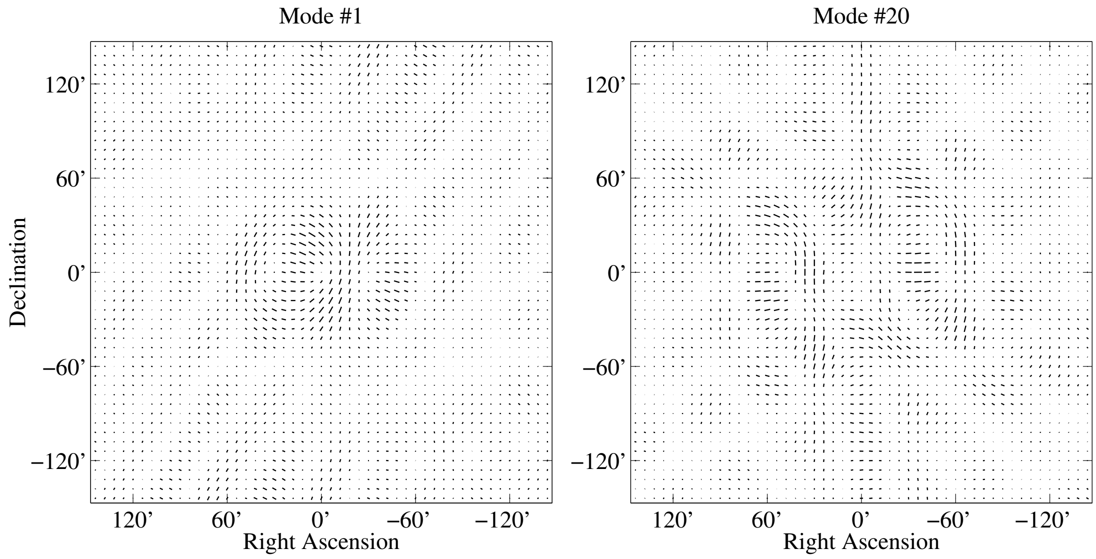

Figure 5.3 Response patterns of the 1st and the 20th signal to noise eigenmodes considered in Figure 5.2. These patterns are visibly E in character. Although the main beam taper has not been explicitly included in the mapping algorithm, it is evident because the formation of these s/n modes selects linear combinations of visibilities which interfere constructively.

of structure apparent in them.

For CMB analysis, linear map making algorithms are preferred, as these preserve the Gaussian properties of signal and noise. An estimate of the pixelated true sky map $\mathbf{x}$ is formed from the data vector $\widetilde{\mathbf{x}} = \mathbf{W}\boldsymbol{\Delta}$. Many different prescriptions for constructing the map making matrix $\mathbf{W}$ have been used, depending on the desired statistical properties of the estimated map (Tegmark 1997a). For interferometry, the convention known as 'direct Fourier transform' mapping (which we follow here) is to build the columns of $\mathbf{W}$ to correspond to the response patterns of the visibilities (corrugations) without reference to the primary beam taper. The corrugations for each measured visibility, suitably weighted and normalized, combine to produce a map in which uncorrelated noise appears uniformly distributed, while signal from the sky appears tapered by the primary beam.

Shown in Figure 5.4 are temperature maps constructed from the full sum and

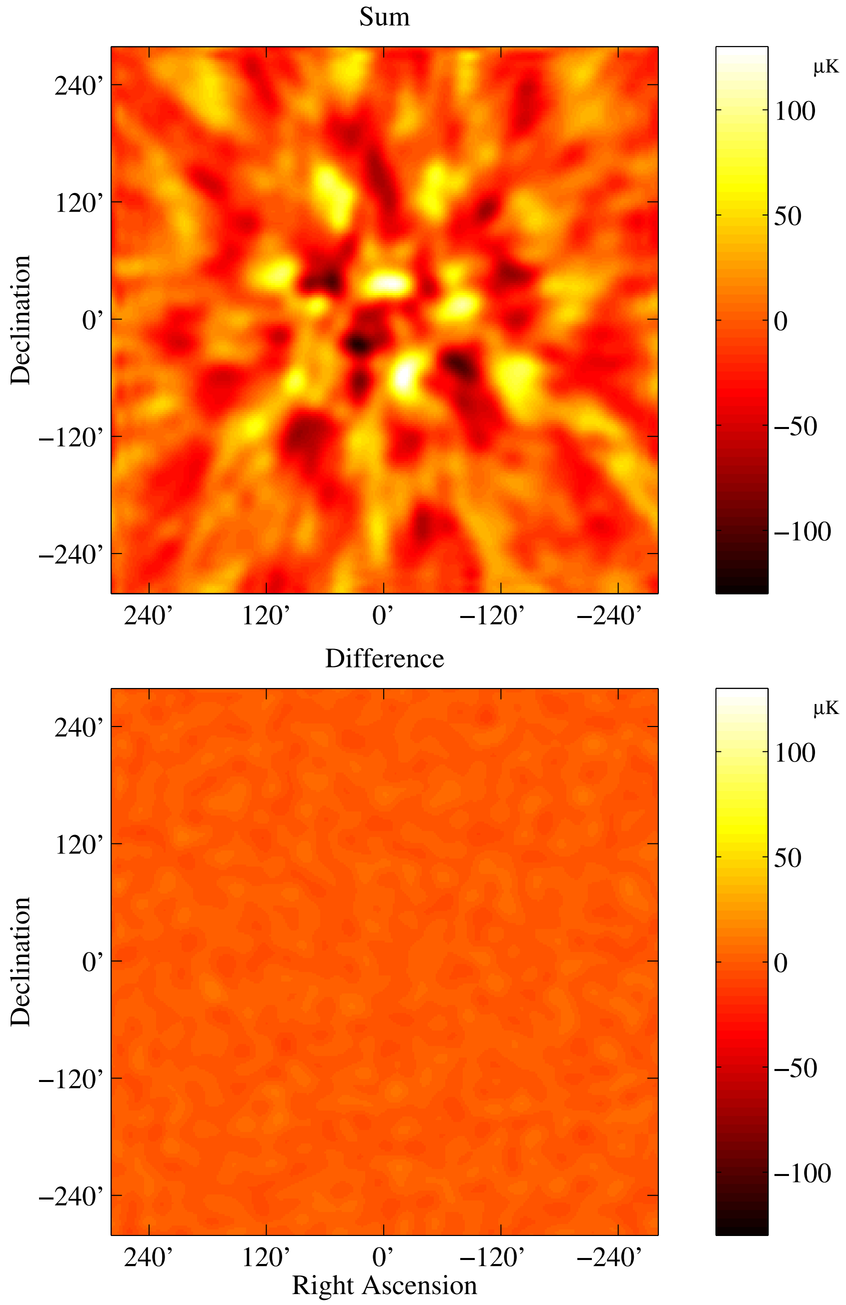

Figure 5.4 Temperature maps of the differenced (C2–C3) CMB fields. Shown are maps constructed from full temperature dataset that has been split by epoch, and formed into sum or difference data vectors, as reported in §5.5.2. The detected structure is consistent with visibilities measured for these two differenced fields in the 2000 data (Paper I). The noise level in the map is 2.8 μK, for a s/n at beam center of ~ 25.

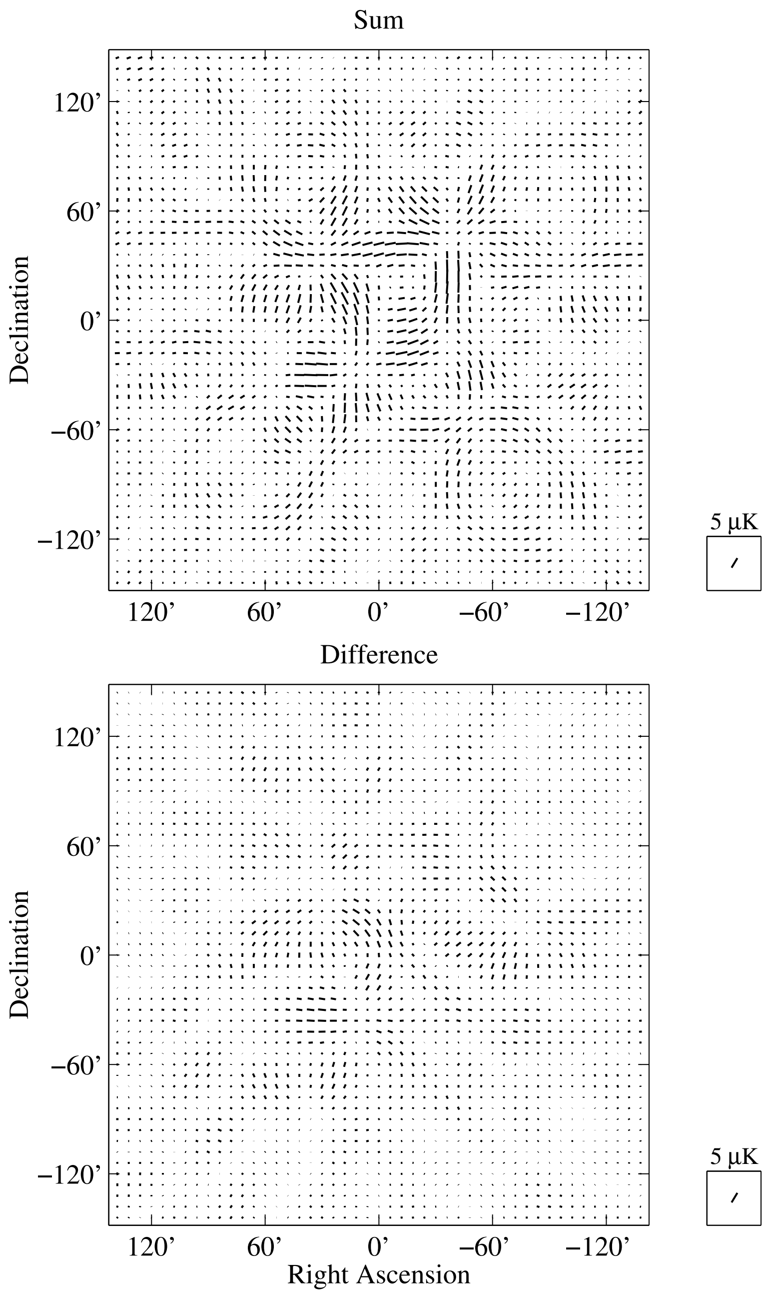

Figure 5.5 Polarization maps formed from high signal/noise eigenmodes. As in Figure 5.4, the maps are constructed from data that have been split by epoch. In order to isolate the most significant signal in our polarization data, we have used the subset of 34 eigenmodes which are expected to have average signal/noise > 1. The difference map is statistically consistent with noise. Comparison of this map to the sum map illustrates the same result depicted for this split/subset in Figure 5.2: that these modes in the polarized dataset show a significant signal.

difference data vectors of the epoch split temperature data. The sum map clearly shows structure enveloped by the primary beam, and as expected from the χ^2 tests, no residual signal is seen in the difference map above the noise. The detected structure is consistent with visibilities measured for these two differenced fields in the 2000 data presented in Paper I. With a noise floor in the difference map of 2.8 μK, we achieve a s/n ratio of approximately 25 at beam center. Natural (inverse noise) weighting of the full set of visibilities has been used, for a synthesized beam of $\sim 22'$.

The polarization map shown in Figure 5.5 gives a visual representation of the repeatable polarization signal. Shown are the epoch split sum and difference polarization maps, constructed using the same s/n > 1 modes of the polarization data in the concordance model s/n eigenmode basis that appear in the table and in Figure 5.2. Because the maps have only 34 independent modes, they exhibit a limited range of morphologies. Also, the formation of the s/n modes selects linear combinations of visibilities which interfere constructively in the primary beam. Therefore, although the same direct Fourier transform mapping algorithm is used, a beam taper is intrinsic to these modes (see Figure 5.3). This taper is evident in the difference map even though it is statistically consistent with noise. Comparison of the level of structure in this map and in the sum map illustrates the result of the χ^2 analyses: that these individual modes in the polarized dataset show a significant repeatable signal.

5.6.2 Significance

It is possible to calculate a similar χ^2 statistic for the data vector formed from the complete, unsplit dataset. Combining all the data without the requirement of forming two equally weighted subsets should yield minimal noise, albeit without an exactly corresponding null (i.e., difference) test. Recalculating the s/n eigenmodes for this complete cross-polar data vector gives 36 modes with expected s/n > 1, for which $\chi^2 = 98.0$ with a PTE $= 1.2 \times 10^{-7}$. This significance is similar to those from the sum data vectors under the various splits, which actually divide the data fairly equally and so are nearly optimal.

It should be noted that our focus so far has been examining the cross-polar data for a signal in excess of the instrumental noise model. We have not addressed the small cross-polar signal expected due to off-axis leakage of the temperature signal. As discussed in §4.5, it is not possible to correct the data elements directly for this effect, but we can account for it in calculating these χ^2 results by including the expected covariance of this leakage signal (see §6.1.4) in the noise matrix $\mathbf{C}_N$. Again recalculating the s/n eigenmodes, we find 34 cross-polar modes with s/n > 1 which give a $\chi^2 = 97.0$ and a PTE $= 5.7 \times 10^{-8}$, a significance which is similar to before. The off axis leakage is also included in the likelihood analyses, where it again is found to have an insignificant impact on the results.

The likelihood analysis described in the next chapter makes use of all of the information in our dataset. Such an analysis, in principle, may yield statistically significant evidence of a signal even in cases of datasets for which it is not possible to isolate any individual modes which have average s/n > 1. However, the existence of such modes in our dataset, which has resulted from our strategy of integrating deeply on a limited patch of sky, allows us to determine the presence of the signal with the very simple analysis described above. It also reduces sensitivity to the noise model estimation in the likelihood results that we report next. Finally, it gives our dataset greater power to exclude the possibility of no signal than it might have had if we had observed more modes but with less s/n in each.

Chapter 6

Likelihood Analysis

The preceding chapter reported strong evidence for the presence of a signal in the polarization dataset. The signal was determined to be a consistent feature of the observations, and cannot be accounted for by instrumental noise. Our goal now is to examine this signal, quantifying its strength and distribution within the dataset. We wish to test, in as many different ways as the data will support, whether the signal is consistent with the predicted signature of the density perturbation E-mode CMB polarization expected under the standard model.

Our basic statistical tool for constructing these tests will be likelihood analysis. The relatively manageable size of the DASI polarization dataset makes a direct likelihood-based approach feasible, and we present results from nine separate such analyses. The first portion of this chapter describes the methods for computing the likelihoods of the various models of the signal that we explore in the analyses. The different choices of parameterization of the CMB spectra in each analysis and the corresponding parameter window functions are discussed, as well as details of our conventions for reporting results.

Next we present the results themselves, organized first into those analyses that use only the polarization data to constrain the E- and B-spectra, followed by analyses of only the temperature data, and finally joint analyses using all of the data to constrain the cross spectra. We conclude the chapter with a discussion of the level of uncertainty due to various instrumental effects or the contribution of foregrounds which could impact these results.

6.1 Likelihood Analysis Formalism

We begin our analysis by considering the data vector to be the sum of signal and noise components,

$$\mathbf{\Delta} = \mathbf{s} + \mathbf{n}, \tag{6.1}$$

which are assumed to be independent and Gaussian distributed with zero mean. Thus the covariance matrix of the data can be written

$$\mathbf{C} = \mathbf{C}_T + \mathbf{C}_N, \tag{6.2}$$

and gives a complete statistical description of the information content of our dataset. The noise covariance matrix $\mathbf{C}_N \equiv \langle \mathbf{n}\mathbf{n}^t \rangle$, is computed internally from the timestream data and subjected to extensive consistency tests (see §5.5). It is regarded as the known component of the covariance.

The theory covariance $\mathbf{C}_T \equiv \langle \mathbf{s}\mathbf{s}^t \rangle$ depends on the the two-point statistics of the CMB temperature and polarization signals on the sky, which are specified by the T, E, and B power spectra and cross spectra. The theory covariance matrix is modeled in terms of parameters κ which specify these spectra. For most analyses, we choose parameters such that the full theory covariance matrix is the sum of components proportional to each parameter,

$$\mathbf{C}_T\left(\kappa\right) = \sum_p \kappa_p \mathbf{B}_T^p. \tag{6.3}$$

In chapter 2 we derived a general expression for components of the theory covariance matrix based on the temperature and polarization response of the visibilities which make up the DASI dataset. From Eq.2.19 we can write

$$B^{p}_{T\ ij} = \frac{1}{2}\alpha_i\alpha_j \int d\mathbf{u}\, C^X(u)\, \widetilde{A}(\mathbf{u}_i - \mathbf{u}, \nu_i) \times \left[\xi_1 \widetilde{A}(\mathbf{u}_j - \mathbf{u}, \nu_j) + \xi_2 \widetilde{A}(\mathbf{u}_j + \mathbf{u}, \nu_j)\right]. \quad (6.4)$$

In this expression the autocorrelation of the aperture field $\widetilde{A}(\mathbf{u}, \nu_i)$ specifies the beam pattern at frequency ν_i, $\alpha_i = \partial B_{\mathrm{Planck}}(\nu_i, T_{\mathrm{CMB}})/\partial T$ converts from units of CMB temperature to flux density (Jy), and the coefficients ξ_1 and ξ_2 take values $\{0, \pm1, \pm2\} \times \{\cos\{2\chi, 4\chi\}, \sin\{2\chi, 4\chi\}\}$ depending on the Stokes states (RR, LL, RL, LR) and selection of real or imaginary visibility for each of the two baselines i, j and on which of the six spectra (T, E, B, TE, TB, EB) is specified by X. For each parameter κ_p, the integration may be limited to annular regions which correspond to $l-$ranges over which the power spectrum C^X is hypothesized to be relatively flat, or else some shape of the spectrum may be postulated (see §6.1.1).

With this parametrized model for the covariance of the signal, we write our model for the full covariance matrix of the data

$$\mathbf{C}(\kappa) \equiv \mathbf{C}_T(\kappa) + \mathbf{C}_N. \quad (6.5)$$

The *likelihood* of the model specified by the parameter vector κ is the probability of obtaining our data vector $\mathbf{\Delta}$ given that model:

$$\begin{aligned} L(\kappa) &= P(\mathbf{\Delta}|\kappa) \\ &= (2\pi)^{-N/2} \det(\mathbf{C}(\kappa))^{-1/2} \exp\left(-\frac{1}{2}\mathbf{\Delta}^t \mathbf{C}(\kappa)^{-1} \mathbf{\Delta}\right). \end{aligned} \quad (6.6)$$

Although the full likelihood function itself, defined over the parameter space explored, is the most fundamental result of each of our likelihood analyses, it is useful to identify and report the values of the parameters that maximize the likelihood (so-called *maximum likelihood (ML) estimators*). These are often interpreted as the most likely values of those parameters within the context of a given model, given a uniform prior in our knowledge of the parameters. Uncertainties in the parameter values can be estimated by characterizing the shape of the likelihood surface, as discussed further in §6.1.7.

The likelihood function allows us directly to compare the compatibility of our dataset with any of the models in the considered parameter space, including those that represent the predicted CMB polarization signal, or radically different polarization signals, or no polarization at all. It is a particularly appropriate tool for the purposes of our current analysis, in which we hope to establish an initial detection of the CMB polarization and to examine whether the observed signal matches the expected one. Indeed, the likelihood approach was originally advocated for CMB analysis (see, for example, Readhead et al. (1989)) to address similar goals among early temperature anisotropy experiments.

An alternative to the likelihood approach is to form parameter estimates directly as quadratic functions of the data,

$$\widetilde{\kappa}_p = \mathbf{\Delta}^t \mathbf{Q}_p \mathbf{\Delta} - b_p \; , \tag{6.7}$$

where the matrices $\mathbf{Q}_p$ and constants b_p are constructed using knowledge of $\mathbf{C}_N$ and an assumed $\mathbf{C}_T(\kappa)$ based on an initial guess at parameter values κ (see Tegmark & de Oliveira-Costa (2001) for an overview of this approach applied to polarization data). Appropriately constructed *quadratic estimators* can be shown, if the initial guess at parameter values is close to the true model, to offer minimum variance estimates of parameter values (Tegmark 1997b) and have the advantages that they can be applied to the data in n^2 operations (while the matrix inversion in evaluating the likelihood scales as n^3) and that their error properties are easily expressed analytically. Indeed, an iterated quadratic estimator quickly converges in parameter space to the ML estimator (Bond et al. 1998), offering an efficient algorithm for use in likelihood evaluation (see §6.1.2 and 6.1.5) rather than a distinct approach. The use of non-iterated quadratic estimators as an alternative to likelihood analysis for power spectrum estimation has gained popularity among recent temperature mapping experiments as larger datasets make direct likelihood evaluation prohibitive. As future polarization experiments map more sky and move beyond the stage of initial detections to precise power spectrum measurements, this pattern is likely to be repeated, and a great deal of recent literature has focused on the construction of E, B, and cross spectra polarization quadratic estimators under various assumptions about sky coverage, etc. (for examples, see Tegmark & de Oliveira-Costa (2001), Kogut et al. (2003), Chon et al. (2003)). For our current dataset, however, exploring the full likelihood function is practical and offers the most complete picture of the information our data holds about CMB polarization.

6.1.1 Likelihood Parameters

In §6.2 we present the results from nine separate likelihood analyses involving the polarization data, the temperature data, or both. Our choice of parameters with which to characterize the six CMB power spectra in constructing $\mathbf{C}_T(\kappa)$ is a compromise between maximizing sensitivity to the signal and constraining the shape of the power spectra. In the different analyses we either characterize various power spectra with a single amplitude parameter covering all angular scales, or split the $l-$range into five bands over which spectra are approximated as piecewise-flat, in units of $l(l+1)C_l/(2\pi)$. Five bands were chosen as a compromise between too many for the data to bear and too few to capture the shape of the underlying power spectra. The $l-$ranges of these five bands are based on those of the nine-band analysis of Paper II; we have simply combined the first four pairs of these bands, and kept the ninth as before. In some analyses we also constrain the frequency spectral indices of the temperature and polarization power spectra as a test for foreground contamination.

The $l-$range to which DASI has non-zero sensitivity is $28 < l < 1047$. That range includes the first three peaks of the temperature power spectrum, and within it the amplitude of that spectrum, which we express in units $l(l+1)C_l/(2\pi)$, varies by a factor of ~ 4. Over this same range, the E-mode polarization spectrum is predicted to have four peaks while rising roughly as l^2 (in the same units), varying in amplitude by nearly two orders of magnitude (Hu & White 1997). The TE correlation is predicted to exhibit a complex spectrum that in fact crosses zero five times in this range.

Single bandpower analyses offer the clearest statistics to test for a potential signal, but the shape of the model power spectrum assumed will have an effect on the sensitivity of the result. In particular, if the assumed shape is a poor fit to the true spectrum preferred by the data, the results will be both less powerful and difficult to interpret. For temperature spectrum measurements, the most common choice in recent years has been the so-called flat bandpower, $l(l+1)C_l \propto$ constant, which matches the gross large-angle "scale-invariant" power law shape of that spectrum. Because of extreme variations predicted in the E and TE spectra over DASI's $l-$range, we do not expect a single flat bandpower parameterization to offer a good description of the entire dataset (although in §6.2.1 we describe results of applying such an analysis to limited l-range subsets of data). A more appropriate definition of "flat bandpower" for polarization measurements sensitive to large ranges of $l < 1000$ might be $C_l \propto$ constant (or $l(l+1)C_l \propto l^2$). Other shapes have been tried, notably the Gaussian autocorrelation function (by the PIQUE group (Hedman et al. 2001)) which reduces to $C_l \propto$ constant at large scales and perhaps offers a better fit to the gross amplitude of the predicted E spectrum than simple power laws.

In our single band analyses, we have chosen a shape for our single bandpower parameters based on the predicted spectra for a cosmological model currently favored by observations. The specific model that we choose—which we will call the *concordance model*—is a ΛCDM model with flat spatial curvature, 5% baryonic matter, 35% dark matter, 60% dark energy, and a Hubble constant of 65 km s^{-1} Mpc^{-1}, ($\Omega_b = 0.05, \Omega_{cdm} = 0.35, \Omega_\Lambda = 0.60, h = 0.65$) and the exact normalization $C_{10} = 700\mu K^2$. As discussed in Chapter 1, this concordance model was defined in Paper III as a good fit to the 2000 DASI temperature power spectrum and other observations. The concordance model spectra for T, E, and TE are shown in Figure 6.6. The five flat bandpower likelihood results shown in the same figure, and discussed in that section, suggest that the concordance shaped spectra do indeed better characterize the data than any power-law approximation. In §6.2.1, we explicitly test the likelihood of the concordance model parameterization against that of the two power laws mentioned above, and find that the concordance model shape is strongly preferred by the data.

6.1.2 Parameter window functions

It should be noted that the likelihood analysis is always model dependent, regardless of whether flat bandpowers or a shaped model is chosen for parameterization. To evaluate the expectation value of the results for a hypothesized theoretical power spectrum, one must use window functions appropriate for the parameters of the particular analysis.

The calculation of such parameter window functions has been given in the literature in the context of flat bandpower parameters in temperature power spectrum likelihood analyses (Knox 1999; Halverson 2002), and for arbitrary quadratic estimators of polarization spectra (Tegmark & de Oliveira-Costa 2001). These derivations are equivalent if a minimum variance quadratic estimator which converges to the ML estimate is chosen. Following the latter, a generic quadratic estimator (Eq. 6.7) has the expectation value

$$\begin{aligned}\langle\widetilde{\kappa}_p\rangle &= \left\langle \mathrm{Tr}\left(\mathbf{Q}_p\mathbf{\Delta}\mathbf{\Delta}^t\right)\right\rangle - b_p \\ &= \mathrm{Tr}\left(\mathbf{Q}_p\mathbf{C}_T\right) + \mathrm{Tr}\left(\mathbf{Q}_p\mathbf{C}_N\right) - b_p \\ &= \sum_{X,l} C_l^X\,\mathrm{Tr}\left(\mathbf{Q}_p\mathbf{B}_T^{X,l}\right) \ . \end{aligned} \tag{6.8}$$

where we have chosen b_p to cancel the noise term in the second line. In the third line we have expanded $\mathbf{C}_T$ as in Eqs. 6.3 and 6.4, using the actual multipole values of the six power spectra C_l^X as our parameters (or approximating this with finely spaced bandpowers). This expression implicitly defines the window function

$$(W_l^X)_p \equiv \mathrm{Tr}\left(\mathbf{Q}_p \mathbf{B}_T^{X,l}\right) \tag{6.9}$$

which gives the sensitivity of our parameter estimate $\widetilde{\kappa}_p$ to each of the underlying power spectra.

Our specific quadratic estimator is constructed using the *Fisher matrix*, which is defined to be the ensemble average of the curvature of the log likelihood

$$\mathbf{F}_{pp'}(\kappa) \equiv -\left\langle \frac{\partial^2 \ln L}{\partial\kappa_p \partial\kappa_{p'}} \right\rangle = \frac{1}{2}\mathrm{Tr}\left(\mathbf{C}^{-1}\frac{\partial \mathbf{C}_T}{\partial\kappa_p}\mathbf{C}^{-1}\frac{\partial \mathbf{C}_T}{\partial\kappa_{p'}}\right) . \tag{6.10}$$

Note that this matrix, which offers an estimate of the paramter uncertainties, is calculated with reference to specific parameter values κ but does not depend on the data. We define the estimator

$$\mathbf{Q}_p \equiv \frac{1}{2}\sum_{p'} \left(\mathbf{F}^{-1}\right)_{pp'} \mathbf{C}^{-1}\frac{\partial \mathbf{C}_T}{\partial\kappa_{p'}}\mathbf{C}^{-1} . \tag{6.11}$$

Iteration of this estimator approximates the Newton-Raphson method for maximizing the likelihood (Bond et al. 1998). Starting near the true parameter values, then, its expectation value approximates the ML estimate. From Eq. 6.9, the corresponding parameter window function is

$$(W_l^X)_p = \sum_{p'} \left(\mathbf{F}^{-1}\right)_{pp'} \frac{1}{2}\mathrm{Tr}\left(\mathbf{C}^{-1}\frac{\partial \mathbf{C}_T}{\partial\kappa_{p'}}\mathbf{C}^{-1}\mathbf{B}_T^{X,l}\right) . \tag{6.12}$$

This expression is equivalent to the flat band-power window function defined in Halverson (2002), generalized to include response to all six power spectra with arbitrary parameterization.

In general, the parameter window function has a non-trivial shape (even for a flat band-power analysis) which is dependent on the shape of the true spectra as well as the intrinsic sensitivity of the instrument as a function of angular scale. Parameter window functions for the E/B and $E5/B5$ polarization analysis are shown in Figure 6.1.

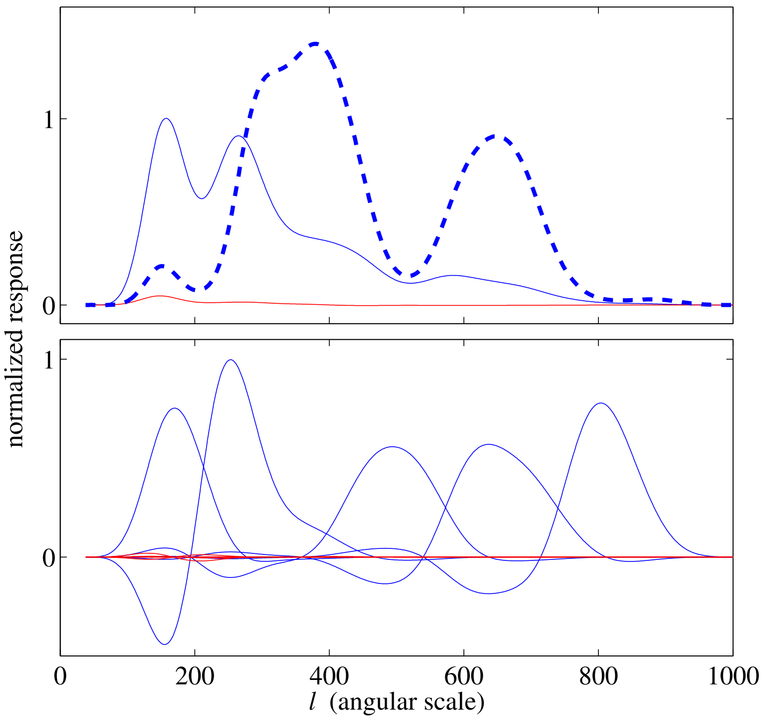

Figure 6.1 Parameter window functions, which indicate the angular scales over which the parameters in our analyses constrain the power spectra. The upper panel shows the functions for the E parameter of our E/B analysis, with the solid blue curve indicating response to the E power spectrum and the solid red (much lower) curve indicating response of the same E parameter to the B spectrum. The blue dashed curve shows the result of multiplying the E window function by the concordance E spectrum, illustrating that for this CMB spectrum, most of the response of our experiment's E parameter comes from the region of the second peak ($300 \lesssim l \lesssim 450$), with a substantial contribution also from the third peak and a smaller contribution from the first. The lower panel shows $E1 - E5$ parameter window functions for the E power spectrum (blue) and B power spectrum (red, again much lower) from our $E5/B5$ analysis. All of these window functions are calculated with respect to the concordance model discussed in the text. DASI's response to E and B is very symmetric, so that E and B parameter window functions which are calculated with respect to a model for which $E = B$ are similar, with the E and B spectral response reversed.

6.1.3 Point Source Constraints

The covariance matrix that we actually construct for our likelihood evaluation has several components in addition to the standard noise and theory covariance terms of Eq. 6.5.

Potentially contaminated modes in the data vector may be eliminated from the analysis by the construction of constraint matrices (Bond et al. 1998). These matrices attribute essentially infinite variance to selected modes, and when added to the noise covariance matrix, they have the effect of assigning zero weight to these modes in the likelihood evaluation. This constraint matrix formalism can be used to remove the effect of point sources of known position without knowledge of their flux densities, as described in Paper II and Halverson (2002). In generalizing this procedure to include the case of polarized point sources, for each point source of known location a constraint matrix can be constructed that projects out two additional modes from the covariance matrix, corresponding to the unknown Q and U polarized flux of the source.

Although we have tested for the presence of point sources in the polarization power spectra using this method, in the final analysis we use constraint matrices to project point sources out of the temperature data only, and not the polarization data (see §6.3.2 for further discussion).

6.1.4 Off-axis Leakage Covariance

Another small correction to the covariance matrix for the polarization data results from the off-axis leakage (see §4.5), which has the effect of mixing some power from the temperature signal T near the edge of our fields into the cross-polar visibilities. Unlike the on-axis leakage, the off-axis leakage cannot be calibrated out of the polarization data baseline-by-baseline, but it can be accounted for in the theory covariance matrix.

Our aperture-plane model of the off-axis leakage field allows us write an expression for the resulting covariance that has the same form as Eq. 6.4, but with the autocorrelation of the usual aperture field $\widetilde{A}(\mathbf{u}, \nu_i)$ replaced by the convolution of this field with the leakage field. An alternative is to derive the resulting covariance statistically from simulated observations of fields with a known input power spectrum C^T in which the polarized signal due to off-axis leakage has been calculated according to our sky-plane model of this leakage. Because our data on the off-axis leakage is more successfully fit by our sky-plane model, we adopt this latter approach, calculating the off-axis leakage covariance due to concordance model temperature anisotropies using 5000 simulated observations. For analyses in which the amplitude of CMB temperature anisotropies is included as a parameter, the amplitude of this covariance component is tied to that parameter; in polarization-only analyses it is fixed at the concordance normalization. In either case, inclusion of off-axis leakage covariance has only a small effect on likelihood results, as discussed in §6.3.

6.1.5 Likelihood Evaluation

Prior to likelihood analysis, the data vector and the covariance matrices can be compressed by combining visibility data from nearby points in the (u, v) plane, where the signal is highly correlated. This reduces the computational time required for the analyses without a significant loss of information about the signal. Like the post-reduction calibration operations described in the Chapter 5, compression is implemented as a matrix operation applied to both the data vector and covariance matrices. Compression techniques ranging in complexity from simple frequency band combination, to explicit uv-plane griding, to signal-to-noise eigenmode transformations were all found to be useful at different stages of the analysis, and our final algorithm is based on iterative minimum-variance combination of those data elements with the highest signal correlations, according to a fiducial theory matrix. All analyses were run on standard desktop workstations. [1]

For each analysis, we use the iterated quadratic estimator described in §6.1.2 to find the ML values of our parameters. To further characterize the shape of the likelihood function, in Paper II we used an offset log-normal approximation. Here, for improved accuracy in calculating confidence intervals and likelihood ratios, we explicitly map out the likelihood function by evaluating Equation 6.6 over a uniform parameter grid large enough to enclose all regions of substantial likelihood. A single likelihood evaluation typically takes several seconds, so this explicit grid evaluation is impractical for the analyses which include five or more parameters. For each analysis we also implement a Markov chain evaluation of the likelihood function (Christensen et al. 2001). We find this to be a useful and efficient tool for mapping the likelihoods of these high-dimensional parameter spaces in the region of substantial likelihood. We have compared the Markov technique to the grid evaluation for the lower-dimensional analyses and found the results to be in excellent agreement (see Figure 6.5). In all cases, the peak of the full likelihood evaluated with either technique is confirmed to coincide with the ML values returned by the iterated quadratic estimator.

6.1.6 Simulations and Parameter Recovery Tests

The likelihood analysis software was extensively tested through analysis of simulated data. The data simulation software was authored independently of the analysis software by a different member of our team (E. Leitch) as a precaution against shared coding errors, and using this software, a number of "blind" parameter recovery tests were performed.

Simulated sky maps were generated from realizations of a variety of smooth CMB power spectra, including both the concordance spectrum and various non-concordance models, both with and without E and B polarization and TE correlations. Multiple

[1] Our standard machines are Linux-based PC's running 32-bit Intel Pentium processors at 1-2 GHz, with 2-6 GB of memory.

independent realizations of the sky were "observed" to construct simulated visibilities with Fourier-plane sampling identical to the real data. The simulations were designed to replicate the actual data as realistically as possible and include artifacts of the instrumental polarization response and calibration, such as the on-axis and off-axis leakages described in §4.4 and §4.5, and the cross-polar phase offset described in §4.1, allowing us to test the calibration operations and treatment of these effects implemented in the analysis software.

Each of the analyses described in §6.2 was performed on hundreds of these simulated datasets with independent realizations of sky and instrument noise, both with noise variances that matched the real data, and with noise a factor of 10 lower. In all cases, we found that the means of the ML estimators recovered the expectation values $\langle\kappa_p\rangle$ of each parameter without evidence of bias, and that the variance of the ML estimators was found to be consistent with the estimated uncertainty given by $\mathbf{F}^{-1}$ evaluated at $\langle\kappa\rangle$, where $\mathbf{F}$ is the Fisher matrix (Eq. 6.10).

6.1.7 Reporting of Likelihood Results

Maximum likelihood parameter estimates reported in this paper are the global maxima of the multidimensional likelihood function. Confidence intervals for each parameter are determined by integrating (marginalizing) the likelihood function over the other parameters; the reported intervals are the equal-likelihood bounds which enclose 68% of this marginal likelihood distribution. This prescription corresponds to what is generally referred to as the *highest posterior density* (HPD) interval. An alternative prescription, so-called *central likelihood* intervals which exclude equal amounts of integrated likelihood above and below the central 68%, is more sensitive to integration over low-likelihood regions (and thus to implicit priors), and for the skewed likelihood distributions typical of parameters that are physically positive generally gives intervals shifted to somewhat higher values (see Fig. 6.5). When calculating the HPD intervals we consider all parameter values, including non-physical ones, because our aim is simply to summarize the shape of the likelihood function. Values are quoted in the text using the convention "ML (HPD-low to HPD-high)" to make clear that the confidence range is not directly related to the maximum likelihood value. Where results are given in units of μK^2, values are for $l(l+1)C_l/(2\pi)$.

In the tabulated results, we also report marginalized uncertainties obtained by evaluating the Fisher matrix at the maximum likelihood model, i.e., $(F^{-1})^{1/2}_{pp}$ for parameter p. Although in most cases, the two confidence intervals are quite similar, we report the HPD interval as the primary result, as it offers more information on the shape of the likelihood function. The scatter of ML estimators returned in multiple simulations is verified to be consistent with the expected uncertainty given by $\mathbf{F}^{-1}$ evaluated at the true input model. Note that this is not necessarily the same uncertainty derived by evaluating $\mathbf{F}^{-1}$ at the ML estimates, which can give much smaller apparent "error-bars" if a power estimate has fluctuated to a low value for a particular simulation.

For parameters which are intrinsically positive we consider placing (physical) upper limits by marginalizing the likelihood distribution as before, but excluding the unphysical negative values. We then test if the 95% integral point has a likelihood smaller than that at zero; if it does we report an upper limit in addition to a confidence interval.

We also report the parameter correlation matrices for our various likelihood analyses to allow the reader to gauge the degree to which each parameter has been determined independently. The covariance matrix is the inverse of the Fisher matrix and the correlation matrix is defined as the covariance matrix normalized to unity on the diagonal, i.e., $\mathbf{C} = \mathbf{F}^{-1}$ and $R_{ij} = C_{ij}/\sqrt{C_{ii}C_{jj}}$.

6.1.8 Goodness-of-Fit Tests

One of the primary goals of our analysis is to determine if our results are consistent with a given model. For example, we would like to examine the significance of any detections by testing for the level of consistency with zero signal models, and we would like to determine if the polarization data are consistent with predictions of the standard cosmological model. These questions are in a sense more basic than the problem of parameter estimation, and we can use the likelihood function to directly address them.

We define as a goodness-of-fit statistic the logarithmic ratio of the maximum of the likelihood to its value for some model $\mathcal{H}_0$ described by parameters κ_0.

$$\Lambda(\mathcal{H}_0) \equiv -\log\left(\frac{L\left(\kappa_{ML}\right)}{L\left(\kappa_0\right)}\right) .$$

The statistic Λ simply indicates how much the likelihood has fallen from its peak value down to its value at κ_0. Large values indicate inconsistency of our data's likelihood result with the model $\mathcal{H}_0$. To assess significance, we perform Monte Carlo (MC) simulations of this statistic under the hypothesis that $\mathcal{H}_0$ is true. From this, we can determine the probability, given $\mathcal{H}_0$ true, to obtain a value of Λ that exceeds the observed value, which we hereafter refer to as PTE.

When considering models which the data indicate to be very unlikely, i.e., for which Λ is large, sufficient MC sampling of the distribution of this statistic becomes computationally prohibitive; our typical MC simulations are limited to only 1000 realizations. In the limit that the parameter errors are normally distributed, our chosen statistic reduces to $\Lambda = \Delta\chi^2/2$. The integral over the χ^2 distribution is described by an incomplete gamma function;

$$\mathrm{PTE} = \frac{1}{\Gamma(N/2)}\int_{\Lambda}^{\infty} e^{-x} x^{\frac{N}{2}-1} dx$$

where $\Gamma(x)$ is the complete gamma function, and N is the number of parameters.

Neither the likelihood function nor the distribution of the ML estimators is, in general, normally distributed, and therefore this approximation must be tested. In all cases where we can compute a meaningful PTE with MC simulations, we find it to be in excellent agreement with the analytic approximation, justifying its adoption.

All results for PTE based on the likelihood ratio statistic are calculated using this analytic expression unless otherwise stated. In multiparameter analyses where we are interested in the goodness-of-fit of a single parameter or subset of parameters, we form a Λ statistic and PTE for the reduced parameter set after marginalizing the likelihood function over the other parameters.

6.2 Likelihood Results

In the following sections we discuss the nine separate likelihood analyses we have conducted, first dealing with analyses based on our polarization data only, then those based on temperature data only, and finally joint temperature-polarization analyses. Final numerical results for the three groups of analyses are given in Tables 6.1, 6.2 and 6.3, on pages 160, 162 and 167, respectively.

6.2.1 Polarization Data Analyses and E and B Results

E/B analysis

The E/B analysis uses two single bandpower parameters to characterize the amplitudes of the E and B polarization spectra. As discussed in §6.1.1, this analysis requires a choice of shape for the spectra to be parameterized. DASI has instrumental sensitivity to E and B that is symmetrical and nearly independent. Although the B spectrum is not expected to have the same shape as the E spectrum, is expected to have negligible amplitude. We choose the same shape for both spectra in order to preserve this symmetry in the analysis.

We first compute the likelihood using a bandpower with $l(l+1)C_l/2\pi =$ constant ("flat" bandpower) including data only from a limited l range in which DASI has high sensitivity, as seen in Figure 6.1. Using the range $300 < l < 450$ which includes 24% of the complete dataset, we find the ML at flat bandpower values $E = 26.5\mu K^2$ and

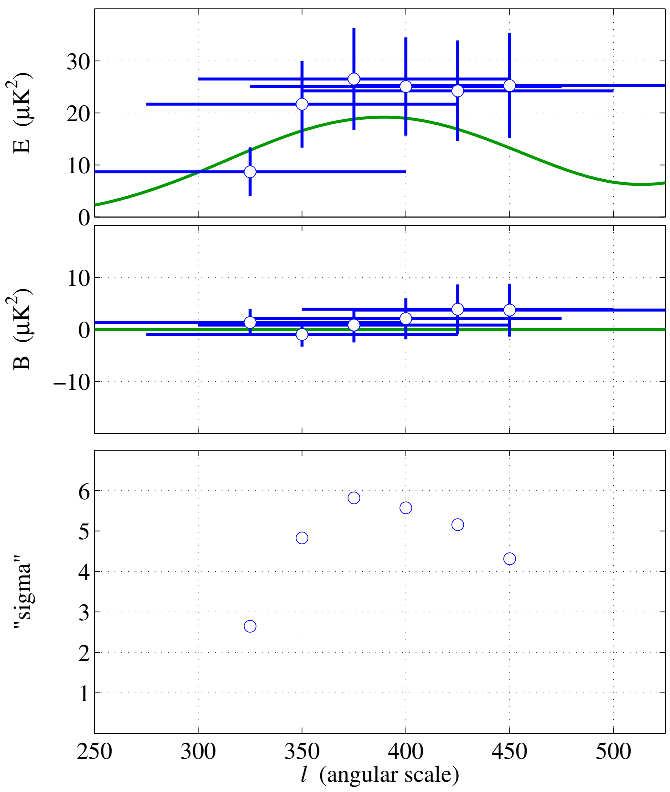

Figure 6.2 Results from E/B flat bandpowers computed on restricted ranges of data. A "flat" bandpower analysis using only baselines in the range $300 < l < 450$, which includes 24% of the complete dataset and covers the angular scales at which DASI is expected to have greatest polarization sensitivity, gives likelihoods that peak at $E = 26.5\mu K^2$ and $B = 0.8\mu K^2$, with a significance of E detection of 5.8σ. These results are quite sensitive to the choice of this range, however, leading us to seek a well motivated bandpower shape with which to perform the analysis over the entire l range sampled by DASI.

$B = 0.8\mu K^2$. The likelihood falls dramatically for the zero polarization *nopol* model $E = 0$, $B = 0$. Marginalizing over B, we find $\Lambda(E = 0) = 16.9$ which, assuming the uncertainties are normally distributed, corresponds to a PTE of 5.9×10^{-9} or a significance of E detection of 5.8σ. As expected, changing the l range affects the maximum likelihood values and the confidence of detection. This is illustrated in Figure 6.2, in which it can be seen that shifting the center of the above l range by ± 25 reduces the confidence of detection to 5.6σ and 4.8σ, respectively. Clearly it is

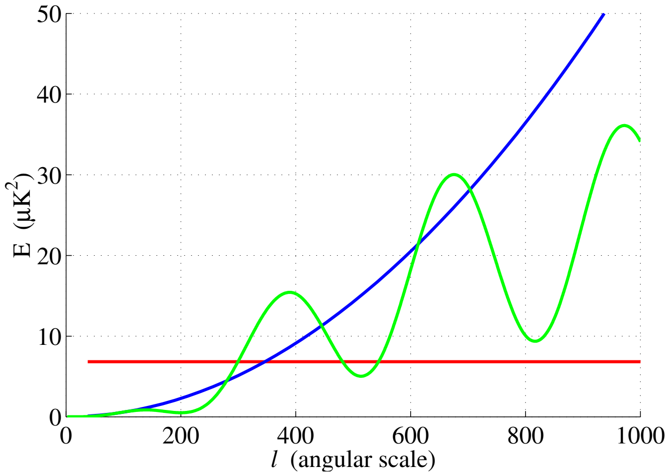

Figure 6.3 Comparison of concordance and two power-law spectrum shapes examined as candidates for single parameter E/B analysis. All three are illustrated at the E spectrum amplitudes which produced maximum likelihoods for each shape, but the likelihood of the best-fit model with a concordance shape (green) is a factor of 200 and 12,000 higher than those of the $l(l+1)C_l \propto l^2$ (blue) and $l(l+1)C_l \propto$ constant (red, "flat") cases, respectively.

desirable to perform the analysis over the entire l range sampled by DASI using a well motivated bandpower shape for the parameterization.

We considered three *a priori* shapes to check which is most appropriate for our data: the concordance E spectrum shape (as defined in §6.1.1), and two power law alternatives, $l(l+1)C_l \propto$ constant ("flat") and $l(l+1)C_l \propto l^2$ (see Fig. 6.3). For any of these shapes, the point at $E = 0,\ B = 0$ corresponds to the same zero-polarization *nopol* model, so that the likelihood ratios $\Lambda(nopol)$ may be compared directly to assess the relative likelihoods of the best-fit models. For the flat $l(l+1)C_l \propto$ constant case, the ML flat bandpower values are $E = 6.8\mu K^2, B = -0.4\mu K^2$, with the log-likelihood at zero falling by a factor of $\Lambda(nopol) = 4.34$. For the $l(l+1)C_l \propto l^2$ case, the ML values are $E = 5.1\mu K^2, B = 1.2\mu K^2$ (for values of $l(l+1)C_l/2\pi$ at $l = 300$), with $\Lambda(nopol) = 8.48$. For the concordance shape, the ML values are $E = 0.80, B = 0.21$ in units of the concordance E spectrum amplitude, with $\Lambda(nopol) = 13.76$. The likelihood of the best fit model in the concordance case is a factor of 200 and 12,000 higher than those of the $l(l+1)C_l \propto l^2$ and $l(l+1)C_l \propto$ constant cases, respectively; compared to the concordance shape either of these is a very poor model for the data. The data clearly prefer the concordance shape, which we therefore use for the E/B and other single bandpower analyses presented in our results tables.

Figure 6.4 illustrates the result of the final E/B polarization analysis, using the concordance shape. The maximum likelihood value of E is 0.80 (0.56 to 1.10 at 68% confidence). For B, the result should clearly be regarded as an upper limit; 95% of the $B > 0$ likelihood (marginalized over E) lies below 0.59.

The upper panel of Figure 6.1 shows the parameter window functions relevant for this analysis. Note that the E parameter has very little sensitivity to B and vice versa — as discussed in Chapter 2, the purity with which DASI can separate these is remarkable. This separation is also demonstrated by the low correlation (-0.046) between the E and B parameters (see Table 6.1).

The likelihood of the zero polarization model (E=0, B=0) is 1.1×10^{-6} that of the ML model, corresponding to $\Lambda(nopolarization) = 13.76$ as mentioned above. Using the Monte Carlo method (§6.1.8) we find that in 1000 simulations with no polarization the largest value of this Λ statistic obtained is 6.4 — far less than the observed value. Assuming that the uncertainties in E and B are normally distributed (§6.1.8), the likelihood ratio $\Lambda(nopol) = 13.76$ implies a probability that our data are consistent with the zero polarization hypothesis of PTE $= 1.05 \times 10^{-6}$. We conclude that the data are highly incompatible with the no polarization hypothesis. Marginalizing over B, we find $\Lambda(E = 0) = 12.1$ corresponding to detection of E-mode polarization at a PTE of 8.46×10^{-7} (or a significance of 4.92σ).

The likelihood ratio for the concordance model gives $\Lambda(E = 1,\ B = 0) = 1.23$, for which the Monte Carlo and analytic PTE are both 0.28. We conclude that our data are consistent with the concordance model.

However, given the precision to which previous measurements have determined the temperature power spectrum of the CMB, even within the ~ 7 parameter class

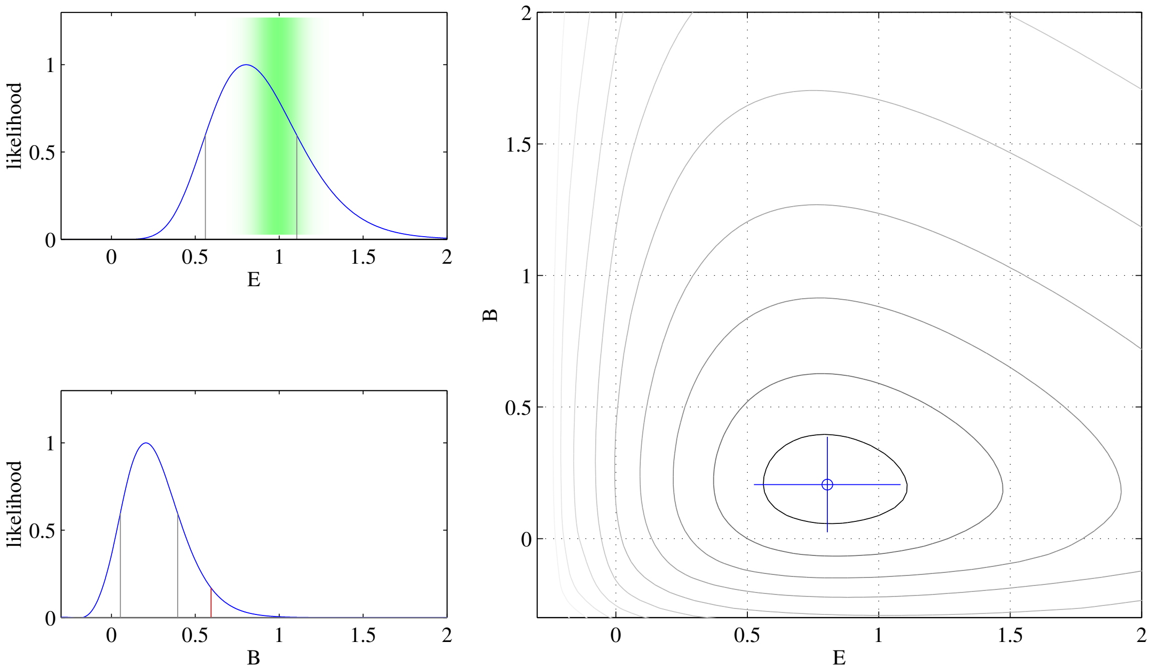

Figure 6.4 Results from the two parameter shaped bandpower E/B polarization analysis. An E-mode power spectrum shape as predicted for the concordance model is assumed, and the units of amplitude are relative to that model. The same shape is assumed for the B-mode spectrum. (right panel) The point shows the maximum likelihood value with the cross indicating Fisher matrix errors. Likelihood contours are placed at levels $\exp(-n^2/2)$, $n = 1, 2...$, relative to the maximum, i.e., for a normal distribution, the extrema of these contours along either dimension would give the marginalized n-sigma interval. (left panels) The corresponding single parameter likelihood distributions marginalized over the other parameter. Note the steep fall in likelihood toward low power values; this likelihood shape (similar to a χ^2 distribution) is typical for positive-definite parameters for which a limited number of high signal/noise modes are relevant. The gray lines enclose 68% of the total likelihood. The red line indicates the 95% confidence upper limit on B-mode power. The green band shows the distribution of E expectation values for a large grid of cosmological models weighted by the likelihood of those models given our previous temperature result (see text).

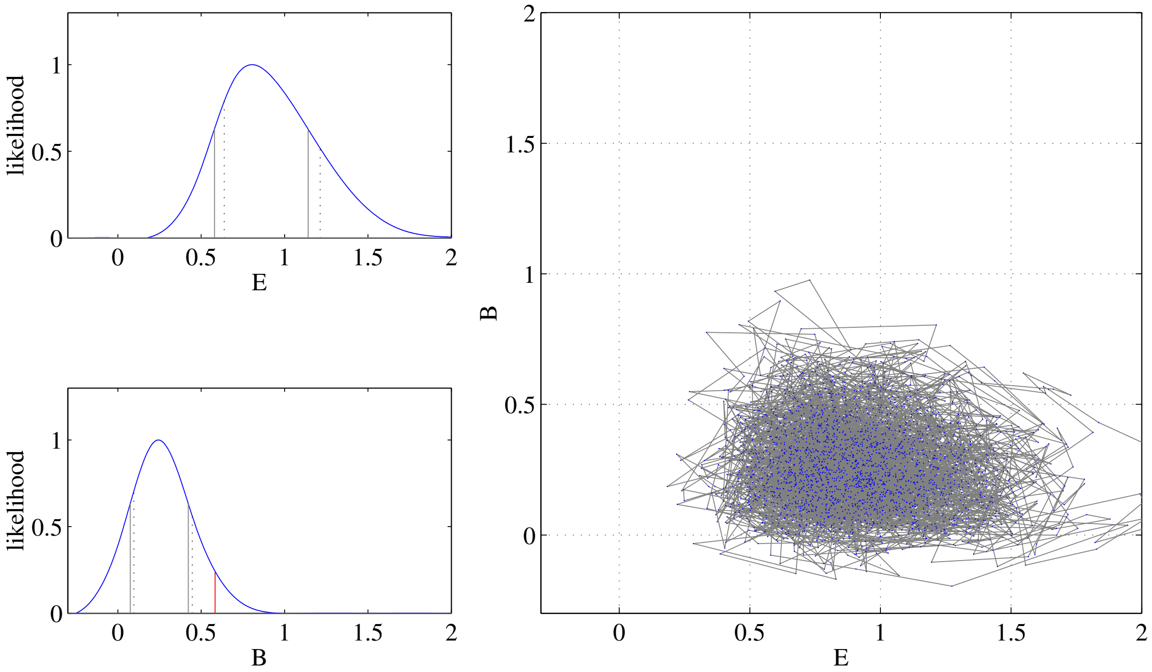

Figure 6.5 Results from the same shaped bandpower E/B polarization analysis of Fig. 6.4 with the likelihood calculated using a Markov chain, rather than an explicit grid evaluation. The Markov chain technique (Christensen et al. 2001) is illustrated with a 3000 point chain in the right panel. Unless a procedure is used to progressively rescale the definition of likelihood, the Markov chain does not effectively map low likelihood ($> 3\sigma$) regions, and we prefer to rely on explicit grid evaluation in our low-dimensional analyses (< 5 parameters) where it is practical. In the regions of high likelihood, the techniques give identical results: 68% intervals derived from the Markov chain, illustrated for each parameter in the left panels, match the corresponding intervals from explicit grid evaluation to 1%. In addition to the 68% HPD intervals (solid gray lines) which we quote in our results, also illustrated are 68% "central likelihood" intervals (dotted lines) which are sometimes used, and which, due to the skewness of these distributions, tend to give higher power estimates.

of cosmological models often considered, the shape and amplitude of the predicted E-mode spectrum are still somewhat uncertain. To quantify this, we have taken the model grid generated for Paper III and calculated the expectation value of the shaped band E parameter for each model using the window function shown in Figure 6.1. We then take the distribution of these predicted E amplitudes, weighted by the likelihood of the corresponding model given our previous temperature results (using a common calibration uncertainty for the DASI temperature and polarization measurements). This yields a 68% credible interval for the predicted value of the E parameter of 0.90 to 1.11. As illustrated in the upper left panel of Figure 6.4, our data are compatible with the expectation for E based on existing knowledge of the temperature spectrum and the standard model of CMB physics.

$E5/B5$ analysis

The top two panels of Figure 6.6 show the results of a ten parameter analysis characterizing the E and B-mode spectra using five flat bandpowers for each. The lower panel of Figure 6.1 shows the corresponding parameter window functions. Note the extremely small uncertainty in the measurements of the first bands $E1$ and $B1$.

To test whether these results are consistent with the concordance model, we calculate the expectation value for the nominal concordance model in each of the 5 bands, yielding E=(0.8,14,13,37,16) and B=(0,0,0,0,0) μK^2. The likelihood ratio comparing this point in the ten dimensional parameter space to the maximum gives $\Lambda = 5.1$, which for ten degrees of freedom results in a PTE of 0.42, indicating that our data are consistent with the expected polarization parameterized in this way. The $E5/B5$ results are highly inconsistent with the zero polarization *nopol* hypothesis, for which $\Lambda = 15.2$ with a PTE = 0.00073.

While quite significant, the PTE for this statistic is considerably weaker than the equivalent one obtained for the single band analysis of §6.2.1due to the higher number of degrees of freedom in this analysis. In this ten dimensional space, all possible random deviations from the *nopol* expectation values E=(0,0,0,0,0), B=(0,0,0,0,0) are treated equally in constructing the PTE for our Λ statistic. Imagining the *nopol* hypothesis to be true, it would be far less likely to obtain a result in this large parameter space that is both inconsistent with *nopol* at this level *and at the same time* is consistent with the concordance model, than it would be to obtain a result that

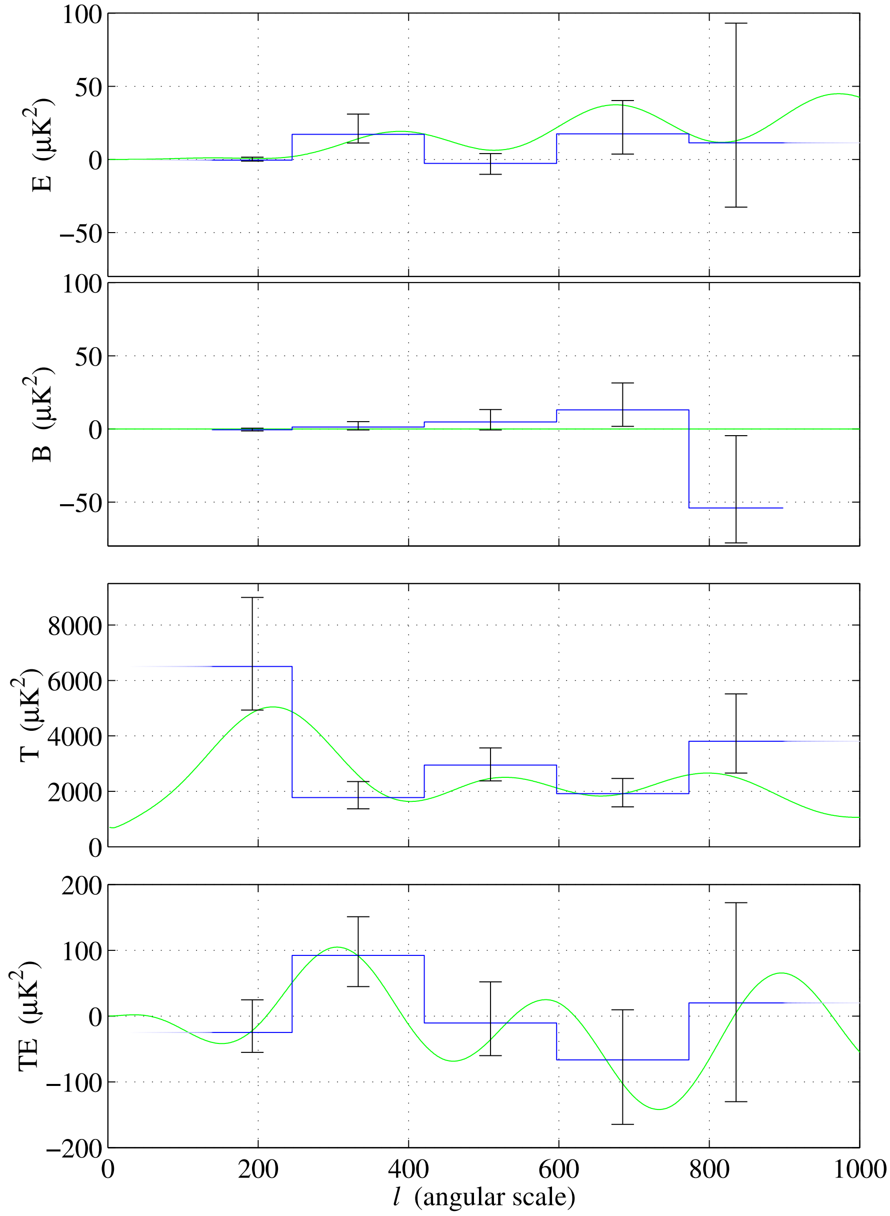

Figure 6.6 Results from the five-band likelihood analyses. The ten parameter $E5/B5$ polarization analysis is shown in the top two panels. The $T5$ temperature analysis is shown in the third panel. The 5 TE bands from the $T/E/TE5$ joint analysis are shown in the bottom panel. All the results are shown in flat bandpower units of $l(l+1)C_l/2\pi$. The blue line shows the piecewise flat bandpower models representing the maximum likelihood parameter values, with the error bars indicating the 68% central region of the likelihood of each parameter, marginalizing over the other parameter values (errors for E and B in the first band are too small to see clearly here). The green line shown for each of the spectra is the concordance model.

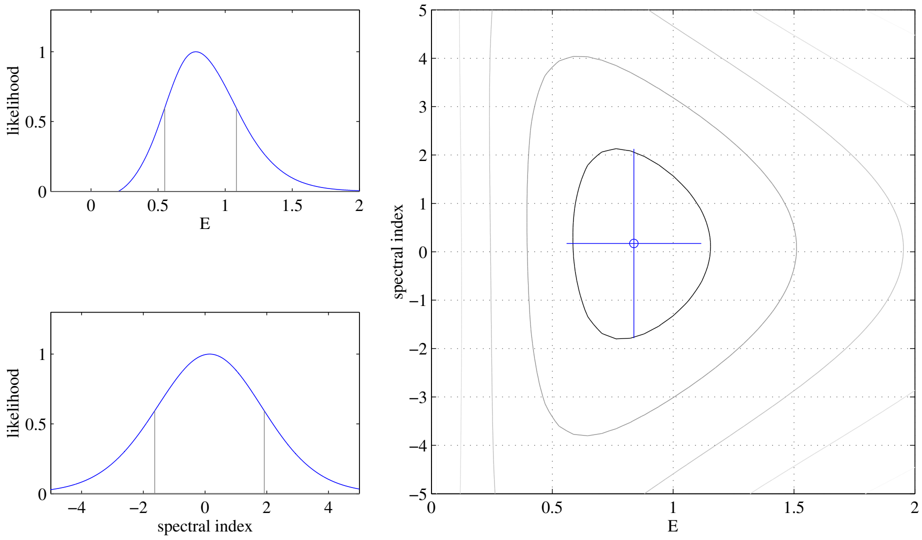

Figure 6.7 Results of $E/beta_E$ polarization shaped bandpower amplitude/spectral-index analyses. The layout of the plot is analogous to Figure 6.4. The concordance power spectrum shape is assumed for E, and in this analysis the B spectrum is set to zero. The spectral index is relative to the CMB, so that 0 corresponds to a 2.73 K Planck spectrum. In these units synchrotron emission would be expected to have an index of approximately -3.

is merely inconsistent with *nopol* in some way at this level. It is the latter probability that is measured by the PTE for our $\Lambda(nopol)$, explaining why this approach to goodness-of-fit weakens upon considering increasing numbers of parameters. One could define a goodness-of-fit statistic that overcomes this limitation by making explicit reference to compatibility with the concordance-expectation-value model, for example by examining the likelihood ratio between this model and the *nopol* model. However, if one is willing to make reference to the concordance model in this way, it is certainly preferable to use the actual concordance power spectrum shape rather than a five-band approximation to it, which is exactly what the goodness-of-fit from the single band E/B analysis of the previous section accomplishes.

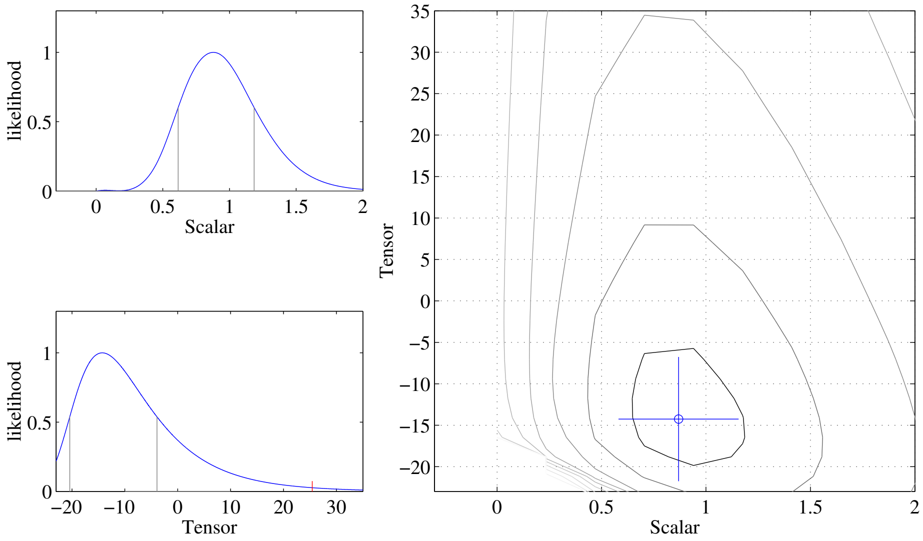

Figure 6.8 Results of Scalar/Tensor polarization analysis.

E/β_E analysis

We have performed a two parameter analysis to determine the amplitude of the E-mode polarization signal as above and the frequency spectral index β_E of this signal relative to the CMB (Figure 6.7). As expected, the results for the E-mode amplitude are very similar to those for the E/B analysis described in the previous section. The spectral index is found to be consistent with CMB: the maximum likelihood value is $\beta_E = 0.17$ (-1.63 to 1.92). Although the constraint is not strong, this result nevertheless disfavors the domination of the polarization signal by foregrounds (see §6.3.2 below).

Scalar/Tensor analysis

As discussed in Chapter 1, predictions exist for the shape of the E and B-mode spectra which would result from primordial gravity waves, also known as tensor perturbations. And although the amplitude of tensors is not well constrained by theory, they are a generic prediction of inflation, and measurement of the tensor amplitude would offer both a compelling confirmation of this remarkable theory and a direct probe of the energy scale at which it occurred. In a concordance-type model including tensors, their contributions to the polarization E and B spectra are expected to peak at $l \sim 100$. Assuming reasonable priors, current measurements of the temperature spectrum (in which tensor and scalar contributions will be mixed) suggest T/S < 0.2 (Wang et al. 2002), where this amplitude ratio is defined in terms of the tensor and scalar contributions to the temperature quadrupole C_2^T. We use the distinct polarization angular power spectra for the scalars (our usual concordance E shape, with $B = 0$) and the tensors (which specify both E_T and B_T) as two components of a likelihood analysis to constrain the amplitude parameters of these components. This analysis is illustrated in Figure 6.8.

In principle, because the scalar B-mode spectrum is zero this polarization-based approach avoids the fundamental sample variance limitations arising from using the temperature spectrum alone. For this reason, a great deal of future CMB polarization experimental effort will be dedicated to constraining the tensor amplitude by targeting these B-modes. However, the $E5/B5$ analysis (§6.2.1) indicates that DASI produces only upper limits to the E and $B-$mode polarization at the angular scales most relevant ($l \lesssim 200$) for the tensor spectra. It is therefore not surprising that our limits on T/S derived from the polarization spectra as reported in Table 6.1 are quite weak.

6.2.2 Temperature Data Analyses and T Spectrum Results

T/β_T analysis

Results are shown in Figure 6.9 for a two parameter analysis to determine the amplitude and frequency spectral index of the temperature signal. The bandpower shape used is that of the concordance T spectrum, and the amplitude parameter is expressed in units relative to that spectrum. As with the E/β_E analysis, the spectral index is relative to the CMB, so that 0 corresponds to a 2.73 K Planck spectrum.

parameter	$l_{\mathrm{low}} - l_{\mathrm{high}}$	ML est.	$\left(F^{-1}\right)_{ii}^{1/2}$ error	68% interval lower	68% interval upper	95% U.L.	units
E/B							
E	–	0.80	±0.28	0.56	1.10	–	frac. of concordance E
B	–	0.21	±0.18	0.05	0.40	0.59	frac. of concordance E
E5/B5							
E1	28 – 245	-0.50	±0.8	-1.20	1.45	2.38	uK^2
E2	246 – 420	17.1	±6.3	11.3	31.2	–	uK^2
E3	421 – 596	-2.7	±5.2	-10.0	4.3	24.9	uK^2
E4	597 – 772	17.5	±16.0	3.8	40.3	47.2	uK^2
E5	773 – 1050	11.4	±49.0	-32.5	92.3	213.2	uK^2
B1	28 – 245	-0.65	±0.65	-1.35	0.52	1.63	uK^2
B2	246 – 420	1.3	±2.4	-0.7	5.0	10.0	uK^2
B3	421 – 596	4.8	±6.5	-0.6	13.5	17.2	uK^2
B4	597 – 772	13.0	±14.9	1.6	31.0	49.1	uK^2
B5	773 – 1050	-54.0	±28.9	-77.7	-4.4	147.4	uK^2
E/β_E							
E	–	0.84	±0.28	0.55	1.08	–	frac. of concordance E
β_E	–	0.17	±1.96	-1.63	1.92	–	temp. spectral index
Scalar/Tensor							
S	–	0.87	±0.29	0.62	1.18	–	frac. of concordance S
T	–	-14.3	±7.5	-20.4	-3.9	25.4	T/(S=1)

parameter correlation matrices

E	B
1	−0.046
	1

E	β_E
1	−0.082
	1

S	T
1	−0.339
	1

E1	E2	E3	E4	E5	B1	B2	B3	B4	B5
1	−0.137	0.016	−0.002	0.000	−0.255	0.047	−0.004	0.000	0.000
	1	−0.117	0.014	−0.002	0.024	−0.078	0.004	0.000	0.000
		1	−0.122	0.015	−0.003	0.010	−0.027	0.003	−0.001
			1	−0.119	0.000	−0.001	0.002	−0.016	0.003
				1	0.000	0.000	0.000	0.002	−0.014
					1	−0.226	0.022	−0.002	0.000
						1	−0.097	0.011	−0.002
							1	−0.111	0.018
								1	−0.164
									1

Table 6.1 Results of the four likelihood analyses using polarization data only, described in §6.2.1. Each parameter set specifies a different prescription for the E and B polarization signals, in units explained in the text. Definitions of the confidence intervals, Fisher matrix uncertainties, and upper limits listed are given in §6.1.7.

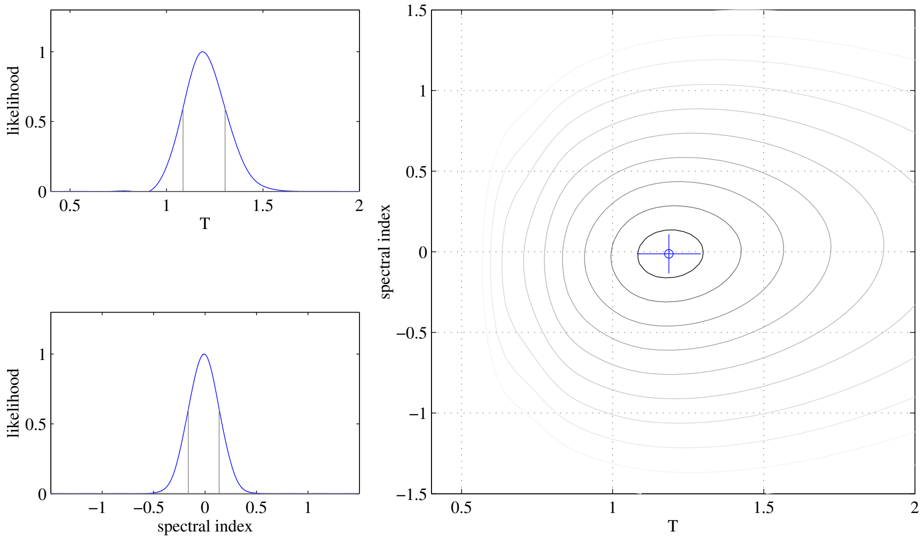

Figure 6.9 Results of $T/beta_T$ temperature shaped bandpower amplitude/spectral-index analyses. The layout of the plot is analogous to Figure 6.7. The concordance power spectrum shape is assumed for T, and spectral index is relative to the CMB blackbody. Determination of the spectral index of the observed temperature signal, unlike its power, is not limited by sample variance, so that significant unpolarized foreground contamination can be ruled out to high precision.

The amplitude of T has a maximum likelihood value of 1.19 (1.09 to 1.30), and the spectral index $\beta_T = -0.01$ (-0.16 to 0.14). While the uncertainty in the temperature amplitude is dominated by sample variance, the spectral index is limited only by the sensitivity and fractional bandwidth (32%) of DASI. Due to the extremely high signal/noise of the temperature data, the constraints on spectral index are superior to those from previous DASI observations (Paper II), strictly limiting the degree of unpolarized foreground contamination in these fields, as further discussed in §6.3.2.

$T5$ analysis

The third panel of Figure 6.6 shows the results of an analysis using five flat bands to characterize the temperature spectrum. These results are completely dominated by the sample variance in the differenced field. They are consistent with, although less

parameter	$l_{\rm low} - l_{\rm high}$	ML est.	$\left(F^{-1}\right)_{ii}^{1/2}$ error	68% interval lower	68% interval upper	units
T/β_T						
T	–	1.19	±0.11	1.09	1.30	fraction of concordance T
β_T	–	-0.01	±0.12	-0.16	0.14	temperature spectral index
T5						
T1	28 – 245	6510	±1610	5440	9630	uK^2
T2	246 – 420	1780	±420	1480	2490	uK^2
T3	421 – 596	2950	±540	2500	3730	uK^2
T4	597 – 772	1910	±450	1530	2590	uK^2
T5	773 – 1050	3810	±1210	3020	6070	uK^2

parameter correlation matrices

T1	T2	T3	T4	T5
1	−0.101	0.004	−0.004	−0.001
	1	−0.092	−0.013	−0.011
		1	−0.115	−0.010
			1	−0.147
				1

T	β_T
1	0.023
	1

Table 6.2 Results of the two likelihood analyses using temperature data only, described in §6.2.2. Each parameter set specifies a different prescription for the temperature signal. Definitions of the confidence intervals and Fisher matrix uncertainties listed are given in §6.1.7.

precise than our previous temperature power spectra described in Paper II; we include them here primarily to emphasize that DASI makes measurements simultaneously in all four Stokes parameters and is able to measure temperature as well as polarization anisotropy.

The usual unpolarized point source constraints have been applied here and in all other analyses of the temperature data. In addition, the temperature power spectrum reported in Paper II included an adjustment to correct for the small power contribution of point sources below the flux threshold of our constraints. This residual point source correction is dependent on the point source population model and is small compared to the uncertainties of the temperature results here; for simplicity it is omitted in reporting the current results.

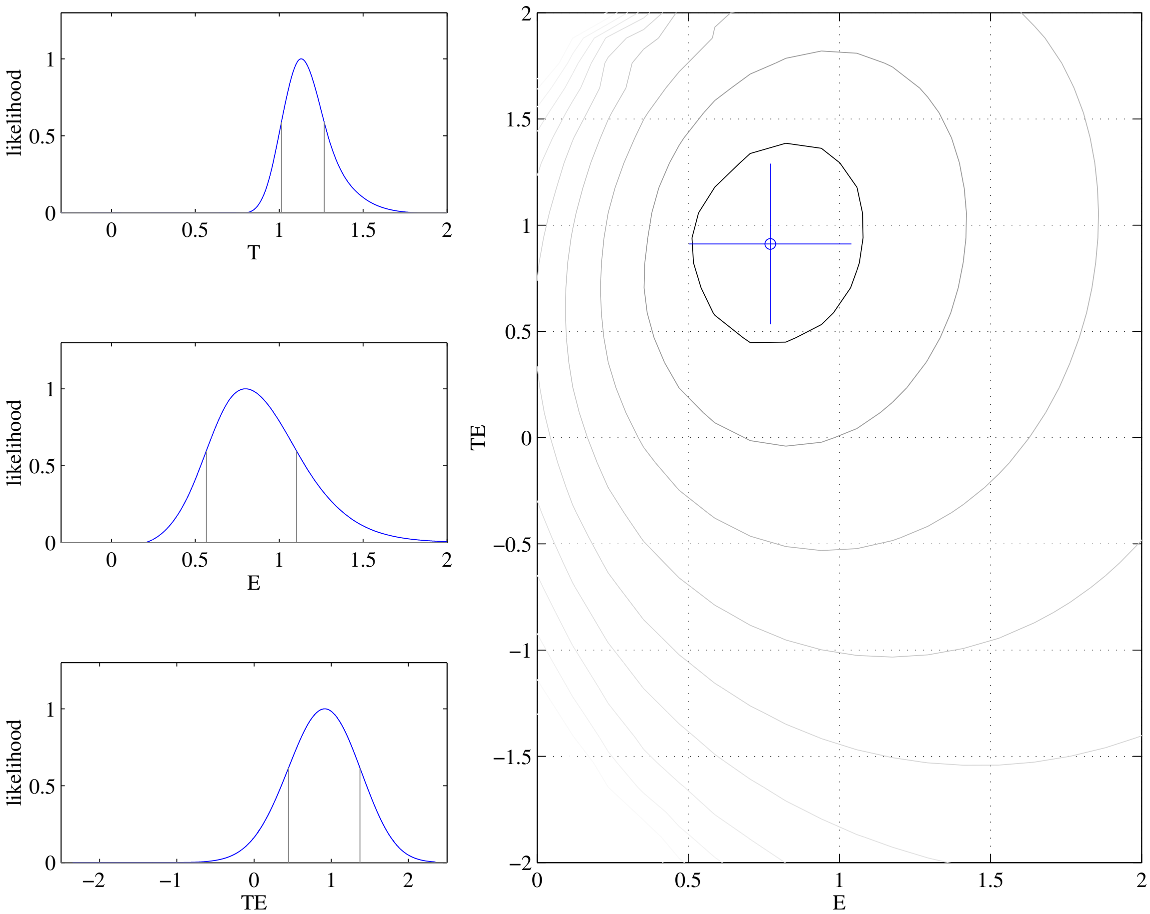

Figure 6.10 Results from the 3 parameter shaped bandpower $T/E/TE$ joint analysis. Spectral shapes as predicted for the concordance model, are assumed and the units are relative to that model. The layout of the plot is analogous to Figure 6.4. The two dimensional distribution in the right panel is marginalized over the T dimension.

6.2.3 Joint Analyses and TE, TB, EB Cross Spectra Results

$T/E/TE$ analysis

Figure 6.10 shows the results of a three parameter single bandpower analysis of the amplitudes of the T and E spectra, and the TE cross correlation spectrum. As before, bandpower shapes based on the concordance model are used. The T and E constraints are, as expected, very similar to those from the E/B, E/β_E and T/β_T analyses described above. The new result here is TE which has a maximum likelihood value of 0.91 (0.45 to 1.37). Note that in contrast to the two dimensional likelihoods shown in other figures, here the contours show apparent evidence of correlation between the two parameters; the parameter correlation coefficients from Table 6.3 are 0.28 for E/TE and 0.21 for T/TE.

Marginalizing over T and E, we find that the likelihood of TE peaks very near 1, so that $\Lambda(TE = 1) = 0.02$ with a PTE of 0.857, indicating excellent consistency with the concordance prediction for the TE cross spectrum. For the no cross correlation hypothesis, $\Lambda(TE = 0) = 1.85$ with an analytic PTE of 0.054 (the PTE calculated from Monte Carlos is 0.047). This result represents a detection of the expected TE correlation at 95% confidence and is particularly interesting in that it suggests a common origin for the observed temperature and polarization anisotropy.

It has been suggested that a quadratic estimator of TE cross correlation constructed using a $TE = 0$ prior may offer greater immunity to systematic errors (Tegmark & de Oliveira-Costa 2001), as it can be constructed exclusively from cross products of the temperature and polarization data. We have confirmed that applying such a technique to our data yields similar results to the above likelihood analysis, with errors slightly increased as expected.

$T/E/TE5$ analysis

We have performed a seven parameter analysis using single shaped band powers for T and E, and 5 flat bandpowers for the TE cross correlation; the TE results from this are shown in the bottom panel of Figure 6.6. In this analysis the B-mode polarization has been explicitly set to zero. Again, the T and E constraints are similar to the values for the other analyses where these parameters appear. The TE bandpowers are consistent with the predictions of the concordance model.

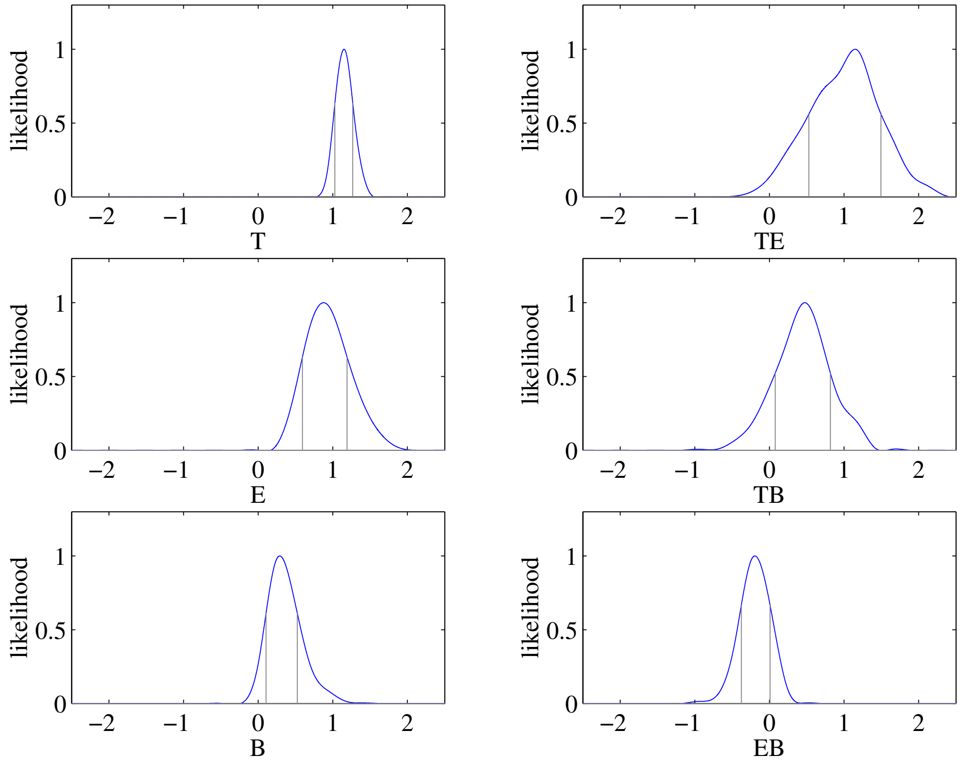

Figure 6.11 Results from the 6 parameter shaped bandpower $T/E/TE/TB/EB$ cross spectra analysis. Spectral shapes as predicted for the concordance model are assumed and the units are relative to that model, with E/B symmetry of the analysis preserved by parameterizing the TB and EB spectra using the shapes of TE and E. The marginalized likelihood curves displayed are smoothed versions of histograms derived from a 6000 point Markov chain; the HPD intervals (gray lines) are calculated using the raw Markov data. The concordance expectation values for T, E, and TE are 1, while the other spectra are expected to be zero. Results for T, E, B and TE are similar to those of previous analyses, while there is no evidence of EB or TB correlations.

$T/E/B/TE/TB/EB$ analysis

Finally, we describe the results of a six shaped bandpower analysis for the three individual spectra T, E and B, together with all three possible cross correlation spectra TE, TB and EB. We include the B cross-spectra for completeness, though previous analyses have shown there is little evidence for any B-mode signal in our data. Because there are no predictions for the shapes of the TB or EB spectra (they are expected to be zero), we preserve the symmetry of the analysis between E and B by simply parameterizing them in terms of the TE and E spectral shapes. The results for T, E, B and TE are similar to those obtained before, with no detection of EB or TB.

6.3 Systematic Uncertainties

6.3.1 Noise, Calibration, Offsets and Pointing

In order to assess the effect of systematic uncertainties on the likelihood results, we have repeated each of the nine analyses with alternative assumptions about the various effects which we have identified which reflect the range of uncertainty on each. Each of these instrumental effects has been discussed separately in previous chapters; in this section we report their final impact on our likelihood results.

Noise model

Much of the effort of the data analysis presented in this thesis has gone into investigating the consistency of the data with the noise model presented in §5.5. As discussed in that section, we find no discrepancies between complementary noise estimates on different timescales, to a level $\ll 1\%$. Numerous consistency tests on subsets of the co-polar and cross-polar visibility data show no evidence for an error in the noise scaling to a similar level. When we re-evaluate each of the analyses described in §6.2 with the noise scaled by 1%, the shift in the maximum likelihood values for all parameters is entirely negligible.

In §5.5.1, we reported evidence of some detectable noise correlations between real/imaginary visibilities and between visibilities from different bands of the same baseline. When these either or both of these noise correlations are added to the covariance matrix at the measured level, the effects are again negligible: the most

parameter	$l_{\mathrm{low}} - l_{\mathrm{high}}$	ML est.	$\left(F^{-1}\right)_{ii}^{1/2}$ error	68% interval lower	68% interval upper	units
T/E/TE						
T	–	1.13	±0.10	1.05	1.29	fraction of concordance T
E	–	0.77	±0.27	0.57	1.10	fraction of concordance E
TE	–	0.91	±0.38	0.45	1.37	fraction of concordance TE
T/E/TE5						
T	–	1.12	±0.10	1.09	1.31	fraction of concordance T
E	–	0.81	±0.28	0.71	1.36	fraction of concordance E
TE1	$28 - 245$	-24.8	±32.2	-55.3	24.7	uK^2
TE2	$246 - 420$	92.3	±38.4	44.9	151.1	uK^2
TE3	$421 - 596$	-10.5	±48.2	-60.1	52.0	uK^2
TE4	$597 - 772$	-66.7	±74.3	-164.6	9.5	uK^2
TE5	$773 - 1050$	20.0	±167.9	-130.3	172.3	uK^2
T/E/B/TE/TB/EB						
T	–	1.13	±0.10	1.03	1.27	fraction of concordance T
E	–	0.75	±0.26	0.59	1.19	fraction of concordance E
B	–	0.20	±0.18	0.11	0.52	fraction of concordance E
TE	–	1.02	±0.37	0.53	1.49	fraction of concordance TE
TB	–	0.53	±0.32	0.08	0.82	fraction of concordance TE
EB	–	-0.16	±0.16	-0.38	0.01	fraction of concordance E

parameter correlation matrices

T	E	TE
1	0.017	0.207
	1	0.282
		1

T	E	B	TE	TB	EB
1	0.026	0.004	0.230	0.136	0.033
	1	-0.027	0.320	-0.040	-0.182
		1	-0.027	0.219	-0.190
			1	-0.150	0.109
				1	0.213
					1

T	E	TE1	TE2	TE3	TE4	TE5
1	0.026	-0.071	0.202	-0.018	-0.075	0.008
	1	-0.067	0.339	-0.023	-0.090	0.008
		1	-0.076	0.006	0.011	-0.001
			1	-0.078	-0.039	0.004
				1	-0.056	0.004
					1	-0.066
						1

Table 6.3 Results of the three likelihood analyses using the joint temperature-polarization dataset, described in §6.2.3. Each parameter set specifies a different prescription for the temperature and the E and B polarization signals and their cross correlations. Definitions of the confidence intervals, Fisher matrix uncertainties, and upper limits listed are given in §6.1.7.

significant shift is in the highest-l band of the E spectrum from the $E5/B5$ analysis (§6.2.1), where the power shifts by $\sim 2\ \mu\mathrm{K}^2$, or 2% of the range of the 68% confidence interval for that parameter.

Absolute cross-polar phase calibration

Errors in the determination of the absolute cross-polar phase offsets will mix power between E and B; these phase offsets have been independently determined from wire-grid calibrations and observations of the Moon, and found to agree to within the measurement uncertainties of $\sim 0.^\circ 4$, as discussed in §4.2. Reanalysis of the data with the measured phase offsets shifted by 2° demonstrates that the likelihood results are immune to errors of this magnitude: most parameters show negligible shifts, with the most significant effect occurring in the highest-l band of the TE spectrum from the $T, E, TE5$ analysis (§6.2.3), where the power shifts by $\sim 25\ \mu\mathrm{K}^2$ (8% of the confidence interval for that parameter).

Leakages

On-axis leakage (§4.4) mixes power from T into E and B. The data are corrected for this effect in the course of reduction, before input to any analyses. When the likelihood analyses are performed without the leakage correction, the largest effects appear in the shaped TE amplitude analysis (§6.2.3), and the lowest-l band of $TE5$ from the $T, E, TE5$ analysis (§6.2.3); all shifts are tiny compared to the 68% confidence intervals. As the leakage correction itself has little impact on the results, the uncertainties in the correction which are at the $< 1\%$ level will have no noticeable effect.

The off-axis leakage at the edge of the DASI primary beam (see §4.5) is a more significant effect, and as described above in §6.1.4 it is accounted for in the likelihood analysis by modeling its contribution to the covariance matrix. Simulations illustrating the effect of this leakage and its removal in our analysis are shown in Figure 6.12.

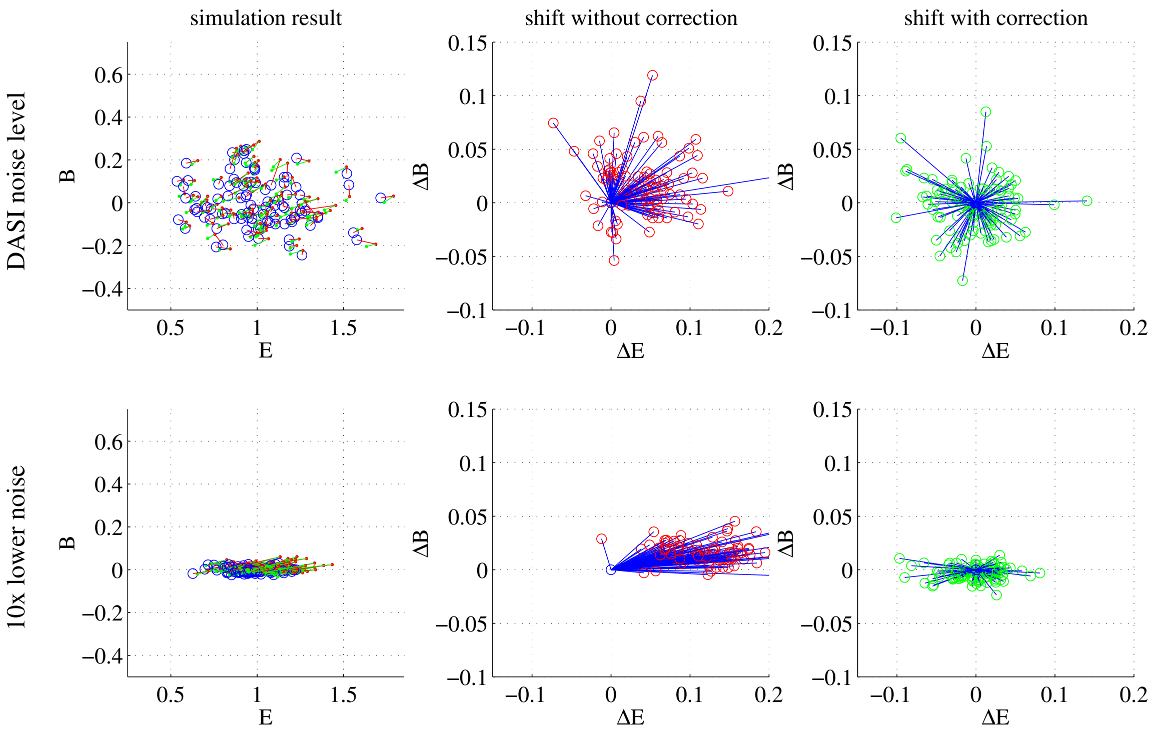

Figure 6.12 Results of simulations of the effect of off-axis leakage on the E/B results. In the upper-left panel, the blue circles give the ML results for 100 simulated observations of concordance-model CMB polarization without off-axis leakage; the scatter in these points reflects the uncertainty due to noise and sample variance for DASI's dataset. The red point connected to each circle reflects the shift in that result upon adding off-axis leakage to the signal. The green points reflect the shift back after the covariance correction is applied. The top middle and top right panels zoom in on these shifts from the original ML estimate, showing them from a common origin, before and after correction. The effect is small compared to the parameter uncertainties; off-axis leakage causes a mean bias in E, B results of 0.04 and 0.02, respectively, with rms scatter of 0.06 and 0.03. Applying the correction removes the bias to very high precision and reduces the rms to 0.04 and 0.02. The lower three panels show the same simulation procedure assuming 10x less noise; here, the E scatter is dominated by sample variance, and once again the correction successfully removes the bias introduced by the off-axis leakage.

When this correction is not applied, the E, B results for our actual dataset shift by ~ 0.04 and ~ 0.02, respectively, as expected from these simulations. Parameters for other analyses shift by similarly small amounts. Although these shifts are small, the covariance correction removes the bias due to off-axis leakage in our data completely to the degree to which we understand the off-axis leakage beam profile. Uncertainties in the leakage profiles of the order of the fit residuals (see §4.5) lead to shifts of less than 1%.

Pointing

The pointing accuracy of the telescope is measured to be better than $2'$ and the rms tracking errors are $< 20''$, as discussed in Papers I and II, this is more than sufficient for the characterization of CMB anisotropy at the much larger angular scales measured by DASI.

Absolute calibration

Absolute calibration of the telescope was achieved through measurements of external thermal loads, transferred to the calibrator RCW38. The dominant uncertainty in the calibration is due to temperature and coupling of the thermal loads. As discussed in §4.3, we estimate an overall calibration uncertainty of 8% ($1\,\sigma$), expressed as a fractional uncertainty on the C_l bandpowers (4% in $\Delta T/T$). This common calibration uncertainty applies equally to all parameters which estimate amplitudes of temperature and polarization power spectra in the analyses presented here.

6.3.2 Foregrounds

Point sources

Extragalactic point sources are a potential contaminant for both temperature and polarization CMB measurements, and are of particular concern at low frequencies and small angular scales. The highest sensitivity point source catalog in our observing region is the 5 GHz Parkes-MIT-NRAO (PMN) survey (Wright et al. 1994). For our first season temperature analysis described in Papers I and II we used constraint matrices to project out sources from our 32 fields whose 5 GHz PMN flux, enveloped with the DASI primary beam, exceeds 50 mJy.

As described in §5.1, our polarization fields were selected for the absence of any significant point source detections in the first season data, and scrutiny of the current much higher signal-to-noise dataset yields at best scant evidence for a correlation between the locations of the 31 brightest PMN sources and the pixel values in the temperature map. Nevertheless, following our previous procedure these sources are projected out of the co-polar data for all of the likelihood results presented here. The resulting temperature spectral index for the temperature data as reported above is consistent with a thermal spectrum: $\beta_T = -0.01$ (-0.16 to 0.14). If none of the PMN sources are projected out, the spectral index shifts to -0.12 (-0.25 to 0.01), indicating possible evidence for a statistical detection of PMN sources, but that the CMB is nevertheless the dominant unpolarized signal in these fields.

Unfortunately the PMN survey is not polarization sensitive. We note that the distribution of point source polarization fractions is approximately exponential (see below). Total intensity is thus a poor indicator of polarized intensity. As a consequence, in the simulations described below, the point sources contributing the strongest polarized fluxes were rarely among the subset selected for removal according to unpolarized flux. Thus, projection of the PMN sources from our polarization analysis does not offer an effective tool for removing contributions from point sources (although it does increase our errors, due to loss of degrees of freedom in the dataset), and although we have verified that the results do not shift substantially upon including such constraints, the final analysis does not use them.

Instead, we calculate the expected contribution of undetected point sources to our polarization results. To do this we would like to know the distribution of polarized flux densities, but unfortunately no such information exists in our frequency range. However, to make an estimate, we use the distribution of total intensities, and then assume a distribution of polarization fractions. We know the former distribution quite well from our own first season 32-field data where we detect 31 point sources and determine that $dN/dS_{31} = (32 \pm 7)S^{(-2.15\pm0.20)}$ Jy^{-1} Sr^{-1} in the range 0.1 to 10 Jy. This is consistent, when extrapolated to lower flux densities, with a result from the CBI experiment valid in the range 5–50 mJy (Mason et al. 2002). The distribution of point source polarization fractions at 5 GHz can be characterized by an exponential with a mean of 3.8% (Zukowski et al. 1999); data of somewhat lower quality at 15 GHz are consistent with the same distribution (Simard-Normandin et al. 1981b). Qualitatively one expects the polarization fraction of synchrotron-dominated sources initially to rise with frequency, and then plateau or fall, with the break point at frequencies $\ll$ 5 GHz (see Simard-Normandin et al. (1981a) for an example). Recent studies have suggested that flat spectrum sources have relatively consistent polarization properties from 5-43 GHz (Tucci et al. 2003). In the absence of more direct measurements, we have conservatively assumed the 5 GHz exponential distribution mentioned above continues to hold at 30 GHz.

Our estimates of the effect of polarized point sources are based on Monte Carlo simulations, generating realizations using the total intensity and polarization fraction distributions mentioned above.[2] For each realization, we generate simulated DASI data by adding a realization of CMB anisotropy and appropriate instrument noise. The simulated data are tested for evidence of point sources and those realizations that show statistics similar to the real data are kept. The effect of off-axis leakage, through which unpolarized point sources near the null of our primary beam acquire an apparent polarized flux, is significant compared to the effect due to intrinsic polarization and is included in these simulations.

When the simulated data are passed through the E/B analysis described in §6.2.1,

[2] These Monte Carlo point source simulations were led by C. Pryke.

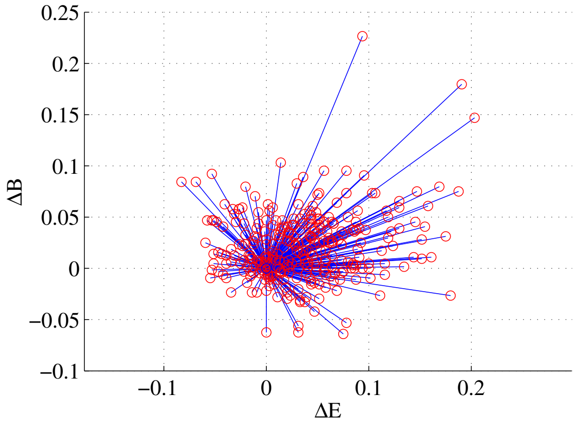

Figure 6.13 Results of Monte Carlo simulations of point source contribution to E/B results. Shown are the shifts in the E/B plane due to adding 300 realizations of a point source population, as discussed in the text. Mean bias on the E parameter is 0.04 with a standard deviation of 0.05; the shifts in B are on average 40% smaller. In 95% of cases the shift distance in the E/B plane is less than 0.13.

the mean bias of the E parameter is 0.04 with a standard deviation of 0.05. The results of 300 simulations are illustrated in Figure 6.13; in 95% of cases the shift distance in the E/B plane is less than 0.13. We conclude that the presence of point sources consistent with our observed data has a relatively small effect on our polarization results.

Diffuse Foregrounds

As discussed in §5.1 and illustrated in Figure 5.1, our fields were selected from regions expected to have minimal galactic foregrounds. In Paper II a cross-correlation analysis against total flux templates for free-free (Hα maps (Gaustad et al. 2000; McCullough 2001)), dust (IRAS 100 μm maps of Finkbeiner et al. (1999)), and synchrotron (408 MHz Haslam survey maps (Haslam et al. 1981; Finkbeiner 2001)) emission confirmed that the contribution of each of these foregrounds to our temperature anisotropy data is negligible.

Unfortunately there are no published polarization maps in the region of our fields, but the level of unpolarized foregrounds allows us to rule out some sources of contamination. Free-free emission exhibits a fractional polarization of less than 1%. Diffuse thermal dust emission may be polarized by several percent (see, e.g., Hildebrand et al. 2000), although we note that polarization of the admixture of dust and free-free emission observed with DASI in NGC 6334 is $\ll 1\%$ (see Paper IV). Likewise, emission from spinning dust is not expected to be polarized to a significant degree (Lazarian & Prunet 2002). The fractional polarization of the CMB is expected to be of order 5-10%. Therefore, given that free-free and dust emission do not contribute significantly to our temperature anisotropy results, they are not expected to contribute to the polarization.

However, synchrotron emission, generated by free electrons spiraling in galactic magnetic fields, can exhibit intrinsic polarizations up to 70%. Because of this, it is by far our greatest concern: even with a a negligible contribution to the temperature data, the synchrotron signal could be significant for polarization measurements. Previous attempts to estimate the angular power spectrum of polarized synchrotron have been guided by surveys of the Galactic plane at frequencies of 1–3 GHz (Tegmark et al. 2000; Giardino et al. 2002). These maps show much more small scale structure in polarization than in temperature, but this is mostly induced by Faraday rotation (Gaensler et al. 2001), an effect which is negligible at 30 GHz. Additionally, our polarization fields lie at Galactic latitudes $-58\overset{\circ}{.}4$ and $-61\overset{\circ}{.}9$, and since synchrotron emission is highly concentrated in the disk of the Galaxy it is unlikely that the angular power spectrum at low Galactic latitudes is relevant to high latitudes (Gray et al. 1999).

There are several strong pieces of evidence from the DASI dataset itself that the polarization results described in this thesis are free of significant synchrotron contamination. The $E5/B5$ analysis indicates an angular-scale dependence of the amplitude of the polarized signal that is unlikely to be produced by any galactic synchrotron model. Galactic synchrotron emission is known to have a temperature spectral index of -2.8 (Platania et al. 1998), with evidence for steepening to -3.0 at frequencies above $1-2$ GHz (Banday & Wolfendale 1991)[3]. At frequencies where Faraday depolarization is negligible (>10 GHz), the same index will also apply for polarization. The dramatically tight constraint on the temperature spectral index of 0.01 (-0.16 to 0.14) indicates that any component of the temperature signal coming from synchrotron emission is negligibly small in comparison to the CMB. More directly, the constraint on the E-mode spectral index $\beta_E = 0.17$ (-1.63 to 1.92) disfavors synchrotron polarization at nearly 2σ. Also, the significant TE correlation shown in Figure 6.10 indicates that the temperature and E-mode signal exhibit the complex pattern of positive and negative correlations expected from the CMB. This scale-dependent pattern of correlations could not be reproduced by synchrotron, even if its contribution to our temperature data were not ruled out. Yet another line of argument is that the complex structures of filaments or cells which emit synchrotron are not expected to produce projected patterns on the sky which prefer E-mode polarization over B-mode (Zaldarriaga 2001), and analyses of polarized synchrotron maps have found them at equal levels (de Oliveira-Costa et al. 2003a). Therefore, our detection of E polarization without a significant B component could be taken as further evidence that the signal we are seeing is not due to synchrotron emission.

[3]New WMAP measurements, discussed in Chapter 7, indicate that away from the galactic plane the synchrotron spectrum steepens to < -3.0 at ¿ 20 GHz (Bennett et al. 2003b).

Chapter 7

Conclusions

Our goal in this work has been to test the current understanding of the physics of the cosmic microwave background by detecting its predicted polarization. The DASI telescope has proven to be an ideal tool for this task. The interferometric technique gives us direct sensitivity to the E and B-mode polarization signals on angular scales of interest. After a reconfiguration with switchable achromatic circular polarizers, DASI observed two $3^\circ\!.4$ FWHM fields in all four Stokes parameters for nearly two years. Over this time the instrument has proven exceptionally stable in its calibration, systematic and noise properties. Our observing strategy, combined with these properties, has produced a compact, high signal-to-noise polarization dataset which has built-in redundancies allowing for extensive consistency tests and which is easily reduced and manipulated in analysis. The previous two chapters have presented a number of analyses which have identified a highly significant polarized signal in the DASI data. We have also found that many properties of this observed signal match our theoretical expectations for CMB polarization under the standard model.

An initial detection of any signal deserves a high degree of scrutiny. CMB measurements are particularly challenging, and the field has developed a strong tradition of carefulness in the standards applied to instrumental characterization and testing of analysis techniques. The success of this tradition has been evident in the striking agreement between the results of recent temperature power spectrum measurements obtained with dramatically different instruments (see Chapter 1 and §7.2 below). A large portion of our experimental effort, and of the text of this thesis, has been dedicated to characterizing the uncertainties in our measurement. In Chapters 3 and 4 we have described our understanding of the instrument response, including our techniques for minimizing instrumental polarization and for calibrating this and other aspects of the response using polarized and unpolarized astronomical sources. In Chapter 5 we scrutinized the noise properties of the CMB dataset using statistics that probe the noise model, performing consistency tests on various splits and subsets of data, and verifying that our data cuts exclude anomalous data while our results remain robust to the cut levels. In Chapter 6 we described simulations with which we have tested each of our likelihood analysis procedures, and we determined that the previously characterized instrumental uncertainties were at a level that does not significantly impact our results.

Below we summarize our principal results, discussing their implications and the statistical confidence with which they can be taken to indicate a detection of CMB polarization. Since the results were announced last September, several experiments, most notably the WMAP satellite, have released exciting new results which further extend our confidence in the standard model of the CMB and refine the picture of our universe it offers us. Meanwhile, DASI has continued to collect polarization data, refining the results presented here. Moreover, a new generation of experiments has already been launched to take CMB polarization measurements to the next level of precision. We conclude this thesis with a discussion of the exciting current state of the data and the prospects for the field.

7.1 Confidence of Detection

We have described several different analyses which have revealed a detection of E-mode polarization in our data. For each of these analyses, we have attempted to offer a measure of the confidence with which the polarization has been detected. The choice of which "confidence of detection" measure is preferred depends on the desired level of statistical rigor and independence from *a priori* models of the polarization.

The χ^2 analyses in §5.5.2 offer the most model-independent results, given that the χ^2 statistic is explicitly constructed to test against a null hypothesis of a dataset that contains only noise. However, even in this analysis the selection of linear combinations of the data used to form the signal-to-noise eigenmodes is guided by consideration of both a theory model and a noise model. For the high signal-to-noise eigenmodes of the polarization data, the probability to exceed (PTE) the measured χ^2 for the sum of the various data splits ranges from 1.6×10^{-8} to 8.7×10^{-7}, while the χ^2 for the differences are found to be consistent with noise. The PTE for the χ^2 found for the total (not split) high signal-to-noise polarization eigenmodes, corrected for the beam offset leakage, is 5.7×10^{-8}.

Likelihood analyses are in principle more model-dependent, and the analyses reported make different assumptions for the shape of the polarization power spectrum. Nonetheless, if the range of considered models includes some that are close to a true description of the signal, the likelihood ratio statistic can be useful for excluding the hypothesis of no polarization.

Using our theoretical expectation to select the angular scales on which DASI should be most sensitive, we calculate the likelihood for a flat bandpower in E and B over the multipole range $300 < l < 450$, and with the likelihood ratio test we find the data are consistent with $B = 0$ over this range, but that $E = 0$ can be rejected with a PTE of 5.9×10^{-9}. This approach requires minimal assumptions about the shape of the power spectrum, but like the χ^2 analyses it requires the selection of a subset of data to consider, based on the expected signal.

When the full l range of the DASI data is analyzed, the choice of the model bandpower is more important. In this case, the likelihood analyses indicate that a $l(l+1)C_l \propto l^2$ model for the E-mode spectrum is 60 times more likely than a $l(l+1)C_l =$

constant ("flat") model. Further, a bandpass shape based on the concordance model is found to be 12,000 times more likely than the flat bandpower. Using this concordance shaped bandpower, a likelihood analysis finds a level of E-mode polarization that is consistent with the predicted amplitude of the concordance model, with an ML amplitude of 0.80 (68% range 0.56 to 1.10) compared to a concordance prediction of 0.9 to 1.1. The likelihood ratio test excludes $E = 0$ with a PTE of 8.5×10^{-7} in this analysis, corresponding to a confidence of detection of 4.9σ. For all three of these considered shapes, B is found to be consistent with zero as expected in the concordance model.

The above statistical tests – derived from the χ^2 and the restricted and full-range E/B likelihood analyses – each offer evidence for the detection of an E-mode polarization signal at confidence levels ranging between 4.9 and 5.8σ. Moreover, the full-range E/B likelihood analysis has offered support for the shape and amplitude for this E spectrum signal predicted by the concordance model.

The results of the five-band piecewise-flat analysis, $E5/B5$, also support the concordance model, and offer constraints on the shape of the detected E spectrum which allow us to test some of the physical predictions of the standard model. The upper limit for the first E band at $28 \leq l \leq 245$ is only $2.38\mu\mathrm{K}^2$, a factor of 30 lower in power than the previous upper limit. The next band at $246 \leq l \leq 420$ is detected with a maximum likelihood value of $17.1\mu\mathrm{K}^2$. Such a sharp rise in power with increasing l is expected in the E-mode spectrum (see Figure 6.6) due to the length scale introduced by the mean free path at last scattering. As discussed in Chapter 1, the polarization of the larger modes is suppressed because their velocity differences are not as large on the scale of the mean free path. In fact, the E spectrum is expected to increase as $l(l+1)C_l \propto l^2$ at small l. This dependence is not expected to continue to the higher l's to which DASI is sensitive, due to diffusion damping, which suppresses power on scales smaller than the mean free path. The maximum likelihood values of the higher l bands of the DASI five band E analysis are consistent with the damped concordance model, but lie below a simple extrapolation of the l^2 power law. As in the other analyses, the B-mode spectrum in the five-band analysis is consistent with the concordance prediction of zero.

The TE analysis provides further confidence in our detection of CMB polarization and for the concordance model. From the $T/E/TE$ likelihood analysis, the $TE = 0$ hypothesis is rejected with a PTE of 0.054. Note that our TE amplitude parameter could be negative as well as positive, so the probability of a false detection at this level which, like our data, also has the sign predicted by the concordance model is only PTE = 0.027.

Lastly, the measured T frequency spectral index, 0.01 (-0.16 to 0.14), is remarkably well constrained to be thermal and is inconsistent with any known foregrounds. The E frequency spectral index, 0.17 (-1.63 to 1.92), is also consistent with the CMB, and although less well constrained than the T index, is inconsistent with diffuse foreground synchrotron emission at nearly 2σ. Also, as discussed in §6.3.2, the shape of the detected E spectrum as well as the lack of a detectable B signal are both features that would be hard to attribute to foreground emission, while they are consistent with expectations for CMB polarization,

7.2 New Data and Future Directions

The DASI polarization results described above were announced September 19, 2002 at a special session of the Cosmo-02 workshop in Chicago, IL. An initial detection of CMB polarization had long been sought, and with its achievement contemporary cosmology passed a significant milestone. However, if DASI had not found CMB polarization at a level consistent with the standard model, it would certainly have been startling news. The remarkable convergence the field has enjoyed in recent years in fitting the results of precise temperature power spectrum measurements within the standard model framework has given us a great deal of confidence in our ability to understand the CMB. As one published review of the DASI polarization result said, "The new discovery further confirms our theoretical grasp of the CMB, but more importantly, it opens a whole new window to the early universe" (Hivon & Kamionkowski 2002). We therefore conclude with a brief look at what new and future CMB polarization measurements can tell us within the framework of the standard model and beyond it.

In the months since last September, several groups have released exciting new CMB results. Last October, precise temperature power spectrum results from the Archeops experiment (Benoît et al. 2003) filled in the gap between COBE and degree angular scales. In December the high-resolution ACBAR experiment (Kuo et al. 2002) released T spectrum measurements covering scales up to $l \approx 2500$. Both of these new constraints on the temperature spectrum were well-fit by the standard concordance model.

The most eagerly anticipated results came this February with the release of first-year data from the Wilkinson Microwave Anisotropy Probe (WMAP) satellite (Bennett et al. 2003a). WMAP has produced all-sky maps of the CMB which offer exquisitely precise measurements of the temperature spectrum on large and degree angular scales, limited by fundamental cosmic variance on scales $l < 350$ (Hinshaw et al. 2003). Showing excellent agreement with previous temperature spectrum measurements, the WMAP T data have allowed a further refinement of the concordance model (Spergel et al. 2003) (see top panel of Figure 7.1). The most qualitatively new constraints, however, have come from WMAP's polarization measurements. Although at this writing WMAP has not yet released direct polarization results, they have released measurements of the TE-cross spectrum on angular scales up to $l = 450$ (Kogut et al. 2003). This measurement is in good agreement with the DASI TE spectrum on degree angular scales where they overlap (lower panel of Figure 7.1). Like the DASI polarization measurements, these degree-scale TE constraints confirm of

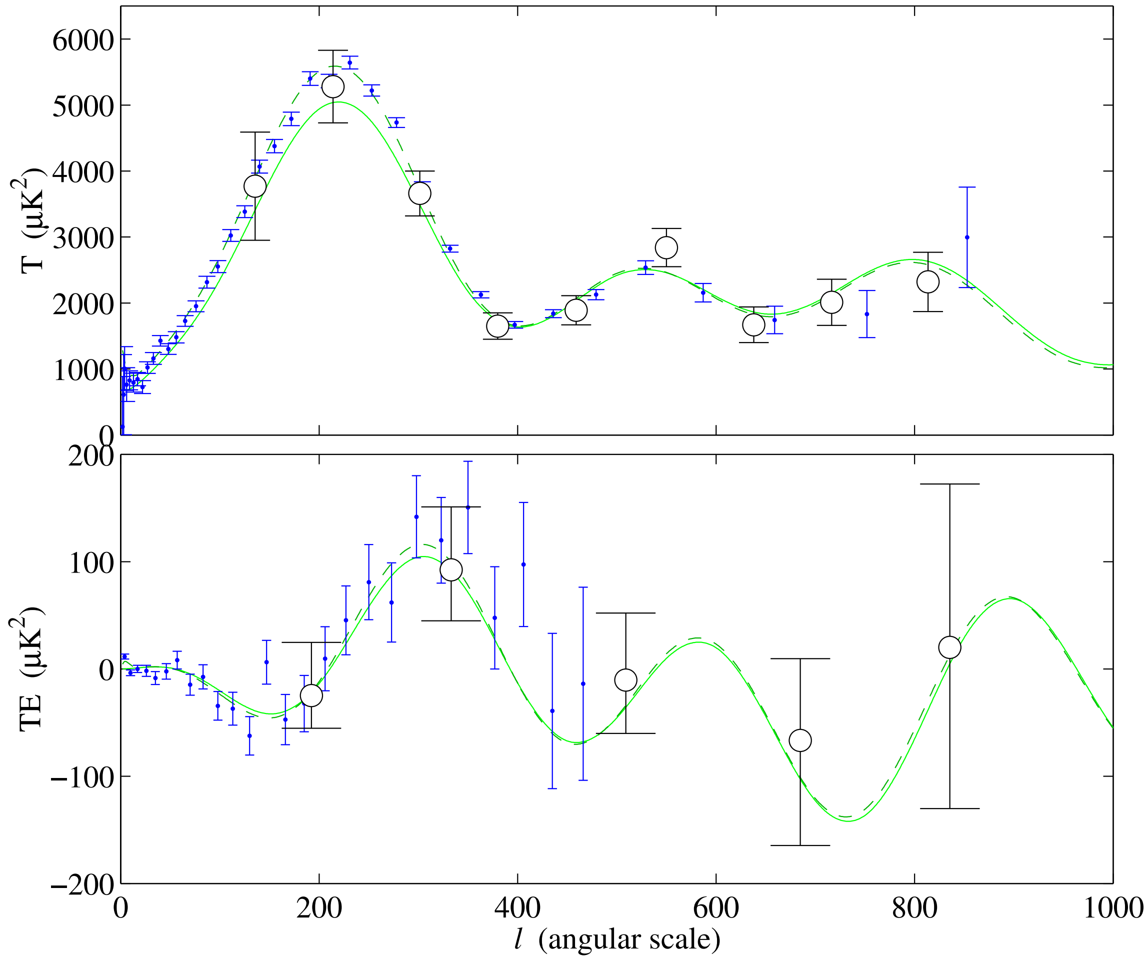

Figure 7.1 New WMAP results for the T power spectrum (Hinshaw et al. 2003) and TE cross spectrum (Kogut et al. 2003) (blue closed circles). Previous DASI results (open circles) are overplotted, including the nine-band results for T from (Halverson et al. 2002) and the five-band results for TE described in this thesis and published in (Kovac et al. 2002). The all-sky WMAP measurements have exquisite precision on large angular scales, and agree well with the DASI results where they overlap on the degree scales that are emphasized in this plot. The highly significant WMAP TE detection at $l < 10$, visible as the first point in the lower panel, is interpreted as due to early reionization. Power spectra of our previous concordance model (solid green) and the new WMAPext-defined concordance model (dashed green) are both consistent with the DASI T results and using either gives essentially the same results for our polarization analyses.

our understanding of the physics of the CMB, but are not yet of high enough precision to significantly improve cosmological parameter estimates derived from the T spectrum alone. The surprise comes at large angular scales, where WMAP also detects significant TE correlations. Interpreted as a signature of early reionization due to formation of the first stars, this polarization arises from rescatterings which occur out to redshifts $11 < z_r < 30$. The large scales of the fluctuations correspond to that epoch's horizon size, over which the local CMB quadrupole varies. This early reionization and large optical depth to last scattering $\tau = 0.17 \pm 0.04$ (Kogut et al. 2003) from the WMAP TE measurements are the first example of CMB polarization offering new constraints on the history of our universe.

Meanwhile, DASI has continued to collect data. Given that our E and B uncertainties on all scales are still noise dominated, we have determined that our best observing strategy is to continue to integrate deeper on our current two fields. Being noise dominated, our errorbars will shrink roughly in proportion to total observing time. We collected 18 additional days of polarization observation in the 2002 winter season, and have continued in this mode this year, with a total of 120 new days as of July 8, 2003. With the data reduction and analysis tools described in this thesis already in place, it is straightforward to incorporate this new data. Initial analyses show good consistency between new data and our previous dataset. Preliminary results of including this new data in our $E5/B5$ analysis are shown in Figure 7.2. A complete analysis of this and the additional data that will be taken this season will be presented in Leitch et al. (2003).

While the DASI results will continue to improve, much greater sensitivity will be needed to make the precision measurements of CMB E-mode spectrum which will substantially improve constraints on the parameters of the standard model over those from temperature measurements alone (Zaldarriaga et al. 1997; Eisenstein et al. 1999). A host of new experiments is already working toward this challenge. This year, polarization-sensitive versions of the two balloon-based bolometer experiments,

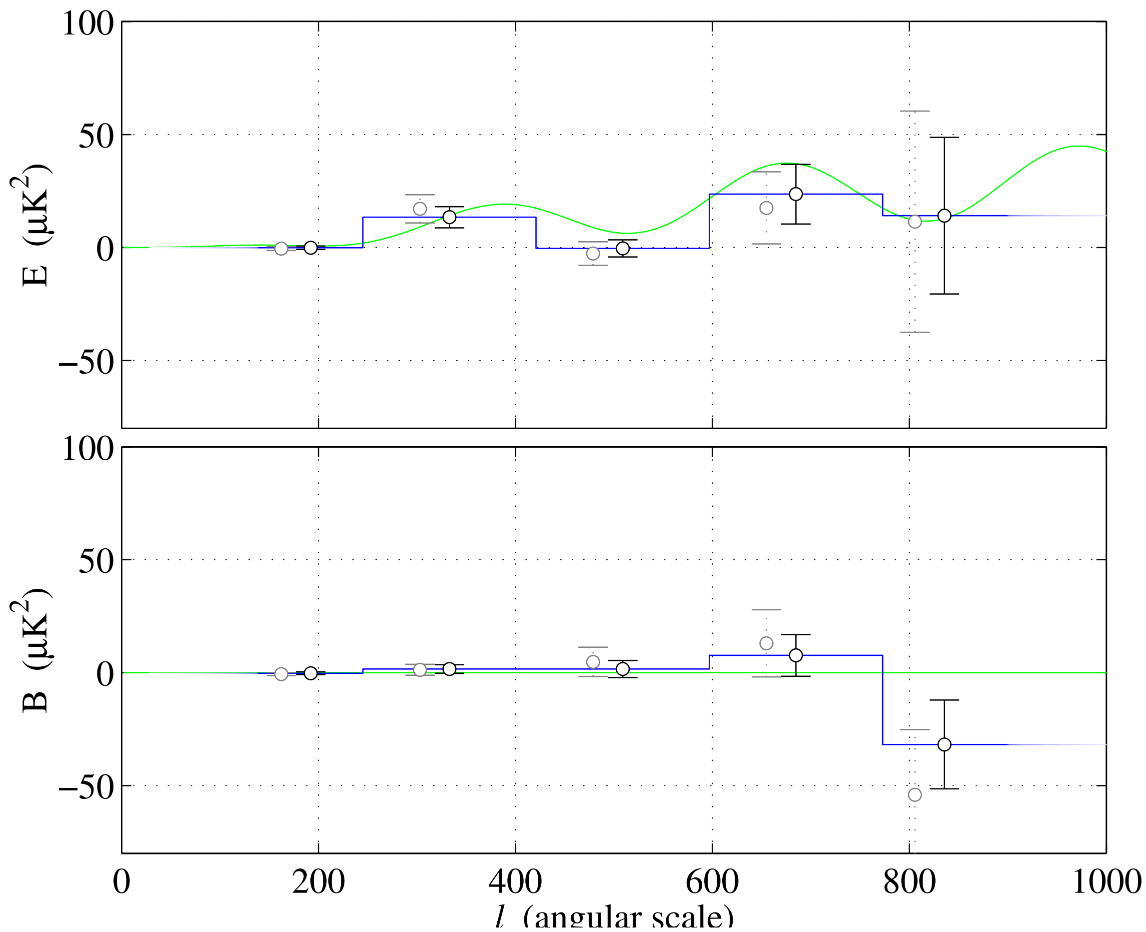

Figure 7.2 Preliminary results from new (2003) DASI data. Shown is the five-band E and B spectrum likelihood analysis previously illustrated in Figure 6.6, before (dotted gray) and after (solid black) inclusion of additional data through mid-July 2003. Errorbars (in this case, derived from the Fisher matrix) are still noise-dominated at all angular scales, and so they will shrink roughly in proportion to total observing time. Final results will be presented in (Leitch et al. 2003).

Boomerang (Montroy et al. 2003) and Maxima (Johnson et al. 2003), have flown collecting data which hopefully will produce new polarization detections. The CAPMAP experiment (Barkats 2003), a successor to the PIQUE correlation polarimeter, has begun collecting data using the 7m Crawford Hill telescope, targeting the E spectrum around $l \sim 1000$ where it is expected to peak. Also targeting these angular scales is the CBI interferometer, which has been upgraded this year with DASI achromatic polarizers and has begun dedicated polarization observations in a close-packed configuration which maximizes sensitivity.

The great challenge for the future of the CMB is likely to be the search for B mode polarization. As discussed in §1.3, at $l \gtrsim 200$ the B modes generated from E modes which have been gravitationally lensed will directly probe the growth of mass structures at high redshift. Their measurement could constrain neutrino mass and the evolution of dark energy. At larger scales, if B modes from primordial tensor perturbations prove observable, they will take us beyond the standard model to directly constrain the physics of inflation. The Planck satellite, scheduled to launch in 2007, should measure the E spectrum to high precision, but is unlikely to have the sensitivity to detect either of these faint B signals. For this mission, new generations of dedicated experiments are already being built. The required sensitivity demands massive detector arrays, long integration times, and control over systematics.

The stability and control offered by interferometry would be well suited to this mission, but to reach the required array sizes the scaling limitations of existing correlators will have to be overcome. Focal plane bolometer arrays are considered more easily scalable, and much of the current focus is on the development of polarization experiments based on these. Two such experiments now plan to begin searching for CMB B-mode polarization from the South Pole as early as 2004: BICEP, which targets inflationary gravity waves (Keating et al. 2003), and QUEST, which will observe E modes and lensing B modes, reusing the DASI mount (Church et al. 2003). Looking ahead, a CMB polarimeter has been planned for the 10m South Pole Telescope, and in the past year momentum has been gathering to develop a new B-mode satellite mission, currently dubbed “CMBpol”.

The DASI detection of CMB polarization reported here has provided strong support for our understanding of the physics underlying the generation of CMB anisotropy. These results have lent confidence to the values of the cosmological parameters and to the extraordinary picture of the origin and composition of the universe that has been derived from CMB measurements. Many ongoing and planned CMB experiments are taking up the challenge of pursuing precision polarization measurements to extend our understanding of the universe. The detection of CMB polarization at the predicted level has pointed to a promising future for the field.

Bibliography

Alpher, R. A. and Herman, R. C. 1949, Physical Review, 75, 1089

Banday, A. J. and Wolfendale, A. W. 1991, MNRAS, 248, 705

Barkats, D. 2003, in the proceedings of the workshop on "The Cosmic Microwave Background and its Polarization," New Astronomy Reviews, ed. S. Hanany & K. A. Olive (Elsevier), astro-ph/0306002

Bennett, C. L. *et al.* 2003a, ApJ submitted, astro-ph/0302207

—. 2003b, ApJS, 148, 97

Benoît, A. *et al.* 2003, A&A, 399, L19, astro-ph/0210305

Bond, J. R. and Efstathiou, G. 1984, ApJ, 285, L45

Bond, J. R., Jaffe, A. H., and Knox, L. 1998, Phys. Rev. D, 57, 2117

—. 2000, ApJ, 533, 19, astro-ph/9808264

Bucher, M., Moodley, K., and Turok, N. 2001, Phys. Rev. Lett., 87, 191301 (4 pages)

Burles, S., Nollett, K. M., and Turner, M. S. 2001, Phys. Rev. D, 63, 063512, astro-ph/0008495

Caderni, N., Fabbri, R., Melchiorri, B., Melchiorri, F., and Natale, V. 1978, Phys. Rev. D, 17, 1908

Carroll, S. 2001, astro-ph/0107571, also April 2002 APS Meeting Abstracts, 1001

Cartwright, J. K. 2003, PhD thesis, Caltech

Chandrasekhar, S. 1960, Radiative Transfer (New York: Dover)

Chon, G., Challinor, A., Prunet, S., Hivon, E., and Szapudi, I. 2003, astro-ph/0303414

Christensen, N., Meyer, R., Knox, L., and Luey, B. 2001, Classical and Quantum Gravity, 18, 2677

Church, S. *et al.* 2003, in the proceedings of the workshop on "The Cosmic Microwave Background and its Polarization," New Astronomy Reviews, ed. S. Hanany & K. A. Olive (Elsevier), astro-ph/0308****

Coulson, D., Crittenden, R. G., and Turok, N. G. 1994, Physical Review Letters, 73, 2390

Crane, P. C. and Napier, P. J. 1989, in ASP Conf. Ser. 6: Synthesis Imaging in Radio Astronomy, 139

Crittenden, R., Davis, R. L., and Steinhardt, P. J. 1993, ApJ, 417, L13

de Bernardis, P. *et al.* 2000, Nature, 404, 955

de Oliveira-Costa, A., Tegmark, M., O'Dell, C., Keating, B., Timbie, P., Efstathiou, G., and Smoot, G. 2003a, in the proceedings of the workshop on "The Cosmic Microwave Background and its Polarization," New Astronomy Reviews, ed. S. Hanany & K. A. Olive (Elsevier), astro-ph/0305590

de Oliveira-Costa, A., Tegmark, M., Zaldarriaga, M., Barkats, D., Gundersen, J. O., Hedman, M. M., Staggs, S. T., and Winstein, B. 2003b, Phys. Rev. D, 67, astro-ph/0204021

Dicke, R. H., Peebles, P. J. E., Roll, P. G., and Wilkinson, D. T. 1965, ApJ, 142, 414

Eisenstein, D. J., Hu, W., and Tegmark, M. 1999, ApJ, 518, 2

Finkbeiner, D. P. 2001, private communication

Finkbeiner, D. P., Davis, M., and Schlegel, D. J. 1999, ApJ, 524, 867

Fixsen, D. J., Cheng, E. S., Gales, J. M., Mather, J. C., Shafer, R. A., and Wright, E. L. 1996, ApJ, 473, 576

Fomalont, E. B., Kellermann, K. I., and Wall, J. V. 1984, ApJ, 277, L23

Gaensler, B. M., Dickey, J. M., McClure-Griffiths, N. M., Green, A. J., Wieringa, M. H., and Haynes, R. F. 2001, ApJ, 549, 959

Gaustad, J. E., Rosing, W., McCullough, P. R., and van Buren, D. 2000, PASP, 220, 169

Giardino, G., Banday, A. J., Górski, K. M., Bennett, K., Jonas, J. L., and Tauber, J. 2002, A&A, 387, 82

Gray, A. D., Landecker, T. L., Dewdney, P. E., Taylor, A. R., Willis, A. G., and Normandeau, M. 1999, ApJ, 514, 221

Grego, L., Carlstrom, J. E., Reese, E. D., Holder, G. P., Holzapfel, W. L., Joy, M. K., Mohr, J. J., and Patel, S. 2001, ApJ, 552, 2

Högbom, J. A. 1974, A&AS, 15, 417

Halverson, N. W. 2002, PhD thesis, Caltech

Halverson, N. W., Carlstrom, J. E., Dragovan, M., Holzapfel, W. L., and Kovac, J. 1998, in SPIE Conf. Proc., Vol. 3357, Advanced Technology MMW, Radio, and Terahertz Telescopes, 416

Halverson, N. W. *et al.* 2002, ApJ, 568, 38

Hanany, S. *et al.* 2000, ApJ, 545, L5, astro-ph/0005123

Haslam, C. G. T., Klein, U., Salter, C. J., Stoffel, H., Wilson, W. E., Cleary, M. N., Cooke, D. J., and Thomasson, P. 1981, A&A, 100, 209

Hedman, M. M., Barkats, D., Gundersen, J. O., McMahon, J. J., Staggs, S. T., and Winstein, B. 2002, ApJ, 573, L73

Hedman, M. M., Barkats, D., Gundersen, J. O., Staggs, S. T., and Winstein, B. 2001, ApJ, 548, L111

Hildebrand, R. H., Davidson, J. A., Dotson, J. L., Dowell, C. D., Novak, G., and Vaillancourt, J. E. 2000, PASP, 112, 1215

Hinshaw, G. *et al.* 2003, ApJ submitted, astro-ph/0302217

Hivon, E. and Kamionkowski, M. 2002, Science, 298, 1349

Hu, W. 2002, Phys. Rev. D, 65, 23003

—. 2003, Annals of Physics, 303, 203, astro-ph/0210696

Hu, W. and Dodelson, S. 2002, ARA&A, 40, 171

Hu, W. and Okamoto, T. 2002, ApJ, 574, 566

Hu, W., Spergel, D. N., and White, M. 1997, Phys. Rev. D, 55, 3288

Hu, W. and Sugiyama, N. 1995, ApJ, 444, 489

Hu, W. and White, M. 1997, New Astronomy, 2, 323, astro-ph/9706147

Johnson, B. R. *et al.* 2003, in the proceedings of the workshop on "The Cosmic Microwave Background and its Polarization," New Astronomy Reviews, ed. S. Hanany & K. A. Olive (Elsevier)

Jones, M. E. 1996, in Moriond Astrophysics Meetings, Vol. XVI, Microwave Background Anistropies, ed. B. G. J. V. F.R. Bouchet, R. Gispert (Gif-sur-Yvette: Editions Frontieres), 161, ISBN: 3863322087

Jones, M. E. 1997, in PPEUC proceedings (Cambridge), April 7

Kaiser, N. 1983, MNRAS, 202, 1169

Kamionkowski, M., Kosowsky, A., and Stebbins, A. 1997a, Phys. Rev. Lett., 78, 2058

—. 1997b, Phys. Rev. D, 55, 7368

Kaplinghat, M., Knox, L., and Song, Y. 2003, ArXiv Astrophysics e-prints, astro-ph/0303344

Keating, B. G., Ade, P. A. R., Bock, J. J., Hivon, E., Holzapfel, W. L., Lange, A. E., Nguyen, H., and Yoon, K. 2003, in Polarimetry in Astronomy. Edited by Silvano Fineschi. Proceedings of the SPIE, Volume 4843., 284

Keating, B. G., O'Dell, C. W., de Oliveira-Costa, A., Klawikowski, S., Stebor, N., Piccirillo, L., Tegmark, M., and Timbie, P. T. 2001, ApJ, 560, L1

Kesden, M., Cooray, A., and Kamionkowski, M. 2002, Phys. Rev. Lett., 89, 011304 (4 pages)

Kinney, W. H. 2001, Phys. Rev. D, 63, 43001 (6 pages)

Knox, L. 1999, Phys. Rev. D, 60, 103516 (5 pages), astro-ph/9902046

Knox, L. and Song, Y. 2002, Phys. Rev. Lett., 89, 011303 (4 pages)

Kogut, A. *et al.* 2003, ApJ submitted, astro-ph/0302213

Kolb, E. and Turner, M. 1990, The Early Universe (Redwood City, CA: Addison-Wesley Publishing Company)

Kovac, J. M. and Carlstrom, J. E. 2002, U.S. patent application, 60/357597, provisional filing.

Kovac, J. M., Leitch, E. M., Pryke, C., Carlstrom, J. E., Halverson, N. W., and Holzapfel, W. L. 2002, Nature, 420, 772, astro-ph/0209478

Kraus, J. D. 1986, Radio Astronomy, 2nd ed. (Powell, OH: Cygnus-Quasar Books), 4.1

Krauss, L. and Turner, M. S. 1995, Gen. Rel. Grav. 27, 1137, astro-ph/9504003

Kuo, C. L. *et al.* 2002, ApJ submitted, astro-ph/0202289

Lay, O. P. and Halverson, N. W. 2000, ApJ, 543, 787

Lazarian, A. and Prunet, S. 2002, in AIP Conf. Proc. 609: Astrophysical Polarized Backgrounds, ed. S. Cecchini, S. Cortiglioni, R. Sault, & C. Sbarra (Melville, NY: AIP), 32

Lee, A. T. *et al.* 2001, ApJ, 561, L1

Leitch, E. M., Kovac, J. M., Pryke, C., Carlstrom, J. E., Halverson, N. W., and Holzapfel, W. L. 2003, ApJ, in preparation

Leitch, E. M., Kovac, J. M., Pryke, C., Carlstrom, J. E., Halverson, N. W., Holzapfel, W. L., Reddall, B., and Sandberg, E. S. 2002a, Nature, 420, 763, astro-ph/0209476

Leitch, E. M. *et al.* 2002b, ApJ, 568, 28, astro-ph/0104488

Lier, E. and Schaug-Pettersen, T. 1988, IEEE-MTT, 36, 1531

Lo, K. Y. *et al.* 2001, in AIP Conf. Proc. 586: 20th Texas Symposium on relativistic astrophysics, 172, astro-ph/0012282

Lubin, P., Melese, P., and Smoot, G. 1983, ApJ, 273, L51

Lubin, P. M. and Smoot, G. F. 1979, Phys. Rev. Lett., 42, 129

—. 1981, ApJ, 245, 1

Lyth, D. H. 1997, Phys. Rev. Lett., 78, 1861

Mason, B. S., Pearson, T. J., Readhead, A. C. S., Shepherd, M. C., and Sievers, J. L. 2002, ApJ, submitted, astro-ph/0205384

Mather, J. C. *et al.* 1994, ApJ, 420, 439

Mauskopf, P. D. *et al.* 2000, ApJ, 538, 505

McCullough, P. R. 2001, private communication

Miller, A. D. *et al.* 1999, ApJ, 524, L1

Mitchell, D. I. and De Pater, I. 1994, Icarus, 110, 2

Moffat, P. H. 1972, MNRAS, 160, 139

Mohr, J., Mathiesen, B., and Evrard, A. 1999, ApJ, 517, 627

Montroy, T. *et al.* 2003, in the proceedings of the workshop on "The Cosmic Microwave Background and its Polarization," New Astronomy Reviews, ed. S. Hanany & K. A. Olive (Elsevier), astro-ph/0305593

Morris, D., Radhakrishnan, V., and Seielstad, G. A. 1964, ApJ, 139, 551

Nanos, G. P. 1979, ApJ, 232, 341

Netterfield, C. B. *et al.* 2002, ApJ, 571, 604

Newman, E. and Penrose, R. 1966, J. Math Phys., 7, 863

Ostriker, J. P. and Steinhardt, P. J. 1995, Nature, 377, 600+, astro-ph/9505066

Padin, S., Cartwright, J. K., Shepherd, M. C., Yamasaki, J. K., and Holzapfel, W. L. 2001, IEEE Trans. Instrum. Meas., 50, 1234

Pancharatnam, S. 1955, Proc. Indian Acad. Sci., 130

Partridge, R. B. 1995, 3K: The Cosmic Microwave Background Radiation (New York: Cambridge University Press)

Partridge, R. B., Nowakowski, J., and Martin, H. M. 1988, Nature, 331, 146

Partridge, R. B., Richards, E. A., Fomalont, E. B., Kellermann, K. I., and Windhorst, R. A. 1997, ApJ, 483, 38

Pearson, T. J. *et al.* 2002, ApJ, astro-ph/0205388

Penzias, A. A. and Wilson, R. W. 1965, ApJ, 142, 419

Perlmutter, S. *et al.* 1999, ApJ, 517, 565

Platania, P., Bensadoun, M., Bersanelli, M., De Amici, G., Kogut, A., Levin, S., Maino, D., and Smoot, G. F. 1998, ApJ, 505, 473

Polnarev, A. G. 1985, Soviet Ast., 29, 607

Pospieszalski, M. W., Lakatosh, W. J., Nguyen, L. D., Lui, M., Liu, T., Le, M., Thompson, M. A., and Delaney, M. J. 1995, IEEE MTT-S Int. Microwave Symp., 1121

Pospieszalski, M. W., Nguyen, L. D., Lui, M., Lui, T., Thompson, M. A., and Delaney, M. J. 1994, Proc. 1994 IEEE MTT-S Int. Microwave Symp., San Diego, CA., 1345

Pryke, C., Halverson, N. W., Leitch, E. M., Kovac, J., Carlstrom, J. E., Holzapfel, W. L., and Dragovan, M. 2002, ApJ, 568, 46

Readhead, A. C. S., Lawrence, C. R., Myers, S. T., Sargent, W. L. W., Hardebeck, H. E., and Moffet, A. T. 1989, ApJ, 346, 566

Rees, M. J. 1968, ApJ, 153, L1

Riess, A. G. *et al.* 1998, AJ, 116, 1009

Scott, P. F. and et al. 2002, MNRAS, submitted, astro-ph/0205380

Seljak, U. 1997, ApJ, 482, 6

Seljak, U. and Zaldarriaga, M. 1996, ApJ, 469, 437

—. 1997, Phys. Rev. Lett., 78, 2054

Simard-Normandin, M., Kronberg, P. P., and Button, S. 1981a, ApJS, 45, 97

Simard-Normandin, M., Kronberg, P. P., and Neidhoefer, J. 1981b, A&AS, 43, 19

Sironi, G., Boella, G., Bonelli, G., Brunetti, I., Cavaliere, F., Gervasi, M., Giardino, G., and Passerini, A. 1997, New Astronomy, 3, 1

Smoot, G. F. 1999, in AIP Conf. Proc. 476: 3K cosmology, 1, astro-ph/9902027

Smoot, G. F. *et al.* 1992, ApJ, 396, L1

Spergel, D. N. *et al.* 2003, ApJ submitted, astro-ph/0302209

Srikanth, S. 1997, IEEE-MGWL, 7, 150

Staggs, S. T., Gunderson, J. O., and Church, S. E. 1999, in ASP Conf. Ser. 181: Microwave Foregrounds, ed. A. de Oliveira-Costa & M. Tegmark, 299

Subrahmanyan, R., Ekers, R. D., Sinclair, M., and Silk, J. 1993, MNRAS, 263, 416

Subrahmanyan, R., Kesteven, M. J., Ekers, R. D., Sinclair, M., and Silk, J. 2000, MNRAS, 315, 808

Tegmark, M. 1997a, ApJ, 480, L87

—. 1997b, Phys. Rev. D, 55, 5895

Tegmark, M. and de Oliveira-Costa, A. 2001, Phys. Rev. D, 64, 063001 (15 pages)

Tegmark, M., Eisenstein, D. J., Hu, W., and de Oliveira-Costa, A. 2000, ApJ, 530, 133

Thompson, A. R., Moran, J. M., and Swenson, G. W. 1991, Interferometry and Synthesis in Radio Astronomy (Malabar, Fla. : Krieger Pub., 1991.), 47

Timbie, P. T. and Wilkinson, D. T. 1984, BAAS, 16, 517

Tucci, M., Martinez-Gonzalez, E., Toffolatti, L., Gonzalez-Nuevo, J., and De Zotti, G. 2003, MNRAS submitted, astro-ph/0307073

Turner, M. S. 2002, ApJ, 576, L101, astro-ph/0106035

Uher, Bornemann, and Rosenberg. 1993, Waveguide Components for Antenna Feed Systems: Theory and CAD (Boston, MA: Artech House)

Wang, X., Tegmark, M., and Zaldarriaga, M. 2002, Phys. Rev. D, 65, 123001 (14 pages)

White, M., Carlstrom, J. E., Dragovan, M., and Holzapfel, W. H. 1999a, ApJ, 514, 12, astro-ph/9712195

White, M., Carlstrom, J. E., Dragovan, M., Holzapfel, W. H., Halverson, N. W., Kovac, J., and Leitch, E. M. 1999b, exists only as astro-ph/9912422

Wright, A. E., Griffith, M. R., Burke, B. F., and Ekers, R. D. 1994, ApJS, 91, 111

Zaldarriaga, M. 2001, Phys. Rev. D, submitted, astro-ph/0106174

—. 2003, Carnegie Observatories Astrophysics Series II, astro-ph/0305272

Zaldarriaga, M. and Harari, D. D. 1995, Phys. Rev. D, 52, 3276

Zaldarriaga, M. and Seljak, U. 1997, Phys. Rev. D, 55, 1830

—. 1998, Phys. Rev. D, 58, 23003 (6 pages)

Zaldarriaga, M., Spergel, D. N., and Seljak, U. 1997, ApJ, 488, 1

Zukowski, E. L. H., Kronberg, P. P., Forkert, T., and Wielebinski, R. 1999, A&AS, 135, 571